DEVELOPMENT OF MESHFREE STRONG-FORM METHODS

KEE BUCK TONG, BERNARD

(B. Eng. (Hons.), NUS)

A THESIS SUBMITTED

FOR THE DEGREE OF DOCTOR OF PHILOSOPHY

DEPARTMENT OF MACHANICAL ENGINEERING

NATIONAL UNIVERSITY OF SINGAPORE

2007

Acknowledgements

I would like to express my deepest gratitude to my supervisor, Prof. Liu Guirong, for his dedicated support, guidance and continuous encouragement during my Ph.D. study. To me, Prof. Liu is also a kind mentor who inspires me not only in my research work but also in many aspects of my life. I would also like to extend a great thank to my co-supervisor, Dr. Lu Chun, for his valuable advices in many aspects of my research work.

I would also like to give many thanks to my fellow colleagues and friends in Center for ACES, Dr. Gu Yuan Tong, Dr. Liu Xin, Dr. Dai Keyang, Dr. Zhang Guiyong, Dr. Zhao Xin, Dr. Deng Bin, Mr. Li Zirui, Mr. Zhang Jian, Mr. Khin Zaw, Mr. Song Chengxiang, Ms. Chen Yuan, Mr. Phuong, Mr. Trung, Mr. Chou Cheng-En, Mr. George Xu. The constructive suggestions, professional opinions, interactive discussions among our group definitely help to improve the quality of my research work. And most importantly, these guys have made my life in Center for ACES a joyful one.

I am also indebted to many of my close friends, friends from JBKakis, Man Woei, Kuang Hoe, You Mao, who continuously encourage and motivate me to keep up the good job. Without this valuable friendship and love, my life is not going to be stimulating, interesting and enjoyable.

Great appreciation is extended to my dearest family members, my parents, my sisters, Susanna, Kathy and Karen for their strong support and cares. Not to mention, I own very much to my lovely fiancée, Michelle Ding, who is always giving me strong

support, great tolerance, cares and understanding. It is impossible for me to complete this work without her love. This piece of work is also a present for our wedding.

Lastly, I appreciate the National University of Singapore for granting me research scholarship whick makes my Ph.D. study possible. Thanks A*STAR for the pre-graduate scholarship which supports me during the last year of my undergraduate study. Many thanks are conveyed to Mechanical department and Center for ACES for their material support to every aspect of this work.

Table of contents

Acknowledgements ..... **i**

Table of contents ..... **iii**

Summary ..... **ix**

Nomenclature ..... **xiii**

List of Figures ..... **xvi**

List of Tables ..... **xxviii**

Chapter 1 Introduction **1**

1.1 Background **1**

1.1.1 Motivation of Meshfree Methods 1

1.1.2 Features of Meshfree Methods 3

1.2 Literature review **5**

1.2.1 Classification of Meshfree Methods 6

1.2.2 Meshfree Weak-form Methods 8

1.2.3 Meshfree Strong-form Methods 8

1.2.4 Meshfree Weak-Strong Form Methods 9

1.3 Motivation of the Thesis **9**

1.4 Objectives of the Thesis **11**

1.5 Organization of the Thesis **13**

Chapter 2 Function Approximations **16**

2.1 Introduction **16**

2.2 Smooth Particle Hydrodynamics (SPH) Approximation **17**

2.3 Reproducing Kernel Particle Method (RKPM) Approximation 18

2.4 Moving Least-Squares (MLS) Approximation 19

2.5 Polynomial Point Interpolation Method (PPIM) Approximation 21

2.5.1 Formulation of Polynomial Point Interpolation Method 22

2.5.2 Properties of PPIM Shape Function 24

2.5.3 Techniques to Overcome Singularity in Moment Matrix 26

2.6 Radial Point Interpolation Method (RPIM) Approximation 27

2.6.1 Formulation of Radial Point Interpolation Method 28

2.6.2 Property of RPIM Shape Function 30

2.6.3 Radial Basis Functions 32

2.6.4 Implementation Issues of RPIM Approximation 33

2.6.5 Comparison between RPIM and PPIM Shape Functions 34

Chapter 3 Adaptivity 39

3.1 Introduction 39

3.2 Definition of Errors 40

3.3 Error Estimators 42

3.3.1 Interpolation Variance Based Error Estimator 43

3.3.1.1 Formulation of Interpolation Variance Based Error Estimator 43

3.3.1.2 Remarks 44

3.3.2 Residual Based Error Estimator 45

3.3.2.1 Formulation of Residual Based Error Estimator 46

3.3.2.2 Numerical Examples: 47

3.3.2.3 Remarks 55

3.4 Adaptive Strategy 57

3.4.1 Local Refinement Criterion 57

3.4.2 Stopping Criterion 58

3.5 Refinement Procedure 58

3.5.1 Refinement Procedure for Interpolation Variance based Error Estimator 59
3.5.2 Refinement Procedure for Residual based Error Estimator 59

Chapter 4 Radial Point Collocation Method (RPCM) 73

4.1 Introduction 73

4.2 Formulation of RPCM 74

4.3 Issues in RPCM 76

4.4 Numerical Examples: 79

4.4.1 Example 1: One Dimensional Poisson Problem 79
4.4.2 Example 2: Two dimensional Poisson Problem with Dirichlet Boundary Conditions 81
4.4.3 Example 3: Standard and Higher Order Patch Tests 82
4.4.4 Example 4: Elastostatics Problem with Neumann Boundary Conditions 84

4.5 Remarks: 86

Chapter 5 A Stabilized Least-Squares Radial Point Collocation Method (LS-RPCM) 94

5.1 Introduction 94

5.2 Stabilized Least-squares Procedure 95

5.3 Numerical Examples 100

5.3.1 Example 1: A Cantilever Beam Subjected to a Parabolic Shear Stress at the Right End 100
5.3.2 Example 2: Poisson Problem with Neumann Boundary Conditions 103
5.3.3 Example 3: Infinite Plate with Hole Subjected to an Uniaxial Traction in the Horizontal Direction 105
5.3.4 Example 4: A L-shaped Plate Subjected to a Unit Tensile Traction in the Horizontal Direction 106

5.4 Remarks 107

Chapter 6 A Least-Square Radial Point Collocation Method (LS-RPCM) with Special Treatment for Boundaries 119

6.1 Introduction 119

6.2 Least-square Procedure with Special Treatment for Boundaries 120

6.3 Numerical Examples 123

6.3.1 Example 1: Infinite Plate with Hole Subjected to a Uniaxial Traction in the Horizontal Direction 124

6.3.2 Example 2: Cantilever Beam Subjected to a Parabolic Shear Traction at the End 125

6.3.3 Example 3: Poisson Problem with Smooth Solution 127

6.3.4 Example 4: A Thick Wall Cylinder Subjected an Internal Pressure 128

6.3.5 Example 5: A Reservoir Full Filled with Water 130

6.4 Remarks 131

Chapter 7 A Regularized Least-Square Radial Point Collocation Method (RLS-RPCM) 151

7.1 Introduction 151

7.2 Regularization Procedure 152

7.2.1 Regularization Equations 152

7.2.2 Regularization Least-square Formulation 154

7.2.3 Determination of Regularization Factor 155

7.3 Numerical Examples 156

7.3.1 Example 1: Cantilever Beam 157

7.3.2 Example 2: Hollow Cylinder with Internal Pressure 159

7.3.3 Example 3: Bridge with Uniform Loading on the Top 160

7.3.4 Example 4: Poisson Problem with High Gradient Solution 161

7.3.5 Example 5: Poisson Problem with Multiple Peaks Solution 163

7.4 Remarks 165

Chapter 8 A Subdomain Method Based on Local Radial Basis Functions 184

8.1 Introduction 184

8.2 Formulation of Subdomain Method 186

8.3 Numerical Examples 192

8.3.1 Example 1: Standard and Higher order Patch Tests 193

8.3.2 Example 2: Connecting Rod Subjected to Internal Pressure 193

8.3.3 Example 3: A Cantilever Beam Subjected to a Parabolic Shear at End 194

8.3.4 Example 4: Adaptive Analysis of Elastostatics Problem 195

8.3.5 Example 5: Adaptive Analysis of Short Beam Subjected to Uniform Loading on the Top Edge 196

8.3.6 Example 6: Adaptive Analysis of Bridge Subjected to Uniform Loading on the Top Edge 198

8.3.7 Example 7: Adaptive Analysis of Crack Problem 199

8.4 Remarks 200

Chapter 9 Effects of the Number of Local Nodes for Meshfree Methods Based on Local Radial Basis Functions 220

9.1 Introduction 220

9.2 Nodal Selection 222

9.3 Concept of Layer 224

9.4 Numerical Examples 225

9.3.1 Examples 1: Curve Fitting 225

9.3.2 Examples 2: LC-RPIM (Weak-form Method) for Elastostatics Problem 227

9.3.3 Examples 3: RPCM (Strong-form Method) for Torsion Problem 228

9.3.4 Examples 4: RLS-RPCM (Strong-form) for Elastostatics Problem 231

9.3.5 Examples 5: Adaptive RPCM for Dirichlet Problem 232

9.5 Remarks 234

Chapter 10 Conclusion and Future Work 255

10.1 Conclusion Remarks 255

10.2 Recommendation for future work 259

References 261

Publications Arising From Thesis 270

Summary

Meshfree method is a new promising numerical method after the finite element method (FEM) has been dominant in computational mechanics for several decades. The feature of mesh free has drawn a lot of attention from mathematicians and researchers. Development of meshfree method has achieved remarkable success in recent years. Among the meshfree methods, the progress of the development of meshfree strong-form method is still very sluggish. As compared to meshfree weak-form method, the relevant research works dedicated to meshfree strong-form method are still not abundantly available in the literature. Nonetheless, strong-form meshfree method possesses many attractive and distinguished features that facilitate the implementation of the adaptive analysis.

In this study, the two primary objectives are:

(1) To provide remedies to stabilize the solution of strong-form meshfree method

(2) To extend strong-form meshfree method to adaptive analysis

Radial point collocation method (RPCM) is a strong-form meshfree method studied in this work. Instability is a fatal shortcoming that prohibits RPCM from being used in adaptive analysis. The first contribution of this thesis is to propose several techniques that can be employed to stabilize the solution of RPCM before it can be used in adaptive analysis. Stabilized least-squares RPCM (LS-RPCM) is the first proposed meshfree strong-form method that uses stabilization least-squares technique to restore the stability of RPCM solution. In the stabilization procedure, additional governing

equation is suggested to be imposed along Dirichlet boundaries in order to achieve certain degree of equilibrium.

Next, another new least-square RPCM (LS-RPCM) with special treatment on the boundaries is proposed. According to the literature reviews and my close examination, the cause of the instability is due to the existence of Neumann boundary condition and "strong" requirement of the satisfaction of boundary conditions. Hence, more collocation points (*not nodes*) are introduced along the boundaries to provide a kind of "relaxation" effect for the imposition of the boundary conditions.

In addition, regularization technique is suggested to restore the stability of the RPCM solution. Although regularization technique is a well-known technique that is widely used in the ill-posed inverse problems, it is a very new idea to adopt the regularization technique in the forward problem. The stability of RPCM solution has been effectively restored by the Tikhonov regularization technique as demonstrated in the regularized least-squares radial point collocation method (RLS-RPCM).

Besides the strong-form method, a very classical subdomain method is also presented in this thesis. Unlike the strong-form method that satisfies the governing equation on the nodes, subdomain method allows the governing equation to be satisfied in an average sense in the local subdomain. Through the valuable experiences gained in the meshfree methods, meshfree techniques are integrated in the subdomain method. The subdomain that incorporates with the meshfree techniques has demonstrated great numerical performance in term of accuracy and stability.

The second significant contribution of this work is the development of an error estimator for strong-form meshfree method. Most of the existing error estimators for adaptive meshfree method are an extension of the conventional error estimators for FEM which is formulated in term of weak-form. Thus, developing a robust, effective and feasible error estimator for strong-form method is a primary task before meshfree strong-form can be extended to adaptive analysis. A novel residual based error estimator is proposed in this thesis. In fact, this versatile error estimator has been shown not only feasible for strong-form method but also for weak-form method. Furthermore, the residual based error estimator is also applicable for many numerical methods regardless of the use of mesh.

As an error estimator that is feasible for strong-form meshfree method is available and stability of the RPCM solution is restored, all the presented meshfree strong-form methods and subdomain method have been successfully extended to adaptive analysis. All the presented adaptive meshfree methods have been shown to be very simple and easy to implement due to the features of mesh free. Neither remeshing nor complicated refinement technique is needed in the adaptation.

Last of all, a very thorough study on the effects of the number of local nodes for meshfree methods based on local radial basis functions (RBFs) is undertaken. As local RBFs are used in the RPIM approximation in this present work, a comprehensive study for local RBFs is very important. Although the effects of shape parameters have been greatly discussed in literature, the effects of the number of local nodes for meshfree methods based on local RBFs are still not well studied. The final significant

contribution of my work is to provide an insight and comprehensive study in this aspect. Many meshfree methods that use local RBFs are studied on the effects of the number of local nodes and decisive conclusions for using local RBFs are drawn in the study. Approximation using local RBFs has demonstrated incredible advantages in my investigation.

Nomenclature

$\mathbf{a}$	Coefficient vector
A	Area of the domain
$\mathbf{b}$	Body force vector
$\mathbf{B}$	Strain matrix
d_c	Characteristic length (average nodal spacing)
div	Divergence operator
$\mathbf{D}$	Elasticity matrix for linear elastic material
E	Young's modulus
e_n	Error norm
$\|e\|$	Energy norm for error
$\mathbf{f}$	Force vector
$\mathbf{F}_r$	Regularized force vector
G	Shear modulus
I	Moment of inertia of section
$\mathbf{K}$	Stiffness matrix
$\mathbf{K}_r$	Regularized stiffness matrix
$L(\ ), B(\ )$	Differential operator
$\mathbf{n}$	Vector of unit outward normal
n	Number of supporting nodes
N	Total number of field nodes
$P(\mathbf{x})$	Polynomial basis function
$\mathbf{P}_m$	Polynomial moment matrix
q	Shape parameter of MQ radial basis function
r	Distance

Res^T	Residual at the Delaunay cell T
$R(\mathbf{x})$	Radial basis function
$\mathbf{R}_Q$	Moment matrix of radial basis function
$s(\mathbf{x}_i)$	Interpolation value at $\mathbf{x}_i$
T	Delaunay cell
$\mathbf{t}$	Specified traction vector
$\mathbf{U}$	Displacement vector
$\mathbf{U}_s$	Displacement vector of local support domain
$\bar{\mathbf{u}}$	Specified displacement vector
u	Field function
u_r	Field function on regularization point
u^h	Approximation of field function u
$\mathbf{x} = [x\ y\ z]^T$	Cartesian coordinate
α	Stabilization factor
α_r	Regularization factor
α_c	Parameter of MQ radial basis function
Γ	Boundary of problem domain
Γ_u	Dirichlet boundary
Γ_t	Neumann boundary
δ	Kronecker delta
Δl	Length of the edge of subdomain
$\boldsymbol{\varepsilon}$	Strain tensor
η_i	Local error estimator based on interpolation variance.
η_L	Local error estimator based on residual

η_G	Estimated global residual norm
η_{ML}	Maximum value of η_L in the entire problem domain
η_{MG}	Maximum value of η_G throughout the adaptation
κ_l	Refinement coefficient
κ_g	Tolerant coefficient of the estimated global residual norm
φ_i	Shape function component
$\mathbf{\Phi}$	Shape function vector
υ	Poisson's ratio
$\boldsymbol{\sigma}$	Stress tensor
$\boldsymbol{\Omega}$	Problem domain
$\boldsymbol{\Omega}^T$	Local domain of Delaunay cells
$\boldsymbol{\Omega}_s$	Local subdomain

List of Figures

Figure 2.1 Pascal triangle of monomials for two dimensional spaces 38

Figure 3.1 Estimated global residual norm at each adaptive step. 61

Figure 3.2 Nodal distribution of the model of cylinder at each adaptive step. 61

Figure 3.3 Error norm of displacements at each adaptive step. 62

Figure 3.4 Energy norm for error at each adaptive step. 62

Figure 3.5 Displacements in y-direction along $x = 0$ at each adaptive step. 63

Figure 3.6 Normal stress σ_{xx} along $y = 0$ at each adaptive step. 63

Figure 3.7 Exact solution of a Poisson problem with steep gradient. 64

Figure 3.8 Meshes at first, second, fourth and final step. 64

Figure 3.9 Contour plot of the gradient of field function and the meshes at the final step. 65

Figure 3.10 Estimated global residual norm at each adaptive step. 65

Figure 3.11 Convergent rate of the solution for uniform refinement and present adaptive analysis.

Figure 3.12 A quarter model of an infinite plate with hole. 66

Figure 3.13 Meshes at first, third, sixth and final of the adaptive step. 67

Figure 3.14 Convergency of the error norm of displacements. 67

Figure 3.15 Convergency of the energy norm. 68

Figure 3.16 (a) A full model and (b) a half model of the crack panel. 68

Figure 3.17 Initial meshes of the crack panel model for the adaptive analysis. 69

Figure 3.18 Meshes of the final step in the adaptive analysis using conventional residual based estimator. 69

Figure 3.19 Meshes of the final step in the adaptive analysis using present estimator. 69

Figure 3.20 Comparison of the convergency in term of the error norm of displacements. 70

Figure 3.21 Comparison of the convergency in term of the energy norm. 70

Figure 3.22 Comparison of the efficiency of the error estimators in term of energy norm. 71

Figure 3.23 The (a) Initial nodal distribution in the domain, (b) Voronoi diagram is constructed, (c) additional nodes are inserted on the vertex of cell and (d) new nodal distribution is formed. 71

Figure 3.24 Additional nodes inserted at internal and external Delaunay cells in the refinement process. 72

Figure 4.1 A problem governed by PDEs in domain Ω. 87

Figure 4.2 The exact solution of one dimensional Poisson Problem for field function and it first derivative. 88

Figure 4.3 Solution of RPCM at first, 10^{th}, 25^{th} and final step. 88

Figure 4.4 Solution of RPCM for field function and its derivatives at final step. 89

Figure 4.5 The number of field nodes, global residual norm and error norms of solutions at each adaptive step. 89

Figure 4.6 The analytical solution of the Poisson problem. 90

Figure 4.7 Nodal distribution of 11×11 regularly distributed nodes in the $\Omega:[0,1]\times[0,1]$. 90

Figure 4.8 The solution of RPCM along $y=0.5$ for the Poisson problem. 90

Figure 4.9 (a) Patch A with regular distributed nodes and (b) Patch B with irregularly distributed nodes 91

Figure 4.10 (a) Patch C with regularly distributed nodes and (b) Patch D with irregularly

distributed nodes. 91

Figure 4.11 A cantilever beam subjected to a parabolic shear traction at the right end. 92

Figure 4.12 Deflection of the cantilever beam for model with 951 and nodes 963 without the Neumann boundary condition. 92

Figure 4.13 Deflection of the cantilever beam for model with 951 and nodes 963 with the Neumann boundary condition. 93

Figure 5.1 A model of cantilever beam with 273 regularly distributed nodes. 109

Figure 5.2 Comparison of the deflection of the cantilever beam computed by LS-RPCM, RPCM and FEM along the bottom edge. 109

Figure 5.3 Comparison of the (a) shear stress τ_{xy} and (b) normal stress σ_{yy} of the cantilever beam computed by stabilized LS-RPCM, RPCM and FEM along the bottom edge 110

Figure 5.4 Deflection of cantilever beam along bottom edge along $x = 24m$ computed by stabilized LS-RPCM using 4 different set nodal distributions, (a) 273 nodes, (b) 287 nodes, (c) 308 nodes and (d) 325 nodes. 110

Figure 5.5 Nodal distribution at each adaptive step for Poisson problem 111

Figure 5.6 Exact error norm at each adaptive step for Poisson problem 111

Figure 5.7 A quarter model of an infinite plate subjected to uniaxial traction in the horizontal direction. 112

Figure 5.8 Nodal distribution of the infinite plate with circular hole at each adaptive step. 112

Figure 5.9 Error norms of Von-Mises stress computed by stabilized LS-RPCM at each adaptive step. 113

Figure 5.10 Error norm of displacements computed by stabilized LS-RPCM at each adaptive step.

113

Figure 5.11 Displacement u_y along $x = 0$ computed the stabilized LS-RPCM at final step.

114

Figure 5.12 Normal stress σ_{xx} along $x = 0$ computed the stabilized LS-RPCM at final step.

114

Figure 5.13 L-shaped plate subjected to a unit tensile stress in the horizontal direction. 115

Figure 5.14 Nodal distribution at each adaptive step for the L-shaped plate problem. 115-117

Figure 5.15 A model of L-shaped plate with 7902 nodes in ANSYS for references solution. 117

Figure 5.16 Normal stress σ_{yy} distribution of L-shaped plate computed by (a) the LS-RPCM and (b) the reference solution. 118

Figure 5.17 Normal stress τ_{yy} distribution of L-shaped plate computed by (a) the LS-RPCM and (b) the reference solution. 118

Figure 6.1 Field nodes and additional collocation points in a problem domain and on the boundaries. 133

Figure 6.2 Model of an infinite plate with hole with (a) 435 nodes and (b) with additional 18 nodes to the model of 435 nodes. 133

Figure 6.3 Displacement in *y*-direction along $x = 0$ for (a) Model A and (b) Model B. 134

Figure 6.4 Normal stress σ_{xx} along $x = 0$ for (a) Model A and (b) Model B. 134

Figure 6.5 Normal stress σ_{yy} along the top edge: the result obtained using RPCM is oscillating on the boundary. 135

Figure 6.6 Comparison of CPU times among RPCM, LS-RPCM and FEM. 135

Figure 6.7 Comparison of error norm of displacements among RPCM, LS-RPCM and FEM. 136

Figure 6.8 Comparison of error norm of stresses among RPCM, LS-RPCM and FEM. 136

Figure 6.9 Comparison of energy norm among RPCM, LS-RPCM and FEM. 137

Figure 6.10 Comparison of efficiency in term of energy norm among RPCM, LS-RPCM and FEM. 137

Figure 6.11 Nodal distribution of the model of cantilever beam at each adaptive step. 138

Figure 6.12 Estimated global residual norm at each adaptive step. 138

Figure 6.13 The error norm of displacements at each adaptive step. 139

Figure 6.14 The energy norm at each adaptive step. 139

Figure 6.15 Three dimensional plot of the exact solution of Poisson problem. 140

Figure 6.16 The estimated global residual norm at each adaptive step. 140

Figure 6.17 The nodal distribution at each adaptive step. 141

Figure 6.18 The error norm at each adaptive step. 141

Figure 6.19 The LS-RPCM solution of the field functions along $y = 0.5$ at initial and final steps. 142

Figure 6.20 The LS-RPCM solution of the $\frac{\partial u}{\partial x}$ along $y = 0.5$ at initial and final steps. 142

Figure 6.21 Nodal distribution of the model of hollow cylinder at each adaptive step. 143

Figure 6.22 Estimated global residual norm at each adaptive step. 143

Figure 6.23 Exact error norm of displacements at each adaptive step. 144

Figure 6.24 Energy norm at each adaptive step. 144

Figure 6.25 The displacement in y-direction along $x = 0$ at initial and final step. 145

Figure 6.26 The normal stress σ_{xx} along $x = 0$ at initial and final step. 145

Figure 6.27 The model of the reservoir full filled with water. 146

Figure 6.28 The nodal distribution of the model of reservoir during adaptation. 146

Figure 6.29 The estimated global residual norm at each adaptive step. 147

Figure 6.30 The approximated energy at each adaptive step. 147

Figure 6.31 The displacements (a) u_x and (b) u_y along the curvy edge. 148

Figure 6.32 Contour plot of normal stress σ_{xx} at final step. 149

Figure 6.33 Contour plot of normal stress σ_{yy} at final step. 149

Figure 6.34 Contour plot of shear stress τ_{xy} at final step. 150

Figure 6.35 Stresses along the curvy edge at the final adaptive step. 150

Figure 7.1 Regularization points scattered in the problem domain and on the boundaries 166

Figure 7.2 Deflection of the cantilever beam along $y = 0$ with two similar sets of nodal distribution. 166

Figure 7.3 Comparison of convergence rate among the FEM, RPCM and RLS-RPCM. 167

Figure 7.4 Comparison of computational time among the FEM, RPCM and RLS-RPCM. 167

Figure 7.5 A quarter model of hollow cylinder with internal pressure. 168

Figure 7.7 The estimated global residual norm at each adaptive step. 168

Figure 7.8 Exact error norm of displacements at each adaptive step. 169

Figure 7.9 Exact error norm of stresses at each adaptive step 169

Figure 7.10 Energy norm at each adaptive step. 170

Figure 7.11 Displacements in y-direction along the left edge at initial and final steps. 170

Figure 7.12 The normal stress σ_{xx} along the left edge at initial and final steps. 171

Figure 7.13 (a) A full model and (b) the a model of a bridge subjected to a constant pressure on top. 171

Figure 7.14 Nodal Distribution at 1st, 3rd, 5th and 7th steps in the adaptation for the bridge problem. 172

Figure 7.15 Estimated residual norm at each adaptive step for the bridge problem. 172

Figure 7.16 Model of the bridge used in ANSYS for reference solution. 173

Figure 7.17 Displacement u_y obtained by RLS-RPCM (a) along the left edge and (b) on top of the bridge at initial and final steps. 174

Figure 7.18 Normal stress (a) σ_{xx} and (b) σ_{yy} obtained by RLS-RPCM along the left edge at initial and final steps 175

Figure 7.19 Solution of Poisson problem with high gradient. 176

Figure 7.20 The gradient of the solution, $\frac{\partial u}{\partial x}$, along $y = 0$. 176

Figure 7.21 Nodal distribution at initial, 3rd, 5th, final steps. 177

Figure 7.21 Nodal distribution at initial, 3rd, 5th, final steps. 177

Figure 7.23 Estimated global residual at each adaptive step. 178

Figure 7.24 Exact error norm of u at each adaptive step. 178

Figure 7.25 The solution of *u* along $y = 0.5$ at initial and final steps. 179

Figure 7.26 The solution of $\frac{\partial u}{\partial x}$, along $y = 0.5$ at initial and final steps. 179

Figure 7.27 The exact solution of Poisson problem with multiple peaks. 180

Figure 7.28 The estimated global residual norm at each adaptive step. 180

Figure 7.29 The nodal distribution at initial, 4th, 8th and final steps. 181

Figure 7.30 Enlarged view of the nodal distribution at final step. 181

Figure 7.31 The exact error norm at each adaptive step. 182

Figure 7.32 The solution of *u* along $y = 0.5$ at initial, 4th, 7th, 9th and final steps. 182

Figure 7.33 The solution of $\frac{\partial u}{\partial x}$ along $y = 0.5$ at initial, 4th, 7th, 9th and final steps. 183

Figure 8.1 Reposition of an interior node to the centre of its first layer of supporting nodes. 202

Figure 8.2 Subdomains constructed by the background mesh formed using Delaunay Diagram. 202

Figure 8.3 (a) Node *i* in the interior domain and (b) its subdomain. 203

Figure 8.4 (a) Node *i* on the Neumann boundary and (b) its subdomain. 203

Figure 8.5 The model and dimension of the connecting rod. 204

Figure 8.6 The models of connecting rod with (a) 339, (b) 1092, (c) 2979 and (d) 4541 nodes. 204

Figure 8.7 The approximated energy obtained by the subdomain method with different field nodes. 205

Figure 8.8 The displacements in x-direction obtained by subdomain method along AB with 339 and 4106 nodes in domain. 205

Figure 8.9 The normal stress σ_{xx} obtained by subdomain method along AB with 339 nodes and 4106 nodes in domain. 206

Figure 8.10 The normal stress σ_{yy} obtained by subdomain method along AB with 339 nodes and 4106 nodes in domain. 206

Figure 8.11 The convergent rate in term of the error norm of displacements for the FEM (3-nodes element) and subdomain method. 207

Figure 8.12 The convergent rate in term of the energy norm for the FEM (3-nodes element) and subdomain method. 207

Figure 8.13 The comparison of the computational cost for the FEM (3-node element) and present method. 208

Figure 8.14 Efficiency in term of energy norm of the present method. 208

Figure 8.15 The nodal distribution at each adaptive step. 209

Figure 8.16 Approximated global residual norm at each adaptive step. 209

Figure 8.17 Error norm of displacements at each adaptive step. 210

Figure 8.18 Energy norm at each adaptive step. 210

Figure 8.19 The normal stress σ_{xx} obtained by the subdomain method along left edge at initial and final adaptive steps. 211

Figure 8.20 The normal stress σ_{yy} obtained by the subdomain method along left edge at initial and final adaptive steps. 211

Figure 8.21 Model of a short beam subjected to a uniform loading on top edge. 212

Figure 8.22 Nodal distribution for the model of short beam at each adaptive step. 212

Figure 8.23 The displacement of Point A at each adaptive step. 213

Figure 8.24 The approximated energy obtained by subdomain method at each adaptive step. 213

Figure 8.25 The estimated global residual norm at each adaptive step. 214

Figure 8.26 The nodal distribution at each adaptive step. 214

Figure 8.27 The approximated energy at each adaptive step. 215

Figure 8.28 Contour plot of the approximated stresses obtained by present method at final adaptive step. 215

Figure 8.29 Normal stresses (a) σ_{xx} (b) σ_{yy} along the left edge at initial and final steps. 216

Figure 8.30 Displacements along the left edge at initial and final steps. 217

Figure 8.31 Nodal distributions at 1^{st}, 3^{rd}, 6^{th} and final step. 217

Figure 8.32 Global residual norm at each adaptivel steps. 218

Figure 8.33 Displacements norm at each adaptivel step. 218

Figure 8.34 Energy norm at each adaptive step. 219

Figure 8.35 Energy at each ada 219

Figure 9.1 (a) Appropriate and (b) inappropriate selection of local nodes for local RBFs. 240

Figure 9.2 (a) Immediate layer and (b) the second layer of supporting nodes. 240

Figure 9.3 The given field function *u*, and the analytical solutions of $\frac{\partial u}{\partial x}$, $\frac{\partial^2 u}{\partial x^2}$ and $\frac{\partial^2 u}{\partial x \partial y}$ .241

Figure 9.4 The error norms of the approximated $\frac{\partial u}{\partial x}$, $\frac{\partial^2 u}{\partial x^2}$ and $\frac{\partial^2 u}{\partial x \partial y}$ with different number of local nodes. 241

Figure 9.5 Computational time of the interpolation scheme using different local nodes. 242

Figure 9.6 The absolute error distribution of $\frac{\partial u}{\partial x}$ approximation. 242

Figure 9.7 The absolute error distribution of $\frac{\partial^2 u}{\partial x^2}$ approximation. 243

Figure 9.8 The absolute error distribution of $\frac{\partial^2 u}{\partial x \partial y}$ approximation. 243

Figure 9.9 Error norms of displacements of the LC-RPIM using different number of local nodes. 244

Figure 9.10 Energy norms of the LC-RPIM using different number of local nodes. 244

Figure 9.11 Condition number of the stiffness matrix of the LC-RPIM using different number of local nodes. 245

Figure 9.12 Distribution of a set of 100 randomly scattered nodes in a square domain. 245

Figure 9.13 (a) Dimension of a triangular cross section bar, (b) a model of the bar with 120 field nodes. 246

Figure 9.14 Error norm of the RPCM solution with different number of local nodes. 246

Figure 9.15 Computational time of the RPCM with different number of local nodes. 247

Figure 9.16 Condition number of the coefficient matrix of the RPCM with different number of local nodes. 247

Figure 9.17 Comparison of the convergent rate in term of the error norm among the different schemes. 248

Figure 9.18 Comparison of the computational time among different schemes. 248

Figure 9.19 Comparison of the condition number of the coefficient matrices among different schemes. 249

Figure 9.20 Comparison of the efficiency among different schemes. 249

Figure 9.21 Error norm of the displacements obtained by RLS-RPCM. 250

Figure 9.22 Error norm of the stresses obtained by RLS-RPCM. 250

Figure 9.23 Computational time required for the RLS-RPCM with different number of local nodes. 251

Figure 9.24 Efficiency of the RLS-RPCM with different local nodes in term of energy norm. 251

Figure 9.25 Condition number of the coefficient matrix of RLS-RPCM using different number of local nodes. 252

Figure 9.26 The plot of the field function *u* and its derivatives. 252

Figure 9.27 (a) The initial distribution, and the final nodal distribution for the adaptive RPCM using (b) global nodes, (c) 25 local nodes and (d) double layers of the local nodes. 253

Figure 9.28 The comparison of the error norms of the field function at each adaptive step. 253

Figure 9.29 The comparison of the computational efficiency among different schemes. 254

Figure 9.30 The comparison of the condition number of the coefficient matrice among different schemes at each adaptive step. 254

List of Tables

Table 2.1 Coordinate of the six nodes selected for constructing moment matrix. 38

Table 2.2 Typical conventional form of radial basis functions. 38

Table 4.1 Error norm of RPCM for linear patch test. 87

Table 4.2 Error norm of RPCM for higher order patch test. 87

Table 5.1 Exact error norm of the solution obtained by the stabilized LS-RPCM at each adaptive step for the Poisson problem. 108

Table 5.2 Exact error norm of the displacement obtained by the stabilized LS-RPCM at each adaptive step for the infinite plate with hole subjected to uniaxial traction. 108

Table 8.1 Error norms of the subdomain method for linear patch test. 201

Table 8.2 Error norms of the subdomain method for higher order patch test. 201

Table 8.3 Error norm of displacements, energy norm and computational time of the subdomain method and FEM. 201

Chapter 1

Introduction

1.1 Background

1.1.1 Motivation of Meshfree Methods

Finite element method (FEM) is one of the most successful and dominant numerical methods in the last century. Although the advent of FEM can be traced back as early as the 60s [3,15], the development of FEM only became progressive after the technology of digital computer is more advanced and popular. The FEM has achieved remarkable success and it has been widely used in various fields such as engineering and sciences. Nowadays, many FEM commercial software e.g. ABACUS, ANSYS, PATRAN etc are available to help engineers and scientists to solve their problems. However, while the problem of computational mechanics becomes more challenging, the conventional FEM that relys very much on the mesh is no longer able to deal with it easily.

Using meshes is a salient feature of the FEM, mesh is known as the connectivity of the nodes in a predefined manner. Due to the use of the mesh, the FEM has encountered several limitations as follows.

(1) High computational cost for meshing

Creating mesh is a prerequisite of FEM. The problem domain has to be modelled using mesh at the beginning step. Although linear triangular element can be created easily, the accuracy of FEM solution is low. To obtain better FEM solution, higher quality mesh, for example, quadrilateral mesh has to be used. However, the meshing procedure for high quality mesh can be very complicated and costly. For large scale problem, the cost for constructing the mesh can be the major cost of the entire computation.

(2) Low accuracy in the derivatives of the primary field functions

As FEM is derived from the variational principle and regarded as a weak-form method, only weak-solution can be obtained. The weak-solution can only guarantee the solution of the primary field function is continuous, but not its derivatives. Hence, some important quantity in mechanics, for instance, stress, is suffering from low accuracy due to the discontinuous solution of the derivative of the primary field function. To obtain a better FEM solution for stress, special post-processing treatments are required.

(3) Difficulties in the implementation of adaptive analysis

Adaptive analysis is a very important study in computational mechanics. During the adaptation, refinement or coarsening process has to be executed to improve the model of the problem. Remeshing process is also necessary at each adaptive process. Due to the use of mesh, the refinement or coarsening process

can very cumbersome and expensive. Remeshing process in not only costly but also difficult for those high order element, i.e., quadrilateral element.

(4) Limitation in several challenging and complicated computational mechanics problems

a) FEM solution is suffering from low accuracy in high deformation problem as the mesh is severely distorted.

b) Simulation of failure process, e.g., crack growth, is very difficult to be investigated by FEM as interface of the elements are not coincide.

c) FEM is also not suitable to be used for the study of explosion problem as element of the FEM can not be broken during the computation.

From the above reasons, the difficulties caused by the use of mesh restrict the application of the FEM. A new class of numerical method, meshfree method, which is formulated without using the mesh, is therefore in great demand.

1.1.2 Features of Meshfree Methods

The motivation of the meshfree methods has been clearly stated in the last section. Furthermore, close examination has revealed the difficulties caused by the use of mesh in the FEM. To get rid of the mesh, a new class of the numerical method, meshfree method, is devised. In this section, general features of meshfree methods will be discussed as follows.

Although the definition of mesh free is still an open issue, generally, the meshfree

methods should possess the following features:

(1) No mesh or nodal connectivity is needed in the formulation procedure.

(2) The shape function is not constructed based on mesh. Great flexibility should be provided in the nodal selection for constructing shape functions.

(3) Although background mesh is needed in some meshfree methods, the implementation of adaptive analysis and boundary moving problems should be done with ease.

(4) Meshfree methods should provide a better accuracy for the solution of the derivative of the primary field function such as stress.

(5) Meshfree methods should be able to provide solution with higher accuracy for high deformation problem. The accuracy of the meshfree method's solution is not severely affected from mesh distortion.

Although meshfree methods have achieved remarkable progress, there is still a room for improvement. Some of the most frequently addressed concerns for the existing meshfree methods are listed as follows.

(1) Generally, the computational cost of the meshfree methods is high. As the shape functions are usually constructed with more nodes, the cost of constructing the shape function is more expensive. Solving simultatneous equations with wider bandwidth coefficient matrix also incurs higher computational cost.

(2) At current stage, a lot of the meshfree methods are still can not totally get rid of mesh. Background mesh is still somehow needed in the computation, e.g., element-free Galerkin (EFG) method [9] etc.

(3) If meshfree methods use shape functions which does not possess Kronecker Delta property, e.g., Meshless Local Petrov-Galerkin (MLPG) Method [2], Diffuse Element Method (DEM) [79], the imposition of the essential boundary condition is not straightforward. Additional technique such as penalty approach is required.

Still, it is one of the very promising method to overcome some of the problems which caused by the use of mesh. The attractive features of meshfree methods are drawing a lot of attention and gaining many efforts from researchers and scientists.

1.2 Literature review

As the problems of computational mechanics grow more and more challenging, the conventional numerical methods that based on regular mesh or grid, for instance, finite element method (FEM), finite difference method (FDM) and finite volume method (FVM), are no longer suited well. The demand of new class of numerical method that is formulated without the reliance of mesh or grid becomes more significant. This motivation drives the leap of the meshfree methods in the last three decades. Meshfree method has become one of the hottest research topics in the computational mechanics community and many meshfree methods have been well established and discussed.

The pioneering research work of the meshfree methods can be traced back to many decades ago. The smooth particle hydrodynamics (SPH) method [64] proposed by Lucy in 1977 is always regarded as one of the earliest contribution to development of the meshfree method. The initial idea of SPH method is to study the astrophysical phenomena without boundaries such as exploding stars and dust cloud. Monaghan and his co-workers have also dedicated great contribution to extend the application of SPH method [21,76-77]. A comprehensive discussion of the recent research works of SPH method can be found in Ref. [54].

Besides the SPH method, the collocation method is another well-known meshfree method which has great influence to the development of meshfree methods. As early as 80s, to get rid of the regular grids in the formulation of finite difference method (FDM), many research works have been devoted to establish a collocation method based on arbitrary scattered nodes. General finite difference method (GFDM) is therefore well discussed and proposed by many researchers, which includes the works by Girault [22], Perrone [82], Liszka and Orkizs [37,38] etc.

The purpose of this section is just to provide a brief history of meshfree methods. More comprehensive overview of the development of meshfree methods is abundantly available in literature [8,40,46].

1.2.1 Classification of Meshfree Methods

As meshfree method is developing progressively, it is very important to classify the meshfree methods into different categories for better understanding. Indeed, there

are many ways to classify the meshfree methods. In this section, various types of classification will be briefly introduced.

The first type of classification categorizes the meshfree methods according to the interpolation or approximation function. Popular approximations include SPH approximation [21,64], RKPM approximation [58-60], MLS approximation [9,79], partition of unity methods [5,73] etc.

There is another type of classification that categorizes the meshfree methods according to the domain representation. This type of classification categorizes the meshfree method into two categories: domain-type and boundary-type of meshfree methods. In domain-type of meshfree methods, both problem domain and boundary are will represented by field nodes. Examples of this type of meshfree methods includes element-free Galerkin (EFG) method [9], point interpolation method (PIM) [41], local radial point interpolation method (LRPIM) [42], SPH method [64] etc. On contrary, only boundary is represented by field nodes in the boundary-type of meshfree methods, for example, boundary node method (BNM) [78], boundary point interpolation method (BPIM) [25], boundary radial point interpolation method (BRPIM) [26].

In this thesis, meshfree methods are classified according to the formulation procedure is adopted. They can be largely categorized into three different categories, namely meshfree weak-form method, meshfree strong-form method and meshfree weak-strong form method. The details of the different categories are given in the following section.

1.2.2 Meshfree Weak-form Methods

Meshfree method formulated based on the weak formulation is known as a meshfree weak-form method. Due to the success of variational principle used in the finite element method, the meshfree weak-form method is the most well established and dominant meshfree method. As compared to meshfree strong-form method, meshfree weak-form method is able to provide more stable and accurate solution. However, meshfree weak-form methods is not regarded as a truly mesh free method, since background cells are somehow still needed globally or locally. Typical meshfree weak-form methods include diffuse element method (DEM) [79], element-free Galerkin (EFG) method [9], meshless local Petrov-Galerkin (MLPG) method [2], local point interpolation method (LPIM) [41], local radial point interpolation method (LRPIM) [42,56,91], linear conforming point interpolation method (LC-PIM) [97], linear conforming radial point interpolation method (LC-RPIM) [36, 53] etc.

1.2.3 Meshfree Strong-form Methods

Meshfree strong-form method has a longer history of development in meshfree methods. Meshfree method that is formulated based on the strong formulation is known as meshfree strong-form method. This class of meshfree method directly discretizes the partial differential equations (PDEs) and boundary conditions at nodes by collocation technique. Therefore, the computational efficiency of strong-form method is highest among the other classes of meshfree methods. It is always regarded as a truly mesh free method as no mesh is needed throughout the formulation. However, the instability issue

is always the greatest concern for strong-form methods. The earliest research works dedicated to the meshfree strong-form methods includes SPH method [21,64], GFDM [22,37,38,82]. Other meshfree strong-form methods include finite point method [80,81] and hp-cloud method [39]. Recently, Liu et al have proposed strong-form collocation method based on local RBFs, namely radial point collocation method (RPCM) [62-63].

1.2.4 Meshfree Weak-Strong Form Methods

As its name implies, meshfree weak-strong form (MWS) method is formulated based on both weak and strong formulations. To overcome the instability problem in the strong-form method caused by Neumann boundary conditions, the weak formulation is applied along the boundary of the problem domain while the strong formulation is still remained for the field nodes in the interior domain. This idea of coupling both weak and strong formulation is originally suggested by Liu and Gu [43]. Through such procedure, the background cells are kept to minimum and only applied along boundary. The MWS method has been successfully developed to solve for many solid mechanics and fluid mechanics problems [22,44,55].

1.3 Motivation of the Thesis

Among these three major categories of meshfree methods, meshfree strong-form methods possess the most attractive features that facilitate the implementation of adaptive analysis. The advantages of meshfree strong-form methods for adaptive analysis include:

(1) The formulation procedure of meshfree strong-form methods is very simple and straightforward. Neither formulation procedure nor construction of shape function requires numerical integration. It is the most efficient meshfree method.

(2) The truly mesh free feature eases the refinement or coarsening procedure in adaptive analysis. Nodal can be inserted or removed without worry of the nodal connectivity.

(3) Remeshing process is needed in adaptive analysis for conventional numerical methods relying on the mesh. Since meshfree strong-form method is a truly mesh free method, the costly and cumbersome remeshing procedure is therefore eliminated.

Nevertheless, the development of meshfree strong-form methods still remains very challenging. Currently, most of the reliable strong-form methods are still very much relying on the structured grids and are restricted only for regular domain. Finite difference method (FDM) is considered as the most classical, reliable and earliest strong-form method [17,85]. However, while dealing with more geometrically complex and practical problems, the FDM that relys on the structure grids has encountered great difficulty. A strong-form meshfree method that is formulated without relying on the structured grid is therefore very attractive. Although methods like GFDM [22,37,38,82,88] claims that it can be used for irregular domain and unstructured grids, a proper stencil (nodal selection) is somehow still needed for function approximation.

The cumbersome and inflexible procedure of nodal selection constrains the strong-form methods from being used in the adaptive process as nodal distribution during the adaptation can be highly irregular and hence difficult to form 'proper' stencils.

In addition, instability problem is another crucial issue that limits the applications of strong-form methods, especially in adaptive analyses. The strong-form solution is usually not stable and less accurate than the weak-form solution. Without an effective stabilization measure, it is impossible to use meshfree strong-form method in adaptive analyses. Although researchers have provided several suggestion such as, adding derivatives term to the primary field variable [99], introducing auxiliary collocation points [98], coupling weak and strong formulation [43,44,27], augmenting additional term to the original governing equation [81], the stabilization effect is yet to be satisfied and the implementation of these procedures can be complicated for adaptive analysis.

1.4 Objectives of the Thesis

Compared to the meshfree weak-form method, the development of strong-form method is relatively sluggish. Available literature for strong-form meshfree methods in adaptive analysis is very little. As instability is still the fatal shortcoming of strong-form methods, it is impossible to extend strong-form methods to adaptive analysis without an effective measure to restore the stability of the solution. In this work, several techniques are proposed to restore the stability of the strong-form solution. As stable and accurate solution can be obtained, the features of strong-form method can then facilitate an easier implementation of adaptive analysis.

Error estimator is another important study of this thesis. Currently, most of the well established error estimators in the adaptive analysis are only available for weak-form methods. Developing a novel error estimator that can be used for strong-form adaptive analysis is crucial and in great demand. A very robust, versatile and effective error estimator has to be developed for the adaptive strong-form method. By incorporating a good error estimator, an efficient adaptive analysis can then be achieved by strong-form meshfree methods.

As strong-form methods studied in this thesis are based on the local radial basis function (RBFs), hence a thorough study of the local RBFs is very important. RBFs are very well-known for its excellent performance in scattered data interpolation and curve fitting and it is very commonly used in the mathematics community. The earliest works of the strong-form collocation method based on RBFs can be traced back to early 90s. Kansa is considered one of the pioneers who use RBFs for solving PDEs by collocation technique [65]. In contrast to the conventional RBFs that use global nodes, Liu et al have dedicated a series of research works that are based on local RBFs recently. The study of the dimensionless shape parameters of the local RBFs have been already well studied in literatures [40,46,92], however, the effects of the number of local nodes for RBF is not thoroughly investigated. The influences of the local nodes can be very significant to the accuracy and stability of the solution. A comprehensive and insightful study on the effects of the number of local nodes will be investigated in this work.

1.5 Organization of the Thesis

This thesis consists of ten chapters and is organized as follows.

In **Chapter 1**, background and literature review of the research work are provided. The motivation and the objective of this thesis are clearly described in this chapter.

Function approximation plays crucial roles in the meshfree methods. In **Chapter 2**, five types of commonly used function approximation: smooth particle hydrodynamics (SPH), reproduced kernel particle method (RKPM), moving least-square (MLS), polynomial point interpolation method (PPIM) and radial point interpolation method (RPIM) are introduced. As PPIM and RPIM approximations are adopted throughout this work, greater details of the formulation and properties are given.

All the proposed strong-form methods in this work are extended to adaptive analysis. Error estimators, adaptive strategy and refinement procedure for adaptive strong-form meshfree method are well described in **Chapter 3**. A new error estimator, residual based error estimator, is proposed and introduced in this chapter.

The focus of this thesis is on the development of strong-form meshfree methods. Sereval stabilization procedures are proposed to stabilize the solution of a strong-form meshfree method, radial point collocation method (RPCM). Therefore, a close examaination is conducted for RPCM. **Chapter 4** presents the detailed formulation procedure and the several issues of the RPCM.

Chapter 5 to **Chapter 7** provide meshfree strong-form methods that use different

techniques to restore the stability of RPCM solution. In **Chapter 5**, a stabilized least-squares RPCM is introduced. In the formulation of stabilized least-squares RPCM, additional governing equations are satisfied along the Dirichlet boundaries. Next, in **Chapter 6**, least-square technique with special treatment for boundaries is adopted to establish a least-square RPCM (LS-RPCM). Additional collocation points are allocated along the boundaries (Neumann and Dirichlet boundaries). As the number of discretized equations is more than the number of unknown variable, a simple least-square technique is adopted to solve for the resultant algebraic equations. Last, regularization technique that often be used in the inverse problem is adopted to stabilize the RPCM solution for the forward problems. A regularized least-square RPCM (RLS-RPCM) is presented in **Chapter 7**.

Chapter 8 presents a subdomain method based on the RBFs. In this chapter, the meshfree shape function (RPIM shape function) is integrated into the classical subdomain method to present a subdomain method based on the local RBFs. By applying the Green's theorem, only boundary integral is involved in the formulation procedure. Excellent accuracy and great stability can be obtained in the sundomain method, and it has been successfully extended to adaptive analysis as well.

From **Chapter 5** to **Chapter 8**, four different meshfree methods based on the local RBFs are presented. Hence, study of the local RBFs is not only essential but also very important. In literature, the study of the dimensionless shape parameters of RBFs is abundantly available. However, the study on the effects of the number of local nodes for meshfree methods based on RBFs is still lacking in the literature. Thus, a

comprehensive and insightful study on the effect of the number of local nodes for the meshfree methods based on RBFs is provided in **Chapter 9**.

Last, **Chapter 10** presents the conclusive remarks and some recommendations for the future works.

Chapter 2

Function Approximations

2.1 Introduction

Function approximation plays a very important and crucial role in the meshfree methods. Considering a problem that is governed by PDEs and given boundary conditions, the unknown field function has to be first approximated by trial function before the discretized system equations can be formed and solved. The quality of the numerical solution highly depends on the function approximation.

In the finite element method (FEM), the function approximation is based on the predefined connectivity or mesh. However, this type of element based approximation incurs several shortcomings as mentioned in Chapter 1. On the contrary to the FEM, meshfree methods adopt function approximation that does not rely on mesh.

In the following sections, five most commonly used approximations in meshfree methods are introduced. They are smooth particle hydrodynamics (SPH) approximation, reproducing kernel particle method (RKPM) approximation, moving least-squares (MLS) approximation, polynomial point interpolation method (PPIM) approximation and radial point interpolation method (RPIM) approximation. As SPH,

RKPM and MLS approximations are not used in this study, only a brief introduction is given. Details for their formulations can be referred by the respective references. In this thesis, PPIM and RPIM approximations are mostly used and hence more comprehensive details are provided.

2.2 Smooth Particle Hydrodynamics (SPH) Approximation

The smooth particle hydrodynamics (SPH) method [64,21] is always regarded as one of the earliest developed meshfree methods. In contrast to many conventional shape functions, for instance, FE shape function, the SPH shape function is represented in an integral form. In the formulation of SPH approximation, the field function u at an interest point $\mathbf{x}$ can be expressed in the following integral form.

$$u^h(\mathbf{x}) = \int_{\Omega_\xi} u(\xi)\widehat{W}(\mathbf{x}-\xi,h)\,d\Omega_\xi \,, \tag{2.1}$$

where $\widehat{W}$ is known as a kernel or weight or smoothing function, h denotes the smoothing length, and Ω_ξ is known as the influence domain in SPH approximation.

Monaghan had listed 5 conditions to be satisfied by the kernel function in his paper [74] as below.

1. $\widehat{W}(x-\xi,h) > 0$ over Ω_ξ (2.2)

2. $\widehat{W}(x-\xi,h) = 0$ outside Ω_ξ (2.3)

3. $\int_{\Omega_\xi} \widehat{W}(x-\xi,h)\,d\Omega_\xi = 1$ (2.4)

4. $\widehat{W}$ is a monotonically decreasing function (2.5)

5. $\widehat{W}(s,h) \to \delta(s)\ as\ h \to 0$ (2.6)

The most frequently used kernel functions can be found in Ref. [8,54,74-76].

Besides abundant research works that are dedicated by Monaghan [74-76], more comprehensive discussions on the properties of the SPH approximation and the recent development of the SPH method can also be found in the paper of Belyschko et al [8] and the book of Liu and Liu [54].

2.3 Reproducing Kernel Particle Method (RKPM) Approximation

Reproducing kernel particle method (RKPM) is another well-known meshfree method proposed by Liu et al [58-60]. In the formulation of RKPM approximation, the field function *u* is approximated and represented in an integral form. By adding a correction function into the SPH approximation given in the Eq. (2.1), the integral representation of a field function *u* can be shown as

$$u^h(\mathbf{x}) = \int_{\Omega_\xi} u(\xi)\widehat{C}(\mathbf{x},\xi)\widehat{W}(\mathbf{x}-\xi,h)\,d\Omega_\xi\,, \tag{2.7}$$

where $\widehat{C}(\mathbf{x},\xi)$ is the correction function.

Example of correction function for one dimensional case is given as follows.

$$\widehat{C}(\mathbf{x},\xi) = c_1(\mathbf{x}) + c_2(\mathbf{x})(\mathbf{x}-\xi), \tag{2.8}$$

where $c_1(\mathbf{x})$ and $c_2(\mathbf{x})$ are the coefficients. Both coefficients can be obtained by enforcing the corrected kernel to reproduce the field function [58].

It has been shown that correction kernel has effectively improved the approximation near the boundaries as well as providing C^1 consistency. More details of the RKPM approximation are abundantly available in literature [58-60].

2.4 Moving Least-Squares (MLS) Approximation

Moving least-squares (MLS) approximation is one of the most popular approximations widely be used in the meshfree methods. It is originaly used for data fitting and surface construction in the mathematic community [24,34,72]. Nayroles et al [79] were the pioneers who adopted MLS approximation in the meshfree methods. Other meshfree methods that use MLS approximation include EFG [9], FPM [81] etc.

In the formulation of MLS approximation, a field function u at any interest point $\mathbf{x}$ can be approximated in the following form:

$$u^h(\mathbf{x}) = \sum_{i=1}^{m} p_i(\mathbf{x}) a_i = \mathbf{P}^T(\mathbf{x})\mathbf{a}(\mathbf{x}), \tag{2.9}$$

where m is the number of basis used in the approximation, $p_i(\mathbf{x})$ is the basis function and a_i is the corresponding coefficient.

The coefficients vector in the Eq. (2.9) can be obtained by minimizing the

weighted L_2 norm of the residual as

$$\frac{\partial J}{\partial \mathbf{a}} = 0, \tag{2.10}$$

where weighted L_2 norm of the residual is known as,

$$\begin{aligned} J &= \sum_{i=1}^{n} \widehat{w}_i (\mathbf{x} - \mathbf{x}_i) \left[u^h(\mathbf{x}) - u_i \right]^2 \\ &= \sum_{i=1}^{n} \widehat{w}_i (\mathbf{x} - \mathbf{x}_i) \left[\mathbf{P}^T(\mathbf{x}) \mathbf{a}(\mathbf{x}) - u_i \right]^2. \end{aligned} \tag{2.11}$$

where *n* is the number of supporting nodes and $\widehat{w}_i$ is the weight function. One should note that the number of supporting nodes is equal or greater than the number of basis in the approximation, $n \geq m$.

Eq. (2.10) leads to the following linear relationship between **a** and $\mathbf{U}_s$,

$$\mathbf{P}_m^T \widehat{\mathbf{W}} \mathbf{P}_m \mathbf{a} = \mathbf{P}_m^T \widehat{\mathbf{W}} \mathbf{U}_s, \tag{2.12}$$

where

$$\mathbf{P}_m = \begin{bmatrix} p_1(\mathbf{x}_1) & p_2(\mathbf{x}_1) & \cdots & p_m(\mathbf{x}_1) \\ p_1(\mathbf{x}_2) & p_2(\mathbf{x}_2) & \cdots & p_m(\mathbf{x}_2) \\ \vdots & \vdots & \ddots & \vdots \\ p_1(\mathbf{x}_n) & p_2(\mathbf{x}_n) & \cdots & p_n(\mathbf{x}_n) \end{bmatrix}_{n \times m}, \tag{2.13}$$

$$\widehat{\mathbf{W}}_{n \times n} = diag[\widehat{\mathbf{w}}_1 \quad \widehat{\mathbf{w}}_2 \quad \cdots \quad \widehat{\mathbf{w}}_n], \tag{2.14}$$

$$\mathbf{a}_{m \times 1} = [\mathbf{a}_1 \quad \mathbf{a}_2 \quad \cdots \quad \mathbf{a}_m]^T. \tag{2.15}$$

Hence, the coefficients vector can be solved as

$$\mathbf{a} = \left[\mathbf{P}_m^T \widehat{\mathbf{W}} \mathbf{P}_m \right]^{-1} \mathbf{P}_m^T \widehat{\mathbf{W}} \mathbf{U}_s , \tag{2.16}$$

and the MLS approximation can be expressed in the following form in term of the MLS shape functions:

$$u(\mathbf{x})^h = \left\{ \phi_1(\mathbf{x}) \quad \phi_2(\mathbf{x}) \quad \cdots \quad \phi_n(\mathbf{x}) \right\}^T \mathbf{U}_s = \Phi^T(\mathbf{x}) \mathbf{U}_s , \tag{2.17}$$

where

$$\Phi^T(\mathbf{x}) = \mathbf{P}(\mathbf{x}) \left[\mathbf{P}_m^T \widehat{\mathbf{W}} \mathbf{P}_m \right]^{-1} \mathbf{P}_m^T \widehat{\mathbf{W}} , \tag{2.18}$$

The details description of MLS approximation can be found in the Ref. [34,40,46].

High continuity shape functions and high flexibility in nodal selection are the great advantages of using MLS approximation. However, as least-squares procedure is used in the function approximation, the MLS shape function does not possess Kronecker delta property, which can cause difficulties in the imposing of Dirichlet conditions.

2.5 Polynomial Point Interpolation Method (PPIM) Approximation

Polynomial function is one of the earlier basis function used in the interpolation scheme. As its name implies, polynomial function is used as a basis function in the polynomial point interpolation method (PPIM) approximation.

2.5.1 Formulation of Polynomial Point Interpolation Method

Consider a smooth and continuous field function u in a problem domain Ω. The approximated field function u^h at any interest point $\mathbf{x}$ can be represented in the form given in Eq. (2.9),

$$u^h(\mathbf{x}) = \sum_{i=1}^{m} p_i(\mathbf{x}) a_i = \mathbf{P}^T(\mathbf{x})\mathbf{a}. \tag{2.9}$$

In the PPIM approximation, $P_i(\mathbf{x})$ is the monomial of the polynomial function in the Euclidean space and a_i is the corresponding coefficient.

Completed polynomial basis function is usually preferred in the PPIM approximation. For examples, completed polynomial basis functions used in one-dimensional and two-dimensional space:

$$\mathbf{p}^T(\mathbf{x}) = [1\ x],\ m = 2,\ p = 1, \qquad \text{(1D)} \tag{2.19}$$

$$\mathbf{p}^T(\mathbf{x}) = \left[1\ x\ y\ x^2\ xy\ y^2\right],\ m = 6,\ p = 2, \qquad \text{(2D)} \tag{2.20}$$

where p is the order of polynomial and m is the number of monomials. Pascal's triangles [100] can be utilized to determine the basis of the approximation. Pascal's triangles used for two-dimensional space are given in **Figure 2.1**.

To obtain the undetermined coefficient a_i, the approximation function in Eq. (2.9) is enforced to pass through the field value at each supporting nodes and it can be expressed as the following matrix form.

$$\mathbf{U}_s = \mathbf{P}_m \mathbf{a}, \tag{2.21}$$

where $\mathbf{U}_s$ denotes the vector of field value at supporting nodes,

$$\mathbf{U}_s = \left\{ u_1 \; u_2 \; u_3 \cdots u_n \right\}^T, \tag{2.22}$$

$\mathbf{P}_m$ denotes the moment matrix,

$$\mathbf{P}_m = \begin{bmatrix} 1 & x_1 & y_1 & x_1 y_1 & \cdots & p_n(\mathbf{x}_1) \\ 1 & x_2 & y_2 & x_2 y_2 & \cdots & p_n(\mathbf{x}_2) \\ 1 & x_3 & y_3 & x_3 y_3 & \cdots & p_n(\mathbf{x}_3) \\ \vdots & \vdots & \vdots & \vdots & \ddots & \vdots \\ 1 & x_n & y_n & x_n y_n & \cdots & p_n(\mathbf{x}_n) \end{bmatrix}, \tag{2.23}$$

and $\mathbf{a}$ denotes the vector of coefficient of monomials,

$$\mathbf{a} = \left\{ a_1 \; a_2 \; a_3 \cdots a_n \right\}^T. \tag{2.24}$$

The unknown coefficients can be easily obtained as

$$\mathbf{a} = \mathbf{P}_m^{-1} \mathbf{U}_s, \tag{2.25}$$

if $\mathbf{P}_m^{-1}$ is not singular. One should note that to form a square moment matrix $\mathbf{P}_m$, the number of supporting nodes must be equal to the number of monomials in the polynomial function,

$$n = m. \tag{2.26}$$

Substituting the Eq. (2.25) into Eq. (2.9) yields to the following expression,

$$\begin{aligned} u^h(\mathbf{x}) &= \mathbf{P}^T(\mathbf{x})\mathbf{P}_m^{-1}\mathbf{U}_s \\ &= \sum_{i=1}^{n}\phi_i(\mathbf{x})u_i \\ &= \mathbf{\Phi}(\mathbf{x})\mathbf{U}_s \end{aligned}, \tag{2.27}$$

where $\Phi(\mathbf{x})$ is a vector of shape functions defined as

$$\mathbf{\Phi}(\mathbf{x}) = \mathbf{P}^T(\mathbf{x})\mathbf{P}_m^{-1}(\mathbf{x}) = \left\{\phi_1(\mathbf{x}) \quad \phi_2(\mathbf{x}) \quad \phi_3(\mathbf{x}) \quad \cdots \quad \phi_n(\mathbf{x})\right\}, \tag{2.28}$$

and $\phi_i(\mathbf{x})$ is the PPIM shape function for supporting node *i*.

The derivatives of the approximated field function can be easily expressed in term of the derivatives of shape functions, because PPIM shape function is in the form of polynomial function. For instance, the first derivative of the approximated field function respect to *x* can be expressed as

$$u_{,x}^{\ h}(\mathbf{x}) = \frac{\partial}{\partial x}\mathbf{P}^T(\mathbf{x})\mathbf{P}_m^{-1}(\mathbf{x}) = \mathbf{\Phi}_{,x}(\mathbf{x})\mathbf{U}_s . \tag{2.29}$$

2.5.2 Properties of PPIM Shape Function

Apparently, construction of PPIM shape function is very simple and straightforward as shown in the above section. In addition, the PPIM shape function has also possesses numerous attractive properties as follows [40,41,45,46].

(1) Kronecker Delta property

The shape function possesses Kronecker Delta property,

$$\phi_i(\mathbf{x}_j) = \begin{cases} 1 & if\ i = j, \quad j = 1,2,\cdots,n \\ 0 & if\ i \neq j, \quad i,j = 1,2,\cdots,n \end{cases}. \tag{2.30}$$

The possession of Delta property is because the PPIM shape function is obtained by enforcing the approximation to pass through the field value at each supporting node. With this important property, Dirichlet boundary conditions can be handled very easily.

(2) Reproducibility of polynomial function

As PPIM shape function is in the form of polynomial function, it can reproduce any polynomial function that is included in the basis functions.

(3) Partition of unity

PPIM shape function also has the property of partition of unity,

$$\sum_{i=1}^{n} \phi_i(\mathbf{x}) = 1. \tag{2.31}$$

This can be easily proved by assuming all nodal values equal to a constant,

$$\mathbf{U}_s = \{c\ c\ c \cdots c\}^T, \tag{2.32}$$

and the PPIM approximation can be shown as

$$u^h(\mathbf{x}) = \sum_{i=1}^{n} \phi_i(\mathbf{x}) u_i = c \cdot \sum_{i=1}^{n} \phi_i(\mathbf{x}) = c, \tag{2.33}$$

which leads to the conclusion of Eq. (2.31).

(4) Compact support

As PPIM shape function is only constructed using vicinity nodes of the point of interest, it is considered as a compact support shape function.

(5) No weight function

Unlike other meshfree approximations, for instance, MLS, no weight function or kernel function is used in the construction of PPIM shape function.

2.5.3 Techniques to Overcome Singularity in Moment Matrix

Although PPIM shape function possesses many attractive properties, guarantee of the invertible moment matrix still remains the most challenging issue to be resolved [40,45,46]. The construction of PPIM shape function is not flexible and robust. As mentioned in the above section, the number of supporting nodes must be equal to the number of monomial in the polynomial used in the approximation. Such strict criterion causes great difficulty for nodal selection. Furthermore, the inappropriate selection of monomial or supporting nodes will result in non-invertible moment matrix.

For instance, consider six nodes listed in **Table 2.1** are selected to construct the PPIM shape function with completed 2^{nd} order polynomial bases in a two-dimensional space. The moment matrix can therefore be formed as

$$\mathbf{P}_m = \begin{bmatrix} 1 & 0 & 0 & 0 & 0 & 0 \\ 1 & 0.5 & 0 & 0.25 & 0 & 0 \\ 1 & 1 & 0 & 1 & 0 & 0 \\ 1 & 0 & 1 & 0 & 0 & 1 \\ 1 & 0.5 & 1 & 0.25 & 0.5 & 1 \\ 1 & 1 & 1 & 1 & 1 & 1 \end{bmatrix}. \tag{2.34}$$

The moment matrix given in Eq. (2.34) is easily shown singular and hence fails to construct the PPIM shape function as shown in Eq. (2.28).

To overcome the singular moment matrix $\mathbf{P}_m$, Liu and Gu have proposed a matrix triangularization algorithm (MTA) [45] to efficiently select the proper enclosure of nodes and monomials. The MTA provides a versatile procedure to exclude the nodes and removes the monomials that cause singular moment matrix $\mathbf{P}_m$. As singularity problem is overcome through the MTA procedure, invertible moment matrix can be formed and hence PPIM shape function can be constructed.

Besides the MTA procedure, weighted least-squares (WLS) method is also a very common technique to avoid the singular moment matrix $\mathbf{P}_m$ in the procedure of forming the shape function. As mentioned in the previous section, in the formulation of MLS approximation, weight function is introduced to an overdetermined moment matrix $\mathbf{P}_m$ and shape functions are constructed through seeking the minimal of residual. Of course, augmenting the polynomial basis with radial basis functions (RBFs) in the approximation is also a very good idea to construct shape function using arbitrary field nodes. The details of such approximation are given in the following section.

2.6 Radial Point Interpolation Method (RPIM) Approximation

Radial basis functions (RBFs) are very well-known for its excellent performance in interpolation and scattered data fitting [19,31,83]. It has been widely used in the mathematics community for many decades. The intensive reviews of the RBFs can be found in Refs. [40,46,83].

2.6.1 Formulation of Radial Point Interpolation Method

First, assume that a field function u is smooth and continuous, and it is in a problem domain Ω which is represented by a set of arbitrary scattered nodes. In the radial point interpolation method (RPIM) approximation, where radial basis functions are augmented with polynomial functions, the field function u at any interest point $\mathbf{x}$ can be approximated in the following form:

$$u^h(\mathbf{x}) = \sum_{i=1}^{n} a_i R_i\left(\|\mathbf{x}-\mathbf{x}_i\|\right) + \sum_{j=1}^{m} b_j p_j(\mathbf{x}) = \mathbf{R}(\mathbf{x})\mathbf{a} + \mathbf{P}(\mathbf{x})\mathbf{b}, \tag{2.35}$$

where n is the total number of supporting nodes selected from the surrounding of the point of interest $\mathbf{x}$, m is the number of monomials in the polynomial function, $R_i\left(\|\cdot\|\right)$ is the radial basis function and $p_j(\mathbf{x})$ is the monomials in polynomial function for augmentation. a_i and b_j are the undetermined coefficients of radial basis functions and monomials of polynomial function respectively. The vectors in Eq. (2.35) are defined as

$$\mathbf{R}(\mathbf{x}) = \left[R_1\left(\|\mathbf{x}-\mathbf{x}_1\|\right) \quad R_2\left(\|\mathbf{x}-\mathbf{x}_2\|\right) \quad \cdots \quad R_n\left(\|\mathbf{x}-\mathbf{x}_n\|\right) \right], \tag{2.36}$$

$$\mathbf{P}(\mathbf{x}) = \left[1 \quad x \quad y \quad \cdots \quad p_m(\mathbf{x}) \right], \tag{2.37}$$

$$\mathbf{a} = \left\{ a_1 \quad a_2 \quad \cdots \quad a_n \right\}^T, \tag{2.38}$$

$$\mathbf{b} = \left\{ b_1 \quad b_2 \quad b_3 \quad \cdots \quad b_m \right\}^T. \tag{2.39}$$

By enforcing the interpolation in Eq. (2.35) passes through field value at

supporting nodes, the following expression can be obtained as

$$\mathbf{U}_s = \begin{bmatrix} \mathbf{R}_Q & \mathbf{P}_m \end{bmatrix} \begin{Bmatrix} \mathbf{a} \\ \mathbf{b} \end{Bmatrix}, \tag{2.40}$$

where $\mathbf{U}_s$ is the vector of field values at supporting nodes

$$\mathbf{U}_s = \{u_1\ u_2 \cdots u_n\}^T, \tag{2.41}$$

and

$$\mathbf{R}_Q = \begin{bmatrix} R_1\left(\|\mathbf{x}_1 - \mathbf{x}_1\|\right) & R_1\left(\|\mathbf{x}_1 - \mathbf{x}_2\|\right) & \cdots & R_1\left(\|\mathbf{x}_1 - \mathbf{x}_n\|\right) \\ R_2\left(\|\mathbf{x}_2 - \mathbf{x}_1\|\right) & R_2\left(\|\mathbf{x}_2 - \mathbf{x}_2\|\right) & \cdots & R_2\left(\|\mathbf{x}_2 - \mathbf{x}_n\|\right) \\ \vdots & \vdots & \ddots & \vdots \\ R_n\left(\|\mathbf{x}_n - \mathbf{x}_1\|\right) & R_n\left(\|\mathbf{x}_n - \mathbf{x}_2\|\right) & \cdots & R_n\left(\|\mathbf{x}_n - \mathbf{x}_n\|\right) \end{bmatrix}_{n\times n}, \tag{2.42}$$

$$\mathbf{P}_m = \begin{bmatrix} 1 & x_1 & y_1 & \cdots & p_n\left(\mathbf{x}_1\right) \\ 1 & x_2 & y_2 & \cdots & p_n\left(\mathbf{x}_2\right) \\ \vdots & \vdots & \vdots & \ddots & \vdots \\ 1 & x_n & y_n & \cdots & p_n\left(\mathbf{x}_n\right) \end{bmatrix}_{n\times m}. \tag{2.43}$$

In order to guarantee an unique approximation, the polynomial term has to be satisfied an additional orthogonal condition [31,66],

$$\mathbf{P}^T\mathbf{a} = 0. \tag{2.44}$$

The combination of Eq. (2.40) and Eq. (2.44) yields to the following form as

$$\begin{Bmatrix} \mathbf{U}_s \\ 0 \end{Bmatrix} = \begin{bmatrix} \mathbf{R}_Q & \mathbf{P}_m \\ \mathbf{P}_m{}^T & 0 \end{bmatrix} \begin{Bmatrix} \mathbf{a} \\ \mathbf{b} \end{Bmatrix} = \mathbf{G} \begin{Bmatrix} \mathbf{a} \\ \mathbf{b} \end{Bmatrix}. \tag{2.45}$$

One should note that the moment matrix corresponding to the RBFs, $\mathbf{R}_Q$, is symmetric, as a result, the matrix $\mathbf{G}$ is also a symmetrical matrix. A unique solution for the

unknown vectors of coefficients $\mathbf{a}$ and $\mathbf{b}$ can be obtained as

$$\begin{Bmatrix} \mathbf{a} \\ \mathbf{b} \end{Bmatrix} = \mathbf{G}^{-1} \begin{Bmatrix} \mathbf{U}_s \\ 0 \end{Bmatrix}, \tag{2.46}$$

if the inverse of $\mathbf{G}$ is exists.

Several research works [83,86,93] already show the inverse of $\mathbf{R}_Q$ is usually exists. As the order of the polynomial function is much lower than the number of radial basis, the singularity problem of $\mathbf{G}$ matrix is therefore not encountered. However, the condition of $\mathbf{R}_Q$ can be ill if too many supporting nodes are used for approximation [46,66].

2.6.2 Property of RPIM Shape Function

Radial Basis functions (RBFs) are getting more famous and widely be used in many meshfree methods. It is not only simply because RBFs are very flexible for interpolating scattered data, but also due to many distinguished properties gained in the constructed shape functions. These properties are well studied and examined in the Liu's book [40, 46] and many research papers [91,92]. Some of the important RPIM shape functions properties are introduced in this section as follows.

(1) Kronecker Delta property

RPIM shape function possesses Kronecker Delta property. With such unique property, the imposition of Dirichlet boundary conditions in meshfree method becomes very straightforward. No special treatment such

as penalty technique has to be applied.

(2) Partition of unity

RPIM shape function possesses property of unity as given in Eq. (2.31) if the linear polynomial terms ($m = 3$) or higher terms are included in the approximation shown in Eq. (2.35).

(3) Reproducibility of polynomial function

RPIM shape function can ensure the reproduction of polynomial function. If *k* order of polynomial function is augmented with RBF in the approximation given in the Eq. (2.35), RPIM shape function can reproduce the same order of polynomial. One should note that without augmented with the polynomial term, approximation using pure RBFs can not reproduce even linear polynomial function.

(4) High continuity

Because of the high continuity of RBFs, RPIM shape function can also obtains higher derivatives.

(5) Compact support

With only surrounding nodes of the point of interest are selected for local approximation, RPIM shape function is considered as a kind of compact support shape function.

(6) No weight function

Similar to the PPIM shape function, no weight function is required in the derivation of RPIM shape function.

A very comprehensive study of RPIM properties can also be found in Refs. [40, 46,91].

2.6.3 Radial Basis Functions

There are plenty types of radial basis function (RBF) are available and widely used in the mathematics community. The characteristics of the RBFs have been well studied in many literature [31,65,83]. Some of the most commonly used RBFs in meshfree methods are listed in **Table 2.2**. In this thesis, a very classic type of RBF, Multi-Quadratic (MQ) [31], with dimensionless shape parameters are adopted in RPIM approximation and it can be expressed in the following form as

$$R_i(\mathbf{x}) = \left[r_i^2 + (\alpha_c d_c)^2 \right]^q, \tag{2.47}$$

where r_i is the Euclidean norm of the point of interest $\mathbf{x}$ and node *i*,

$$r_i = \left\| \mathbf{x} - \mathbf{x_i} \right\|_2, \tag{2.48}$$

and d_c is the characteristic length, α_c and q are the dimensionless shape parameters of MQ-RBF. The characteristic length is also known as an "average" nodal spacing in the local domain. For instance, in the two-dimensional space, it is known as

$$d_c = \frac{\sqrt{A_s}}{\sqrt{n}-1}, \tag{2.49}$$

where A_s is the area of support domain and n is the number of supporting nodes in the support domain.

2.6.4 Implementation Issues of RPIM Approximation

There are several implementation issues of RPIM shape function have to be noted.

(1) Singularity of Moment Matrix

Unlike PPIM approximation, usually, there is no singularity problem encountered in RPIM approximation. Mathematicians have already shown the moment matrix of radial basis function $\mathbf{R}_Q$ in Eq. (2.42) is usually invertible in their works [83,86,93]. If the order of polynomial function m used in Eq. (2.35) is much lower than the number of radial basis n, $m << n$, the inverse of moment matrix $\mathbf{G}$ in Eq. (2.46) is also hardly to be singular [40,46].

(2) Augmentation of polynomial functions

In RPIM approximation, the polynomial terms used in the approximation plays very important role. As mentioned in section **2.6.2**, pure RBF approximation can not reproduce polynomial function. Introducing additional polynomial terms in the approximation has bought several advantages and results in favourable properties of RPIM shape functions [40,46,92]. The use of polynomial function not only reduces the effects of dimensionless shape

parameters on the approximation but also provides better stability. In general, the accuracy of the numerical solution is also improved or at least no undesirable effect. Adding up to linear polynomial function will also ensure the C^1 consistency for meshfree weak-form method. In this thesis, polynomial with completed second order, $m = 6$, is adopted in the RPIM approximation.

(3) Values of dimensionless shape parameters of RBFs

Determination of appropriate shape parameters is a very important study for RBFs. The shape parameters definitely have certain significant effects on the numerical solution. Therefore, determining the optimal shape parameters for RBFs is always the primary task for RPIM approximation. However, the focus of the thesis is not on the study of RBFs and their optimal dimensional shape parameters. As thorough studies of dimensionless shape parameters have been conducted by Liu et al [40,46,91,92], recommended values for shape parameters of MQ-RBF: $\alpha_c = 3.0$ and $q = 1.03$ are used throughout this work.

2.6.5 Comparison between RPIM and PPIM Shape Functions

This thesis is mainly focusing on the development of meshfree strong-form methods. In contrast to meshfree weak-form methods that are derived from the variational principle, the function approximation plays even more crucial role in the meshfree strong-form methods. In this section, a comparison between the RPIM and

PPIM shape functions is therefore made.

Comparing with RPIM approximation, PPIM approximation has some advantages as follows.

(1) Cheaper computational cost

As compared to the RPIM approximation, PPIM approximation requires less number of supporting nodes to construct their shape functions. As a result, the size of the moment matrix of PPIM is much smaller and hence lower computational cost is needed. In addition, since the shape function is in the form of polynomial, obtaining the derivatives of PPIM approximation is very simple and straightforward.

(2) No shape parameters

In the PPIM formulation, no shape parameter is involved. In contrast, the RPIM approximation is required to determine the shape parameters for RBFs in order to obtain good approximation.

(3) Well established theory

Polynomial function has been very well-known and widely used in many different areas. Good understanding of polynomial function has been well established.

Nevertheless, RPIM approximation is still much widely used in meshfree methods. In this work, RPIM approximation is adopted in various strong-form meshfree methods.

The reasons are very obvious as listed in the following.

(1) Flexibility in nodal and basis selection

In the RPIM formulation, the selection of supporting nodes and basis function are much flexible. Unlike the PPIM, the number of supporting nodes in the RPIM approximation can be any number, as long as the number of radial basis is much more than the number of monomials, $n >> m$, as shown in Eq. (2.35).

(2) Non-singularity moment matrix

Singularity problem is the most critical problem in the construction of PPIM shape function. Inappropriate selection nodes and basis can cause singular moment matrix easily. This is one of the fatal shortcomings, which prohibits PPIM shape functions from being used in the adaptive analysis. As moment matrix in the RPIM formulation is always invertible, it makes RPIM approximation more robust and suitable for arbitrary scattered nodes.

(3) Less sensitive to nodal distribution

In the PPIM formulation, unfavourable nodes distribution can cause the moment matrix singular easily. However, RPIM shape function is more robust to the nodal distribution. Such important feature benefits the meshfree methods in the adaptive analysis where nodal distribution can be severely scattered throughout the domain sometime.

(4) Good accuracy

A vast number of research works has shown RPIM approximation is a very good approximation [40,42,46,56,91,92,etc]. RPIM shape function can be used to approximate the field function and their derivatives in very high accuracy. Excellent numerical performance is also exhibited in many meshfree methods that use RPIM approximation.

Point	x	y
1	0	0
2	0.5	0
3	1	0
4	0	1
5	0.5	1
6	1	1

Table 2.1 Coordinate of the six nodes selected for constructing moment matrix.

Type of RBF	Expression	Shape Parameters
Multiquadrics (MQ)	$R_i(\mathbf{x}) = [r_i^2 + (\alpha_c d_c)^2]^q$	α_c , q
Gaussian (EXP)	$R_i(\mathbf{x}) = \exp^{-\alpha_c\left(\frac{r_i}{d_c}\right)^2}$	α_c
Thin plate spline (TPS)	$R_i(\mathbf{x}) = r_i^{\eta}$	η
Logarithmic	$R_i(\mathbf{x}) = r_i^{\eta} \log r_i$	η

Table 2.2 Typical conventional form of radial basis functions.

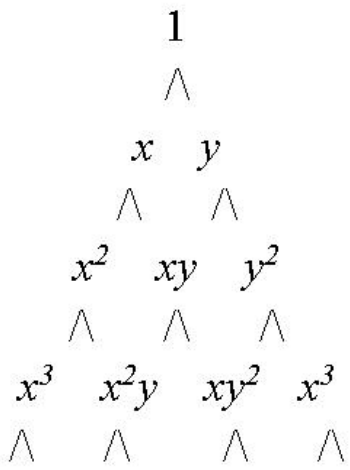

Figure 2.1 Pascal triangle of monomials for two dimensional spaces.

Chapter 3

Adaptivity

3.1 Introduction

Adaptivity has been recognized as an important study in the contemporary computational mechanics. Meshfree method, especially meshfree strong-form method, possesses many attractive and distinguished feastures that facilitate an easier implementation for adaptive analysis. Due to the feature of mesh free, meshfree strong-form method does not require successive remeshings during adaptation. The tremendous cost incurs due to the cumbersome remeshing procedure can therefore be eliminated. Furthermore, as connectivity is not involved in the strong formulation, the refinement and coarsening process in adaptation is rather simple and straightforward.

Nevertheless, adaptive strong-form method is still encountering several challenges. Besides the stability issues in the strong-form method, an effective and robust error estimator that is feasible for strong-form method is also needed. Currently, most of the existing error estimators are an extension from the well established error estimators for the FEM. Such error estimators are suitable for weak-form method but not strong-form method. Available error estimator for strong-form method is very limited. In this chapter, two error estimators that can be used for strong-form method

are introduced.

There are many important aspects in the study of adaptivity; however, it is impossible to cover all aspects in this thesis. Thus, this work is only focusing on the development of error estimator and '*h*-refinement' scheme. A very robust and effective residual based error estimator is proposed in this work and a simple '*h*-refinement' is employed in the adaptation. Although the adaptative strategy introduced in this work is quite simple, the adaptative analysis has been shown very efficient and accurate in many numerical examples. Indeed, simplicity is an advantage of using meshfree strong-form method in the adaptive analysis.

3.2 Definition of Errors

Accuracy of solution is always the greatest concern in the numerical study. Before one proceeds further, it is necessary to define the error used in this thesis. In the present study, error is defined as a difference between exact solution and approximated solution. For instance, the error of displacement is known as

$$e_u = u^{appro} - u^{exact}, \tag{3.1}$$

where u^{appro} is the approximated solution of displacement and u^{exact} is the exact solution of displacement. However, the error given in Eq. (3.1) is quite misleading as it is expressed in a local manner. The local error can not reflect the overall accuracy of solution. For examples, the error of numerical solution at the small high stress concentration region is usually large; however, the solutions at the majority domain are

still acceptable. For this reason, the below scalar norms are defined for better measurements of error.

The following error norm is one of the norms adopted in this thesis:

$$\mathbf{e}_n = \sqrt{\frac{\sum\left(\mathbf{u}^{appro} - \mathbf{u}^{exact}\right)^2}{\sum\left(\mathbf{u}^{exact}\right)^2}}. \tag{3.2}$$

Another norm that often used in this thesis, *energy norm*, is expressed in an integral form. The energy norm is defined for error as [100]:

$$\|\mathbf{e}\| = \left[\int_\Omega \left(\mathbf{e}^T L\mathbf{e}\right) d\Omega\right]^{\frac{1}{2}} = \left[\int_\Omega \left(\mathbf{u}^{appro} - \mathbf{u}^{exact}\right)^T L\left(\mathbf{u}^{appro} - \mathbf{u}^{exact}\right) d\Omega\right]^{\frac{1}{2}}, \tag{3.3}$$

where $L(\ )$ is a differential operator.

In the solid mechanics problem, the above energy norm is also known as

$$\begin{aligned}\|\mathbf{e}\| &= \left[\int_\Omega \left(\boldsymbol{\varepsilon}^{appro} - \boldsymbol{\varepsilon}^{exact}\right)^T \mathbf{D}\left(\boldsymbol{\varepsilon}^{appro} - \boldsymbol{\varepsilon}^{exact}\right) d\Omega\right]^{\frac{1}{2}} \\ &= \left[\int_\Omega \left(\boldsymbol{\varepsilon}^{appro} - \boldsymbol{\varepsilon}^{exact}\right)^T \left(\boldsymbol{\sigma}^{appro} - \boldsymbol{\sigma}^{exact}\right) d\Omega\right]^{\frac{1}{2}},\end{aligned} \tag{3.4}$$

where $\boldsymbol{\varepsilon}$ denotes the strain tensor, $\boldsymbol{\sigma}$ denotes the stress tensor and $\mathbf{D}$ is the elasticity matrix for elastic material. One should note that the strain energy of an elasticity system is also known as

$$energy = \int_\Omega \frac{1}{2}\boldsymbol{\varepsilon}^T \mathbf{D}\boldsymbol{\varepsilon} d\Omega = \int_\Omega \frac{1}{2}\boldsymbol{\varepsilon}^T \boldsymbol{\sigma} d\Omega. \tag{3.5}$$

In this thesis, the norms defined in above will be adopted for quantifying the error of the numerical solution.

3.3 Error Estimators

Error estimator plays a very curcial role in the adaptivity. The refinement or coarsening process can only carried out based on the error estimation. Establishing a robust, accurate and effective error estimator without the knowledge of exact solution is a great challenge. Without a good prediction of error in the adaptive analysis, efficient adaptive scheme is impossible to be achieved.

For finite element method (FEM), the most well established error estimators used in the adaptive analysis can be generally categorized into two types: recovery based error estimator and residual based error estimator. The recovery based error estimator is first introduced by Zienkiewicz and Zhu in 1987 [101]. It is obtained through recovery process and always be expressed in term of energy. Following the work of Zienkiewics et al, many other recover based error estimators have been proposed [10,94,95,102-104]. Besides recovery based error estimator, residual based error estimator is another most common type of error estimators. In fact, residual based error estimator is proposed much earlier than recovery based error estimator. In 1978, Babuska and Rheinboldt first introduced the residual based error estimator in their work [6]. As its name implies, this type of error estimator make use of the residual to approximate the accuracy of the numerical solution. Many research works related to the residual based error estimators have also been published [1,13,84].

Most of the above mentioned error estimators can be further extended for meshfree weak-form method. For example, Duarte and Oden have adopted residual based error estimator [6] in the *hp*-meshless method [18]. Chung and Belytschko have also proposed an error estimator that based on the stress projection [14] and expressed in term of energy norm, which is similar to the work of Zienkiewics in certain respect [101]. Nonetheless, none of the above mentioned error estimators are feasible to be used for strong-form methods. Establishing a novel and reliable error estimator that is customized for meshfree strong-form methods becomes the primary task before meshfree strong-form method can be extended to adaptive analysis. In this thesis, two errors estimator, interpolation variance based error estimator and residual based error estimator, are proposed for the adaptive meshfree strong-form methods.

3.3.1 Interpolation Variance Based Error Estimator

The first error estimator adopted for the meshfree strong-form method in this thesis is first introduced by Iske et al [7, 29]. The local error estimates proposed by Wu and Schaback [96] for RBFs interpolation of scattered data is adopted in his adaptive work for detecting the discontinuities in scattered data approximation. In my work [51], this error estimator is employed in the adaptive analysis using stabilized least-squares radial point collocation method (LS-RPCM) which given in Chapter 6.

3.3.1.1 Formulation of Interpolation Variance Based Error Estimator

In the work of Iske, the definition of the error estimator given in Ref. [7] is known as

$$\eta_i = \left| u_i - s\left(\mathbf{x}_i\right) \right|, \tag{3.6}$$

where u_i is the field value at node *i* and $s\left(\mathbf{x}_i\right)$ is the interpolation value of node *i* computed by a set of supporting nodes except node *i*, $\mathbf{X}_i \setminus \mathbf{x}_i$, where $\mathbf{X}_i = \left\{\mathbf{x}_1, \quad \mathbf{x}_2, \quad \cdots \quad \mathbf{x}_n\right\}$ is the set of supporting nodes for $\mathbf{x}_i$. In my work [51], the definition of the error estimator is further extended as

$$\eta_i = \left| u_i^s - u^{\bar{s}}\left(\mathbf{x}_i\right) \right|, \tag{3.7}$$

where u_i^s denotes the primary field variable or the function of the field variable at node *i*, for instance, effective stress σ; $u^{\bar{s}}$ denotes interpolation value of the primary field variable or the function of field variable for node *i* computed using a set of supporting nodes except node $\mathbf{x}_i$, $\mathbf{X}_i \setminus \mathbf{x}_i$.

The local error estimator η_i reflects the local reproduction quality of the interpolation around node $\mathbf{x}_i$. One should note that η_i will vanish if the field variable is linear around node $\mathbf{x}_i$. The small variance between u_i^s and $u^{\bar{s}}\left(\mathbf{x}_i\right)$ indicates the numerical solution is a good approximated solution. Thus, no refinement is required to perform around node $\mathbf{x}_i$. In contrast, if value of η_i is very large, it indicates that the quality of reproduction is not good enough. Thus, refinement process is required to insert additional nodes around node $\mathbf{x}_i$.

3.3.1.2 Remarks

One should note that this error estimator is determined at nodes and it is based on

the variance between the interpolation value and nodal value. The implementation cost is very low as nodal selection for constructing the shape functions at nodes already available during discretization of the governing equation. Most importantly, unlike the conventional error estimators used for weak-form methods, the interpolation variance based error estimator does not require any mesh to compute the physical quantity, such as energy norm. This unique feature makes this error estimator feasible in the adaptive meshfree strong-form method.

In my paper [51], the interpolation variance based error estimator has successfully implemented in the adaptive analysis. Incorporating with a stabilized least-squares radial point collocation method (LS-RPCM), the interpolation variance based error estimator has demonstrated good performance in adaptive analysis. Numerical examples will be presented in the following chapter for stabilized LS-RPCM.

3.3.2 Residual Based Error Estimator

In this thesis, a novel error estimator is proposed and applied in many adaptive meshfree methods [67-69,97]. This error estimator is formulated based on the residual of the discretized strong-form governing equation. To discretize the strong-form governing equation, RPIM approximation that based on well-known RBFs is used. Due to the higher order continuous feature of RPIM shape function, the higher derivatives of the field function in the strong-form governing equation can be obtained easily.

The proposed residual based error estimator is quite a versatile error estimator. It is not only feasible for numerical method formulated based on mesh, e.g. finite element

method, but also feasible for meshfree methods where the conventional FEM error estimators can not be used. Furthermore the present error estimator is also applicable for numerical method that formulated based on both strong and weak formulation in the adaptive analyses.

3.3.2.1 Formulation of Residual Based Error Estimator

In this work, an error estimator that is formulated based on the residual of the strong-form governing equation is proposed. In fact, this residual based error estimator provides some physical interpretation. This is actually an indicator for the equilibration in the local domain and hence the quality of the approximated solution can be reflected in this measure.

Considering a system is governed by the following partial differential equation (PDE) as

$$L(u)+ f = 0 \text{, in the problem domain } \mathbf{\Omega}, \tag{3.8}$$

where $L(\,)$ is a differential operator and u is the field function in the domain. The residual based error estimator is defined as

$$\eta_L := Res^{\mathrm{T}} = L\left(u^h\right)+ f \,, \tag{3.9}$$

where Ω^T denotes the local domain and Res^T is the residual of strong-form governing equation that measured in the local domain Ω^T using the numerical solution u^h. The residual of the strong-form governing equation is known as follows:

$$Res^T := \left\| L\left(u^h\right) + f \right\|_{L_2}. \tag{3.10}$$

One can use Delaunay diagram to construct the local domain easily. Each Delaunay cell represents a single local domain for the measure of residual. One point Gauss integration scheme is used for the evaluation of the residual in Eq. (3.9). Thus, the local error estimator can further be simplified as

$$\eta_L = Res^T \times |T|, \tag{3.11}$$

where $|T|$ is the area of the respective Delaunay cell. Furthermore, the estimated global residual norm is defined as

$$\eta_G = \left\| \mathrm{Re}\, s^T \right\|_{L_2} = \left[\int_\Omega \left(\mathrm{Re}\, s^T \right)^2 d\Omega \right]^{\frac{1}{2}}, \tag{3.12}$$

which η_G is the L_2 norm of the residual in the entire problem domain.

This is very important to know that in the conventional residual based error estimator [4] used in the FEM is measured in term of the traction jump along the edges between two elements. However, this idea is not feasible for the meshfree strong-form method where mesh is not used.

3.3.2.2 Numerical Examples:

To show the proposed error estimator is robust and effective, four examples are given here. Problems studied in these examples include the Poisson problem and elastostatics problems. In the first numerical example, the residual based error

estimator has been shown successfully be applied in the adaptive meshfree strong-form method. As more examples for adaptive strong-form methods can found in the following chapters, only one example for adaptive strong-form method is provided. Three more examples have been given here to show the present error estimator is also feasible for conventional FEM.

Example 1:

In the first example, the residual based error estimator is used in an adaptive meshfree strong-form method. The meshfree strong-form method used in the adaptive analysis is known as regularized least-square radial point collocation method (RLS-RPCM). As RLS-RPCM is a truly meshfree method, no mesh is used in the formulation. The details of the formulation procedure can be found in **Chapter 7**. A benchmark elastostatics problem, a thick wall cylinder subject to an internal pressure, is studied in this example. The material properties and geometries are given as: internal radius $a = 1$, external radius $b = 5$, Young's modulus $E = 1 \times 10^7$, Poisson's ratio $\upsilon = 0.3$ and internal pressure $P = 1MPa$. The analytical solution of this problem can be found in Ref. [16].

The governing equation of the elastostatics problem is well-known as

$$\sigma_{ij,j} + f_i = 0 \quad \text{in} \quad \Omega . \tag{3.13}$$

The Neumann boundary conditions are given as

$$\sigma_{ij} n_j = t_i \quad \text{on} \quad \Gamma_t . \tag{3.14}$$

And Dirichlet boundary conditions are known as

$$u_i = \bar{u}_i \quad \text{on} \quad \Gamma_u . \tag{3.15}$$

As this problem is symmetric, only quarter of the problem is investigated. Symmetric boundary conditions are imposed along the left and bottom edges.

In this example, only fifteen nodes are used to construct the shape functions. The local refinement coefficient and global residual tolerance are predefined as $\kappa_l = 0.1$ and $\kappa_g = 0.1$ respectively. The adaptive analysis starts with 121 regularly distributed nodes in the domain and stops at the 4^{th} step with 809 nodes irregularly distributed in the domain. The estimated global residual norm at each step is plotted in **Figure 3.1**. From the nodal distributions shown in **Figure 3.2**, one can observe that most of the nodes are inserted close to the internal circumference where the stresses are highly concentrated. The error norm of displacements has been greatly reduced from 14.78% to 0.37% as shown in **Figure 3.3**. The energy norm has also been reduced drastically as shown in the **Figure 3.4**.

The initial and final solutions of displacements and stresses along the edge are also plotted in **Figure 3.5** and **Figure 3.6**. These plots show the adaptive scheme has effectively refines the critical domain based on error estimator and hence the solutions are improved significantly. The residual based error estimator has been demonstrated successfully be applied in the adaptive meshfree strong-form method, good

performance is observed.

Example 2:

The second numerical example is a Poisson problem with a steep gradient solution. An adaptive analysis of FEM using linear triangular element is studied for the following Poisson equation.

$$\nabla^2 u = \frac{2000\left[1+\left(1000x^2y^2-1\right)^2\right]\left(x^2+y^2\right)-2\left(2000xy\right)^2\left(x^2+y^2\right)\left(1000x^2y^2-1\right)}{\left[1+\left(1000x^2y^2-1\right)^2\right]^2}, \tag{3.16}$$

$$\mathbf{x}\in\Omega:[0,1]\times[0,1],$$

with Neumann boundary conditions

$$\frac{\partial u}{\partial x}=\frac{2000xy^2}{1+\left(1000x^2y^2-1\right)^2},\ \mathbf{x}\in\Gamma_n: x=1,$$

and (3.17)

$$\frac{\partial u}{\partial y}=\frac{2000x^2y}{1+\left(1000x^2y^2-1\right)^2},\ \mathbf{x}\in\Gamma_n: y=1.$$

And Dirichlet boundary conditions are given as

$$u=\tan^{-1}(-1),\ \mathbf{x}\in\Gamma_u: x=0\ and\ y=0. \tag{3.18}$$

The exact solution of this problem is known as

$$u=\tan^{-1}\left(1000x^2y^2-1\right). \tag{3.19}$$

The three dimensional plot of the exact solution is shown in **Figure 3.7**. Steep gradient can be observed in the plot.

In this example, the local refinement coefficient and the global residual tolerance are set as $\kappa_l = 0.05$ and $\kappa_g = 0.05$ respectively. Sixteen nodes are used to contruct the RPIM shape function. The adaptation takes 6 steps to complete from a regularly nodal distribution with 100 nodes at initial step and end up with 1062 nodes scattered throughout the domain. The meshes at first, second, 4^{th} and final steps are shown in **Figure 3.8**. From the mesh of the final step, it is obvious that the region with high gradient has been refined as shown in **Figure 3.9**. The estimated global residual norm has been reduced gradually at each adaptive, see **Figure 3.10**. For comparison purpose, the accuracy of the adaptive analysis is compared with the uniform refinement scheme in **Figure 3.11**. The convergent rate of our adaptive scheme is much higher than the uniform refinement scheme. This example clearly exhibits the motivation of the adaptive analysis. And the present error estimator is shown robust and effective for solving problem with high gradient solution in this example.

Example 3:

A benchmark elastostatics problem is studied in Example 3. An infinite plate with hole subjected to a uniaxial traction in the horizontal direction is considered as a plane strain problem here. The dimension and material properties are given as: $b = 2.0m$ and $a = 0.2m$, Young's modulus $E = 1 \times 10^3$ and Poisson's ratio $\upsilon = 0.3$. Due to symmetric, only a quarter of the plate is analysed, see **Figure 3.12**

In this problem, symmetric conditions are applied along the left and the bottom edges of the model and analytical tractions are applied along the rest of the edges. The analytical solution of this problem can be found in Ref. [90].

Finite element method (FEM) with linear triangular element is used in this adaptive analysis. The local refinement coefficient and global residual tolerance are preset as $\kappa_l = 0.1$ and $\kappa_g = 0.01$ respectively. The entire adaptation takes nine steps to complete. The mesh at first, third, sixth and final steps are given in **Figure 3.13**. From the meshes distribution of the final step, one can notice that the region where the stresses are concentrated is refined the most.

For comparison, this problem is studied using uniform refinement scheme as well. From the numerical solutions of the displacements and energy norm, it can be observed that the proposed error estimator with simple *h*-refinement scheme is able to provide a better convergent rate than the uniform refinement scheme as shown in **Figure 3.14** and **Figure 3.15**. The accuracy of the numerical solution is efficiently improved through our adaptive approach. The present error estimator has demonstrated its excellence performance to identify the region where stresses are concentrated and hence leads the simple refinement scheme to achieve a better solution.

Example 4:

In this example, a crack panel shown in **Figure 3.16** is studied. This problem is considered as a plane strain problem and the material properties are known as Poisson's ratio $\upsilon = 0.3$, Young's modulus $E = 3 \times 10^7$. The dimension of the cracked panel is

given in **Figure 3.16**, where $a = 0.5m$.

The cracked panel is subjected to a load along the boundaries which described as

$$\sigma_{xx} = \frac{K_I}{\sqrt{2\pi r}} \cos\frac{\theta}{2}\left(1 - \sin\frac{\theta}{2}\sin\frac{3\theta}{2}\right), \tag{3.20}$$

$$\sigma_{yy} = \frac{K_I}{\sqrt{2\pi r}} \cos\frac{\theta}{2}\left(1 + \sin\frac{\theta}{2}\sin\frac{3\theta}{2}\right), \tag{3.21}$$

$$\tau_{xy} = \frac{K_I}{\sqrt{2\pi r}} \sin\frac{\theta}{2}\cos\frac{\theta}{2}\cos\frac{3\theta}{2}, \tag{3.22}$$

where K_I is stress intensity of mode I. Due to symmetric, only half of the model is analysed, see **Figure 3.16** (b).

In this example, the adaptive analyses of FEM using both conventional residual based error estimator and the present error estimator that using local RBFs are studied. The initial mesh for FEM is given in **Figure 3.17**. Linear triangular element is used in the FEM.

The conventional residual based error estimator is adopted from Babuska's work [4] as

$$\eta_L = \sqrt{|T|^2 \left(I\Pi_T \mathbf{f}\right)^2 + \frac{1}{2}\sum_{\ell \in E_T} |\ell|^2 \mathbf{J}_\ell{}^2}, \tag{3.23}$$

where triangle element $T \in T_h$, E_T is the edges of the element T, $\mathbf{f}$ is the residual in the element and

$$\Pi_T \mathbf{f} := \frac{1}{|T|} \cdot \int_T \mathbf{f} d\Omega \,. \tag{3.24}$$

For each edge of the element, ℓ, $\mathbf{J}_\ell$ is the traction jump along the element interfaces.

The final mesh of the adaptive analysis using both conventional and present error estimator are shown in **Figure 3.18** and **Figure 3.19** respectively. From the final mesh given in **Figure 3.18** and **Figure 3.19**, one can notice that the distributions of the meshes of the FEM using two different estimators are very similar. The present error estimator using local RBFs is able to identify the singularity point at the crack tip and leads the refinement scheme effectively to achieve a better discretization during the adaptive analysis.

From the error norms of displacement and energy norm, both estimators provide excellent performance as shown in **Figure 3.20** and **Figure 3.21**. A uniform refinement scheme is also carried out for comparison. From error norms given in **Figure 3.20** and **Figure 3.21**, the motivation of the adaptive analysis is clearly demonstrated. The adaptive analysis using both error estimators achieve much better accuracy with very lesser mesh as compared to the uniform refinement scheme. The performance of present error estimator is as good as the conventional residual based error estimator. However, from the view of computational cost, the present error estimator is found more cost effective than the conventional estimator as shown in **Figure 3.22**. It is because the procedure of measuring the traction jump along the interface between elements is more expensive than the direct integration of the residual in the local

domain. The direct integration using one Gauss point scheme is shown robust, effective and reliable to evaluate the present error estimator. Most importantly, conventional residual based error estimator is not feasible for meshfree strong-form methods as mesh is not available.

3.3.2.3 Remarks

The residual based error estimator has been shown as a simple, robust and versatile error estimator in the above examples. Excellence performance of the present error estimator in adaptive analyses is observed. The present error estimator has demonstrated that it can be used to reflect the local error effectively. By integrating with a simple adaptive strategy, the present error estimator can efficiently leads the adaptation to a better discretization with simple refinement scheme. As compared to recovery [10,94,95, 101-104] and conventional residual [4] based error estimators, the present error estimator has been shown very more versatile, simple and easy to be implemented in adaptive analysis. To conclude, the advantages of the residual based error estimator using local RBFs are summarized as follows.

1. The formulation of the present estimator is simple and straightforward and the computational cost is lower than the conventional residual based error estimator.

2. The implementation of the present estimator is very simple. It is very convenience to embrace the present error estimator with existing codes of any numerical method, e.g. finite element method.

3. RPIM approximation is very robust for approximation of the higher derivatives of field function using scattered nodes. In contrast, the PPIM approximation is often breakdown due to the singular moment matrix [45,91].

4. Unlike the recovery based error estimator, the present error estimator does no involve recovery process. The cost for recovery process is therefore avoided.

5. Compared to recovery based error estimator, the knowledge for recovery points is not required. For meshfree methods, obtaining recovery points may not be feasible.

6. As conventional residual based error estimator is involved in evaluating the traction jump of the element interface [4], it is not applicable for meshfree methods where element does not exist in their formulation procedure.

7. This error estimator can be applied for solving various types of PDEs. It is not restricted to a particular problems only.

8. It is obvious that the present error estimator is very versatile. It is not only feasible for numerical method that formulated relying on mesh, for instance, finite element method, but also for the meshfree methods. It is also suitable to be used for both weak and strong formulation procedures as well.

9. From the numerous numerical examples, the error estimator is shown robust, effective, versatile and simple.

In the following chapters, this residual based error estimator will be adopted for various strong-form meshfree methods in adaptive analysis.

3.4 Adaptive Strategy

The adaptive strategy adopted in my work is very simple and straightforward. Indeed the simplicity of the implementation of adaptive analysis should thank to the features of mesh free. Prescribed refinement and stopping criteria are provided in the beginning of the adaptive analysis. If the refinement criterion is met, additional node will be inserted into the domain follows the refinement procedure. Adaptive analysis is a kind of autonomous programme; it will proceed adaptively till the given stopping criterion is satisfied. The details of the refinement and stopping criteria are given as follows.

3.4.1 Local Refinement Criterion

After the error estimator is measured in the entire domain, the maximum value of the local error estimator can be found and denoted by η_{ML}. The local refinement procedure will be carried out only if the following criterion is met.

$$\eta_L > \kappa_l \eta_{ML}, \tag{3.25}$$

where η_L is the local error estimator and κ_l is local refinement coefficient.

3.4.2 Stopping Criterion

In this work, the global residual norm given in Eq. (3.12) is used as an indicator for stopping the adaptation. The adaptation will be stop if the following stopping criterion is met as

$$\eta_G < \kappa_g \eta_{MG}, \tag{3.26}$$

where κ_g is the tolerant coefficient of the estimated global residual norm and η_{MG} is the maximum estimated global residual norm throughout the adaptation process.

Take note that both values, κ_l and κ_g are in the range of 0 and 1, $0 \le \kappa_l, \kappa_g \le 1$. If $\kappa_l = 0$, refinement criteria is always met, uniform refinement will be carried out. On the other hand, if $\kappa_l = 1$ no refinement process will be carried out as criteria can never be met. Similarly, if $\kappa_g = 0$, adaptive analysis will be carried on forever. If $\kappa_g = 1$, adaptive analysis will only be carried out one step.

3.5 Refinement Procedure

For finite element method, the adaptative refinement procedures can generally fall into three categories which are *h*-refinement, *r*-refinement and *p*-refinement. In the adaptive *h*-refinement, mesh is enhanced by subdivision, whereas *r*-refinement only involved in nodal reposition, and *p*-refinement is achieved by increasing the order of approximation.

In this thesis, only '*h*-refinement' scheme is considered. Instead of enhancing the mesh by subdivision, nodal is simply inserted in the domain during refinement process.

Compared to the FEM, the present '*h*-refinement' procedure is much simple and straightforward. As no mesh is used, no hanging nodes issue is arisen in the '*h*-refinement' process for meshfree strong-form method. The expensive remeshing procedure is also eliminated. The '*h*-refinement' procedures for two error estimators introduced in this thesis are different. The details of the refinement procedure for each error estimator are described in the following.

3.5.1 Refinement Procedure for Interpolation Variance based Error Estimator

In this procedure, Voronoi diagram is used to locate the position for the additional nodes as shown in **Figure 3.23**. At each adaptive step, a Voronoi diagram will be constructed based on the current nodal distribution. Every node in the problem domain is corresponding to a Voronoi cell. The error estimator is first evaluated at node and additional nodes will be inserted at the vertices of the cell corresponding to the node if the predefined refinement criterion is met. After the new nodal distribution is formed, a numerical solution will then be computed. The adaptation will proceeds until none of the nodes meet the refinement criterion.

3.5.2 Refinement Procedure for Residual based Error Estimator

In the refinement procedure for residual based error estimator, additional nodes will be inserted into the corresponding local domain if the refinement criterion is met. This refinement procedure is very straightforward. For Delaunay cell in the internal

domain, an additional node will be inserted in the centre of the Delaunay cell if refinement criterion is met.

However, afor Delaunay cell located along the global boundary, special refinement procedure is adopted. Instead of inserting node at the centre of the cell, nodes are added in the middle of the three edges of the corresponding cell. This procedure ensures the additional nodes will be inserted on the global boundaries as well and hence a better nodal distribution can be formed. The demonstration of the refinement procedure for internal and external cells is illustrated in **Figure 3.24**.

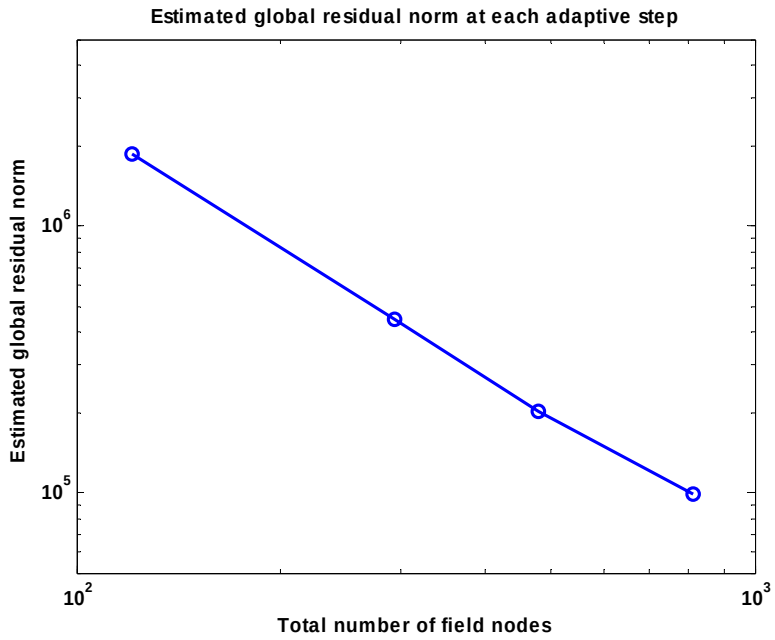

Figure 3.1 Estimated global residual norm at each adaptive step.

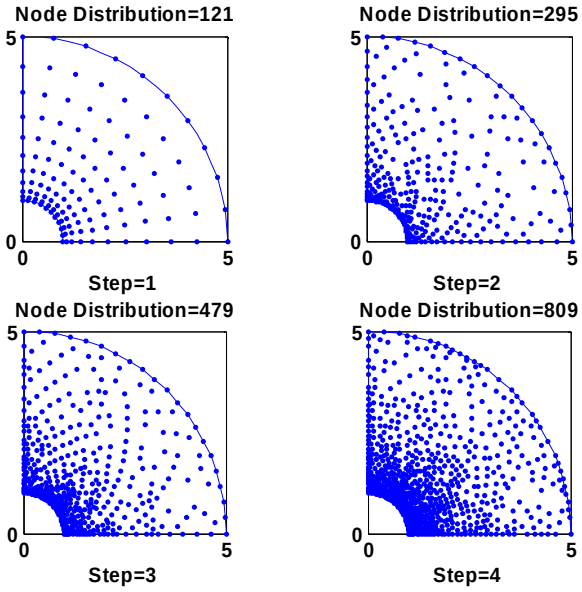

Figure 3.2 Nodal distribution of the model of cylinder at each adaptive step.

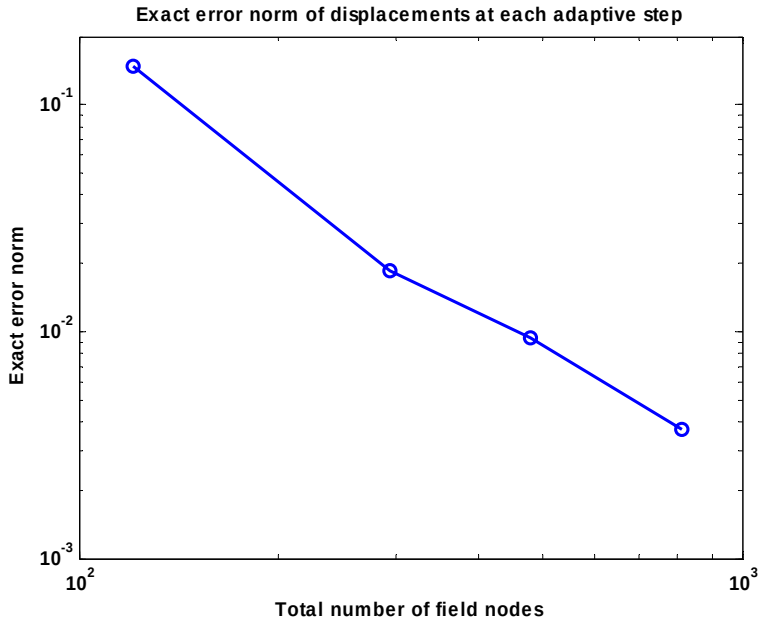

Figure 3.3 Error norm of displacements at each adaptive step.

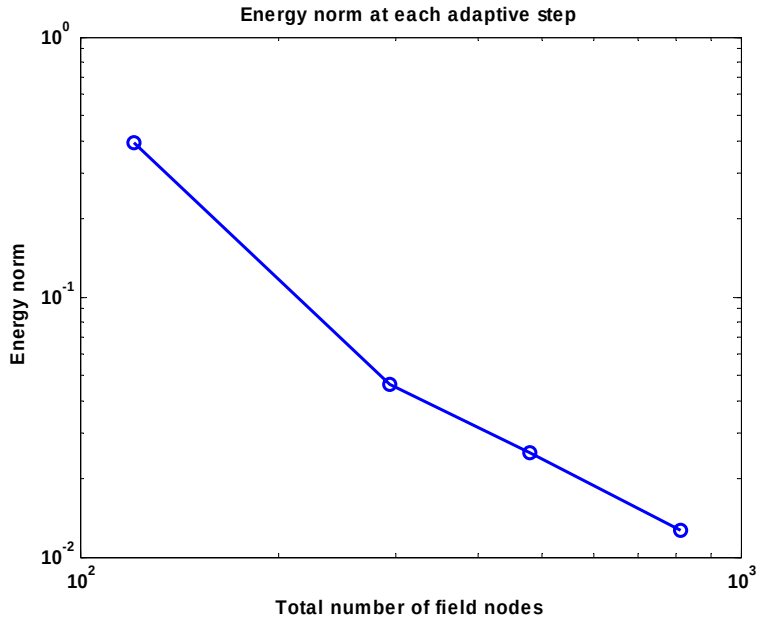

Figure 3.4 Energy norm for error at each adaptive step.

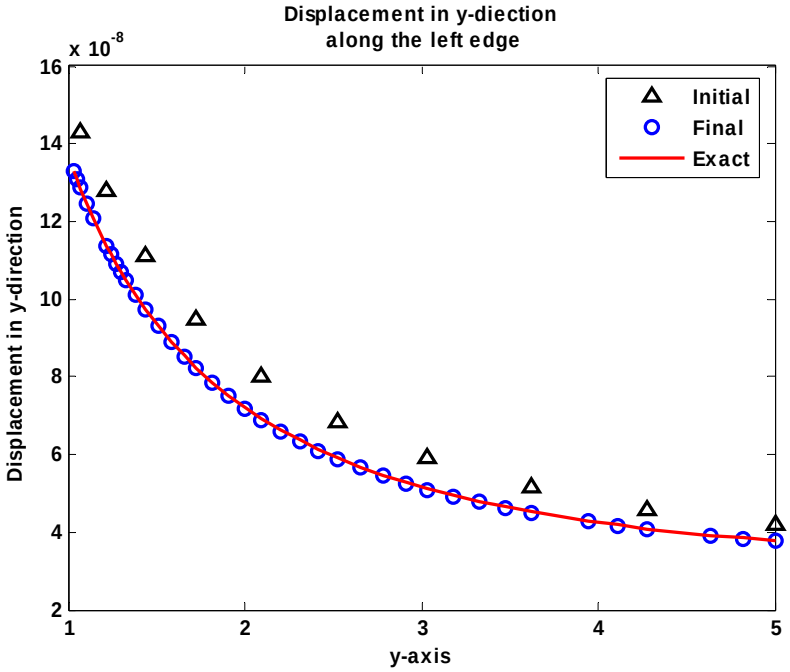

Figure 3.5 Displacements in y-direction along $x = 0$ at each adaptive step.

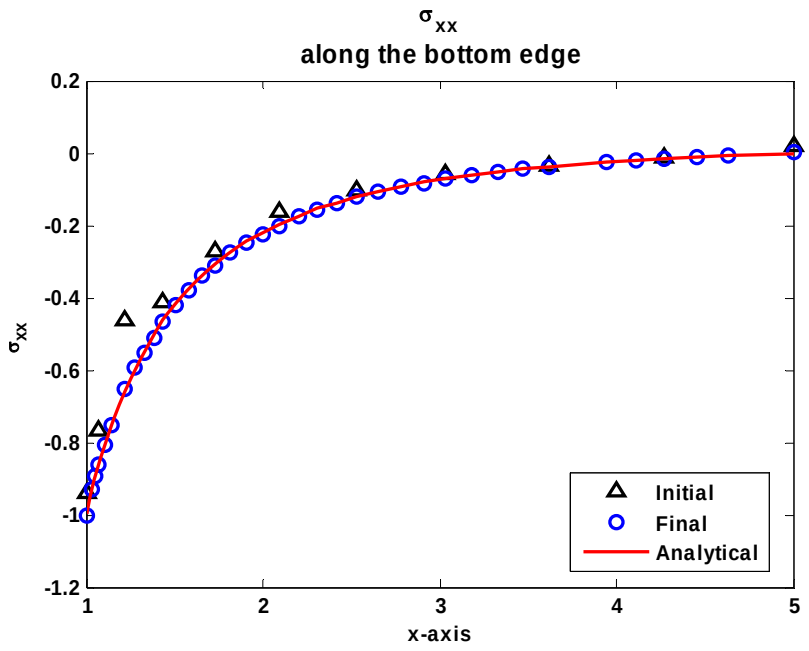

Figure 3.6 Normal stress σ_{xx} along $y = 0$ at each adaptive step.

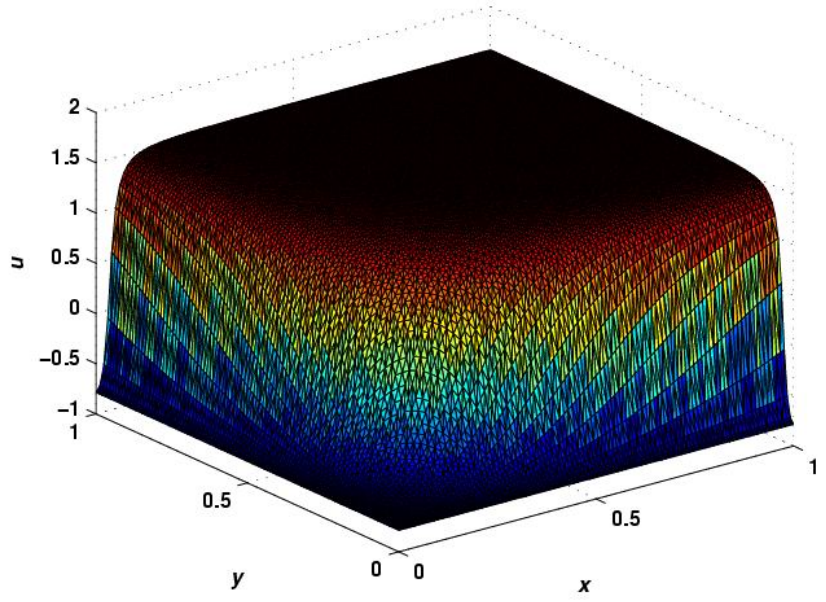

Figure 3.7 Exact solution of a Poisson problem with steep gradient.

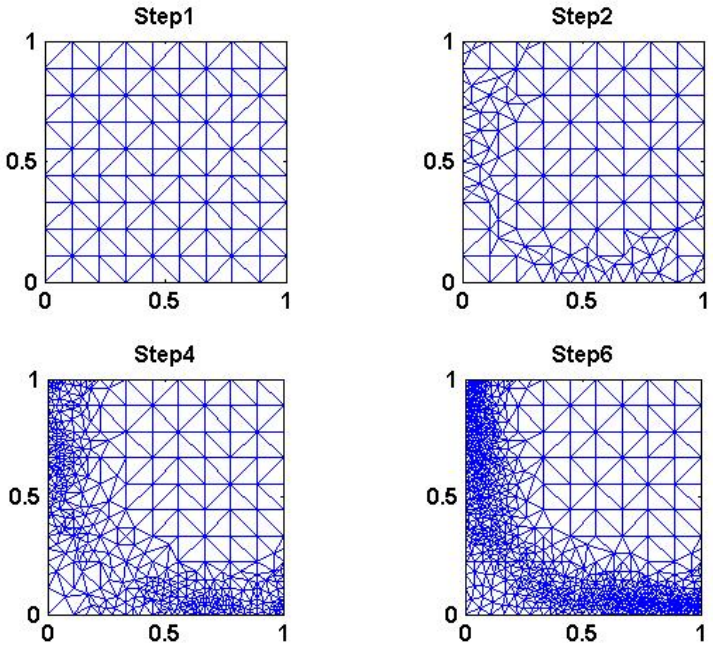

Figure 3.8 Meshes at first, second, fourth and final step.

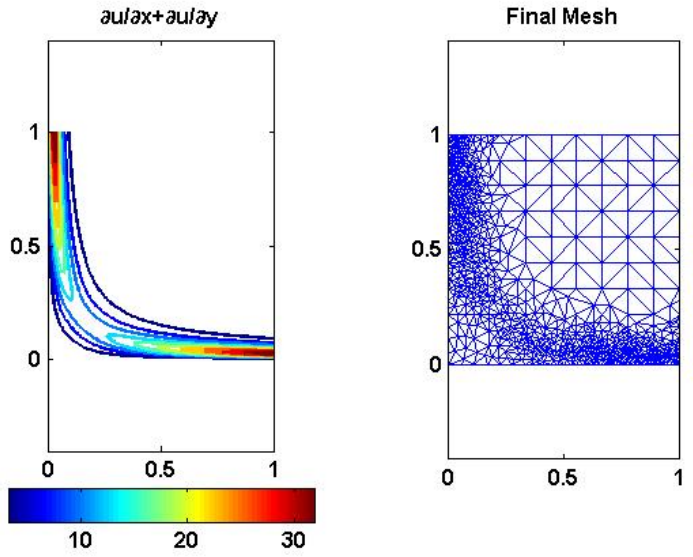

Figure 3.9 Contour plot of the gradient of field function and the meshes at the final step.

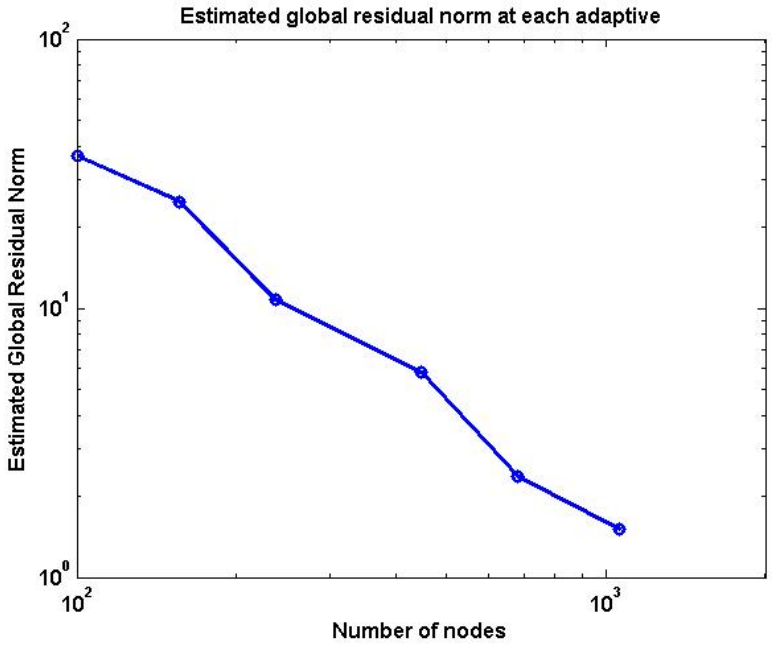

Figure 3.10 Estimated global residual norm at each adaptive step.

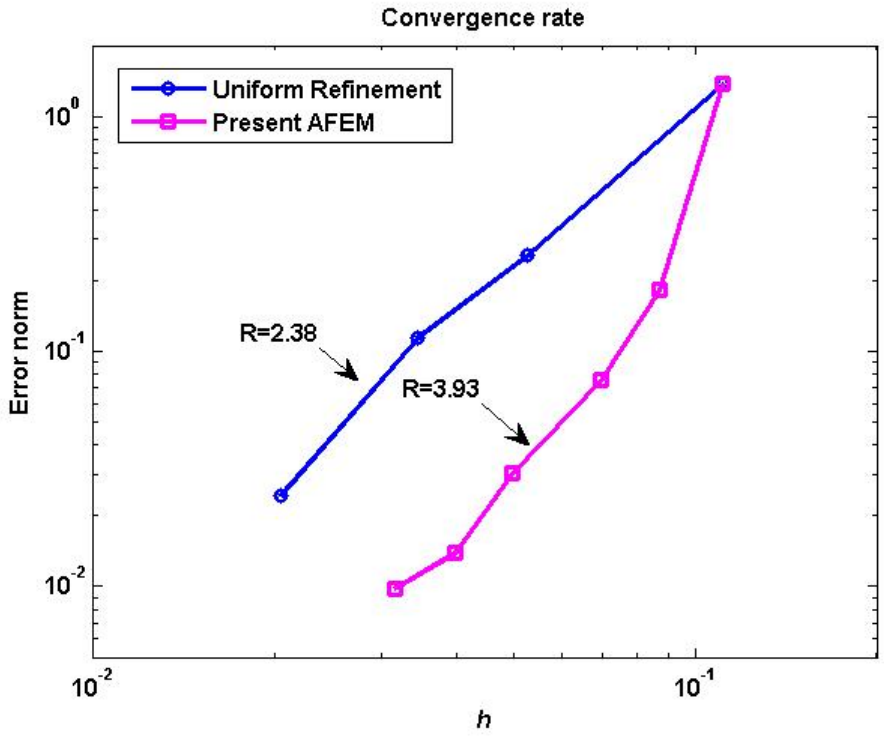

Figure 3.11 Convergent rate of the solution for uniform refinement and present adaptive analysis.

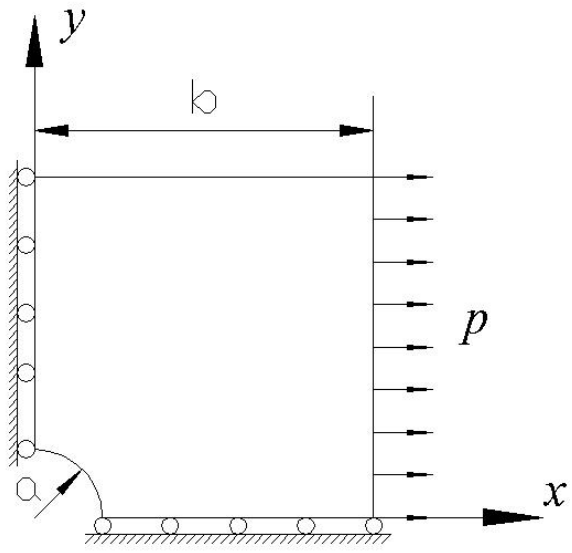

Figure 3.12 A quarter model of an infinite plate with hole.

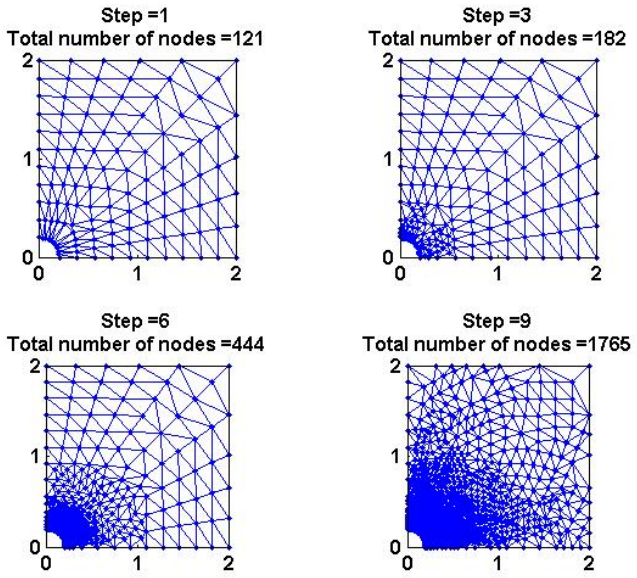

Figure 3.13 Meshes at first, third, sixth and final of the adaptive step.

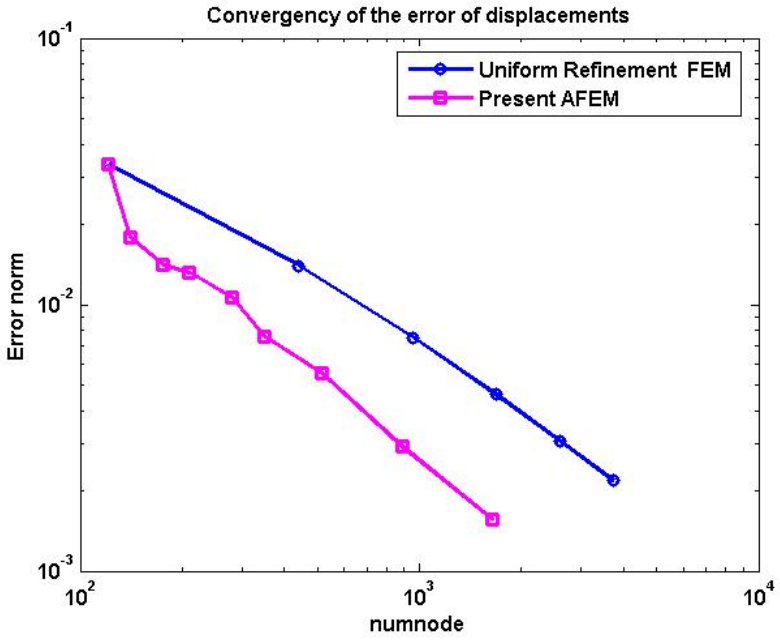

Figure 3.14 Convergency of the error norm of displacements.

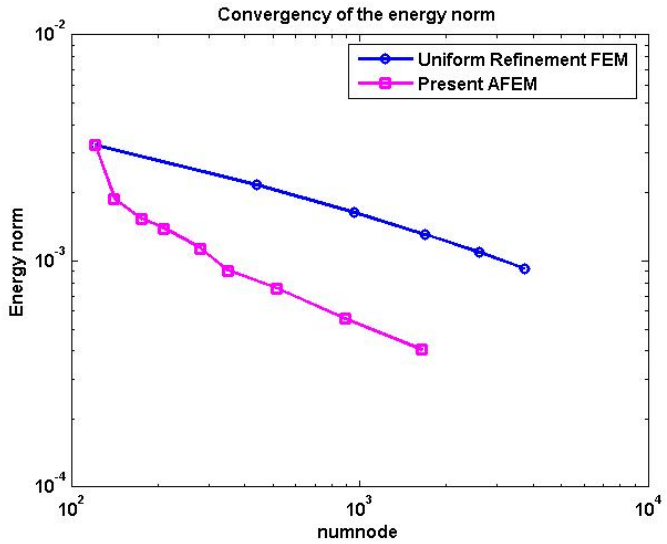

Figure 3.15 Convergency of the energy norm.

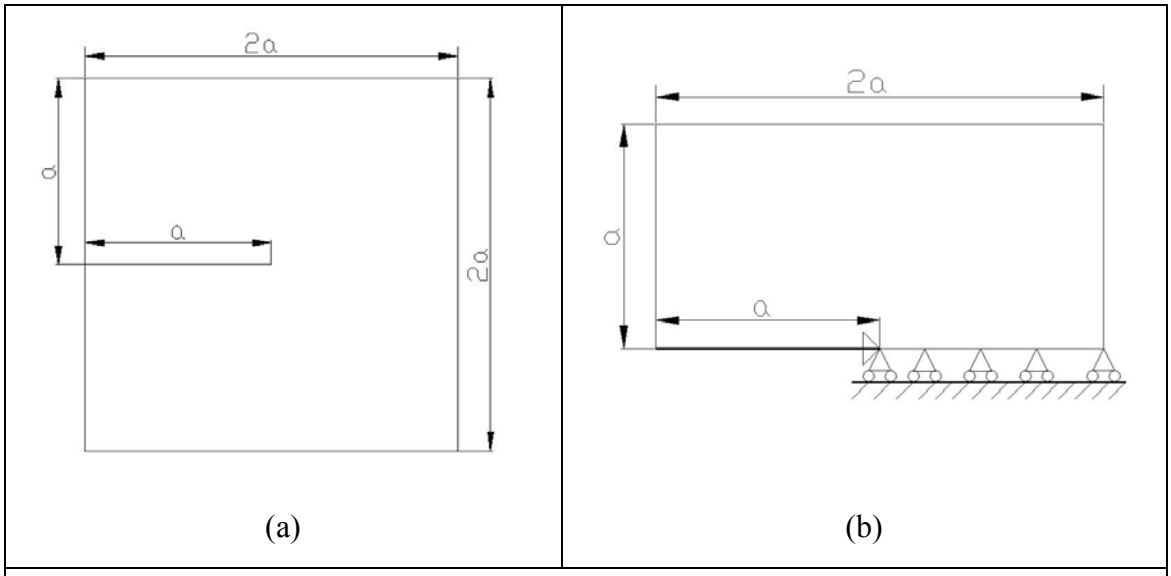

Figure 3.16 (a) A full model and (b) a half model of the crack panel.

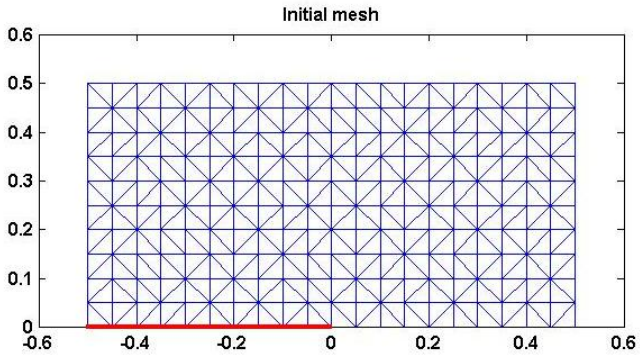

Figure 3.17 Initial meshes of the crack panel model for the adaptive analysis.

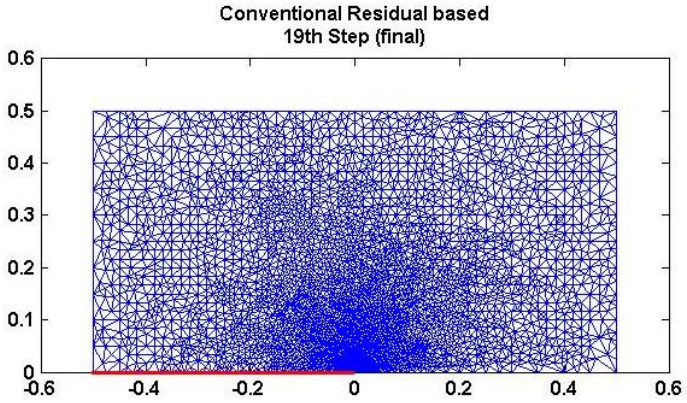

Figure 3.18 Meshes of the final step in the adaptive analysis using conventional residual based estimator.

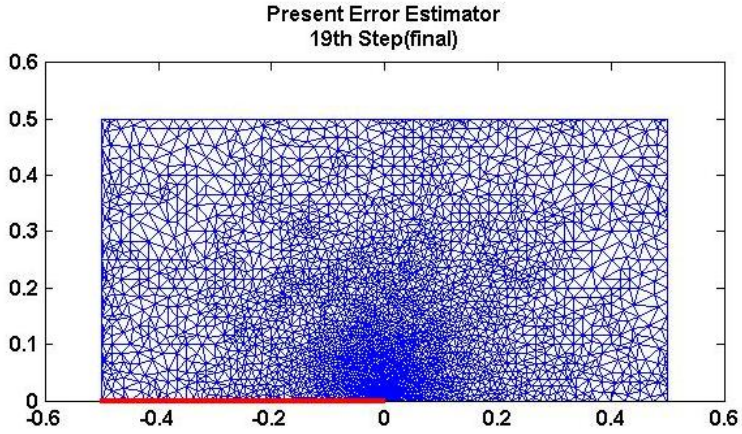

Figure 3.19 Meshes of the final step in the adaptive analysis using present estimator.

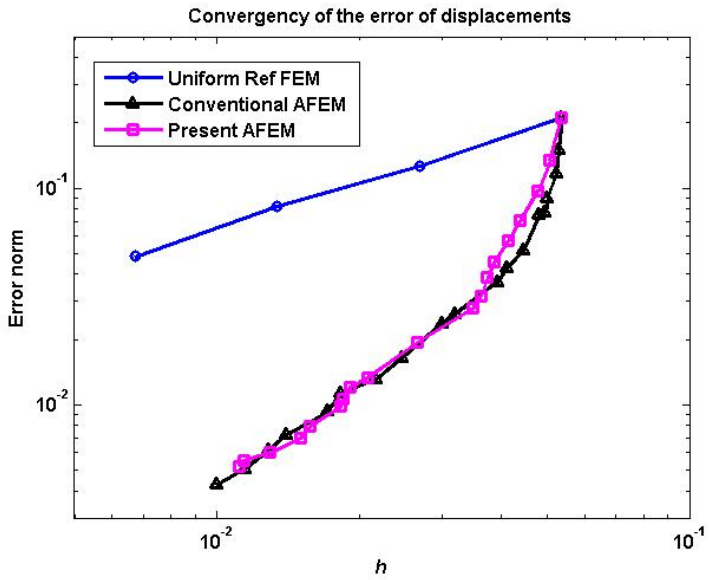

Figure 3.20 Comparison of the convergency in term of the error norm of displacements.

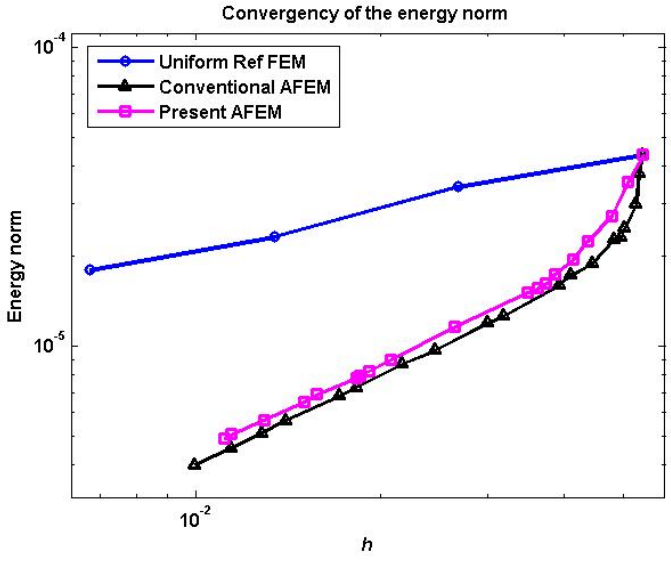

Figure 3.21 Comparison of the convergency in term of the energy norm.

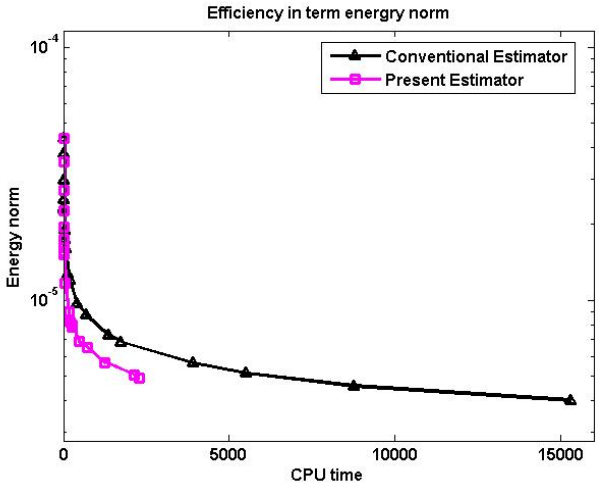

Figure 3.22 Comparison of the efficiency of the error estimators in term of energy norm.

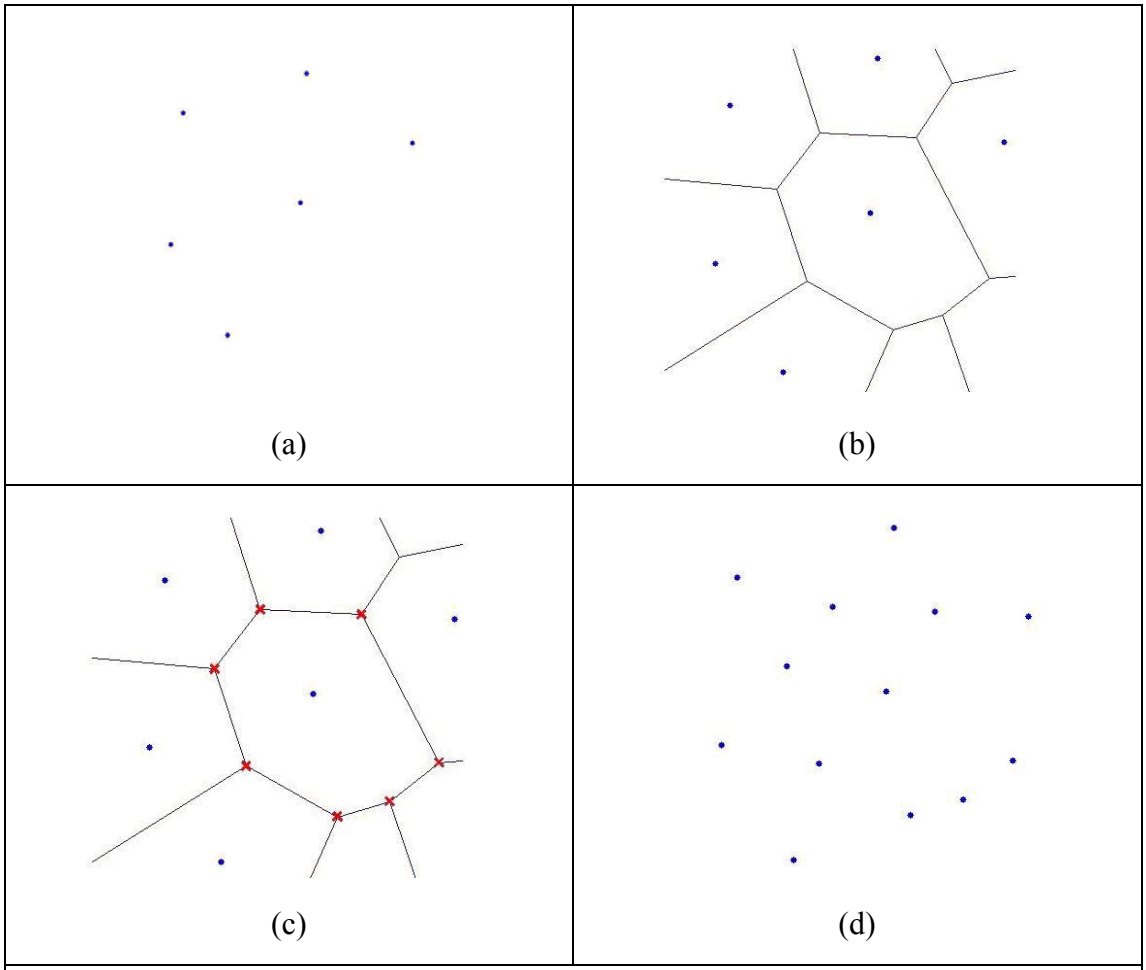

Figure 3.23 The (a) Initial nodal distribution in the domain, (b) Voronoi diagram is constructed, (c) additional nodes are inserted on the vertex of cell and (d) new nodal distribution is formed.

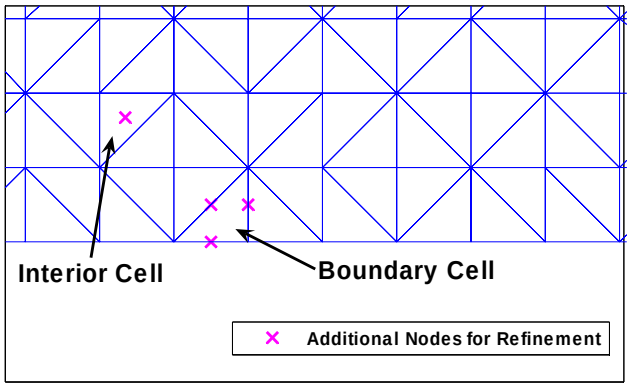

Figure 3.24 Additional nodes inserted at internal and external Delaunay cells in the refinement process.

Chapter 4

Radial Point Collocation Method (RPCM)

4.1 Introduction

Meshfree strong-form method has a relatively longer history than weak-form meshfree method. In the meshfree strong-form methods, collocation technique is employed to discretize the governing partial differential equations (PDEs). Typical strong-form methods has already well introduced in the first chapter of this thesis. Among the strong-form methods, finite different method (FDM) [17] is considered as one of the most classical and earliest works. Many engineering problems have been solved using FDM since it was proposed. However, the constraint of using regular or strucute grids is the major shortcoming of FDM. While engineers are trying to solve for problems with more complicated and irregular domain, FDM requires cumbersome procedure to adapt to the irregular grid [38,39]. This shortcoming limits the application of FDM in solving practical engineering problems.

In early 90s, the well-known radial basis functions (RBFs) were first introduced in the meshfree strong-form methods. Kansa is one of the pioneers who use RBFs in the meshfree strong-form collocation method [65]. As RBFs are able to interpolate

scattered data, such feature provides great flexibility in term of the nodal distribution and hence gets rid of regular grids. Recently, Liu et al have revised the conventional RBFs scheme and proposed a novel RBFs scheme using local nodes. Instead of using all the nodes in the domain for function approximation, on the contrary, only local nodes, the neighbouring nodes of the interest point are selected to approximate the field function and its partial derivatives.

In my work, the strong-form collocation method using local RBFs and collocation technique is called radial point collocation method (RPCM).

4.2 Formulation of RPCM

Consider a problem shown in **Figure 4.1** is governed by the following PDEs:

$$L(u) = f \quad \text{in domain } \Omega, \tag{4.1}$$

with Neumann boundary conditions

$$B(u) = g \quad \text{on boundary } \Gamma_t, \tag{4.2}$$

and Dirichlet boundary conditions

$$u = \bar{u} \quad \text{on boundary } \Gamma_u, \tag{4.3}$$

where $L(\ )$, $B(\ )$ are the differential operators and u is the primary field variable.

Assume that the above equations, Eq. (4.1)-(4.3), can be collocated at the field nodes inside the domain and on the boundaries respectively, the discretized governing

system equations can be shown as follows.

$$L(u_i) = f_i \text{ in } \Omega, \tag{4.4}$$

with Neumann boundary conditions

$$B(u_i) = g_i \text{ on } \Gamma_t, \tag{4.5}$$

and Dirichlet boundary conditions

$$u_i = \bar{u}_i \text{ on } \Gamma_u, \tag{4.6}$$

where subscript "*i*" denotes the collocation point.

In the radial point collocation method (RPCM), RPIM approximation is used to approximate the field function using local nodes. As shown in **Figure 4.1**, the local support domain is formed by the surrounding nodes of the collocation point. The resultant algebraic equations can then be assembled and expressed in the following matrix form as

$$\mathbf{KU} = \mathbf{F}, \tag{4.7}$$

where **K** is the coefficient matrix, **F** is the force vector and **U** is the vector of unknown nodal values. The vector of unknown nodal values can then be easily solved as

$$\mathbf{U} = \mathbf{K}^{-1}\mathbf{F}, \tag{4.8}$$

if **K** is not singular and well-conditioned. It is important to note that the coefficient

matrix of the collocation method is generally unsymmetric.

4.3 Issues in RPCM

Meshfree strong-form method possesses many attractive and distinguished features. As strong-form method is formulated without relying on the mesh, it is always regarded as a truly mesh free method. However, this is not easy to construct shape functions using arbitrary scattered nodes. RPIM approximation is a good candidate to be used for constructing shape functions in the strong-form collocation method. Besides great flexibility for irregular grids, the RPIM shape function also possesses the Kronecker Delta property. Dirichlet boundary conditions can be imposed directly. Furthermore, as compared to PPIM approximation, RPIM approximation is more robust as the moment matrix is always invertible. All those properties of RPIM approximation exhibited in Chapter 2 make radial point collocation method (RPCM) a very promising meshfree strong method.

However, through the thorough study of RPCM, some crucial issues have been found and prohibited RPCM from being a good meshfree strong-form method. First, in the conventional RBF scheme [65,66], all nodes are used to approximate any interest point in the domain. It simply means that a full coefficient matrix is formed and hence limits its application to the large scale problem. Furthermore, the condition of the full coefficient matrix of meshfree collocation method based on global RBFs is often ill [66]. The idea of local RBFs is a very natural choice and it has been proposed by Liu et al [42,51,56,91] to avoid these undesired properties caused by the global

RBFs. In the local scheme, the coefficient matrix is sparse matrix rather than full matrix. The computational cost is drastically reduced. Furthermore, ill-conditioned coefficient matrix caused by the global scheme is also avoided. The idea of local RBF scheme has been devoted to many research works in meshfree methods and significant results have been obtained [42,51,56,62,63,67,91 etc].

Stability is another key issue to be concerned in the RPCM. From many of my studies [40,46,62,63,67], the RPCM solution is found unstable while dealing with the Neumann boundary conditions in higher dimensional space. In one dimensional space, RPCM has always demonstrated well numerical performance. However, RPCM does not always works in the two dimensional space. Although RPCM is still able to provide excellence result without the presence of Neumann boundary conditions, the solution of RPCM becomes unstable whenever Neumann boundary conditions take place. In the following section, numerical examples will be presented to illustrate all these issues in RPCM.

The following are some of the existing strategies or techniques that have been proposed to deal with the Neumann boundary conditions:

(1) Special grids arrangement on the Neumann boundaries

Regular grids are suggested to be arranged along the boundaries such that standard finite difference scheme can adopted. Liszka et al also proposed to have more dense nodal distribution along the boudaries region [39].

(2) Adding ficticous nodes

Adding fictitous nodes outside the domain and close to the boundaries is another suggested option to deal with the Neumann boundaries [66]. Such procedure has already widely adopted in the conventional FDM. Zhang et al also suggested employing more auxillary nodes inside the domain; however, the procedure does not very effectively improve the stability [98].

(3) Special discretization scheme

Special discretization scheme, for instance, Hermite-type collocation scheme, is proposed [99]. In the Hermite-type collocation scheme, derivative variables are included in the interpolation. Onate et al has also suggested augmenting additional stabilization term into the equations for the boundaries nodes [81].

(4) Coupling with weak formulation

Meshfree weak-strong-forms (MWS) method is first proposed by Liu and Gu [44]. As weak solution is much stable, weak formulation is therefore applied for nodes along the Neumann boudaries. Majority of the nodes located inside the domain are still formulated in the strong formulation.

Nevertheless, there is still a room for improvement. Most of the proposed strategies or techniques are either not practical to be extended to adaptive analysis or

not effectively restore stability. Hence, an effective and practical stabilization procedure for strong-form meshfree method is still very desired.

4.4 Numerical Examples:

Several examples are given to demonstrate the excellence performance of RPCM in the one dimensional problem and Dirichlet problems. On the other hand, the shortcoming of RPCM is also revealed here.

4.4.1 Example 1: One Dimensional Poisson Problem

In the first example, a one dimensional Poisson problem is studied. A very steep gradient solution is found in the middle section of the one dimentional domain. Excellent performance of adaptive RPCM is demonstrated in the one dimensional adaptive analysis. A Poisson problem is governed by the following ordinary differential equation (ODE),

$$\frac{d^2u}{dx^2} = \frac{-2a^2(ax-1)}{\left[1+(ax-1)^2\right]^2}, \quad x \in \Omega : [-1,1], \tag{4.9}$$

where a is gradient of the solution. Dirichlet boundary condition is imposed at the left end,

$$u = -\tan^{-1}(a+1) \text{ at } x = -1, \tag{4.10}$$

and Neumann boundary condition is imposed at the right end,

$$\frac{du}{dx} = \frac{a}{1+(ax-1)^2} \quad \text{at} \quad x = 1. \tag{4.11}$$

The exact solution for the above ODE is known as

$$u = \tan^{-1}(ax-1). \tag{4.12}$$

From the exact solution, Eq. (4.12), one can know that the gradient of the field function u depends on the value of a. In this example, an extremely large value of $a = 10^4$ is deliberately selected for the purpose of examining the robustness of the RPCM and the residual based error estimator in one dimensional space. The exact solution of the field function u and its derivative are plotted in **Figure 4.2**.

Only six supporting nodes are used to construct the shape functions for this one dimensional problem. An extremely low global residual tolerance is set as $\kappa_g = 5\times10^{-7}$ and local refinement coefficient is given as $\kappa_l = 0.1$. The entire analysis takes 39 steps to complete and the nodal distributions at first, 10th, 25th and final steps are plotted in **Figure 4.3**. The adaptive strategy is shown simple and yet effective. One can observe that the adaptive RPCM is able to capture and refine the high gradient region. Majority of the nodes have been inserted at the high gradient region as shown in **Figure 4.3**.

The final solution of RPCM in the adaptive analysis using the RPCM is shown in **Figure 4.4**. The approximated solutions obtained by RPCM are in good agreement with the analytical solutions. The estimated global residual norm and the error norms of the

RPCM solutions have been tremendously reduced through our adaptive scheme as shown in the **Figure 4.5**. The numerical solutions for the field function and its gradient are significantly improved by our adaptive approach as shown in **Figure 4.3**.

4.4.2 Example 2: Two dimensional Poisson Problem with Dirichlet Boundary Conditions

In the second example, RPCM is extended to the following Poisson problem in two dimensional space as below.

$$\frac{\partial^2}{\partial x^2}u + \frac{\partial^2}{\partial y^2}u = \sin \pi x \sin \pi y \text{ , in } \mathbf{\Omega} = [0,1]\times[0,1]. \tag{4.13}$$

This problem is considered as a Dirichlet problem and the Dirichlet boundary conditions are given as

$$u = 0 \text{ , along the boundary } \Gamma . \tag{4.14}$$

Analytical solution of this Poisson problem is known as

$$u = -\frac{1}{2\pi^2}\sin \pi x \sin \pi y \text{ ,} \tag{4.15}$$

and plotted in **Figure 4.6**.

This Poisson problem is solved by RPCM using 11×11 regularly distributed nodes as shown in **Figure 4.7**. Ten supporting nodes are used to construct the RPIM shape functions. The error norm of the numerical solution is only 0.82% . The solution of RPCM along $y = 0.5$ is plotted in **Figure 4.8** and it is shown in great agreement

with the analytical solution.

4.4.3 Example 3: Standard and Higher Order Patch Tests

The third numerical example is standard and higher order patch tests.

Standard Patch Test:

RPCM is examined in a standard patch test using two patches as shown in **Figure 4.9**. **Figure 4.9** (a) shows a patch of 25 regularly distributed nodes and **Figure 4.9** (b) shows a patch of 25 irregularly distributed nodes. The dimension of both patches is 1.0 unit by 1.0 unit and the material properties are taken as $E = 1.0$ and $\upsilon = 0.25$. In the standard patch test, the displacement is prescribed on the boundaries by a linear function of *x* and *y*:

$$u_i = x_i + y_i \text{ and } v_i = x_i - y_i . \tag{4.16}$$

Satisfaction of the patch test requires that the displacements of any interior nodes be given by the same linear functions. In the patch test, ten supporting nodes are used to construct the shape functions. As shown in **Table 4.1**, both patches have passed the standard patch test to machine accuracy. The detailed procedure of the standard patch test can be found in Ref. [100].

Higher Order Patch Test:

In the higher order patch test, two patches shown in **Figure 4.10** are subjected to two cases of loading at the right end. There are 35 nodes regularly distributed in patch **C** and irregularly distributed in patch **D** as shown in **Figure 4.10**. The dimension of

both patches is 3.0 units by 6.0 units and the material properties are given as $E = 1.0$ and $\upsilon = 0.25$. In the higher order patch test, twelve supporting nodes are used to construct the shape functions.

Two different cases of boundary conditions are examined in this test. In case one, a uniform axial traction of unit intensity is applied along the right end of the cantilever beam. The exact solution of the displacements for this problem is:

$$u = x \text{ and } v = -y/4. \tag{4.17}$$

Whereas, in case two, a linearly varying normal traction in the horizontal direction, $\sigma_{xx} = y/1.5$, is applied along the right end of the cantilever beam. The exact solution of displacements for this problem is:

$$u = xy/1.5 \text{ and } v = -\left(x^2 + y^2/4\right)/3. \tag{4.18}$$

The accuracy of the solution is very much related to the condition of the constructed stiffness matrix. In the standard patch test, the condition number of constructed stiffness matrix is in the order of 10^2. However, in the higher order patch test, the condition number of the constructed stiffness matrix is in the order of 10^8. The order of the condition number is not only depending on the approximation but also the boundary conditions and the nature of the problem. As $\mathbf{U} = \mathbf{K}^{-1}\mathbf{F}$, we can have $\|-\Delta u\| = \|\mathbf{K}^{-1}\|\|\Delta\mathbf{F}\|$. Therefore, let the error $\Delta\mathbf{F} \approx 10^{-18}$, if the condition of $\mathbf{K}^{-1}$ is in the order of 10^2, the accuracy of $\mathbf{U}$ can be achieved at order of 10^{-16}. In the higher order patch test, $\mathbf{K}^{-1}$ is in the order of 10^8, therefore accuracy can only be

achieved at 10^{-10}. Therefore, the solution of higher order patch test is considered as pass if the accuracy reaches to the order of 10^{-10}, as shown in **Table 4.2**. The detailed procedure of the higher order patch tests can be found in Ref. [100].

One can notice that RPCM passes both standard and higher order patch tests. As the solution for both patch tests are in the form of polynomial (see Eq. (4.16)-(4.18)), RPCM can reproduce the field function without any discretization error. Therefore, RPCM can pass both patch tests to the machine accuracy.

4.4.4 Example 4: Elastostatics Problem with Neumann Boundary Conditions

This problem is presented to demonstrate the instability problem encountered by RPCM. In this numerical example, a benchmark plane stress solid mechanics problem is studied. A cantilever beam with unit thickness is subjected to a parabolic shear stress at the right end as shown in **Figure 4.11**. The material properties and geometrics are given as: Young's modulus $E = 3 \times 10^7$, Poisson's ratio $\upsilon = 0.3$, length of the cantilever $L = 48.0m$ and the height $H = 12.0m$. The loading is known as $\tau_{xy} = -\frac{P}{2I}\left(H^2/4 - y^2\right)$, where I is the moment of inertial of the cross section of the cantilever and $P = 1000N$.

The well-known equilibrium equations for solid mechanics problem is known as

$$\sigma_{ij,j} + b_i = 0 \text{ in } \Omega. \tag{4.19}$$

Neumann boundary conditions are known as

$$\sigma_{ij} n_j = t_i \quad \text{on} \quad \Gamma_t . \tag{4.20}$$

And Dirichlet boundary conditions are known as

$$u_i = \bar{u}_i \quad \text{on} \quad \Gamma_u . \tag{4.21}$$

The analytical solution of this problem can be found in the Ref. [90].

As mentioned in the previous section, Neumann boundary conditions are found as the cause of instability. To demonstrate this argument, the cantilever is first modelled by 951 randomly distributed nodes in the problem domain. Another 12 nodes are added into the first model to make the second model with 963 nodes, which is the fact latter that the model is quite similar to the first model. As analytical solution is known, the Dirichlet boundary conditions are first imposed based on the analytical solution of displacements along all the boundaries. One can observe that the results of deflection along $x = 0$ for both models remain good and close to each other as shown in **Figure 4.12**.

However, if the Dirichlet boundary conditions are only imposed on the left edge and Neumann boundary conditions are imposed on the rest of the edges of the cantilever, RPCM solutions for these two similar models are totally different as shown in **Figure 4.13**. This example clearly reveals the inherited instability problem of RPCM.

4.5 Remarks:

The radial point collocation method (RPCM) has been introduced in detailed at the beginning of this chapter. From the numerous examples given in the last section, the issues in RPCM have been well demonstrated. In the first example, the RPCM has been shown as a good strong-form meshfree method for one dimensional problem and it has been successfully extended to adaptive analysis using residual based error estimator. Good accuracy and stable solution can been obtained by RPCM in one dimensional space. RPCM has also been demonstrated as an excellent strong-form meshfree method for solving Dirichlet problem in the higher dimensional space. Without the involvement of Neumann boundary condition, the RPCM provides great accuracy in the two dimensional problems as shown in Example 2 and Example 3. As Neumann boundary conditions exist in the Example 4, the instability problem encountered by RPCM is evidently revealed. Two very similar models can produce very different solutions.

Although RPCM possesses many attractive features that facilitate the implementation of adaptive analysis, it will never be success without an effective measure to overcome the instability problem. In the following chapters, number of techniques is suggested for RPCM and hence further extends RPCM to adaptive analysis.

Patch	Error norm of u	Error norm of v
Patch **a**	2.0282×10^{-15}	1.9341×10^{-15}
Patch **b**	1.6257×10^{-15}	1.5125×10^{-15}

Table 4.1 Error norm of RPCM for linear patch test.

	Case 1		Case 2	
Patch	u	v	u	v
Patch **c**	6.8140×10^{-12}	2.0732×10^{-10}	6.0052×10^{-11}	1.5908×10^{-8}
Patch **d**	3.9131×10^{-10}	1.5908×10^{-8}	2.5852×10^{-10}	3.2225×10^{-10}

Table 4.2 Error norm of RPCM for higher order patch test.

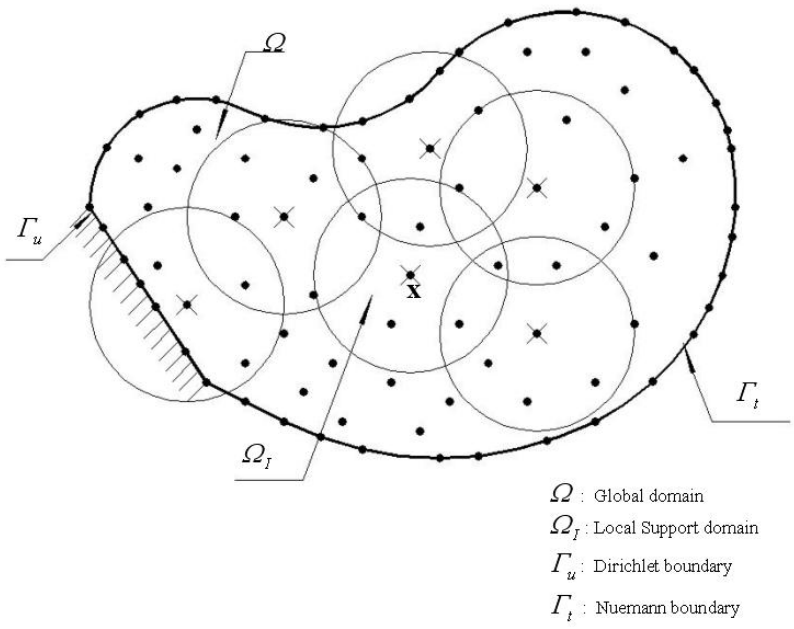

Figure 4.1 A problem governed by PDEs in domain Ω.

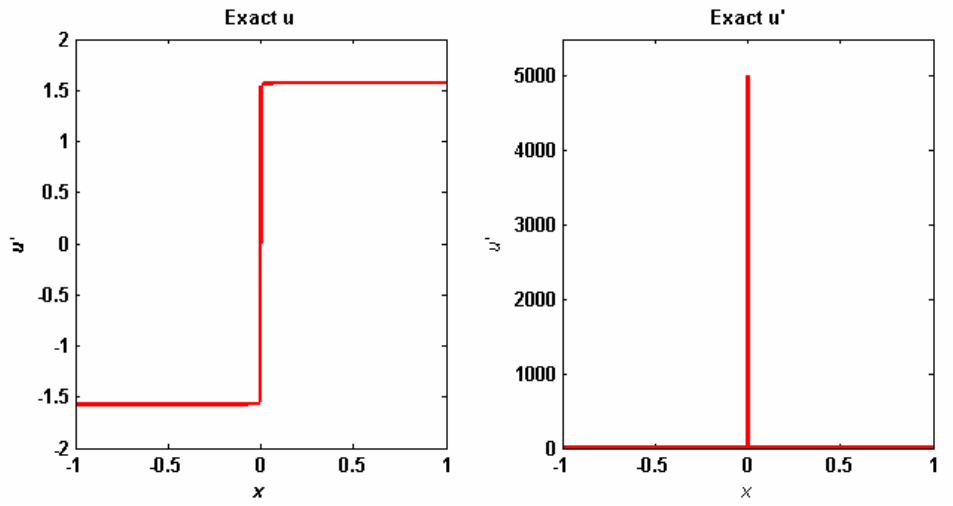

Figure 4.2 The exact solution of one dimensional Poisson Problem for field function and it first derivative.

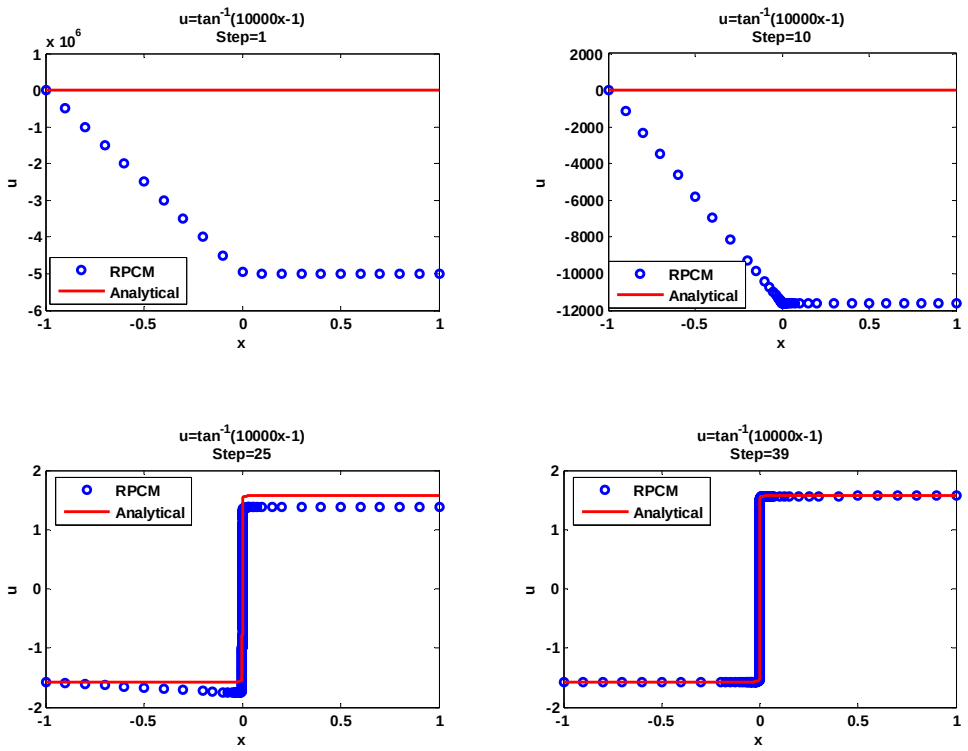

Figure 4.3 Solution of RPCM at first, 10th, 25th and final step.

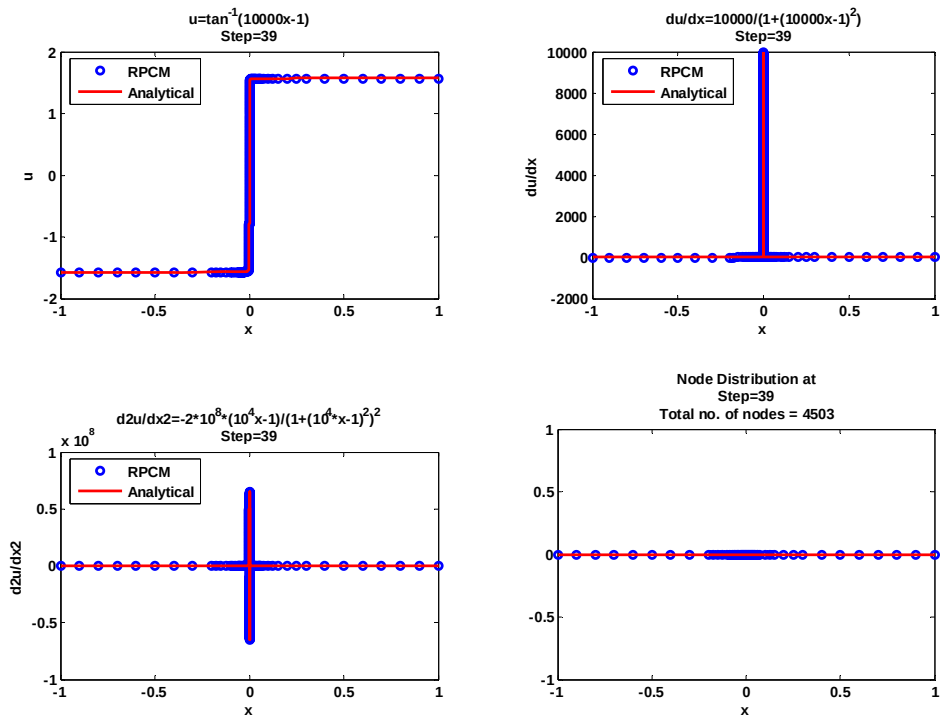

Figure 4.4 Solution of RPCM for field function and its derivatives at final step.

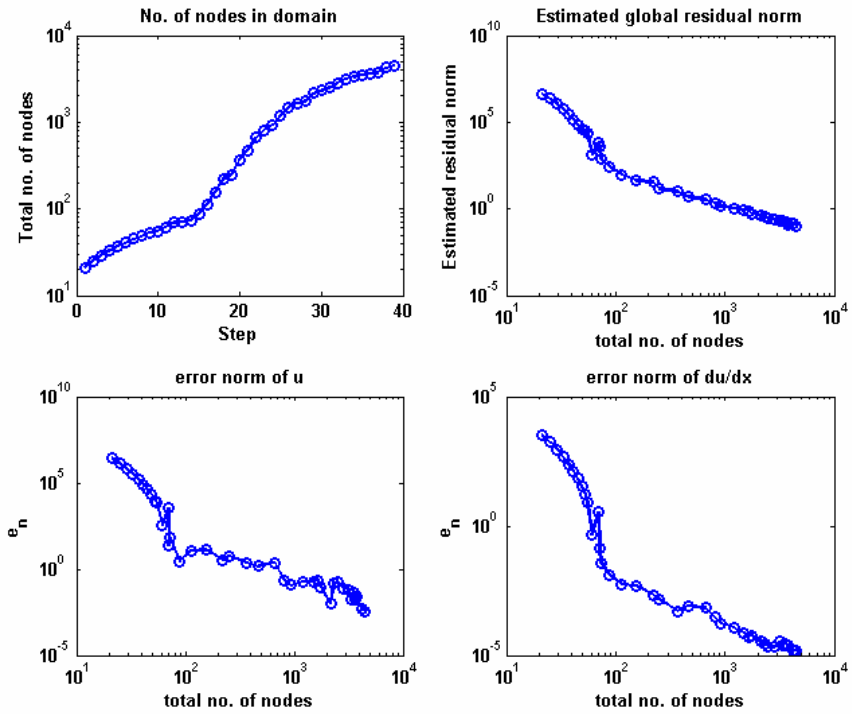

Figure 4.5 The number of field nodes, global residual norm and error norms of solutions at each adaptive step.

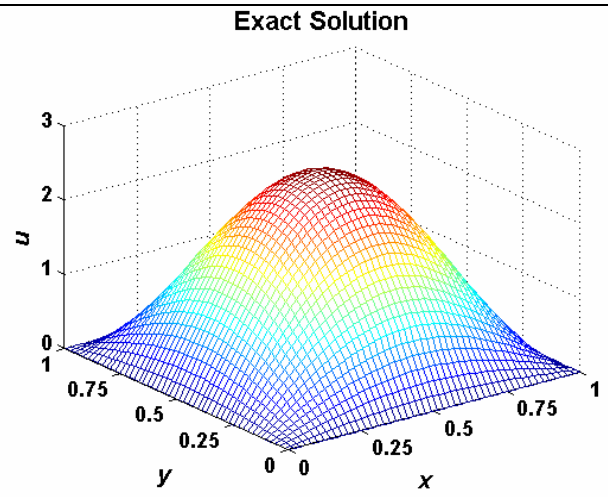

Figure 4.6 The analytical solution of the Poisson problem.

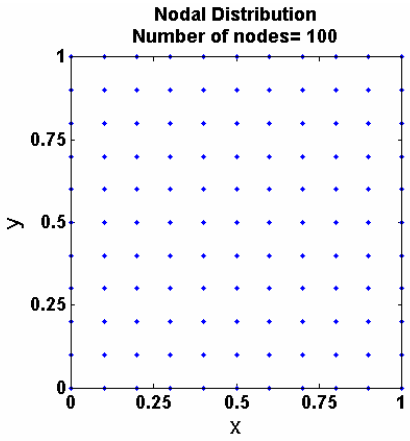

Figure 4.7 Nodal distribution of 11×11 regularly distributed nodes in the $\Omega:[0,1]\times[0,1]$.

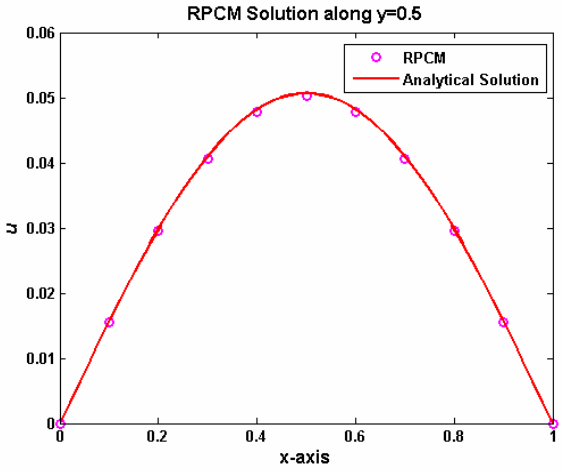

Figure 4.8 The solution of RPCM along $y=0.5$ for the Poisson problem.

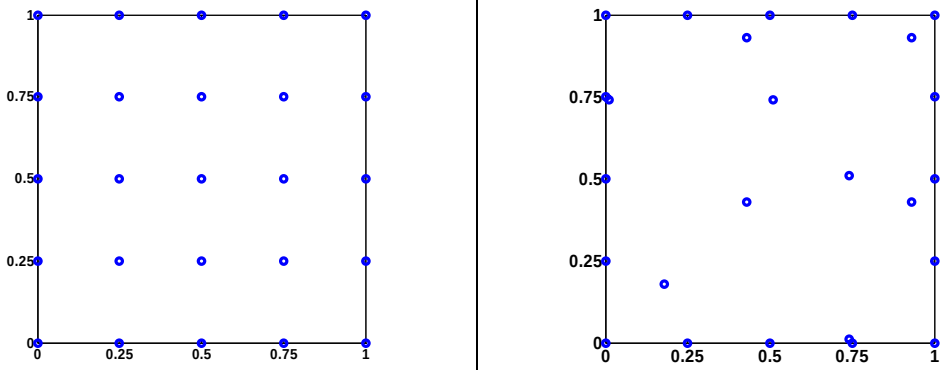

(a) (b)

Figure 4.9 (a) Patch A with regular distributed nodes and (b) Patch B with irregularly distributed nodes

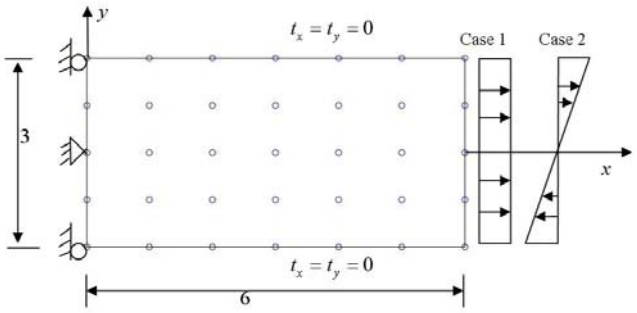

(a)

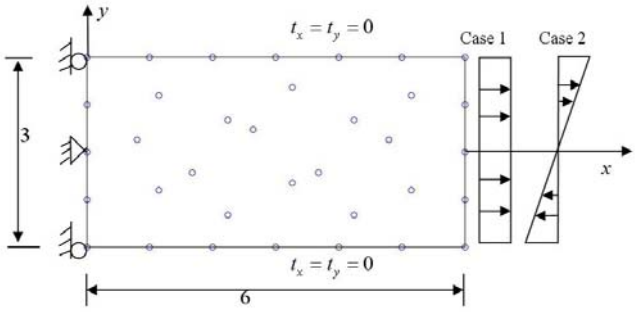

(b)

Figure 4.10 (a) Patch C with regularly distributed nodes and (b) Patch D with irregularly distributed nodes.

Figure 4.11 A cantilever beam subjected to a parabolic shear traction at the right end.

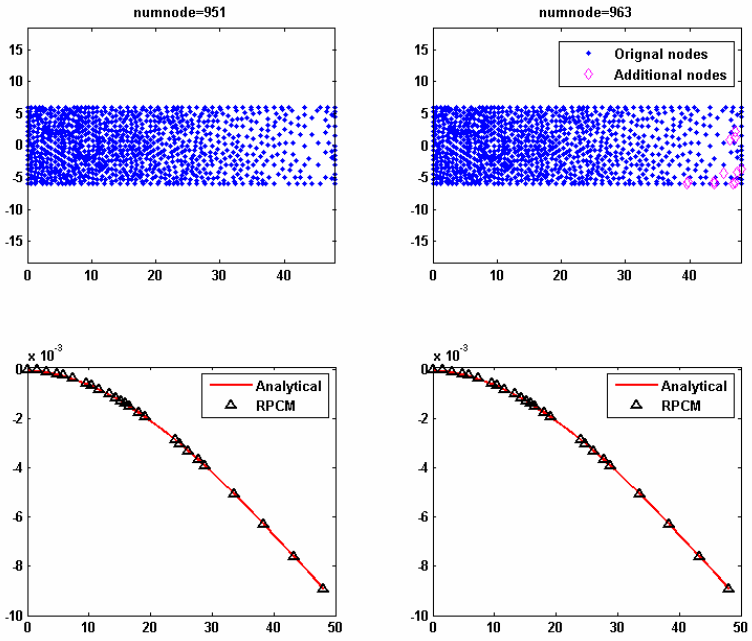

Figure 4.12 Deflection of the cantilever beam for model with 951 and nodes 963 without the Neumann boundary condition.

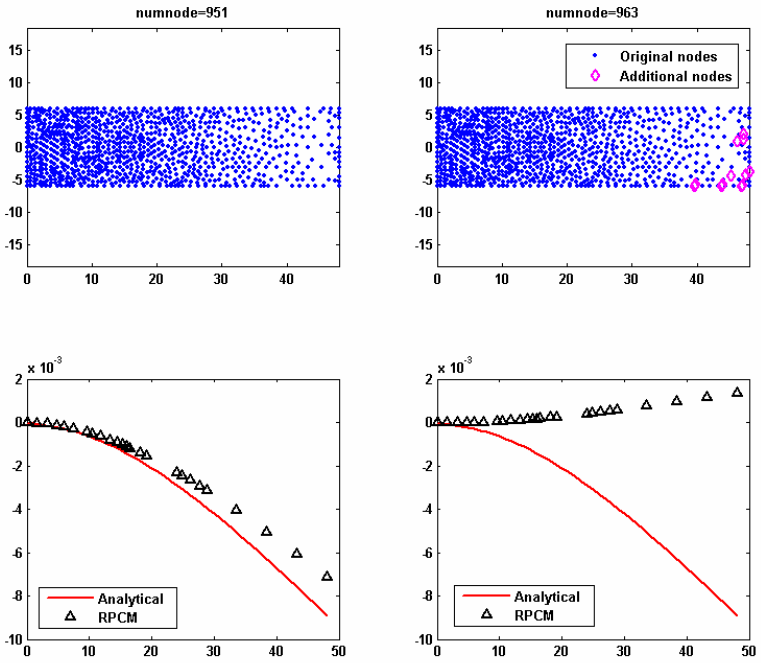

Figure 4.13 Deflection of the cantilever beam for model with 951 and nodes 963 with the Neumann boundary condition.

Chapter 5

A Stabilized Least-Squares Radial Point Collocation Method (LS-RPCM)

5.1 Introduction

In Chapter 4, the radial point collocation method (RPCM) has been discussed in detailed. The solution of RPCM is unstable whenever Neumann boundary conditions exist. Thus, it is impossible to implement adaptive analysis using RPCM without an effective measure to stabilize the solution.

In this work, a stabilized RPCM is proposed for adaptive analysis using least-squares stabilization technique [48,51]. The key idea of this work is to incorporate stabilization technique that based on least-squares procedure into the RPCM in order to obtain stable solutions. Through this stabilization measure, the stability of RPCM can be restored so as to perform adaptive analysis. Good stiffness matrix properties such as symmetric and positive definite (SPD) are also gained via the least-squares stabilization procedure, and the feature of simplicity in the formulation procedure is still retained. The SPD properties also help to solve the resultant set of algebraic equations more efficiently and accurately using better linear equation solver such as the Cholesky

solver. Many advantages have been gained from the least-squares stabilization procedure with only a little additional computational cost.

As the stability is restored, the stabilized LS-RPCM has then been successfully applied to adaptive analyses. Interpolation variance based error estimator that suggested by Iske et al. [7,29] is adopted in the adaptive analysis study. In the refinement procedure, Voronoi diagram is used to identify the position for the additional nodes. Due to mesh free feature, the refinement process for adaptive RPCM can be performed easily by inserting additional nodes into the problem domain without worry about the nodal connectivity.

5.2 Stabilized Least-squares Procedure

As instability can arise in the RPCM, stabilization technique is essential to stabilize the solution, which is especially crucial for the success of implementing the RPCM in the adaptive analysis. In this work, a least-squares stabilization technique is employed in the following procedure to restore the stability and local nodes are still used in the formulation.

Follow the procedure in RPCM, the governing equations can be discretized at interior nodes and also at nodes on the Dirichlet boundary, and Neumann boundary conditions can be discretized on the Neumann boundary nodes to form Eq. (4.7), $L(u_i) = f_i$. After each equation is normalized by the value of the largest element in the corresponding row, and Eq. (4.7), becomes

$$\mathbf{K}^o\mathbf{U} = \mathbf{F}^o . \tag{5.1}$$

where $\mathbf{K}^o$ is the normalized stiffness matrix and $\mathbf{F}^o$ is the normalized force vector.

The normalized stiffness matrix and force vector in Eq. **(5.1)** can be decomposed in the following form.

$$\mathbf{K}^o = \begin{bmatrix} 0 & 0 \\ \mathbf{K}_{21}^{EE} & \mathbf{K}_{22}^{EE} \end{bmatrix} + \begin{bmatrix} \mathbf{K}_{11}^{EBC} & \mathbf{K}_{12}^{EBC} \\ 0 & 0 \end{bmatrix} \tag{5.2}$$

and

$$\mathbf{F}^o = \begin{bmatrix} \mathbf{F}^{EBC} \\ \mathbf{F}^{EE} \end{bmatrix}. \tag{5.3}$$

where $\mathbf{K}_{11}^{EBC}$, $\mathbf{K}_{12}^{EBC}$ and $\mathbf{F}^{EBC}$ are the element of $\mathbf{K}^o$ which corresponding to the governing equations on the Dirichlet boundary nodes and $\mathbf{K}_{21}^{EE}$, $\mathbf{K}_{22}^{EE}$ and $\mathbf{F}^{EE}$ are the element of $\mathbf{K}^o$ which corresponding to the governing equations on the interior nodes and the Neumann conditions on the Neumann boundary nodes. $\mathbf{K}_{11}^{EBC}$ and $\mathbf{K}_{21}^{EE}$ are those submatrices corresponding to the degrees of freedom (DOFs) of the nodes on the Dirichlet boundary.

Therefore, Eq. **(5.1)** becomes

$$\left\{ \begin{bmatrix} 0 & 0 \\ \mathbf{K}_{21}^{EE} & \mathbf{K}_{22}^{EE} \end{bmatrix} + \begin{bmatrix} \mathbf{K}_{11}^{EBC} & \mathbf{K}_{12}^{EBC} \\ 0 & 0 \end{bmatrix} \right\} \begin{bmatrix} \mathbf{U}^{EBC} \\ \mathbf{U}^{EE} \end{bmatrix} = \begin{bmatrix} \mathbf{F}^{EBC} \\ \mathbf{F}^{EE} \end{bmatrix}. \tag{5.4}$$

where $\mathbf{U}^{EBC}$ is the vector of field variables (such as the nodal displacements) on the

Dirichlet boundary and $\mathbf{U}^{EE}$ is the vector of field variables on the non-Dirichlet boundary.

By introducing a stabilization factor α to the governing equations corresponding to the Dirichlet boundary nodes, the following equation is obtained.

$$\left\{\begin{bmatrix} 0 & 0 \\ \mathbf{K}_{21}^{EE} & \mathbf{K}_{22}^{EE} \end{bmatrix} + \alpha \begin{bmatrix} \mathbf{K}_{11}^{EBC} & \mathbf{K}_{12}^{EBC} \\ 0 & 0 \end{bmatrix}\right\} \begin{bmatrix} \mathbf{U}^{EBC} \\ \mathbf{U}^{EE} \end{bmatrix} = \begin{bmatrix} \alpha \mathbf{F}^{EBC} \\ \mathbf{F}^{EE} \end{bmatrix}. \tag{5.5}$$

Note that mathematically, Eq. **(5.5)** is not changed, as α is multiplied on both sides of these equations. The value of α should lie between zero and 1.

$$0 \le \alpha \le 1. \tag{5.6}$$

Note that how to determine α is still an open issue. In this work, it is determined through numerical trials. The main purpose of introducing α is for the stabilization of the solutions, therefore it should be generally small. Based on the large number of numerical tests, $\alpha = 0.05$ has been found working well for all the problems studied in this work.

The above equation, Eq. (5.6), can be written in a concise form of

$$\mathbf{K}^{\alpha}\mathbf{U} = \mathbf{F}^{\alpha}. \tag{5.7}$$

A functional Π can be defined in the form of

$$\Pi = \left\{\mathbf{K}^{\alpha}\mathbf{U} - \mathbf{F}^{\alpha}\right\}^{T} \left\{\mathbf{K}^{\alpha}\mathbf{U} - \mathbf{F}^{\alpha}\right\}. \tag{5.8}$$

where Π is the L_2 norm of the residuals obtaining in Eq. (5.8).

$$\frac{\partial \Pi}{\partial \mathbf{U}} = \left[\mathbf{K}^{\alpha}\right]^{T}\left\{\mathbf{K}^{\alpha}\mathbf{U} - \mathbf{F}^{\alpha}\right\} = 0 . \tag{5.9}$$

In seeking the minimal of the functional Π, one can have

$$\left[\mathbf{K}^{\alpha}\right]^{T}\mathbf{K}^{\alpha}\mathbf{U} = \left[\mathbf{K}^{\alpha}\right]^{T}\mathbf{F}^{\alpha} . \tag{5.10}$$

By substituting Eq.(5.2) and Eq.(5.3) into Eq. (5.10), the following equation is obtained

$$\begin{aligned}
&\left\{\begin{bmatrix} \left[\mathbf{K}_{21}^{EE}\right]^{T}\mathbf{K}_{21}^{EE} & \left[\mathbf{K}_{21}^{EE}\right]^{T}\mathbf{K}_{22}^{EE} \\ \left[\mathbf{K}_{22}^{EE}\right]^{T}\mathbf{K}_{21}^{EE} & \left[\mathbf{K}_{22}^{EE}\right]^{T}\mathbf{K}_{22}^{EE} \end{bmatrix} + \alpha^{2}\begin{bmatrix} \left[\mathbf{K}_{11}^{EE}\right]^{T}\mathbf{K}_{11}^{EE} & \left[\mathbf{K}_{11}^{EE}\right]^{T}\mathbf{K}_{12}^{EE} \\ \left[\mathbf{K}_{12}^{EE}\right]^{T}\mathbf{K}_{11}^{EE} & \left[\mathbf{K}_{12}^{EE}\right]^{T}\mathbf{K}_{12}^{EE} \end{bmatrix}\right\}\begin{bmatrix} \mathbf{U}^{EBC} \\ \mathbf{U}^{EE} \end{bmatrix} \\
&= \begin{bmatrix} \left[\mathbf{K}_{21}^{EE}\right]^{T}\mathbf{F}^{EE} + \alpha^{2}\left[\mathbf{K}_{11}^{EBC}\right]^{T}\mathbf{F}^{EBC} \\ \left[\mathbf{K}_{22}^{EE}\right]^{T}\mathbf{F}^{EE} + \alpha^{2}\left[\mathbf{K}_{12}^{EBC}\right]^{T}\mathbf{F}^{EBC} \end{bmatrix}
\end{aligned} \tag{5.11}$$

Dirichlet boundary conditions can then be imposed directly as

$$\mathbf{U}^{EBC} = \bar{\mathbf{U}} . \tag{5.12}$$

where $\bar{\mathbf{U}}$ is the specified field variables (e.g. nodal displacements) on the Dirichlet boundary. The system equations finally become the following matrix form.

$$\begin{aligned}
&\left\{\begin{bmatrix} 0 & 0 \\ \left[\mathbf{K}_{22}^{EE}\right]^{T}\mathbf{K}_{21}^{EE} & \left[\mathbf{K}_{22}^{EE}\right]^{T}\mathbf{K}_{22}^{EE} \end{bmatrix} + \alpha^{2}\begin{bmatrix} \mathbf{I} & 0 \\ \left[\mathbf{K}_{12}^{EBC}\right]^{T}\mathbf{K}_{11}^{EBC} & \left[\mathbf{K}_{12}^{EBC}\right]^{T}\mathbf{K}_{12}^{EBC} \end{bmatrix}\right\}\begin{bmatrix} \bar{\mathbf{U}} \\ \mathbf{U}^{EE} \end{bmatrix} \\
&= \begin{bmatrix} \alpha^{2}\bar{\mathbf{U}} \\ \left[\mathbf{K}_{22}^{EE}\right]^{T}\mathbf{F}^{EE} + \alpha^{2}\left[\mathbf{K}_{12}^{EBC}\right]^{T}\mathbf{F}^{EBC} \end{bmatrix}
\end{aligned} \tag{5.13}$$

Hence, the unknown $\mathbf{U}^{EE}$ can then be obtained by solving the following

$$\begin{aligned}&\left[\left[\mathbf{K}_{22}^{EE}\right]^T\mathbf{K}_{22}^{EE}+\alpha^2\left[\mathbf{K}_{12}^{EBC}\right]^T\mathbf{K}_{12}^{EBC}\right]\mathbf{U}^{EE}\\&=\left[\left[\mathbf{K}_{22}^{EE}\right]^T\mathbf{F}^{EE}+\alpha^2\left[\mathbf{K}_{12}^{EBC}\right]^T\mathbf{F}^{EBC}\right]-\left[\left[\mathbf{K}_{22}^{EE}\right]^T\mathbf{K}_{21}^{EE}+\alpha^2\left[\mathbf{K}_{12}^{EBC}\right]^T\mathbf{K}_{11}^{EBC}\right]\bar{\mathbf{U}}\end{aligned} \tag{5.14}$$

or

$$\hat{\mathbf{K}}\mathbf{U}=\hat{\mathbf{F}}. \tag{5.15}$$

where

$$\hat{\mathbf{K}}=\left[\left[\mathbf{K}_{22}^{EE}\right]^T\mathbf{K}_{22}^{EE}+\alpha^2\left[\mathbf{K}_{12}^{EE}\right]^T\mathbf{K}_{12}^{EE}\right], \tag{5.16}$$

and

$$\hat{\mathbf{F}}=\left[\left[\mathbf{K}_{22}^{EE}\right]^T\mathbf{F}^{EE}+\alpha^2\left[\mathbf{K}_{12}^{EBC}\right]^T\mathbf{F}^{EBC}\right]-\left[\left[\mathbf{K}_{22}^{EE}\right]^T\mathbf{K}_{21}^{EE}+\alpha^2\left[\mathbf{K}_{12}^{EBC}\right]^T\mathbf{K}_{11}^{EE}\right]\bar{\mathbf{U}}. \tag{5.17}$$

It is clear that stiffness matrix $\hat{\mathbf{K}}$ in Eq. (5.16) is symmetric and positive definite (SPD) through the least-squares stabilization procedure. Unknown $\mathbf{U}^{EE}$ can be then obtained using a standard linear equation solver, such as the Cholesky solver.

Note that in the least-squares stabilization procedures, Dirichlet boundary conditions are fully satisfied. Governing equations are partially satisfied with a weight of the stabilization factor α on the Dirichlet boundary.

5.3 Numerical Examples

Stabilization factor used in the least-squares procedure for the presented numerical examples is $\alpha = 0.05$. For the examples of adaptive analysis, the interpolation variance based error estimator proposed by Iske et al [7,29] is adopted in the adaptive scheme. The details of formulation of the error estimator are well given in Chapter 3. In the refinement procedure, the Voronoi diagram is used to locate the position for the additional nodes as shown in **Figure 3.23**. At each adaptive step, a Voronoi diagram will be constructed based on the current nodal distribution. Every node in the problem domain is corresponding to a Voronoi cell. If the predefined refinement criterion is met at the node, additional nodes will be inserted at the vertices of the cell. The adaptive process will be carried on until none of the nodes meet the refinement criterion.

In the given numerical examples in this chapter, polynomial with completed second order, $m = 6$, is adopted in the RPIM approximation and shape parameters of MQ-RBF are known as $\alpha_c = 3.0$ and. $q = 1.03$.

5.3.1 Example 1: A Cantilever Beam Subjected to a Parabolic Shear Stress at the Right End

The main purpose of this example is to validate the feasibility of the least-squares stabilization technique for stabilizing the solution of RPCM. A cantilever beam subjected to a parabolic shear stress at the right end is examined in this example as shown in **Figure 4.11**, and is considered as a plane stress elastostatics problem here. The dimension of the cantilever beam and the material properties are given as length

$L = 48.0m$, height $D = 12.0m$, Young's modulus $E = 3 \times 10^7 N/m^2$, Poisson's ratio $\upsilon = 0.3$. The shear stress loading applied along the right end is known as (integration of the distributed traction) $P = 1000N$. There are 273 nodes are used in the model of cantilever beam as shown in **Figure 5.1**.

The PDEs that govern the two dimensional elastostatics problem are given in Eq. (4.19) to Eq. (4.21). In this problem, Dirichlet boundary conditions are imposed on the left edge and Neumann boundary conditions are imposed on the rest of the three edges. Analytical solution for this problem can be found in the Ref.[90].

Beside validating the feasibility of the least-squares stabilization technique, the solution obtained by the stabilized LS-RPCM is also compared with the RPCM, FEM and analytical solution. The model shown in **Figure 5.1** is solved by the stabilized LS-RPCM, RPCM and FEM. In the FEM, 4-node standard element is adopted and 3 by 3 gauss integration points are used in the numerical integration scheme. Twenty supporting nodes are used to construct the shape functions for the stabilized LS-RPCM and RPCM.

The deflection of the cantilever beam along the bottom edge plotted in **Figure 5.2** shows RPCM are inaccurate, however after stabilized through the least-squares stabilization procedure, the solution of deflection has been improved very much. In this problem, the stabilized LS-RPCM not only provides accurate solution in term displacements but also in term of stresses. In addition, the FEM requires post processing procedure to produce better results as it is suffering from discontinuity in

stresses, whereas stabilized LS-RPCM has no difficulty to obtain continuous stresses. As shown in **Figure 5.3**, the shear stress τ_{xy} and normal stress σ_{yy} computed by the stabilized LS-RPCM are smoother than the FEM. From this point of view, the stabilized LS-RPCM does perform better than the FEM in computing the stresses.

To further illustrate the instability solution of the RPCM that is suffering from the existence of Neumann boundary conditions, four similar sets of nodal distribution are give in **Figure 5.4**. The deflections of cantilever beam along the bottom edge are plotted in **Figure 5.4** (a) to **Figure 5.4** (d) for the 4 different nodal distributions. Although there are only slight variations in the nodal distributions, the results obtained by the RPCM are varied very much. In **Figure 5.4** (b), a fluctuation in deflection of cantilever beam is observed near the left edge. On the other hand, the stabilized LS-RPCM has shown clearly in **Figure 5.4** for its capability to provide very stable and accurate results. The deflections obtained by the stabilized LS-RPCM for this four similar sets of nodal distributions is very consistence as shown in **Figure 5.4**. Observing from **Figure 5.4**, it is evidently clear that the least-squares stabilization technique has been successfully stabilize the solution.

To have better understanding of the computational cost for the stabilized LS-RPCM, a cost analysis is conducted in this example. In general, the FEM and RPCM require lesser CPU running time than stabilized LS-RPCM. For instance, the FEM requires 2.2680 seconds and the RPCM is 13.0988 seconds for solving the cantilever beam problem using model shown in **Figure 5.1**, whereas the stabilized LS-RPCM takes 18.1962 seconds to obtain the solution. Note that although FEM is

more efficient, but mesh is required. On the other hand, the RPCM can not promise a stable solution also.

The CPU times required for the stabilized LS-RPCM and RPCM in this example has little difference, and the reason is revealed by the following analysis of complexity of the two methods. The operations needed for creating the stiffness matrix $\mathbf{K}^o$ are basically the same for both the stabilized LS-RPCM and RPCM. The total cost difference is mainly due to the cost of solving the system equations. In the stabilized LS-RPCM, the matrix multiplication $\mathbf{K}^T\mathbf{K}$ requires $4Np^2$ operations, where $\mathbf{K}$ is banded matrix of $N \times N$ and bandwidth p. The bandwidth of $\mathbf{K}^T\mathbf{K}$ becomes $2p-1$ and therefore the operations for Cholesky solver is $4Np^2$. Hence, the total operations required by stabilized LS-RPCM is estimated as $8Np^2$. In the RPCM, the operations required for the Gaussian Elimination with partial pivoting (asymmetric $\mathbf{K}$) is $4Np^2$. Therefore the stabilized LS-RPCM takes twice CPU time in the worst case for any DOFs to solve the system equations. In our tested examples, however, the CPU times for both methods are very close. This is because the amount of the "overheads" computation is quite significant compared to the equations solving, and the "overheads" CPU time is largely the same for both methods.

5.3.2 Example 2: Poisson Problem with Neumann Boundary Conditions

An adaptive analysis is conducted using the stabilized LS-RPCM for solving the Poisson's equation in this example. Consider a Poisson problem as below,

$$\frac{\partial^2}{\partial x^2}u+\frac{\partial^2}{\partial y^2}u=\sin\pi x\sin\pi y\,. \tag{5.18}$$

The problem domain is $\mathbf{\Omega}=[0,1]\times[0,1]$, with Neumann boundary conditions

$$\frac{\partial u}{\partial x}=\frac{1}{2\pi}\sin\pi y \quad \text{along } x=1, \tag{5.19}$$

and Dirichlet boundary conditions

$$u=0 \quad \text{along } x=0,\ y=0 \text{ and } y=1. \tag{5.20}$$

The analytical solution for this Poisson problem is known as

$$u=-\frac{1}{2\pi^2}\sin\pi x\sin\pi y\,. \tag{5.21}$$

The adaptive analysis starts with regular distribution of 6×6 nodes at the initial step. Ten supporting nodes are used to construct the shape functions. Tolerant values for the error estimator are given as $\kappa_1=0.2$ and $\kappa_1=0.0025$.

In **Figure 5.5**, nodal distributions at each adaptive step are shown. Starting with 36 regularly distributed nodes, the computation ends at 5th step with 278 nodes, the overall error norm of field variable u has been gradually improved from 7.25% to 0.36% as shown in **Figure 5.6** and **Table 5.1**. One should note that due to the smooth nature of the problem, the nodal distribution in the final stage is largely uniform for this problem.

5.3.3 Example 3: Infinite Plate with Hole Subjected to an Uniaxial Traction in the Horizontal Direction

In this example, a 2D elastostatics plane strain problem is studied. An infinite plate with circular hole is subjected to a uniaxial traction in horizontal direction. The dimension and material properties are given as $a = 0.2m$, $b = 2.0m$, Young's modulus $E = 1 \times 10^3 N/m^2$, Poisson's ratio $\upsilon = 0.3$. The governing equations used for this problem are given in Eq. (4.19) to Eq. (4.21). Due to symmetric, only quarter of the problem domain is modelled as shown in **Figure 5.7**. Symmetric conditions are imposed along the left and the bottom edges. The prescribed values of stresses along the top and right edge are given by the analytical solution given in Ref. [90].

The adaptive analysis starts with irregular distribution of 145 nodes at the initial step. To evaluate the error estimator, Von Mises stress is used to compute the interpolation variance. Thirty supporting nodes are used to construct the shape functions. The tolerant values for error indicator are $\kappa_1 = 0.035$ and $\kappa_2 = 0.0025$.

The adaptive analysis takes five steps to complete. Nodal distribution at each adaptive step is plotted in **Figure 5.8**. Starting with 145 regularly distributed nodes, the computation ends at fifth step with 765 nodes, and the error norm of effective stress has been gradually reduced from 72.55% to 1.08% as shown in **Figure 5.9**. The error norm of the displacements is found drastically reduced adaptively. **Figure 5.10** and **Table 5.1** show the error norm of displacements achieve 0.44% from 66.33% at the beginning step. From numerical solution of displacement u_y and normal stress σ_{xx} along the y

axis on the left edge plotted in **Figure 5.11** and **Figure 5.12**, one can notice that the solutions obtained by the stabilized LS-RPCM is in good agreement with the analytical solutions. Apparently, the proposed adaptive strategy has achieved remarkable success in improving the solutions by effective refinement. The initial solutions of displacement and stress shown in **Figure 5.11** and **Figure 5.12** have been greatly improved.

5.3.4 Example 4: A L-shaped Plate Subjected to a Unit Tensile Traction in the Horizontal Direction

In the last example, a L-shaped plate subjected to a unit tensile traction in the horizontal direction is investigated. This example is a typical problem used for examining the effectiveness and efficiency of the adaptive scheme. The model of the L-shaped plated is given in **Figure 5.13**. As there is a singularity point (point A), an adaptive scheme is required to identify the singularity point and to refine the critical region.

This problem is considered as a plane stress case with material properties $E = 1GN/m^2$, $\upsilon = 0.3$ and the geometry of the L-shaped plate is shown in the **Figure 5.13**. The coefficient of refinement and global residual tolerance are preset as $\kappa_1 = 0.05$ and $\kappa_2 = 0.0005$. In this example, sixteen local nodes are used to construct the shape function. The nodal distributions from first to 15^{th} steps are all plotted in **Figure 5.8** and show the adaptive scheme able to detect the singularity point and refine the surrounding area accordingly. For justification purpose, a model which consists of

7902 nodes as shown in **Figure 5.15** is solved by ANSYS as a reference solution. The normal stress σ_{yy} and shear stress τ_{xy} distributions at the 15th step have been given in **Figure 5.16** and **Figure 5.17** respectively and shown in good agreement with reference solution.

5.4 Remarks

In this chapter, least-squares stabilization is introduced to overcome the instability problem that encountered in the RPCM. By incorporating the present least-squares stabilization technique, not only stability is restored but it also lead to a SPD coefficient matrix. Yet, the formulation procedure of the stabilized least-squares RPCM is still kept simple and straightforward. With the SPD properties, the resultant set of algebraic equations can be solved more efficiently and accurately using standard linear equation solver such as Cholesky solver. Good numerical perform is observed in the numerical examples given in this chapter. Since the stability issue is resolved, the unique features of the strong-form method can facilitate the implementation of adaptive analysis. The success of the adaptive analyses shows also that the simple adaptive scheme based on stabilized LS-RPCM is feasible and effective.

Nevertheless, there is still some room for improvement. Currently, the stabilized LS-RPCM is restricted for linear problems only, it may further be extended for solving non-linear problems, but the efficiency issues related to the use of least-squares formulation need to be resolved.

Step	Number of field nodes	Exact error norm
1	66	7.25%
2	59	3.61%
3	89	2.02%
4	170	0.74%
5	278	0.36%

Table 5.1 Exact error norm of the solution obtained by the stabilized LS-RPCM at each adaptive step for the Poisson problem.

Step	Number of field nodes	Exact error norm of displacement
1	145	66.33%
2	256	11.10%
3	345	2.94%
4	539	1.62%
5	765	0.44%

Table 5.2 Exact error norm of the displacement obtained by the stabilized LS-RPCM at each adaptive step for the infinite plate with hole subjected to uniaxial traction.

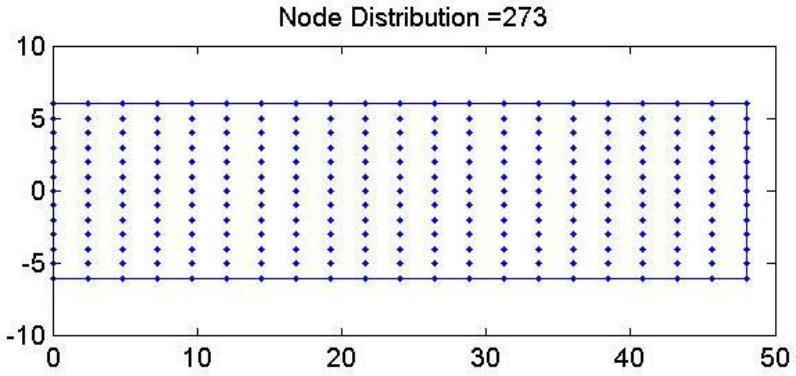

Figure 5.1 A model of cantilever beam with 273 regularly distributed nodes.

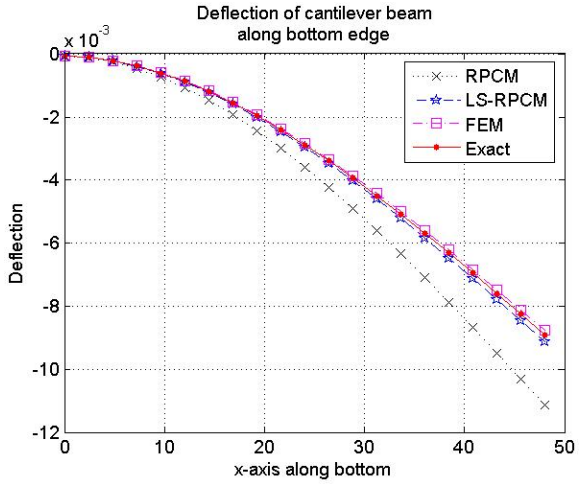

Figure 5.2 Comparison of the deflection of the cantilever beam computed by LS-RPCM, RPCM and FEM along the bottom edge.

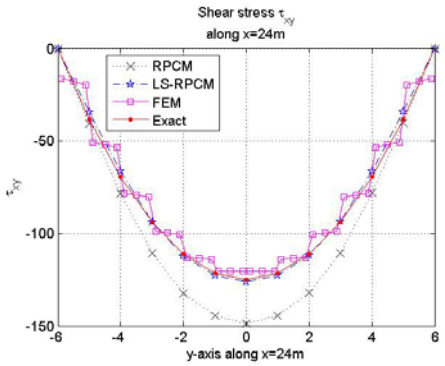

(a)

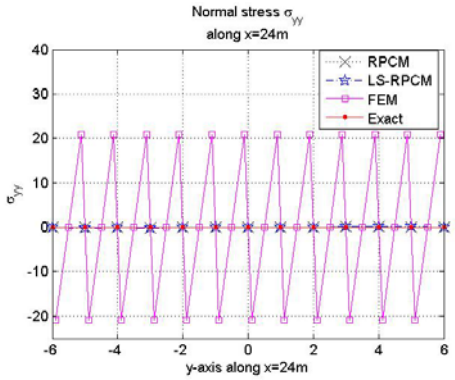

(b)

Figure 5.3 Comparison of the (a) shear stress τ_{xy} and (b) normal stress σ_{yy} of the cantilever beam computed by stabilized LS-RPCM, RPCM and FEM along the bottom edge.

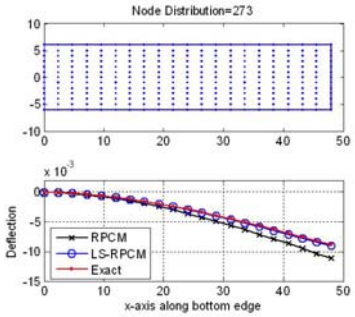

(a)

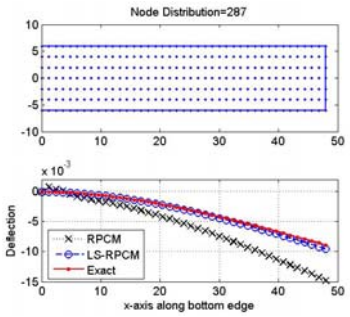

(b)

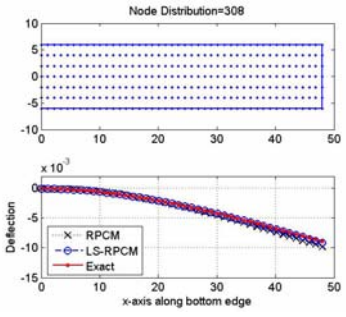

(c)

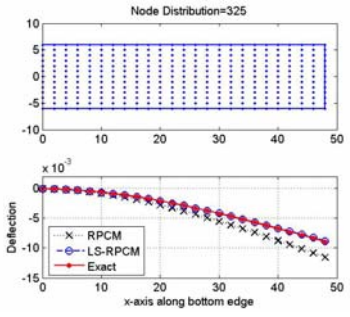

(d)

Figure 5.4 Deflection of cantilever beam along bottom edge along $x = 24m$ computed by stabilized LS-RPCM using 4 different set nodal distributions, (a) 273 nodes, (b) 287 nodes, (c) 308 nodes and (d) 325 nodes.

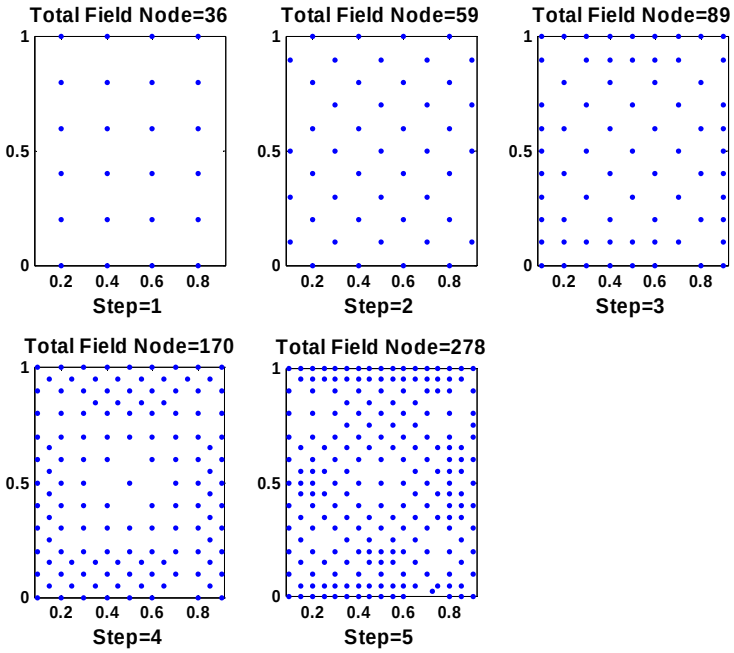

Figure 5.5 Nodal distribution at each adaptive step for Poisson problem.

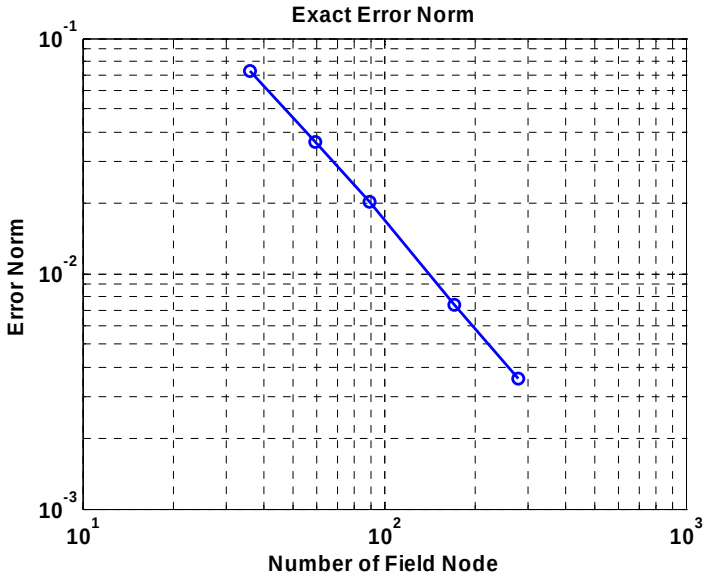

Figure 5.6 Exact error norm at each adaptive step for Poisson problem.

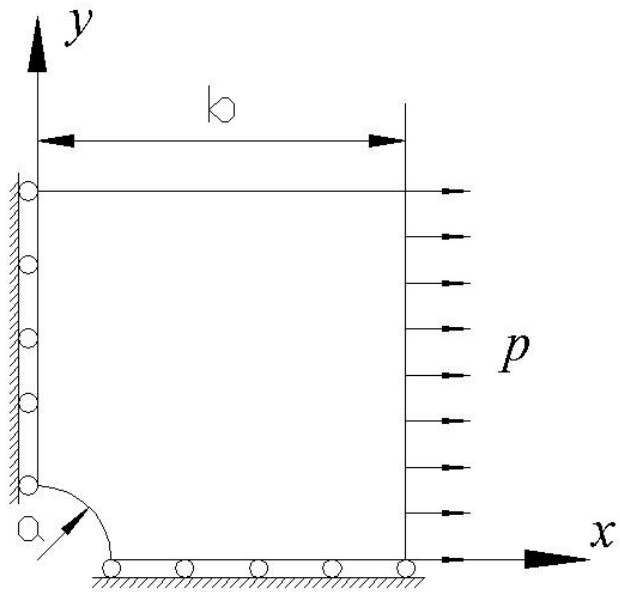

Figure 5.7 A quarter model of an infinite plate subjected to uniaxial traction in the horizontal direction.

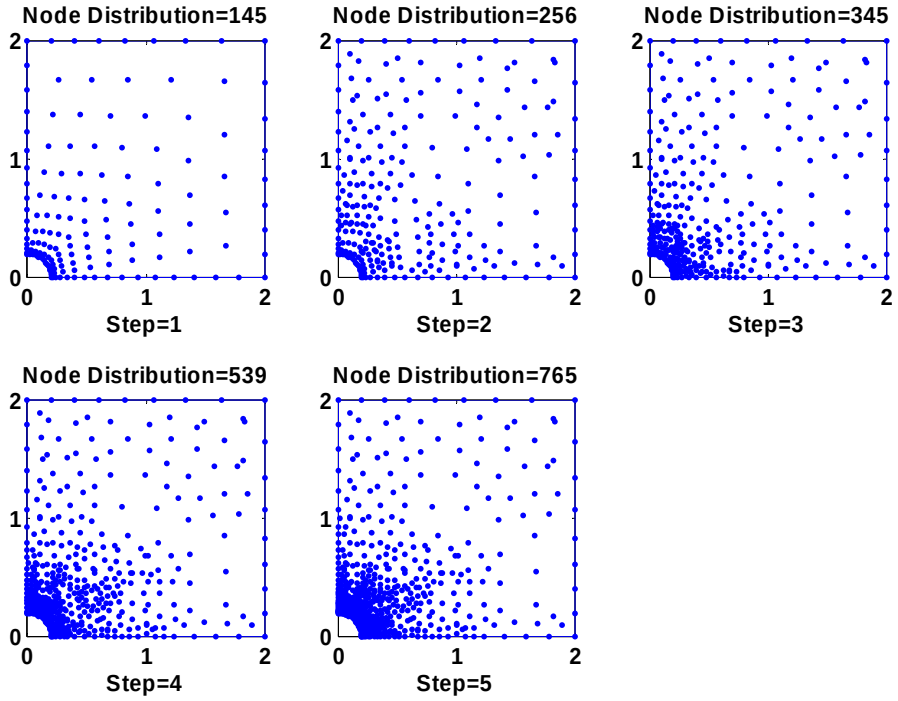

Figure 5.8 Nodal distribution of the infinite plate with circular hole at each adaptive step.

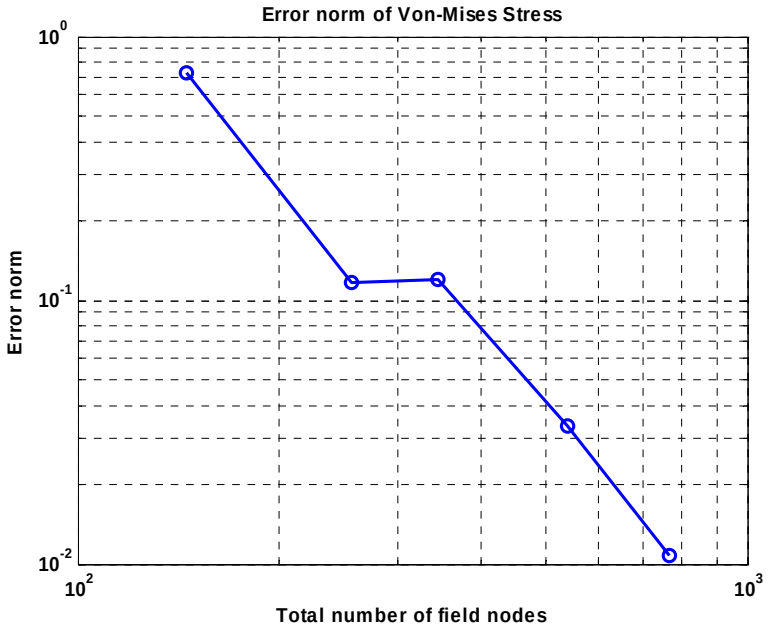

Figure 5.9 Error norms of Von-Mises stress computed by stabilized LS-RPCM at each adaptive step.

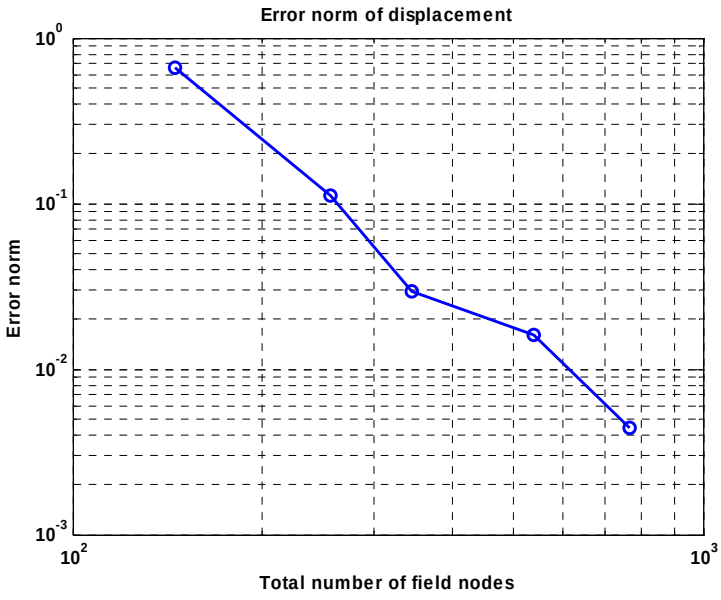

Figure 5.10 Error norm of displacements computed by stabilized LS-RPCM at each adaptive step.

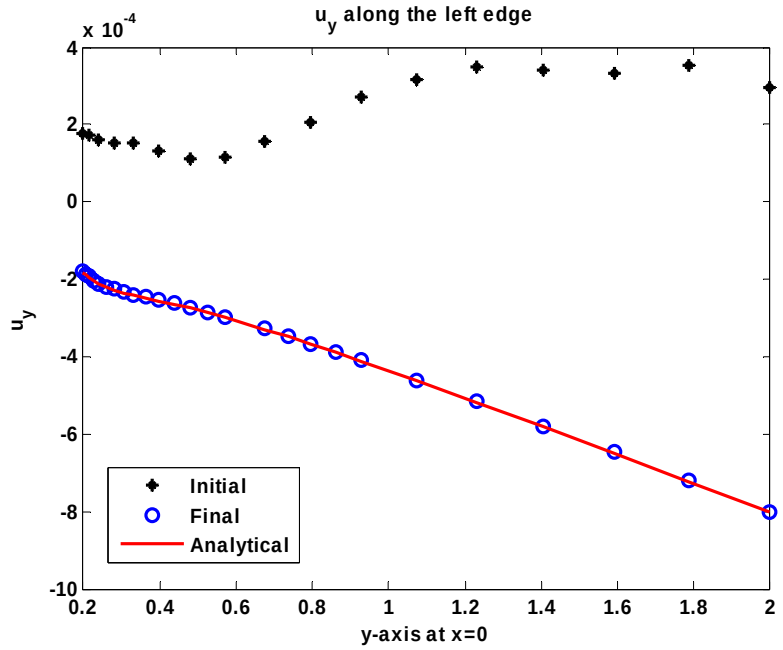

Figure 5.11 Displacement u_y along $x = 0$ computed the stabilized LS-RPCM at final step.

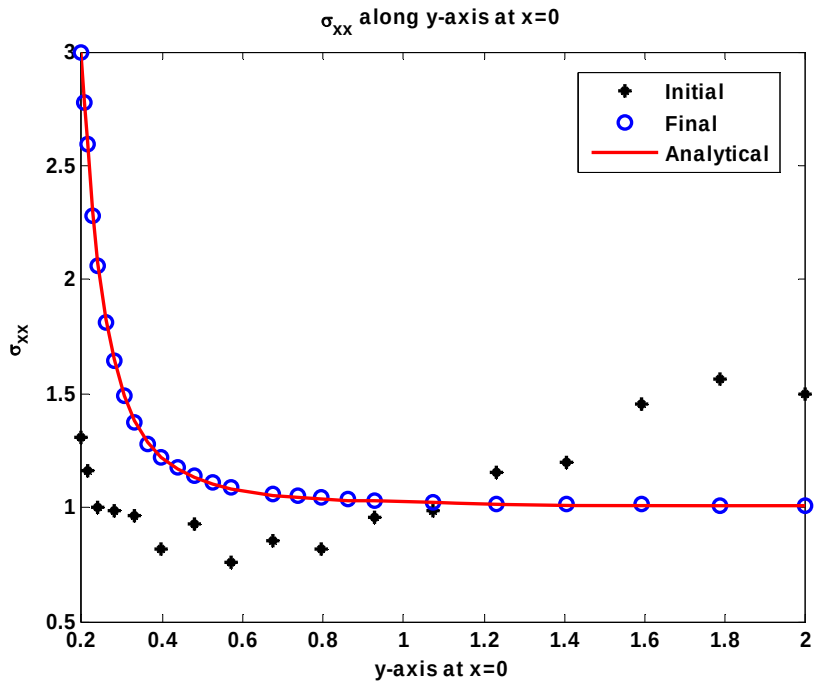

Figure 5.12 Normal stress σ_{xx} along $x = 0$ computed the stabilized LS-RPCM at final step.

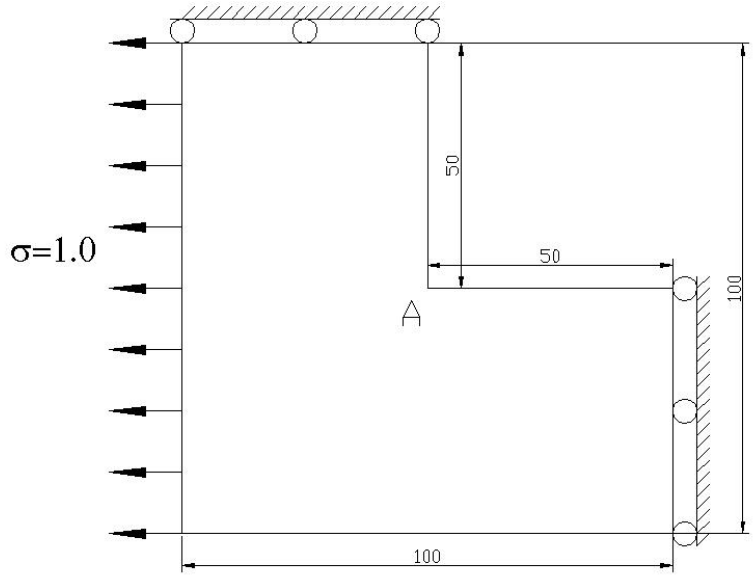

Figure 5.13 L-shaped plate subjected to a unit tensile stress in the horizontal direction.

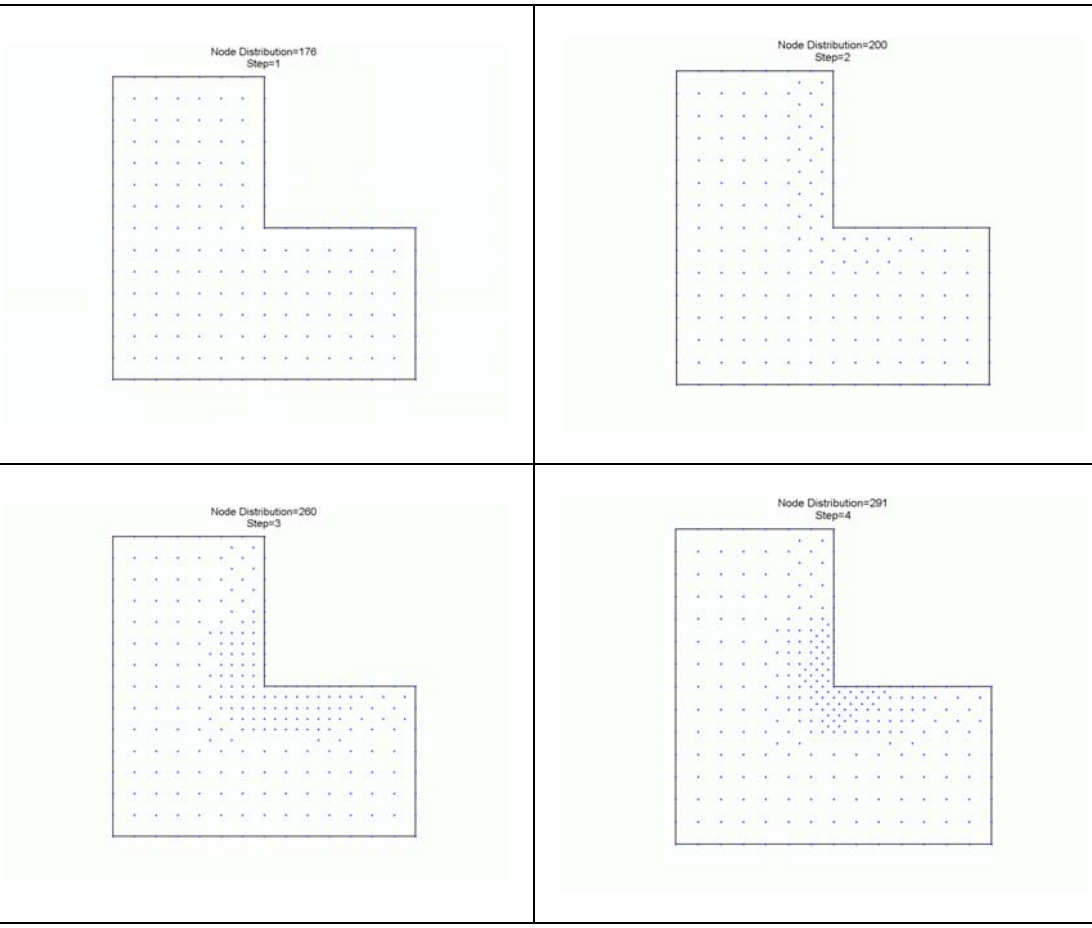

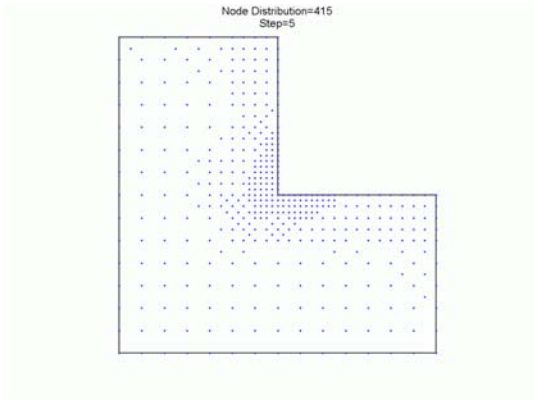
Node Distribution=415
Step=5

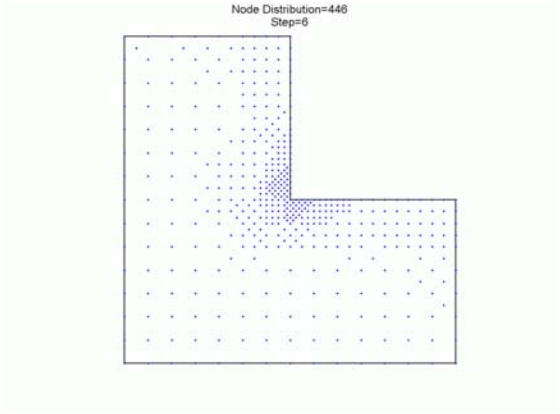
Node Distribution=446
Step=6

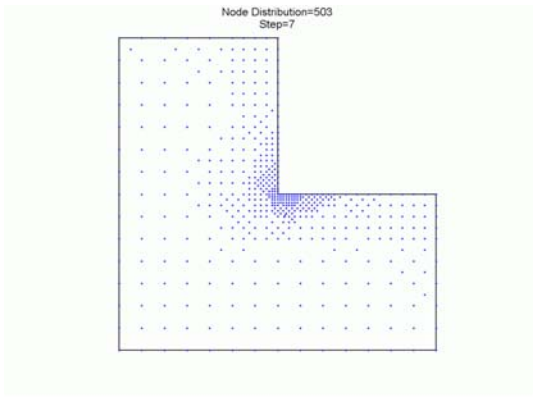
Node Distribution=503
Step=7

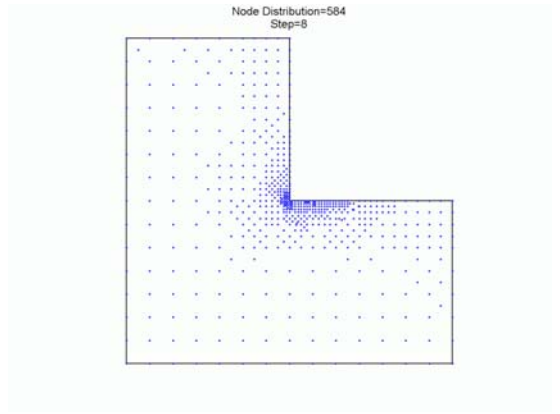
Node Distribution=584
Step=8

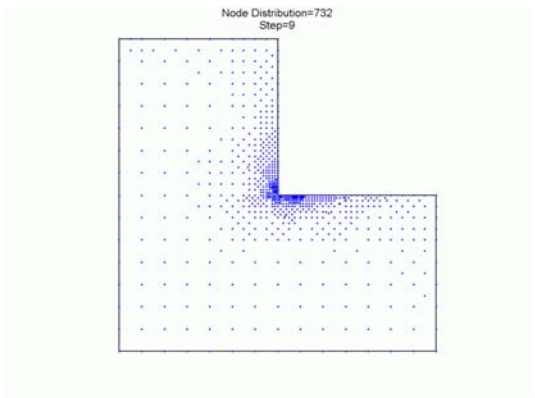
Node Distribution=732
Step=9

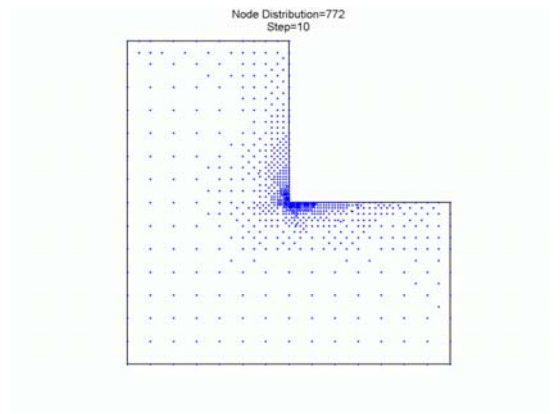
Node Distribution=772
Step=10

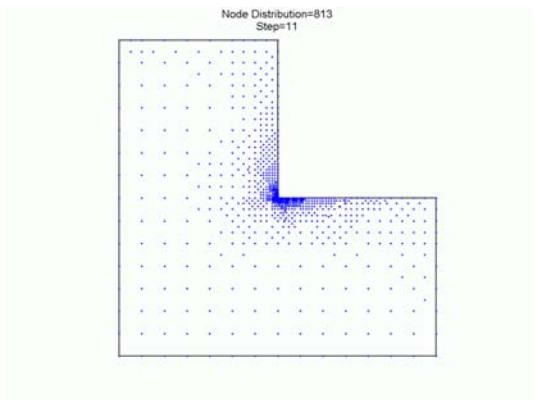
Node Distribution=813
Step=11

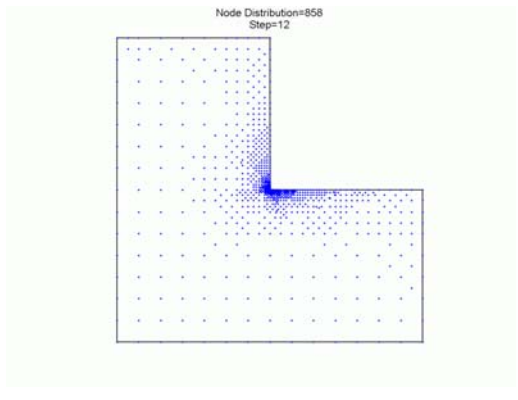
Node Distribution=858
Step=12

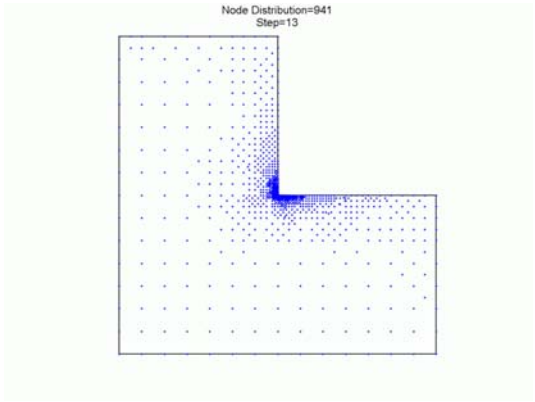

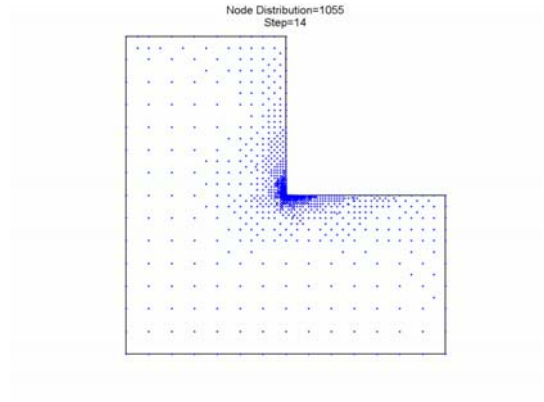

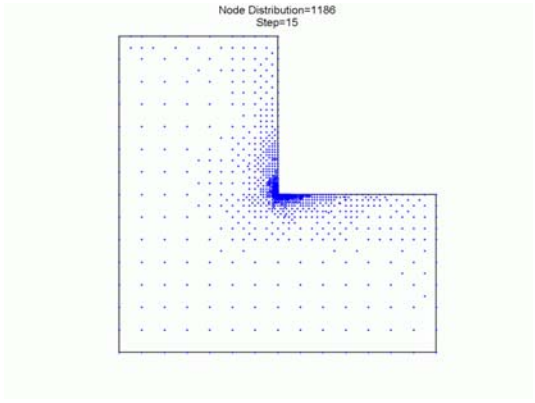

Figure 5.14 Nodal distribution at each adaptive step for the L-shaped plate problem.

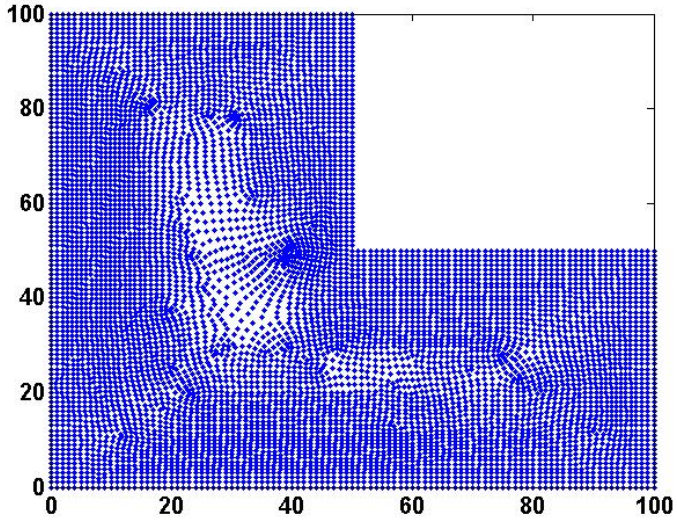

Figure 5.15 A model of L-shaped plate with 7902 nodes in ANSYS for references solution.

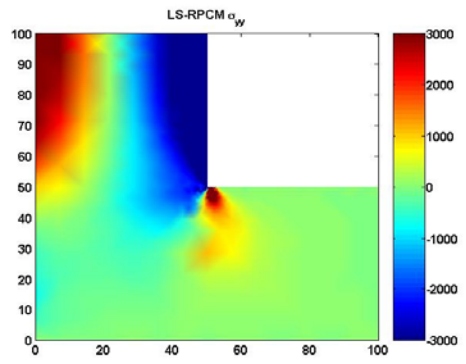

(a)

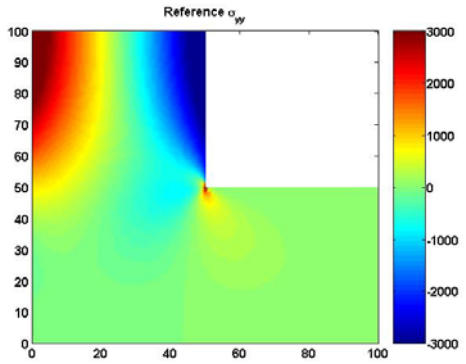

(b)

Figure 5.16 Normal stress σ_{yy} distribution of L-shaped plate computed by (a) the LS-RPCM and (b) the reference solution.

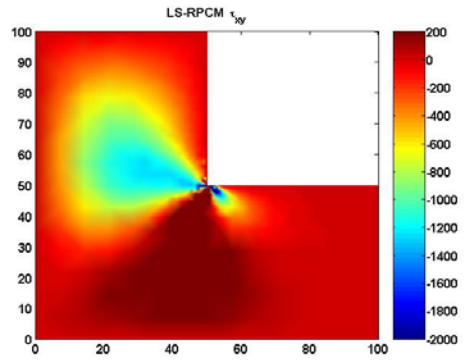

(a)

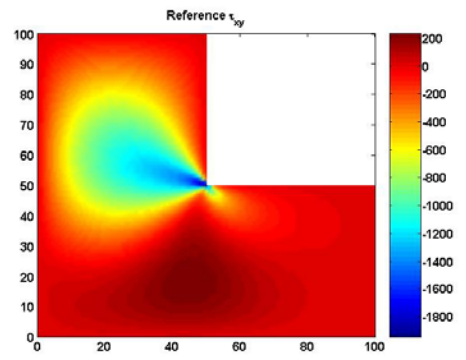

(b)

Figure 5.17 Normal stress τ_{yy} distribution of L-shaped plate computed by (a) the LS-RPCM and (b) the reference solution.

Chapter 6

A Least-Square Radial Point Collocation Method (LS-RPCM) with Special Treatment for Boundaries

6.1 Introduction

In this chapter, a least-square radial point collocation method (LS-RPCM) with special treatment for boundaries is presented [68]. Aiming to solve for the instability problem in the conventional RPCM using local nodes, a simple and yet effective procedure that uses the well-known least-square technique has been proposed to restore the stability.

From the intensive numerical studies for solid mechanics problems, the strong-form solution is found oscillating heavily on the boundary of the problem domain. It is believed that such oscillation is caused by the "strong" requirement for the approximated field variable to satisfy governing equations and boundary conditions "exactly" at all the nodes. Based on the observation and understanding on the oscillation phenomenon, a novel and simple procedure called least-square procedure with special treatment for boundaries is proposed based on the strong formulation. In

this formulation procedure, additional collocation points (*not nodes*) are inserted *only* on the boundary. A common technique, least-square technique, is then adopted to provide certain "relaxation" effect upon the strong formulation.

In this chapter, the intensive numerical study will show stable and accurate solution can be obtained from the present procedure. Furthermore, the LS-RPCM with special treatment for boundaries is also successfully implemented in adaptive analyses. The present formulation of LS-RPCM remains simple and straightforward. No integration procedure is needed throughout the formulation. Great stability and advantages of the LS-RPCM are well demonstrated in the numerical examples.

6.2 Least-square Procedure with Special Treatment for Boundaries

As meshfree strong-form methods can not ensure the solution is stable, it is difficult to use them in the adaptive analysis. In this work, a simple and yet effective procedure, least-square procedure with special treatment on the boundaries, is proposed to obtain stable solutions [68].

Through observation, Neumann boundary condition is the causes of the instability. The conventional RPCM is always performing well for solving one dimensional problem and Dirichlet problem. However, the solution of conventional RPCM becomes unstable while Neumann boundary condition exists. Oscillation phenomenon is observed on the boundary. It could be due to the 'strong' requirement of satisfaction of the Neumann boundary condition in the strong formulation. To provide a kind of

'relaxation' effect, least-square approach is a natural choice to be adopted.

In the present formulation, the boundaries of the domain are specially treated. Additional collocation points (not nodes) are added along the boundaries and allocated in between the boundary nodes as shown in the **Figure 6.1**. The Neumann and Dirichlet boundary conditions in the form of Eq (4.2) and Eq. (4.3) can be collocated at the additional collocation points along the boundaries respectively. The additional algebraic equations can be assembled and expressed in the matrix form as follows:

$$\begin{bmatrix} \mathbf{K}_{N'} \\ \mathbf{K}_{D'} \end{bmatrix} \mathbf{U} = \begin{bmatrix} \mathbf{F}_{N'} \\ \mathbf{F}_{D'} \end{bmatrix}$$

or

$$\mathbf{K}_a \mathbf{U} = \mathbf{F}_a, \tag{6.1}$$

where $\mathbf{K}_{N'}\mathbf{U} = \mathbf{F}_{N'}$ and $\mathbf{K}_{D'}\mathbf{U} = \mathbf{F}_{D'}$ are the additional sets of algebraic equations for additional collocation points on the Neumann and Dirichlet boundaries respectively. Both equations are constructed by discretizing the respective boundary conditions on the collocation points along the boundary. In this case, $\mathbf{K}_{D'} = \mathbf{I}$ is the identity matrix and $\mathbf{F}_{D'} = \overline{\mathbf{U}}$ is the given nodal value. Augmented the additional algebraic equations to the original system equations, one can obtain an "over-posed" problem [47],

$$\begin{bmatrix} \mathbf{K} \\ \mathbf{K}_a \end{bmatrix} \mathbf{U} = \begin{bmatrix} \mathbf{F} \\ \mathbf{F}_a \end{bmatrix}$$

or

$$\widetilde{\mathbf{K}}\mathbf{U} - \widetilde{\mathbf{F}} = 0 \quad (6.2)$$

As the number of algebraic equations is more than the number of unknown variable **U**, a common least-square technique using QR-algorithm is applied to solve for the vector of unknowns **U** by minimizing the residual in Eq. (6.2). Before the set of equations is solved, to have equal weight for each algebraic equation, each equation should be normalised by the value of the largest entry in the corresponding row of the coefficient matrix $\widetilde{\mathbf{K}}$. The normalized algebraic equations can be expressed in the following matrix form,

$$\hat{\mathbf{K}}\mathbf{U} = \hat{\mathbf{F}}, \quad (6.3)$$

where $\hat{\mathbf{K}}$ denotes the normalized coefficient matrix and $\hat{\mathbf{F}}$ denotes the normalized force vector. In the conventional RPCM, although the boundary conditions are fully satisfied at the boundary nodes, stable solution can not be ensured. From my study [49-52,67], the cause of instability could be due to the imposition of Neumann boundary conditions. By introducing more collocation points along the boundaries, the least-square procedure is expected believed that able to provide certain degree of "relaxation" upon the strong formulation and hence a more stable solution can be obtained. The key point of the least-square procedure is that having additional collocation points along the boundary is enough to stabilise the solution. Introducing additional collocation points in the internal domain may help but it is not necessary. This finding is in line with the principle of the MWS method [27,55].

In the formulation procedure of MWS method, the formulation procedure is constructed using strong formulation except on the boundaries. Weak formulation is used for boundary nodes to provide a better stability. In the paper of MWS method [27,55], instability is believed to be caused by the Neumann boundary conditions. By applying weak formulation procedure, it helps to relax the strong requirement along the Neumann boundary.

6.3 Numerical Examples

Incorporating with the residual based error estimator, the least-square radial point collocation method (LS-RPCM) with special treatment for boundaries is extended to adaptive analysis. The details of the residual based error estimator and the adaptive strategy adopted in this work are well described in Chapter 3.

As LS-RPCM with special treatment for boundaries is a truly mesh free method, the implementation of the adaptive analysis is very simple and straightforward. Simple *h*-refinement scheme based on the Delaunay diagram is employed in this work. Due to mesh free feature, additional nodes can be simply just inserted into the domain in this *h*-refinement procedure without worry about the connectivity.

In the given numerical examples in this chapter, polynomial with completed second order, $m = 6$, is adopted in the RPIM approximation and shape parameters of MQ-RBF are known as $\alpha_c = 3.0$ and. $q = 1.03$.

6.3.1 Example 1: Infinite Plate with Hole Subjected to a Uniaxial Traction in the Horizontal Direction

In the first example, a benchmark plane strain solid mechanics problem is studied to reveal the instability problem encountered by RPCM. An infinite plate with circular hole subjected to a unit traction *P* in the horizontal direction is investigated. Due to symmetry, only quarter of the problem is modelled as shown in **Figure 5.7**. Symmetric boundaries conditions are imposed along the left and bottom edges. The geometry and material properties are given as: $a = 0.2$, $b = 2.0$, Young's modules $E = 1 \times 10^3$ and Poisson's ratio $\upsilon = 0.3$. The governing equations and boundaries conditions that govern the elastostatics problem are given in Eq. (4.19) to Eq. (4.21). The analytical solution of this problem can be found in Ref. [90].

To demonstrate the instability problem of the RPCM, two similar sets of nodal distribution are studied, see **Figure 6.2**. Model A is made up of 435 nodes and eighteen nodes are added into Model A to form Model B. Although only little difference between Model A and Model B, the RPCM solutions based on these two models are tremendously different. The numerical solutions of the displacements and the stresses along the left edge are plotted in **Figure 6.3** and **Figure 6.4**. It is clear that the solution computed by the RPCM is unstable. Both solutions of displacements and stresses for Model A and Model B are significantly different. As compared to the RPCM, the solutions obtained by the LS-RPCM with special treatment for boundaries are very stable and much more accurate.

In the original RPCM formulation procedure, the boundary conditions are fully satisfied on the boundary nodes. On the contrary, boundary conditions are satisfied in a least-square sense in the present formulation. In this example, $\sigma_{yy} = 0$ is the Neumann boundary condition along the top edge. From **Figure 6.5**, one can observe that although the boundary condition along the top edge ($\sigma_{yy} = 0$) is fully satisfied by the RPCM at the boundary nodes, the value of σ_{yy} is frustrating along the top edge. Except at the boundary nodes, the interpolation value of σ_{yy} can be varied significantly from zero (the exact condition) along the top edge as shown in **Figure 6.5**. In the present formulation, the least-square procedure with special treatment on the boundaries provides a kind of 'relaxation' effect against the 'strong' requirement of the boundary conditions in strong formulation. Good approximated solutions obtained by the LS-RPCM are clearly shown in **Figure 6.4**.

6.3.2 Example 2: Cantilever Beam Subjected to a Parabolic Shear Traction at the End

To examine the computational efficiency of the LS-RPCM, a benchmark elastostatics plane stress problem is studied. A cantilever beam with unit thickness is subjected to a parabolic shear stress at the right end as shown in **Figure 4.1**. The material properties and geometrics are given as: Young's modulus $E = 3 \times 10^7$, Poisson's ratio $\upsilon = 0.3$, length of cantilever $L = 48.0m$ and the height $H = 12.0m$. The loading is known as $\tau_{xy} = -\frac{P}{2I}\left(H^2/4 - y^2\right)$, where *I* is moment of inertial of the cross section of cantilever and $P = 1000N$. Analytical solution can be found in Ref.

[90].

In this example, solutions for four sets of regular nodal distribution: 5×11, 9×21, 17×41 and 33×81, are computed. Sixteen supporting nodes are used to construct the shape functions. From **Figure 6.6**, it shows the computational time required for the LS-RPCM is higher that the RPCM and the FEM. It is due to the use of the least-square procedure in the LS-RPCM.

The convergent rates of the error norm of displacements and energy norm are approximately about 2.29 and 2.06 respectively as shown in **Figure 6.7** to **Figure 6.9**. The accuracy of the LS-RPCM for displacements is comparable with FEM as shown in **Figure 6.7**. In term of the accuracy of the stresses and the convergent rate of the energy norm, LS-RPCM performs better than FEM as shown in **Figure 6.8** and **Figure 6.9**.

From the efficiency rate in term of energy norm plotted in **Figure 6.10**, LS-RPCM has been shown as the best among these three methods. Although RPCM seems performing well in the regular nodal distribution in **Figure 6.7** to **Figure 6.9**, the instability issue is still fatal shortcoming that prohibits RPCM from being used in adaptive analysis.

This example is also further extended to adaptive analysis. The LS-RPCM is incorporated with the residual based error estimator to performance adaptive analysis subsequently. Sixteen nodes are used to construct the shape functions. The local refinement coefficient and the global residual tolerance are predefined as $\kappa_l = 0.1$ and $\kappa_g = 0.2$ respectively. The adaptive analysis starts with 55 nodes regularly distributed

in the problem domain and is ended at 4^{th} step with 1252 nodes irregularly distributed in the problem domain as shown in **Figure 6.11**.

As shown in **Figure 6.12**, the estimated global residual norm is gradually reduced at each adaptive step. Excellent stability of LS-RPCM is demonstrated. The error norm of displacements and energy norm at each adaptive are also reduced gradually and plotted in **Figure 6.13** and **Figure 6.14**. It is evidently clear that the accuracy of both displacements and stresses have been greatly improved through our effective adaptive scheme.

6.3.3 Example 3: Poisson Problem with Smooth Solution

A simple Poisson problem is solved by the adaptive LS-RPCM. Consider the following Poisson equation,

$$\frac{\partial^2}{\partial x^2}u+\frac{\partial^2}{\partial y^2}u=\sin\pi x\sin\pi y, \quad \text{in } \mathbf{\Omega}=[0,1]\times[0,1], \tag{7.4}$$

with Neumann boundary conditions

$$\frac{\partial u}{\partial x}=\frac{1}{2\pi}\sin\pi y, \quad \text{along } x=1, \tag{7.5}$$

and Dirichlet boundary conditions

$$u=-\frac{1}{2\pi^2}\sin\pi x\sin\pi y, \quad \text{along } x=0,\ y=0 \text{ and } y=1, \tag{7.6}$$

The adaptive analysis starts with regular distribution of 5×5 nodes at the initial step. Ten supporting nodes are used to construct the shape functions. In this adaptive

analysis, the tolerant values for the error estimator are predefined $\kappa_l = 0.1$ and $\kappa_g = 0.1$ respectively.

Starting with 25 regularly distributed nodes, the computation ends at 6th step with 2976 nodes. The nodes are progressively inserted to the problem domain according to the adaptive strategy. Nodal distribution at each adaptive step can be found in **Figure 6.17**. Due to the smooth nature of the problem, the nodal distribution in the final step is largely uniform for this problem. **Figure 6.16** show estimated global residual norm has been gradually reduced during adaptation and good numerical performance is observed in this adaptive study. The overall error norm of field variable u has been drastically improved from 6.33% to 0.10% as shown in **Figure 6.18**. From **Figure 6.19** and **Figure 6.20**, the solution of u and $\partial u / \partial x$ along $y = 0$ have been shown greatly be improved from the initial solution. The solution of the final step is much closer to the analytical solution as compared to the solution of initial step. It shows the adaptive strategy has efficiently improved the solutions of field function and its derivatives.

6.3.4 Example 4: A Thick Wall Cylinder Subjected an Internal Pressure

The forth example is a plane strain solid mechanics problem. A thick wall cylinder subjected an internal pressure as shown in **Figure 7.5** is studied. The material properties and geometries are given as: internal radius $a = 1$, external radius $b = 5$, Young's modulus $E = 1 \times 10^7$, Poisson's ratio $v = 0.3$ and internal pressure $P = 1MPa$. The analytical solution of this problem is well-known and can be found in

Ref. [16].

Due to symmetric, only quarter of the problem is modelled as shown in **Figure 7.5**. Symmetric boundary conditions are imposed along the left and bottom edges. In this example, only eighteen nodes are used to construct the shape functions. In the adaptive analysis, the local refinement coefficient and the global residual tolerance are predefined as $\kappa_l = 0.05$ and $\kappa_g = 0.05$ respestively. The adaptive analysis starts with 121 regularly distributed nodes in the domain and stops at the 4^{th} step with 1933 nodes irregularly distributed in domain. Obviously, from nodal distribution plotted in **Figure 6.21**, one can notice that the refinement procedure has effectively been carried out where the stresses are concentrated. The estimated global residual norm at each step given in **Figure 6.22** shows the residual is gradually reduced in the adaptation. The error norm of displacements has been tremendously reduced from 8.46% to 0.13% as shown in **Figure 6.23**. The energy norm has also been reduced drastically as illustrated in the **Figure 6.24**.

For justification purpose, LS-RPCM solution for displacements and stresses along the left edge are plotted and compared with analytical solution as shown in **Figure 6.25** and **Figure 6.26**. These plots evidently show the adaptive scheme has effectively refined the critical domain based on error estimator and hence the solutions are improved gradually. The numerical solutions of the displacements and stresses at initial step are greatly improved and the solutions at the final steps are in very good agreement with the analytical solutions.

6.3.5 Example 5: A Reservoir Full Filled with Water

In this example, the wall of a reservoir full filled with water is analysed by adaptive LS-RPCM. The geometry of the wall is irregular as given in **Figure 6.27**. The material properties of the wall are given as Young's Modulus $E = 1 \times 10^7$ and Poisson's ratio $\upsilon = 0.3$. The bottom of the wall is fixed and the curvy edge of the wall is subjected to a hydrostatic pressure $P = -9800(H - y)MPa$.

As analytical solution is not available in this case, FEM solution computed using a very fine mesh (59,400 linear triangular elements) model will be considered as a reference solution. In the adaptive analysis, the local refinement coefficient and the global residual tolerance are predefined as $\kappa_l = 0.2$ and $\kappa_g = 0.015$ respectively.

As shown in **Figure 6.28**, the adaptive analysis starts with 121 regularly distributed nodes and stops at 19^{th} step with 1519 nodes. The residual based error estimator has been shown effectively identifying the stress concentrated regions. The estimated global residual norm is gradually reduced throughout the adaptive process as shown in **Figure 6.29**. As the singularity points exist in the solution, the residual norm is not progressively reduced at beginning of the adaptation due to the number of nodes is not enough to model the problem. However, the estimated global residual norm is reduced very drastically when number of field nodes is more than 500 nodes. One can observe that this error estimator reflects the error of the approximated energy very well in **Figure 6.30**.

Figure 6.31 shows the numerical solutions of displacements have been adaptively

improved. The contour plots for stresses are also given in **Figure 6.32** to **Figure 6.33**, and have also shown the final solutions of the stresses obtained by LS-RPCM are in very good agreement with the reference solutions. For justification purpose, LS-RPCM solutions of stresses along the curvy edge are also plotted and compared with references solutions in **Figure 6.35**, and it has shown LS-RPCM solutions of the stresses at final step very tally with reference solutions as well.

6.4 Remarks

In this chapter, a least-square radial point collocation method (LS-RPCM) with special treatment for boundaries is proposed. By having additional collocation points on the boundaries, it provides a 'relaxation' effect that reduces the 'strong' requirement for the boundary conditions in the strong formulation. More collocation points included in the interior domain have also been tried out, however it may help but it is not necessary. Such finding is quite in line with the conclusion drawn in meshfree weak-strong (MWS) method [27, 55]. Number of numerical examples has shown that stable solutions can be obtained through the simple and yet effective least-square procedure.

As stable solution can be achieved, the LS-RPCM with special treatment for boundaries has well demonstrated its advantages in adaptive analysis. The residual based error estimator is also shown robust and efficient. *h*-refinement procedure using Delaunay diagram is demonstrated as a simple and yet a versatile refinement procedure to insert additional nodes during adaptation. Numerical examples have shown the

LS-RPCM not only obtained stable and accurate result but also successfully implemented for adaptive analysis which conventional RPCM can not perform.

Although least-square technique is also introduced in Chapter 5, the present formulation procedure is very different. Compared to the stabilized least-squares method introduced in Chapter 5, the present formulation is much simple and straightforward. No stabilization factor has to be determined in the present formulation. The computational cost of the present formulation is also lower.

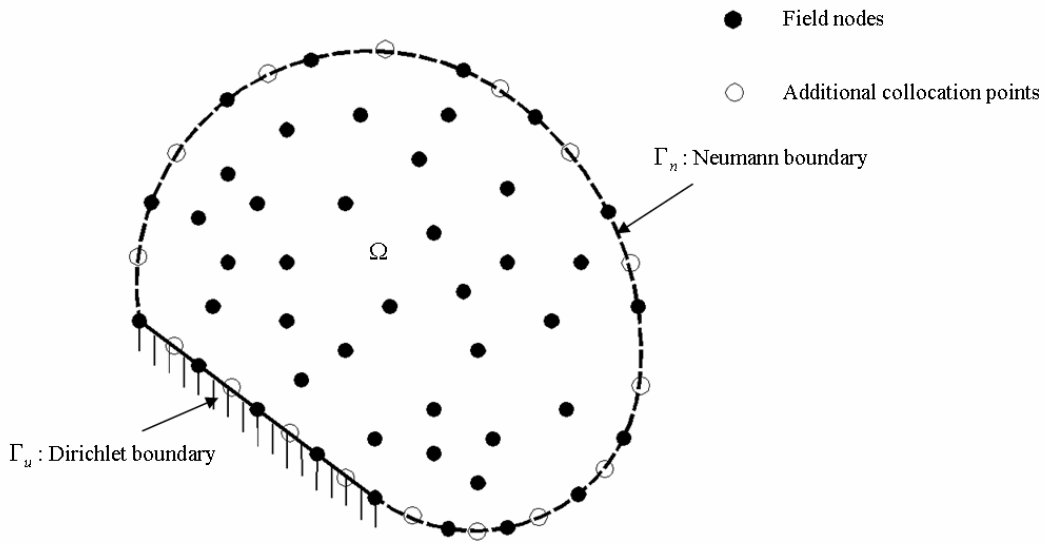

Figure 6.1 Field nodes and additional collocation points in a problem domain and on the boundaries.

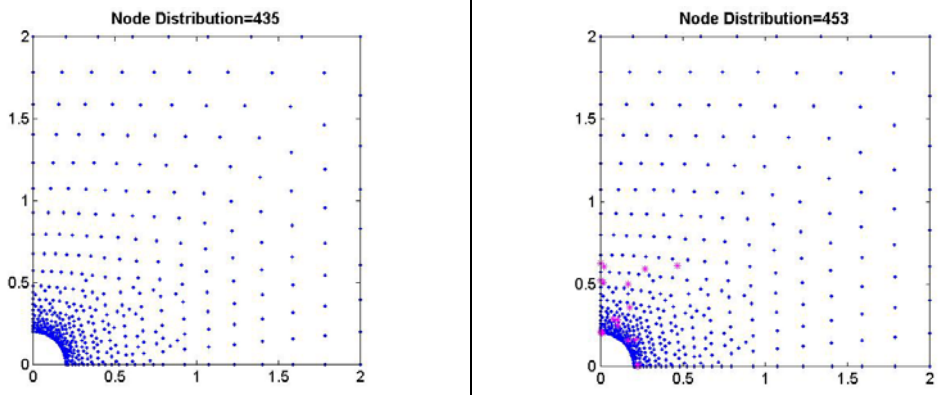

(a) (b)

Figure 6.2 Model of an infinite plate with hole with (a) 435 nodes and (b) with additional 18 nodes to the model of 435 nodes.

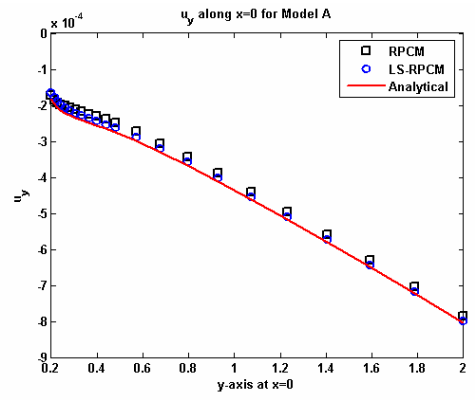

(a)

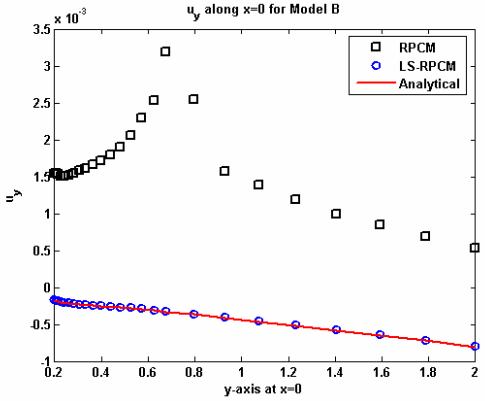

(b)

Figure 6.3 Displacement in *y*-direction along $x = 0$ for (a) Model A and (b) Model B.

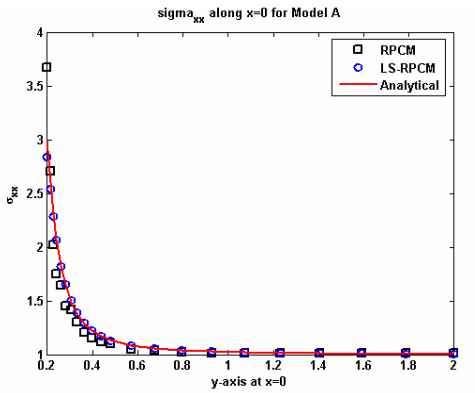

(a)

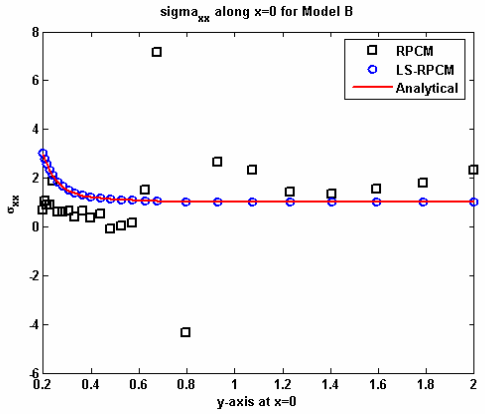

(b)

Figure 6.4 Normal stress σ_{xx} along $x = 0$ for (a) Model A and (b) Model B.

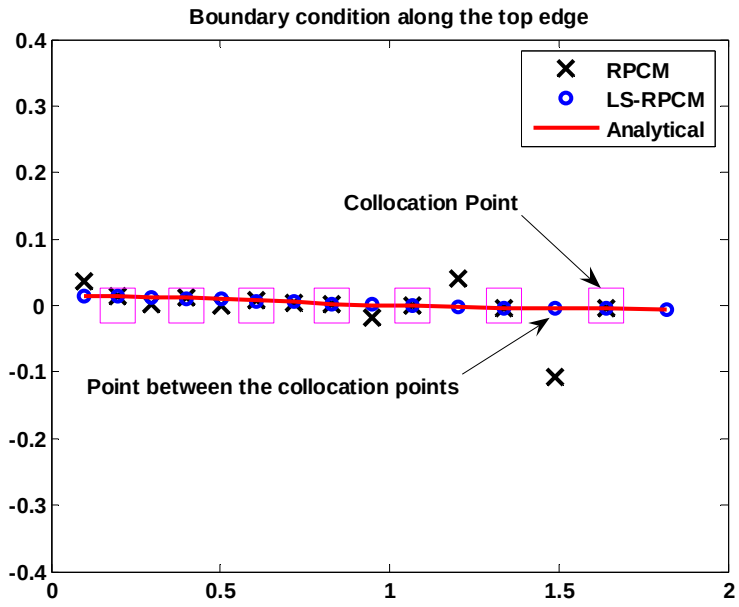

Figure 6.5 Normal stress σ_{yy} along the top edge: the result obtained using RPCM is oscillating on the boundary.

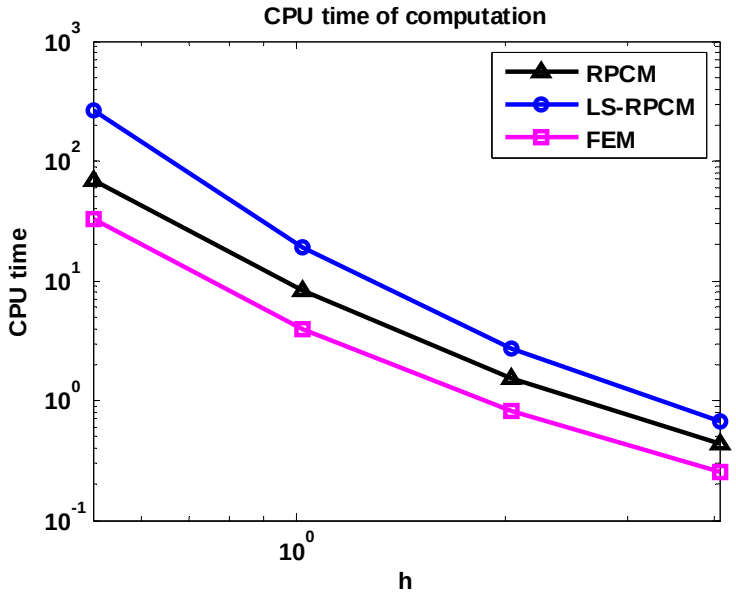

Figure 6.6 Comparison of CPU times among RPCM, LS-RPCM and FEM.

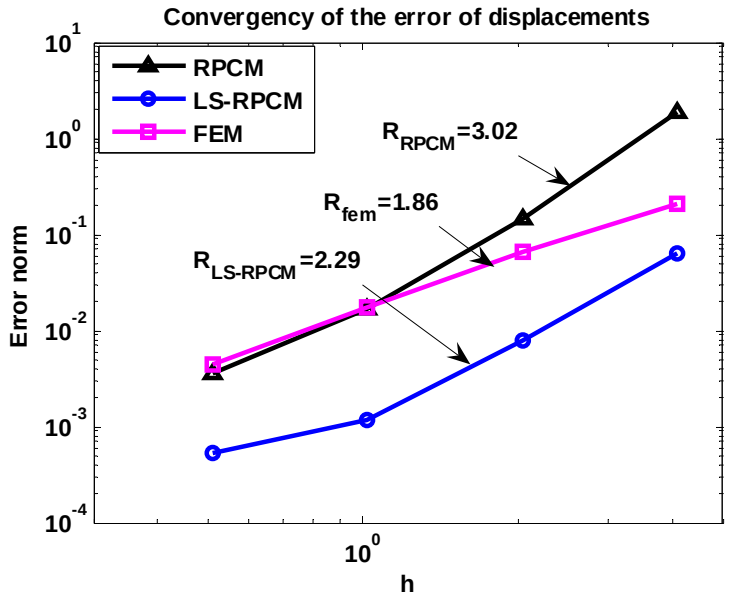

Figure 6.7 Comparison of error norm of displacements among RPCM, LS-RPCM and FEM.

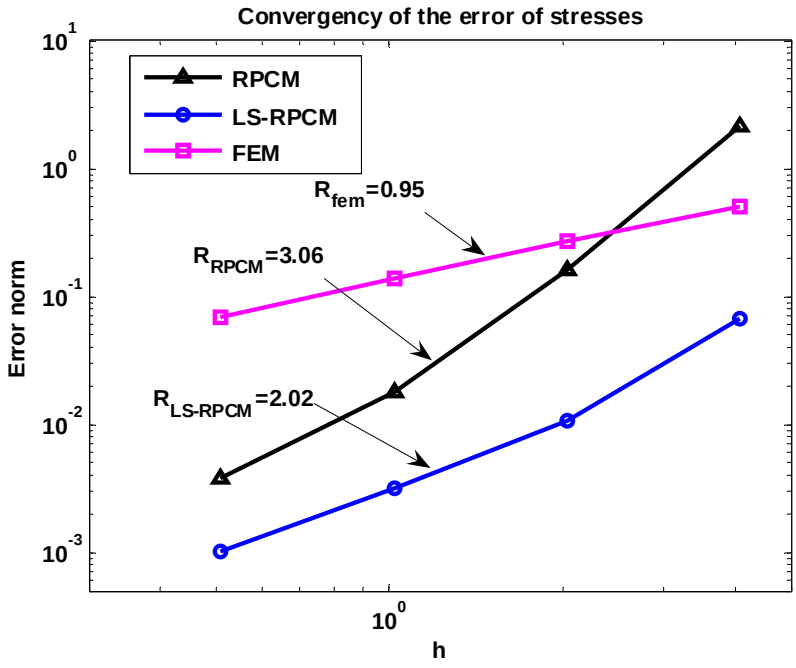

Figure 6.8 Comparison of error norm of stresses among RPCM, LS-RPCM and FEM.

**For RPCM and LS-RPCM, stresses are sampled at the node; for FEM, stresses are sampled at the center of the element*.

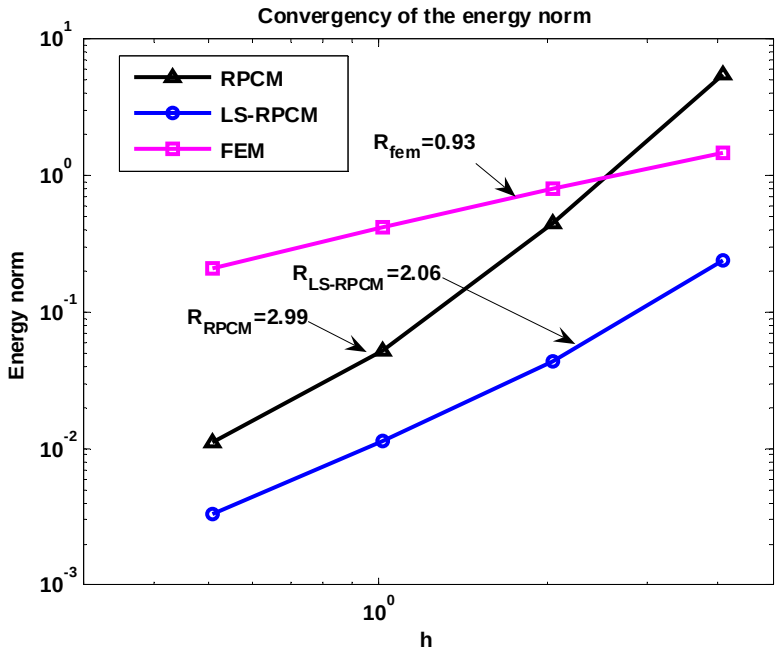

Figure 6.9 Comparison of energy norm among RPCM, LS-RPCM and FEM.

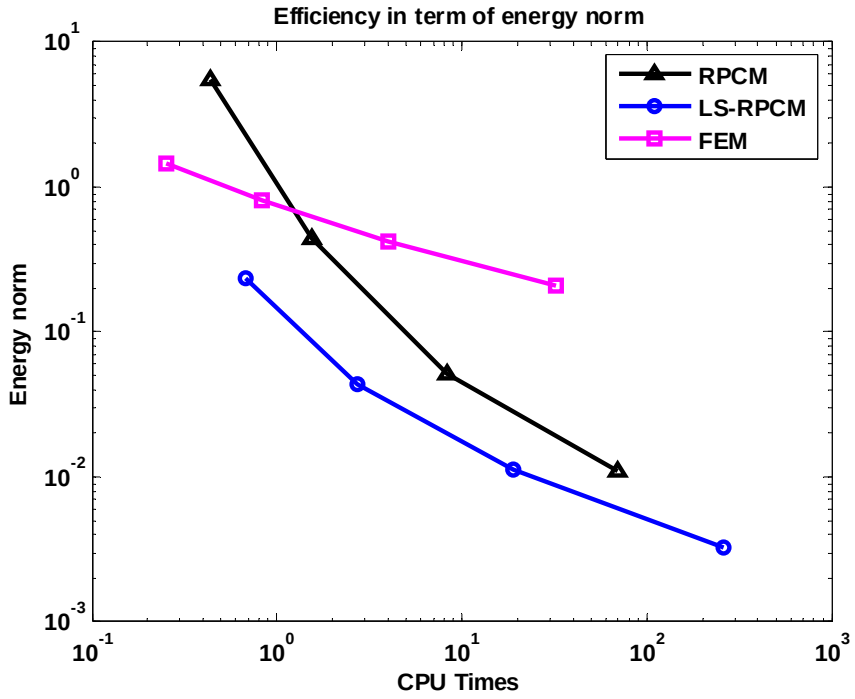

Figure 6.10 Comparison of efficiency in term of energy norm among RPCM, LS-RPCM and FEM.

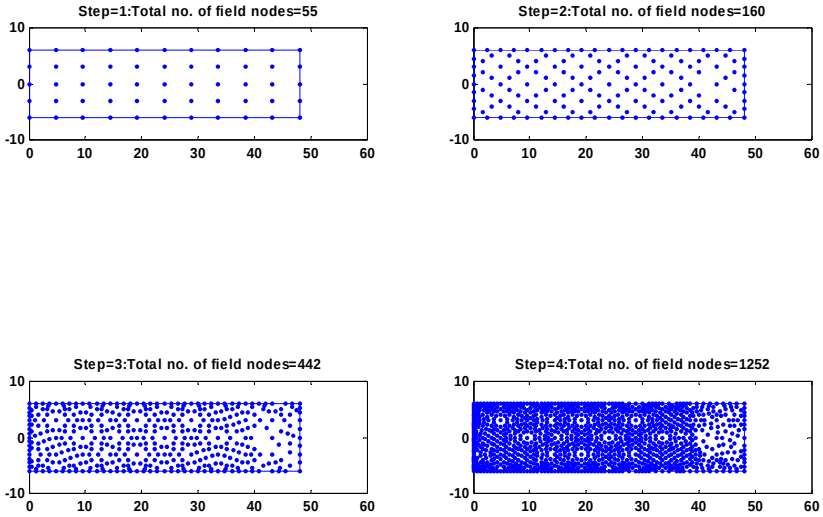

Figure 6.11 Nodal distribution of the model of cantilever beam at each adaptive step.

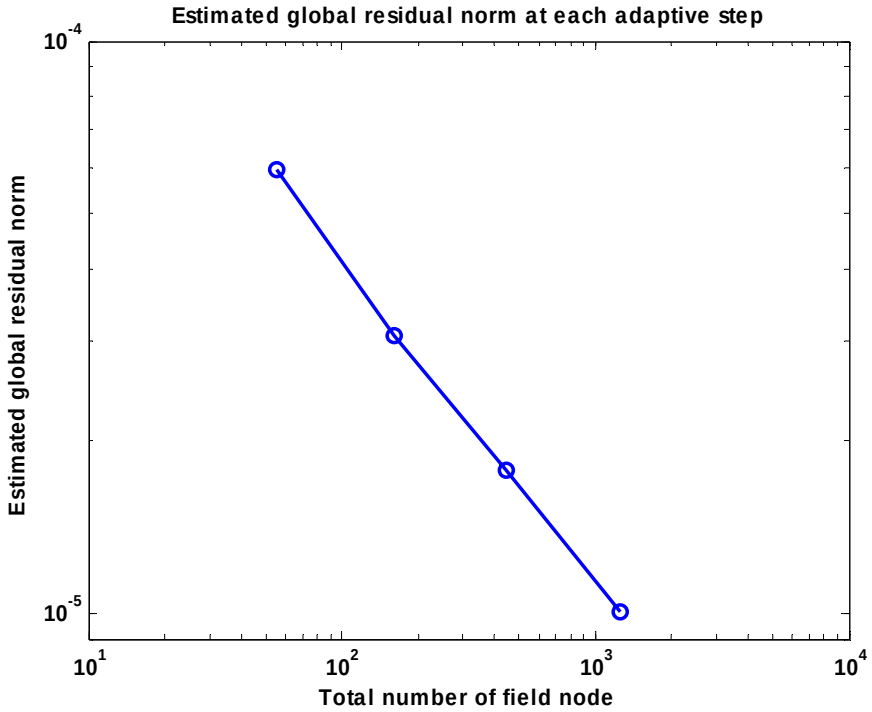

Figure 6.12 Estimated global residual norm at each adaptive step.

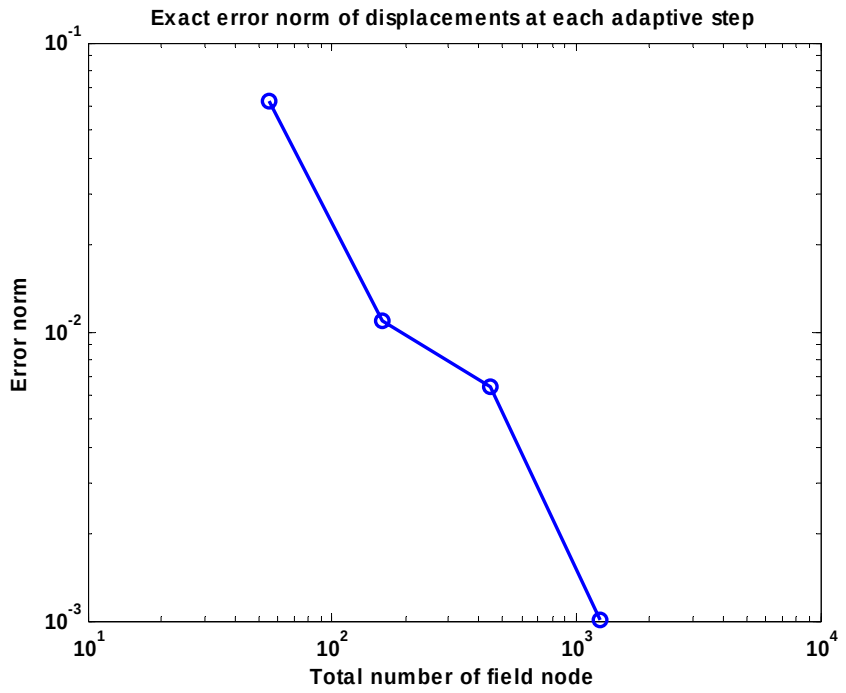

Figure 6.13 The error norm of displacements at each adaptive step.

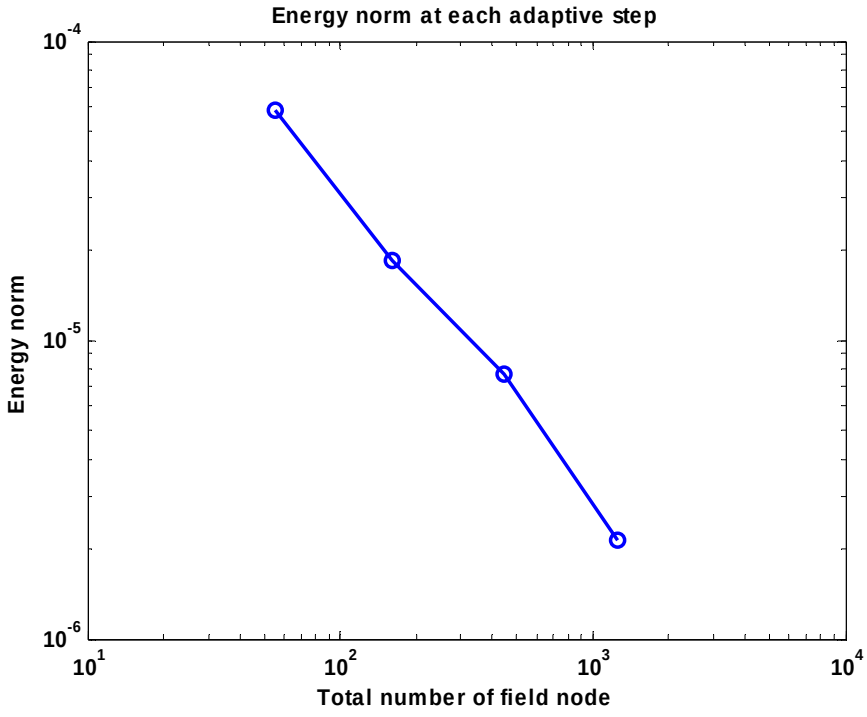

Figure 6.14 The energy norm at each adaptive step.

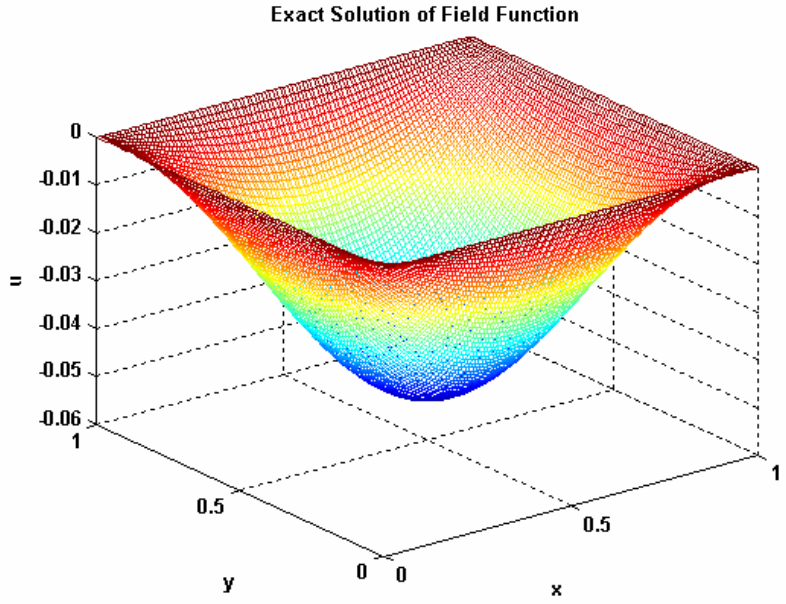

Figure 6.15 Three dimensional plot of the exact solution of Poisson problem.

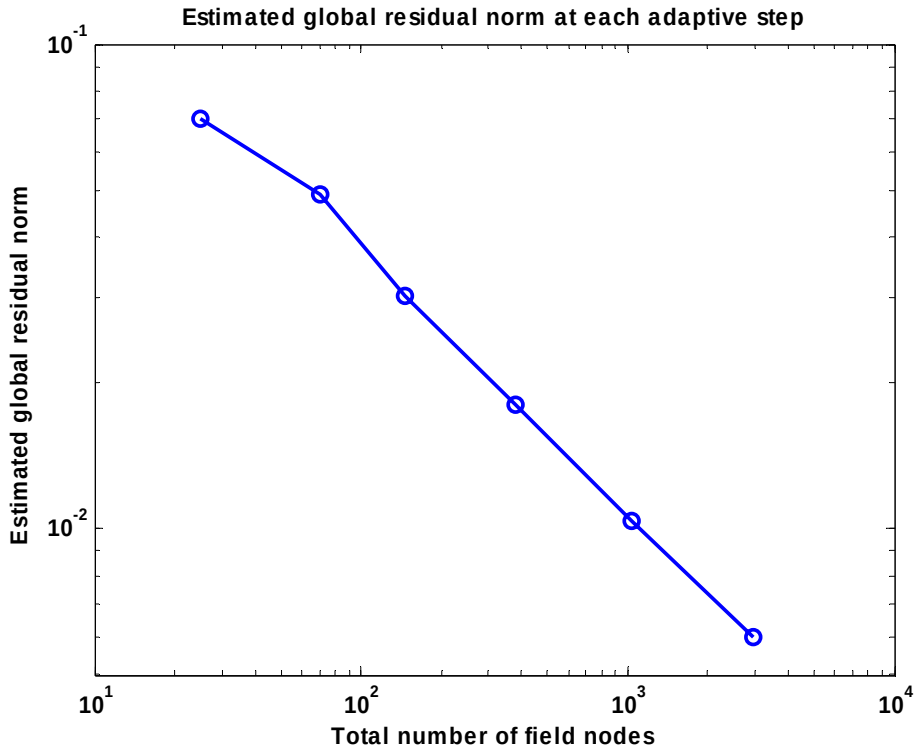

Figure 6.16 The estimated global residual norm at each adaptive step.

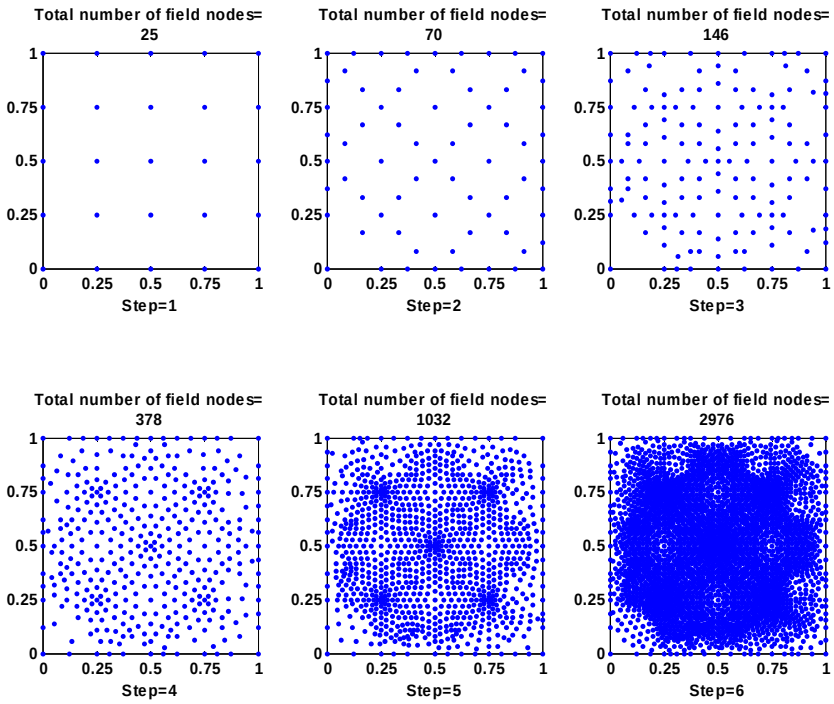

Figure 6.17 The nodal distribution at each adaptive step.

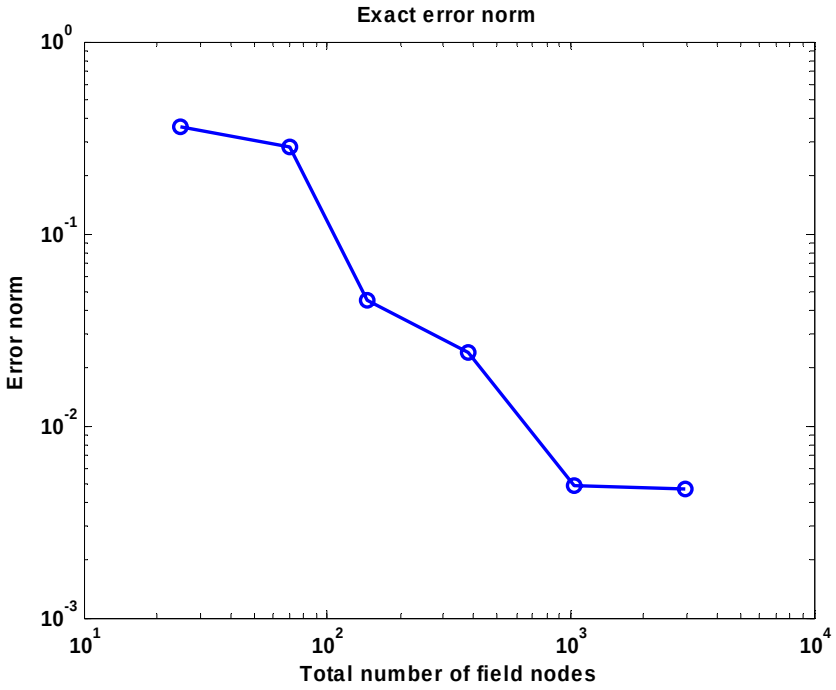

Figure 6.18 The error norm at each adaptive step.

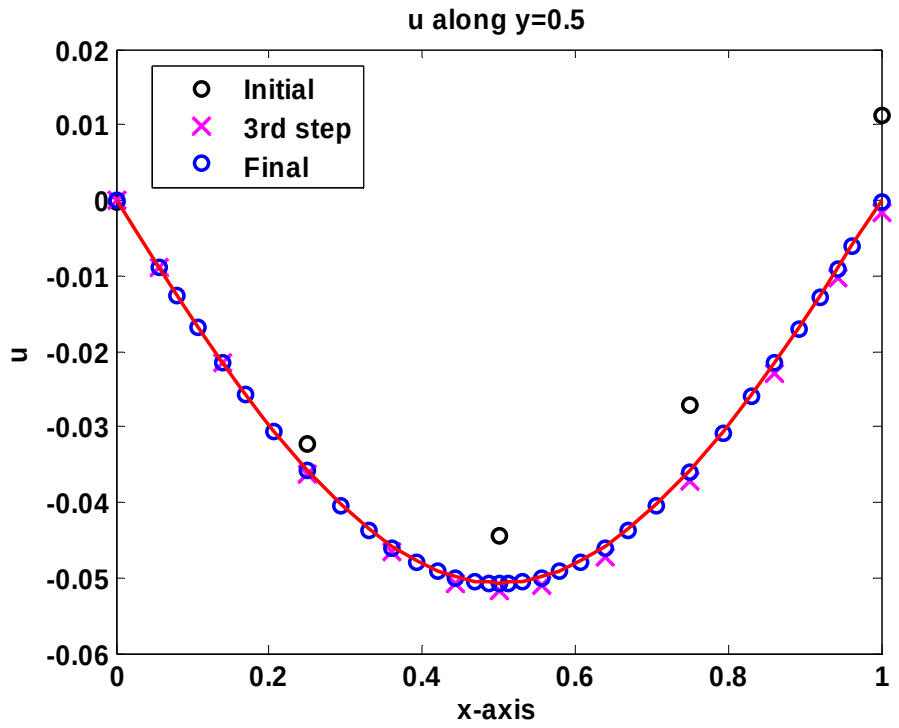

Figure 6.19 The LS-RPCM solution of the field functions along $y = 0.5$ at initial and final steps.

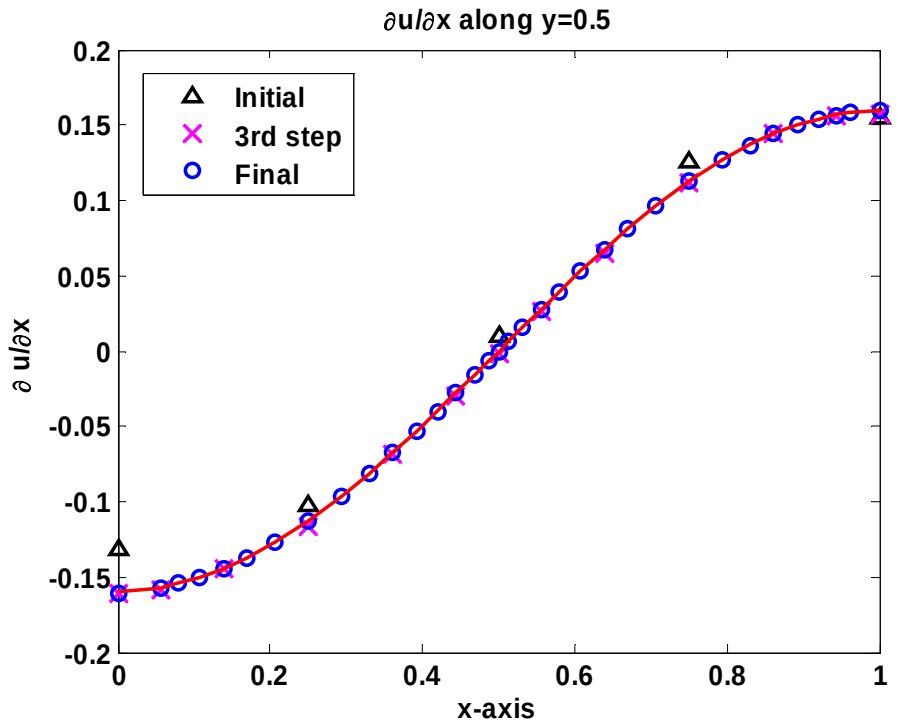

Figure 6.20 The LS-RPCM solution of the $\frac{\partial u}{\partial x}$ along $y = 0.5$ at initial and final steps.

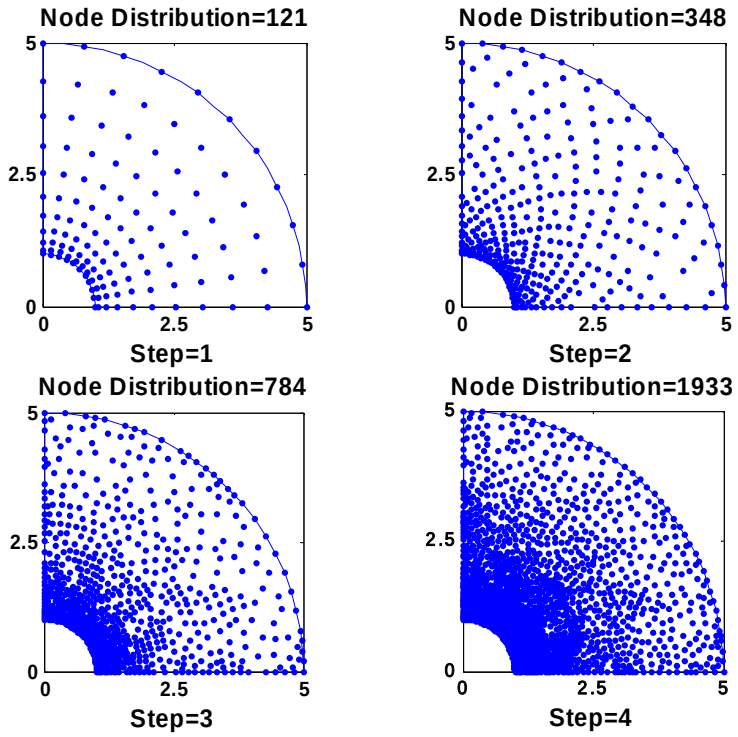

Figure 6.21 Nodal distribution of the model of hollow cylinder at each adaptive step.

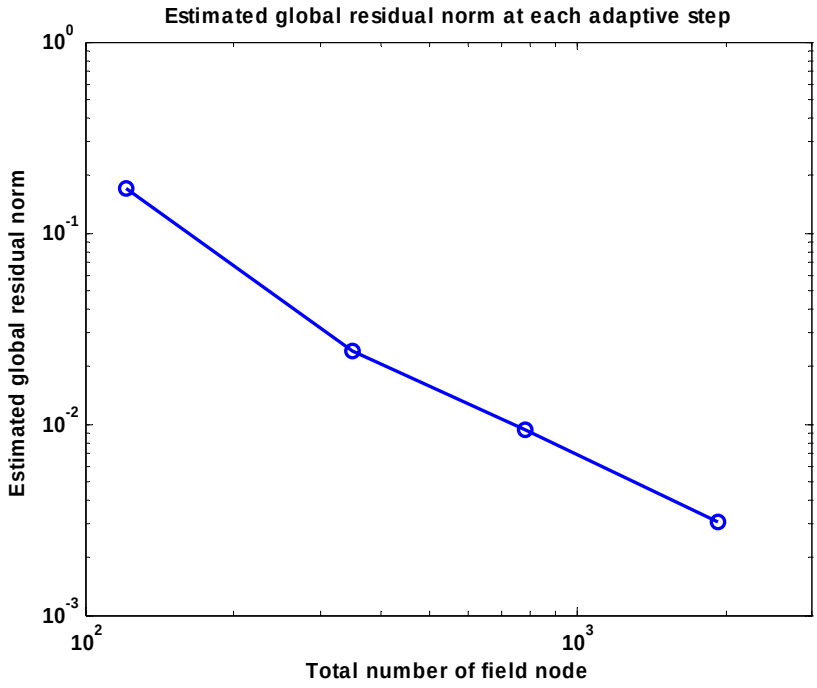

Figure 6.22 Estimated global residual norm at each adaptive step.

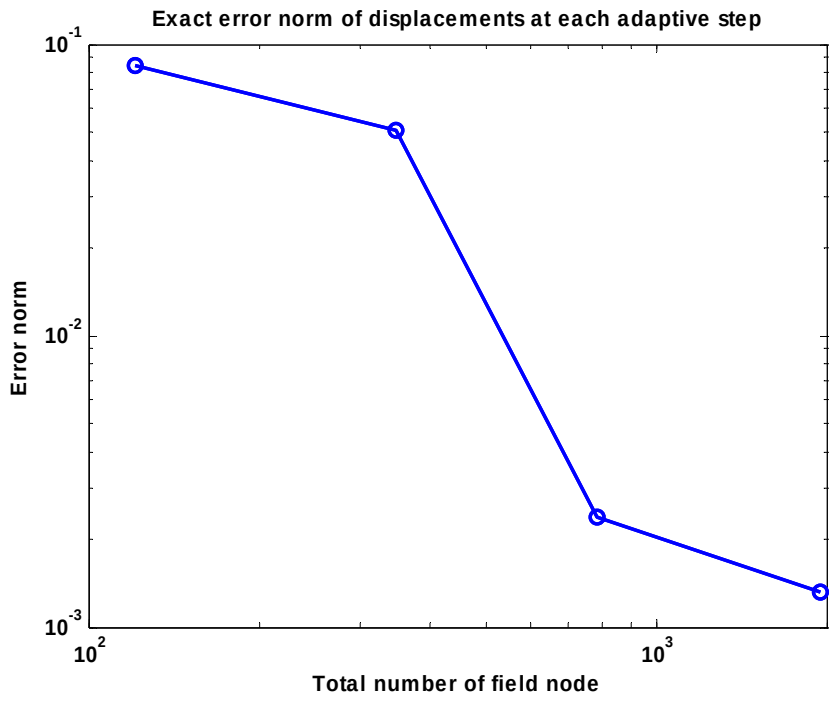

Figure 6.23 Exact error norm of displacements at each adaptive step.

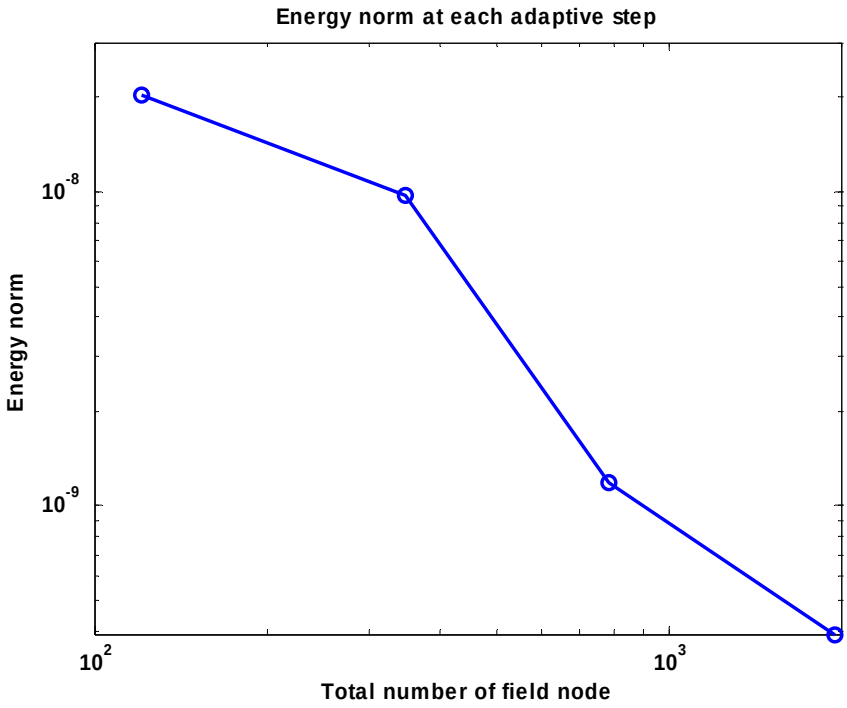

Figure 6.24 Energy norm at each adaptive step.

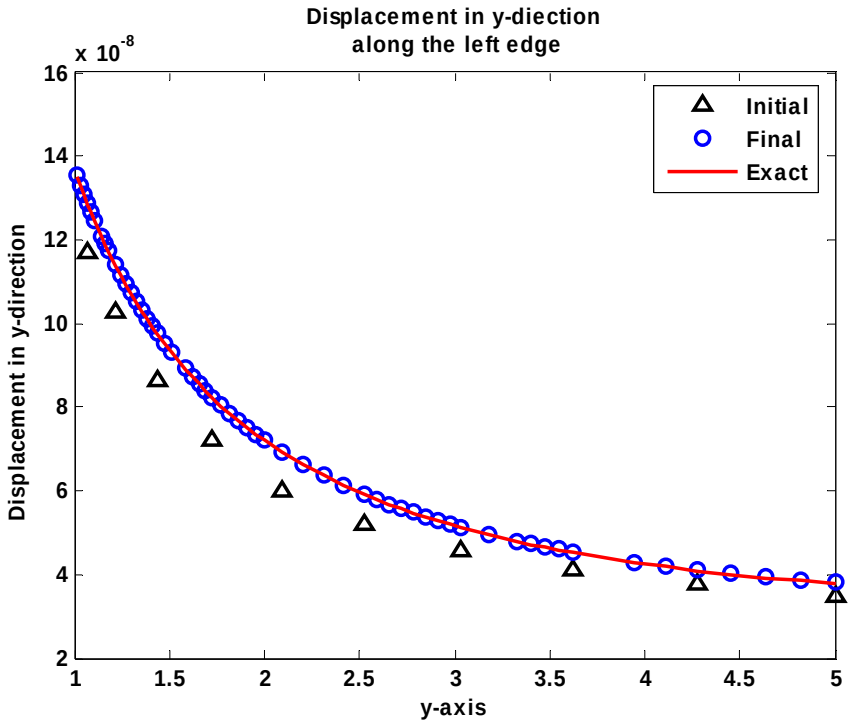

Figure 6.25 The displacement in y-direction along $x = 0$ at initial and final step.

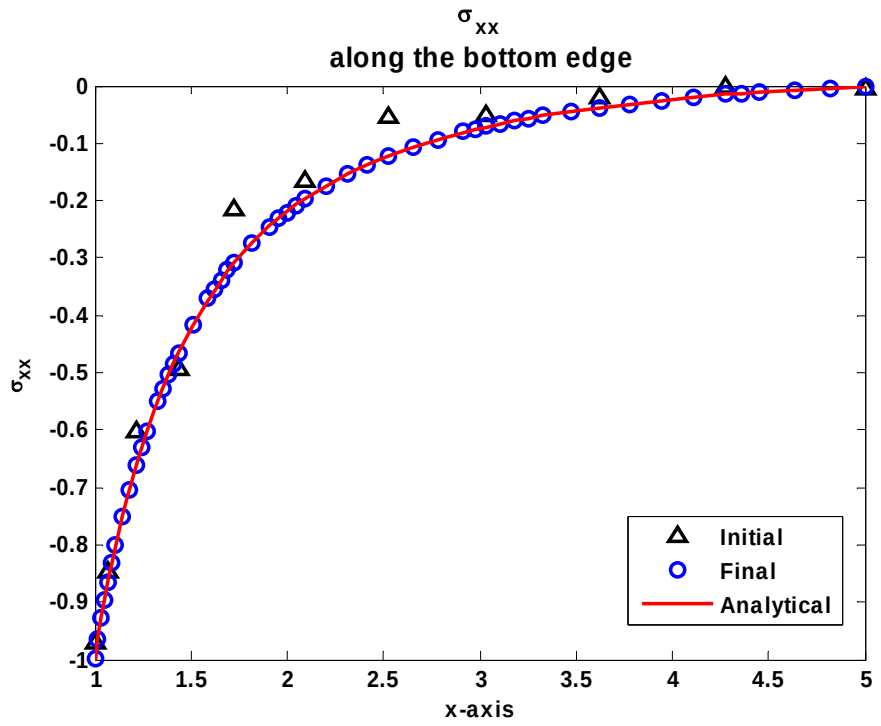

Figure 6.26 The normal stress σ_{xx} along $x = 0$ at initial and final step.

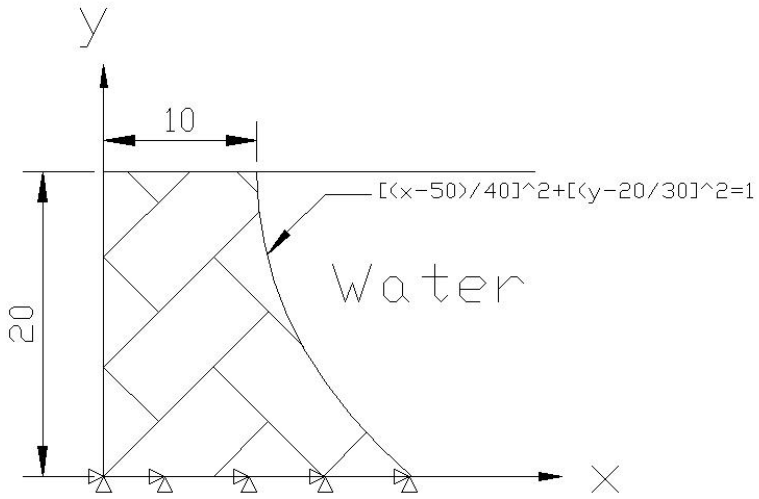

Figure 6.27 The model of the reservoir full filled with water.

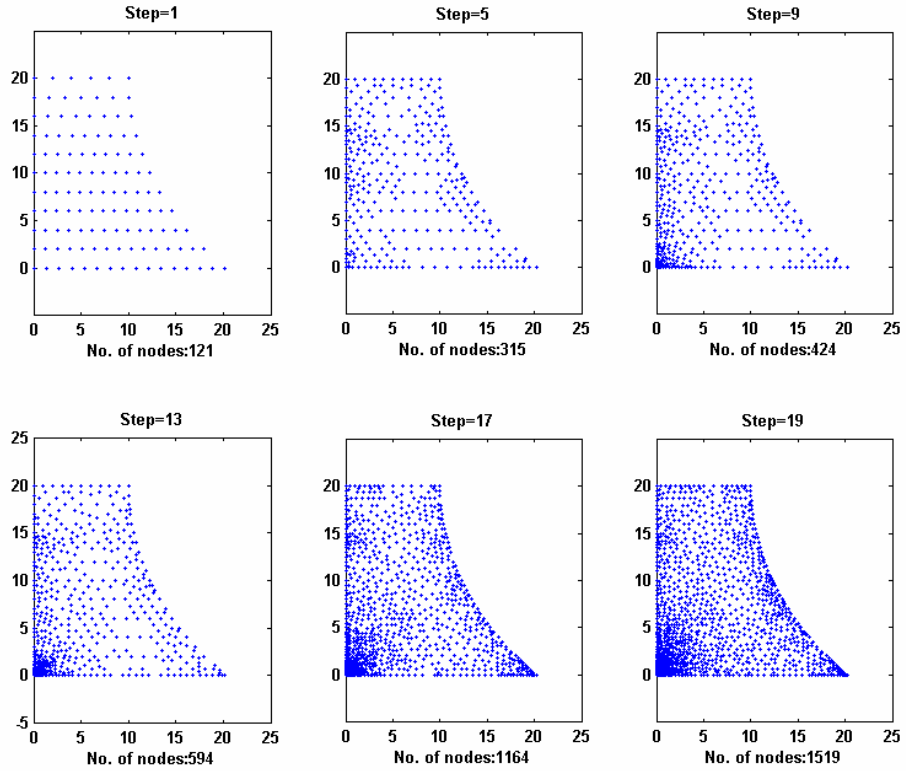

Figure 6.28 The nodal distribution of the model of reservoir during adaptation.

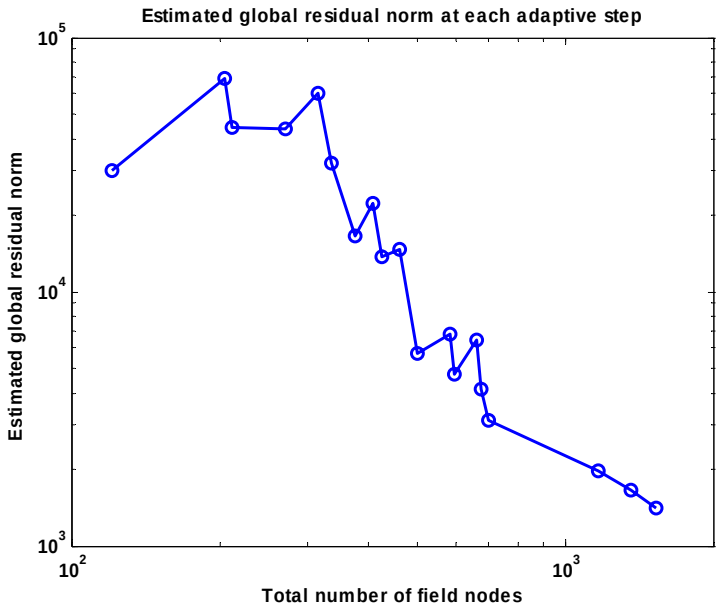

Figure 6.29 The estimated global residual norm at each adaptive step.

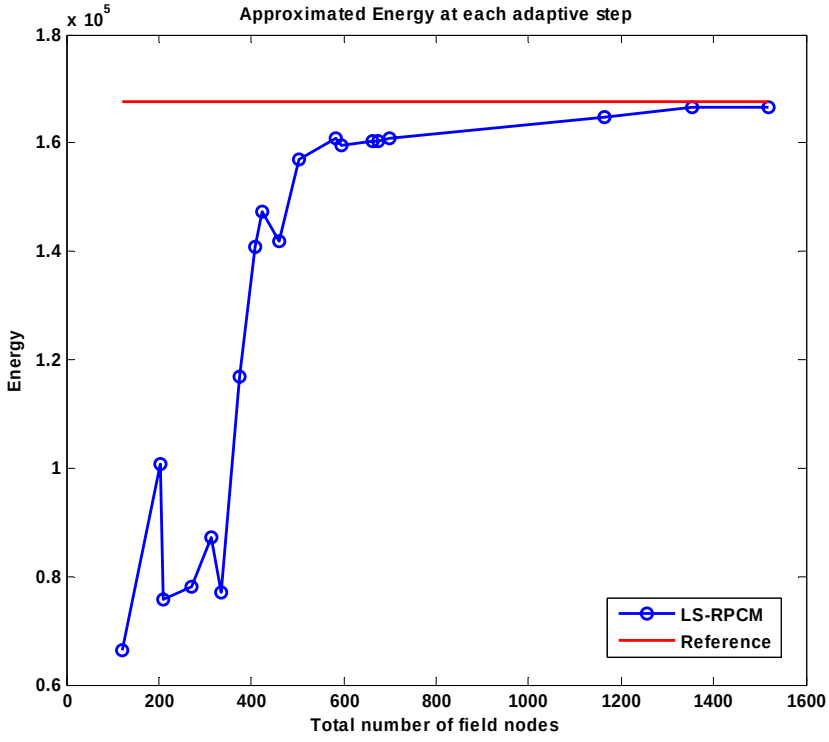

Figure 6.30 The approximated energy at each adaptive step.

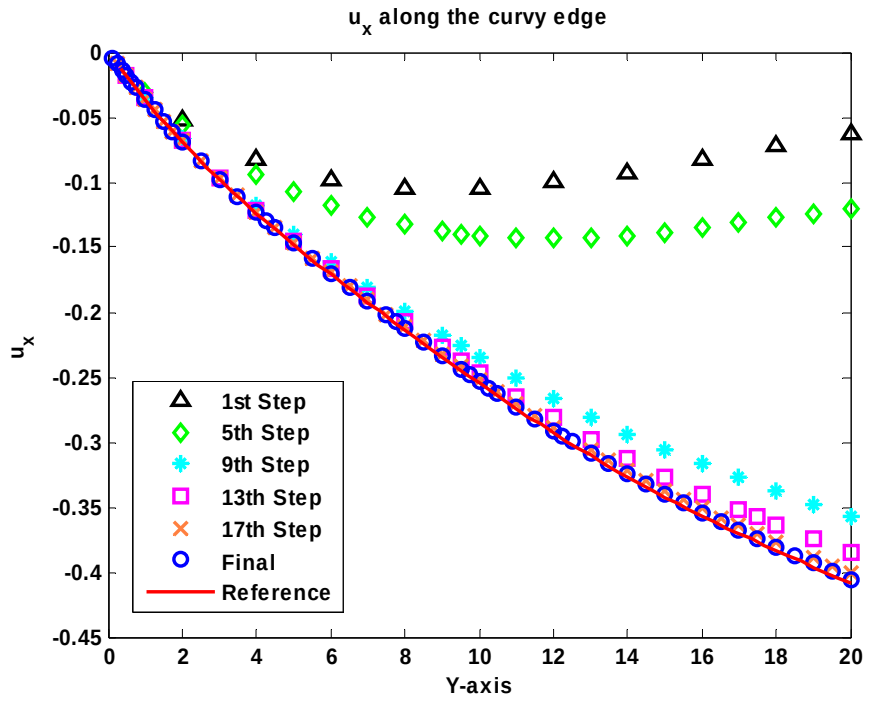

(a)

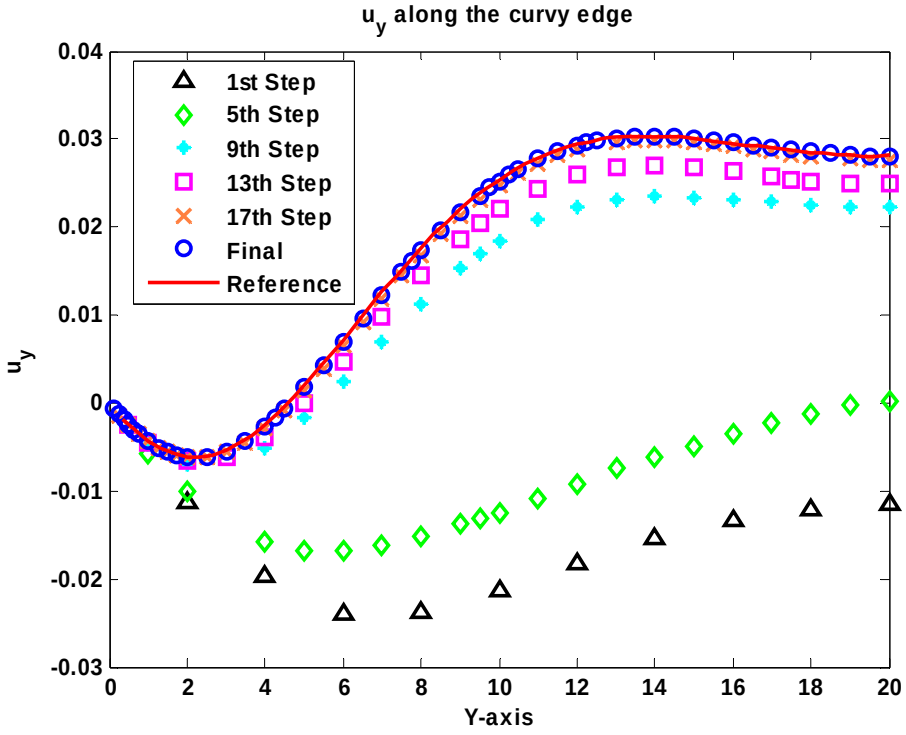

(b)

Figure 6.31 The displacements (a) u_x and (b) u_y along the curvy edge.

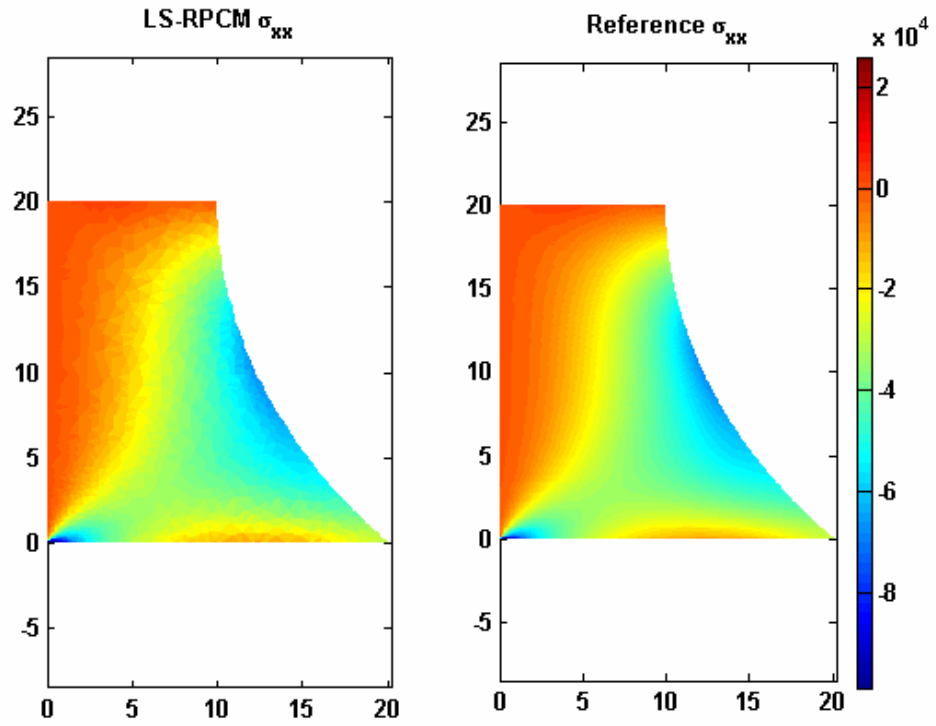

Figure 6.32 Contour plot of normal stress σ_{xx} at final step.

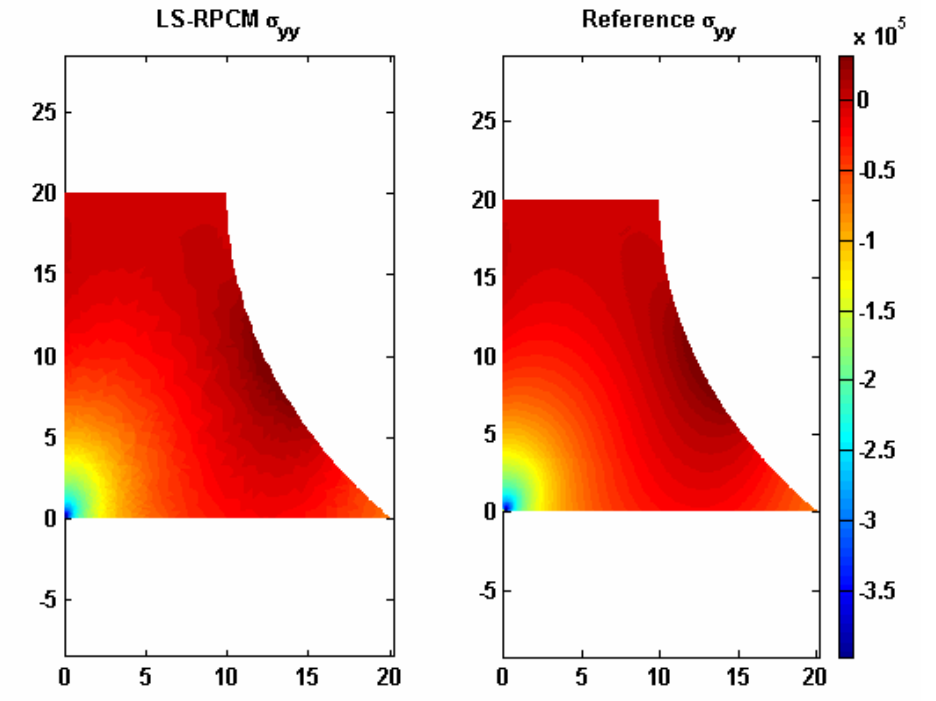

Figure 6.33 Contour plot of normal stress σ_{yy} at final step.

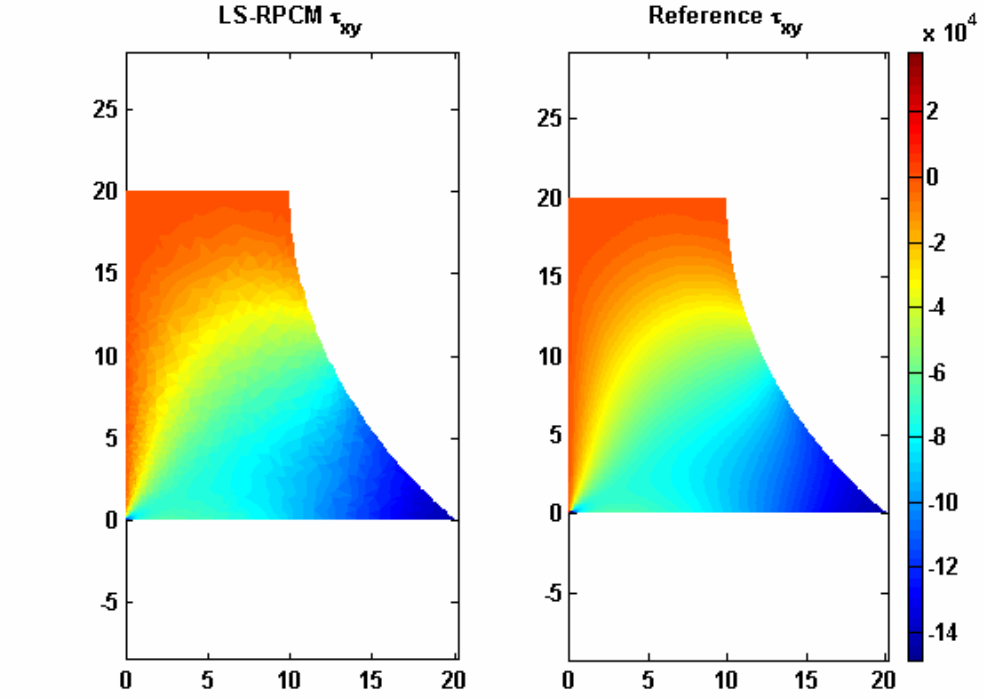

Figure 6.34 Contour plot of shear stress τ_{xy} at final step.

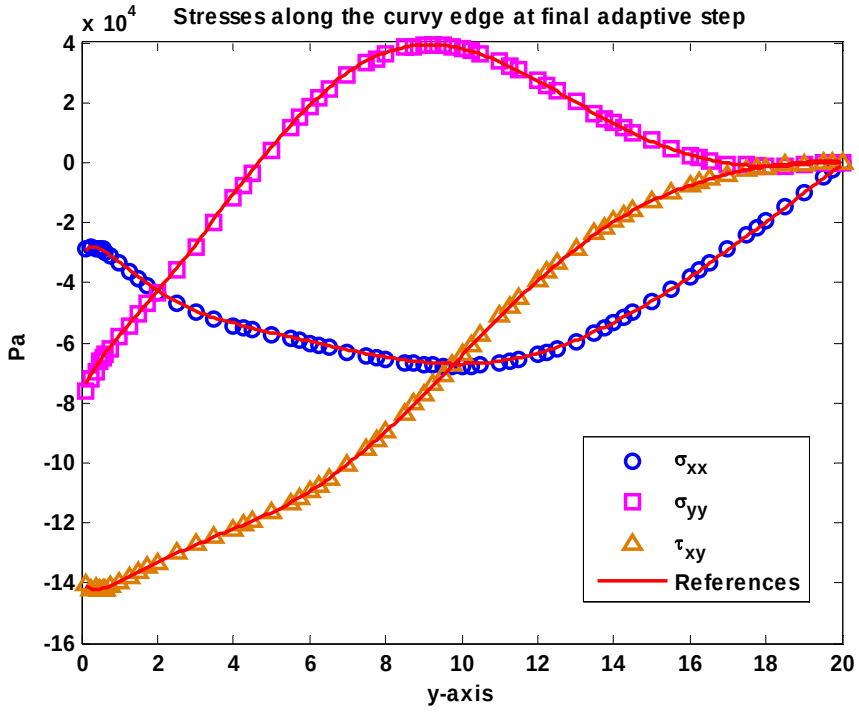

Figure 6.35 Stresses along the curvy edge at the final adaptive step.

Chapter 7

A Regularized Least-Square Radial Point Collocation Method (RLS-RPCM)

7.1 Introduction

To stabilize the solution of radial point collocation method (RPCM), a new stabilization procedure, regularized least-squares procedure, is employed to stabilize the solution of the RPCM in this chapter [67]. Regularization technique that commonly used for stabilizing the solution of ill-posed inverse problem [47] is now employed in the forward problem for restoring the stability of the RPCM solution. A new regularized least-squares radial point collocation method (RLS-RPCP) [67] is introduced in this chapter. Since the stability is restored, the attractive features of the strong-form meshfree method can then be utilized to facilitate an easier implementation of adaptive analysis.

With all these key ingredients of techniques: stabilization, error estimator and nodal refinement, the RLS-RPCM can perform adaptive analysis effectively to obtain solutions with better accuracy efficiently and automatically. In this work, RLS-RPCM not only is a stable strong-form meshfree method but also regarded as a truly mesh free

method as: (1) no mesh is needed for constructing shape functions, and (2) no background mesh is needed in the present formulation. Hence the formulation procedure is simple and straight forward, integration is not required in the formulation procedure which makes it a good candidate for adaptive analysis.

7.2 Regularization Procedure

Regularization technique is a very common technique used for stabilizing the solutions of the ill-posed inverse problems [47]. In this work, instead of using the regularization technique for inverse problems, this technique is employed to stabilize the solutions of the RPCM for the forward problems. In the regularization procedure, Tikhonov regularization technique [47,89] is adopted. Regularization matrix and vector are formed by making use of the governing system equations and boundary conditions as a priori information. The detailed regularization procedure is given as follows.

7.2.1 Regularization Equations

To form the regularization matrix and vector, priori information is required. Consider a problem governed by a set of PDEs as given in Eq. (4.1) to Eq. (4.3), the PDEs can be used as a set of regularization equations to construct the regularization matrix and vector. These regularization equations can be collocated at the regularization points respectively as shown in **Figure 7.1**. Therefore, the following equations can be obtain:

$$L(u_r) = f_r, \quad \text{in } \Omega, \tag{7.1}$$

with Neumann boundary conditions

$$B(u_r) = g_r, \quad \text{on } \Gamma_t, \tag{7.2}$$

and Dirichlet boundary conditions

$$u_r = \bar{u}_r, \text{ on } \quad \Gamma_u, \tag{7.3}$$

where subscript "*r*" denotes the regularization point.

The regularization points in the internal problem domain are the same as the interior field nodes. On the other hand, regularization points along the boundaries are allocated in between the boundary nodes as shown in **Figure 7.1**.

After collocating the regularization equations at their respective regularization points using RPIM approximation, a set of resultant algebraic equations can be formed and expressed as the following matrix form

$$\mathbf{K}_r\mathbf{U} = \mathbf{F}_r, \tag{7.4}$$

where $\mathbf{K}_r$ is the regularization matrix and $\mathbf{F}_r$ is the regularization vector. Note that the total number of algebraic equations is same as the total number of the unknown nodal values in the problem domain.

7.2.2 Regularization Least-square Formulation

Firstly, a functional Π is defined as follows [89],

$$\Pi = \{\mathbf{KU}-\mathbf{F}\}^T \{\mathbf{KU}-\mathbf{F}\} + \alpha_r \{\mathbf{K}_r\mathbf{U}-\mathbf{F}_r\}^T \{\mathbf{K}_r\mathbf{U}-\mathbf{F}_r\}, \tag{7.5}$$

where α_r is the regularization factor which determine the degree of regularization. The first term of Eq. (7.5) is the L_2 norm of the residual of governing equations, and the second term is the L_2 norm of the residual of regularization equations. Hence, functional Π is the total sum of the both residuals in the system.

Seek for the minimal Π with respect to the unknown vector $\mathbf{U}$, the following equation can be obtained,

$$\frac{\partial \Pi}{\partial \mathbf{U}} = 2\mathbf{K}^T \{\mathbf{KU}-\mathbf{F}\} + 2\alpha_r \mathbf{K}_r{}^T \{\mathbf{K}_r\mathbf{U}-\mathbf{F}_r\} = 0. \tag{7.6}$$

The above equation can be rearranged and leads to the following equation,

$$\left[\mathbf{K}^T\mathbf{K} + \alpha_r \mathbf{K}_r{}^T\mathbf{K}_r\right]\mathbf{U} = \mathbf{K}^T\mathbf{F} + \alpha_r \mathbf{K}_r{}^T\mathbf{F}_r$$

or

$$\hat{\mathbf{K}}\mathbf{U} = \hat{\mathbf{F}} \tag{7.7}$$

where $\hat{\mathbf{K}}$ is the regularized coefficient matrix and $\hat{\mathbf{F}}$ is the regularized force vector.

The vector of unknown nodal values can be solved as

$$\mathbf{U} = \hat{\mathbf{K}}^{-1}\hat{\mathbf{F}}, \tag{7.8}$$

if $\hat{\mathbf{K}}$ is invertible and well-conditioned.

7.2.3 Determination of Regularization Factor

From Eq. (7.7) one can notice that the regularization factor α_r directly affects the regularized coefficient matrix and force vector. The degree of regularization solely depends on the values of regularization factor, hence the determination of an appropriate regularization factor is very crucial. The value of regularization factor, α_r, should be positive and ranged from zero to infinity. When $\alpha_r = 0$, the effect of regularization is vanished, RLS-RPCM is reduced to the original RPCM. If α_r is equal to infinity, the effect of regularization is also vanished as the solution is solely based on the Eq. (4.7). Without regularization effect takes part, both solutions can not be stable. The appropriate α_r should provide a minimum residual for both terms in Eq. (7.5) [30,49].

From my previous work [49], only the governing equation, Eq. (4.1), is used for constructing the regularization matrix for the regularization points along the boundary only. With such regularization scheme, L-curve approach [30] was required to determine an appropriate regularization factor. L-curve is constructed by plotting the residual norm of discretized regularization equations, $\|\mathbf{RU} - \mathbf{T}\|$, against residual norm of discretized original equations, $\|\mathbf{KU} - \mathbf{F}\|$ at different regularization factor value,. In Hanse's paper [30], the procedure of constructing L-curve is given. The idea of plotting L-curve is to determine a regularization factor that gives both residual norms at an optimal small value. The determination process could be tedious and an additional computational cost was incurred. In the later work, other regularization schemes based

on different regularization equations are proposed [50,52].

In this chapter, due to the special regularization equations and regularization points used in the present scheme, the determination of regularization factor can be avoided [67]. As one knows, the vector of unknown nodal values $\mathbf{U}$ can actually be solved either by Eq. (4.7) or Eq. (7.4), however, none of the solutions is stable. By solving the same status problem with two different sets of discretized equations, the regularization procedure provides a compromise solution to satisfy both sets of system equations with minimum residual. Hence, $\alpha_r = 1$ is a logical choice to be used in this formulation.

7.3 Numerical Examples

To further extend the RLS-RPCM to adaptive analysis, a novel residual based error estimator is first introduced in this work. By determining the residual of the strong-form governing equation, the residual is able to provide a very reliable and effective error indicator to reflect the quality of the local approximation and the global accuracy of the solution.

As mentioned many times in this thesis, the RPCM is a truly meshfree method, node insertions can be easily implemented without worry about the nodal connectivity. Simple nodal *h*-refinement scheme based on the Delaunay diagram is employed in this work. In contrast to the conventional *h*-refinement scheme for adaptive FEM in which the element is enriched, the additional nodes can be simply just inserted into the domain in this *h*-refinement scheme.

For the examples of adaptive analysis, adaptive strategy given in Chapter 3 is adopted. In the refinement procedure, the Delaunay diagram is used to locate the position for the additional nodes as shown in **Figure 3.24**. If the predefined refinement criterion is met at the node, additional nodes will be inserted at the center of the Delaunay cell. The adaptive process will be carried on until global residual norm meet the stopping criterion.

In the given numerical examples in this chapter, polynomial with completed second order, $m = 6$, is adopted in the RPIM approximation and shape parameters of MQ-RBF are known as $\alpha_c = 3.0$ and. $q = 1.03$.

7.3.1 Example 1: Cantilever Beam

The first example is a benchmark solid mechanics problem. A cantilever beam with unit thickness subjected to a parabolic shear stress at the right end as shown in **Figure 4.11** is studied and considered as a plane stress problem. This example is used to demonstrate the instability problem encountered by the RPCM and shows the solution of the RPCM can be effectively restored by the proposed regularization procedure. The material properties and geometrics are given as: Young's modulus $E = 3 \times 10^7$, Poisson's ratio $\upsilon = 0.3$, length of cantilever $L = 48.0m$ and the height $H = 12.0m$. The loading is known as $\tau_{xy} = -\frac{P}{2I}\left(H^2/4 - y^2\right)$, where *I* is moment of inertial of the cross section of cantilever and $P = 1000N$. The equilibrium equation and boundary conditions that have to be satisfied in the problem domain are given in Eq. (4.19) to Eq. (4.21). The analytical solution of this problem can be found in Ref. [90].

In this problem, the Dirichlet boundary conditions are imposed on the left edge and Neumann boundary conditions are imposed on the rest of the edges of the cantilever. Two very similar nodal distributions shown in **Figure 7.2** are used for computing the numerical solution. The RPCM solutions for these two similar models are totally different as shown in **Figure 7.2**. This example evidently reveals the inherited instability problem in the conventional collocation method such as RPCM. Therefore, an effective stabilization measure is a prerequisite for RPCM before it can be used for the adaptive analysis. The results for both models using the regularized least-squares RPCM (RLS-RPCM) are shown in **Figure 7.2**. The solutions obtained by the RLS-RPCM with two models are good and close to each other. The deflection of the cantilever obtained by RLS-RPCM is also much closer to analytical solution as compared to RPCM.

To provide an overview of the computational cost and the accuracy of RLS-RPCM, the solution of RLS-RPCM is compared with FEM and RPCM. Four sets of regularly distributed nodes are used in this example, which are 25×7, 49×13 and 97×25 nodes. Linear triangular mesh is used in FEM and 9 nodes are used for RPCM and RLS-RPCM to construct their shape functions. The convergence rate and the computational time of three different numerical methods are shown in the **Figure 7.3** and **Figure 7.4**. The convergence rate of FEM and RLS-RPCM is 1.95 and 2.39 respectively. One can found that the accuracy of RLS-RPCM is comparable with FEM. The accuracy of the solutions obtained by RPCM for displacements is lower than other methods. However, the computational time of RLS-RPCM is slightly higher

thanRPCM.

Although RLS-RPCM requires a little more computational time than FEM, RLS-RPCM possesses many attractive features to facilitate an easier implementation of adaptive analysis. No special technique is required in the refinement procedure and no remeshing is required at each adaptive step. A truly meshfree method not only avoid the mesh related problem but also facilitate a simple adaptive scheme. Without the stabilization procedure, it is impossible to use RPCM in adaptive analysis.

7.3.2 Example 2: Hollow Cylinder with Internal Pressure

The second example is also a benchmark solid mechanics problem. A thick wall cylinder subjected to a constant internal pressure is studied. The material properties and geometries are given as: internal radius $a = 1$, external radius $b = 5$, Young's modulus $E = 1 \times 10^7$, Poisson's ratio $\upsilon = 0.3$ and internal pressure $P = 1MPa$. The analytical solution of this problem is well-known and can be found in Ref. [16].

As this problem is symmetric, only quarter of the problem is modelled as shown in **Figure 7.5**. Symmetric boundary conditions are imposed along the left and bottom edges. In this example, only eighteen local nodes are used to construct the shape functions. The local refinement coefficient and the global residual tolerance are predefined as $\kappa_l = 0.05$ and $\kappa_g = 0.05$ respectively. The adaptive analysis starts with 121 regularly distributed nodes in the domain and stops at the 4^{th} step with 1716 nodes irregularly distributed in domain. Nodal distribution at each adaptive step is plotted in the **Figure 7.6**. As the stresses are more concentrated close to the internal

circumference, more nodes are found to be inserted in this region. From **Figure 7.7**, one can observe that the estimated global residual norm is gradually reduced in the adaptation. The error norm of displacements has been greatly reduced from 7.82% to 0.62% as shown in **Figure 7.8**. Furthermore, the error norm of stresses shown in the **Figure 7.9** has also been reduced drastically from 14.32% to 0.57%.

The displacements and stresses along the left edge are plotted and compared with analytical solution as shown in **Figure 7.11** and **Figure 7.12**. As problem domain is only represented by 121 nodes, solutions with high accuracy are not possible to be obtained as the exact solution is not a smooth function over the entired domain. These plots have shown that the adaptive scheme has effectively refined the critical region based on the error estimator and hence the solutions are improved. The numerical solutions of the displacements and stresses at the final steps are in very good agreement with the analytical solutions.

7.3.3 Example 3: Bridge with Uniform Loading on the Top

In this example, an adaptive analysis for a bridge with irregular geometry is studied. A half model of the bridge is analysed. Due to symmetric, and a plane strain problem is considered. The top of the bridge is subjected to a constant pressure $P = 1000N/m^2$. The dimension of the bridge is shown in **Figure 7.13** and the material properties are given as: Young's modulus $E = 4 \times 10^9$ and Poisson's ratio $\upsilon = 0.15$.

In the adaptive analysis, the local refinement coefficient is preset as $\kappa_l = 0.05$ and the global residual tolerant is predefined as $\kappa_g = 0.05$. The initial nodal

distribution first starts with 246 nodes in the problem domain and the adaptive process is terminated at the 7^{th} step with 1529 nodes as shown in **Figure 7.14**. Only eighteen local nodes are used for the local function approximation. From the nodal distribution given in **Figure 7.14**, the adaptive strategy is shown efficiently refining the region where stresses are concentrated.

The estimated global residual norm is gradually reduced at each adaptive step as given in the **Figure 7.15**. As no analytical solution is available in this case, reference solutions for displacements and stresses are obtained using ANSYS with very fine quadrilateral mesh as given in **Figure 7.16**. The displacements in *y* direction along the left edge and top edge of the bridge are plotted in **Figure 7.17** for justification purpose. The solutions obtained by RLS-RPCM are greatly improved from the initial step through the adaptation and lead to the solution of the final step which is in very good agreement with the references solutions. Besides the displacements, the normal stresses σ_{xx} and σ_{yy} along the left edge are also plotted in **Figure 7.18**. The stresses obtained by RLS-RPCM are also in very good agreement with the reference solutions. Through the proposed adaptive scheme, one can see that the accuracy of the solutions for displacements and stresses have been gradually improved in **Figure 7.17** and **Figure 7.18**.

7.3.4 Example 4: Poisson Problem with High Gradient Solution

In this example, a well-known Poisson problem is studied. An adaptive analysis is conducted for Poisson problem which solution has sharp peak. The Poisson

equation is defined as

$$\nabla^2 u = \left[-400 + (200x-100)^2 + (200y-100)^2\right] \cdot e^{-100\left(x-\frac{1}{2}\right)^2 - 100\left(y-\frac{1}{2}\right)^2}, \tag{7.9}$$

in domain of Ω: $[0,1]\times[0,1]$, with Neumann boundary conditions,

$$\frac{\partial u}{\partial n} = 0, \text{ along } \Gamma_t : x = 0 \text{ and } y = 0, \tag{7.10}$$

and with Dirichlet boundary conditions,

$$u = 0, \text{ along } \Gamma_t : x = 1 \text{ and } y = 1. \tag{6.11}$$

The analytical solution for this problem is known as

$$u = e^{-100\left(x-\frac{1}{2}\right)^2 - 100\left(y-\frac{1}{2}\right)^2}. \tag{7.12}$$

The plots for the exact solution of the field function u are given in the **Figure 7.19**, and the gradient of the field function, $\frac{\partial u}{\partial x}$, along $y = 0.5$ is also plotted in **Figure 7.20**. High gradient can be observed in the centre of the domain from these two figures.

In this case, local refinement coefficient and global residual tolerant are predefined as $\kappa_l = 0.05$ and $\kappa_g = 0.1$ respectively. The adaptive analysis first starts with 100 regularly distributed nodes and stops up at 7th step with 6962 nodes in the problem domain. Nodal distribution at first, 3rd, 5th and final adaptive steps is plotted in **Figure 7.21**. Due to the presence of sharp peak, most of the nodes are inserted at the high gradient region as shown in **Figure 7.22**. From **Figure 7.23**, one can observe that

the estimated global residual norm is reduced gradually. While estimated global residual norm is reduced in the adaptive process, the error norm of the field function is also gradually reduced from 22.88% to 1.90% as shown in **Figure 7.24**.

The approximated values of field function u along $y = 0.5$ at initial and final steps are plotted with analytical solution as shown in **Figure 7.25**. It is evidently showing the proposed adaptive scheme is effective to improve the accuracy of the solution for field function u. Similarly, the derivative of the approximated field function at initial and final steps is also plotted. It has shown that not only that the approximated field function but also the approximated field function derivatives are in very good agreement with analytical solutions in the **Figure 7.26**. The solutions of the approximated field function and its derivative are gradually improved through our adaptive scheme with RLS-RPCM.

7.3.5 Example 5: Poisson Problem with Multiple Peaks Solution

In this example, another Poisson problem which solution has multiple peaks is considered. The purpose of this example is to show the robustness of the simple error estimator for multi peaks solution in a problem domain. The Poisson equation is considered as follows:

$$\nabla^2 u = 2\pi^2 \left(\cos 2\pi x \sin^2 2\pi y + \cos 2\pi y \sin^2 2\pi x\right), \text{ in } \Omega: [-1,1] \times [-1,1], \qquad (7.13)$$

with Neumann boundary conditions

$$\frac{\partial u}{\partial n} = 0, \text{ along } \Gamma_t : x = 1; y = 1, \tag{7.14}$$

and with Dirichlet boundary conditions

$$u = 0, \text{ along } \Gamma_u : x = -1; y = -1. \tag{7.15}$$

The exact solution of field function u is known as

$$u = \sin^2 \pi x \sin^2 \pi y. \tag{7.16}$$

The three dimensional plot of the exact solution is plotted in **Figure 7.27**, four peaks can be observed.

In this example, ten local nodes are used for the local function approximation. The local refinement coefficient is predefined as $\kappa_l = 0.1$ and global residual tolerant value is predefined as $\kappa_g = 0.01$. The adaptive analysis begins with 100 regularly distributed nodes and ends at 12^{th} step with 10764 nodes. Nodal distribution at several steps during adaptation is plotted in **Figure 7.29**. As there are four peaks exist in the problem domain, one can observe four rings of dense nodal distributions appeared at the final step as shown in **Figure 7.30**.

From **Figure 7.31**, it can be noticed that the error norm of the field variable is drastically reduced from 324% to 0.62% in 12 steps. The nodal values u along $y = 0.5$ at first, 4^{th}, 8^{th} and final step are also plotted in the **Figure 7.32**. Apparently, the accuracy of the solution for u is greatly improved through the adaptive scheme. Not only the approximated field function is improved, solution of the approximated

derivative of the field function is also significantly improved as shown in **Figure 7.33**. Once again, the accuracy of RLS-RPCM solution has been shown effectively be improved by the proposed adaptive scheme.

7.4 Remarks

In this chapter, regularization technique which often be used for the ill-posed inversed problems is adopted to stabilise the solution of RPCM for forward problems. Through vast numerical examples, the regularization procedure has been demonstrated successfully stabilising the solution of RPCM for the forward problems. As stable and accurate solution can be obtained by RLS-RPCM, the features of meshfree strong-form methods can therefore be utilized to facilitate an easier implementation of adaptive analysis. The expensive computational cost of remeshing process can be avoided because RLS-RPCM is a truly mesh free method. Simple refinement scheme using Delaunay diagram can also be used without worry of nodal connectivity.

However, RLS-RPCM requires slightly higher computational cost compared to the RPCM. The small additional cost incurred by the regularization procedure is to acquire the crucial stability and accuracy in the solution. Nevertheless, this small amount of additional cost is usually insignificant in the adaptive analysis.

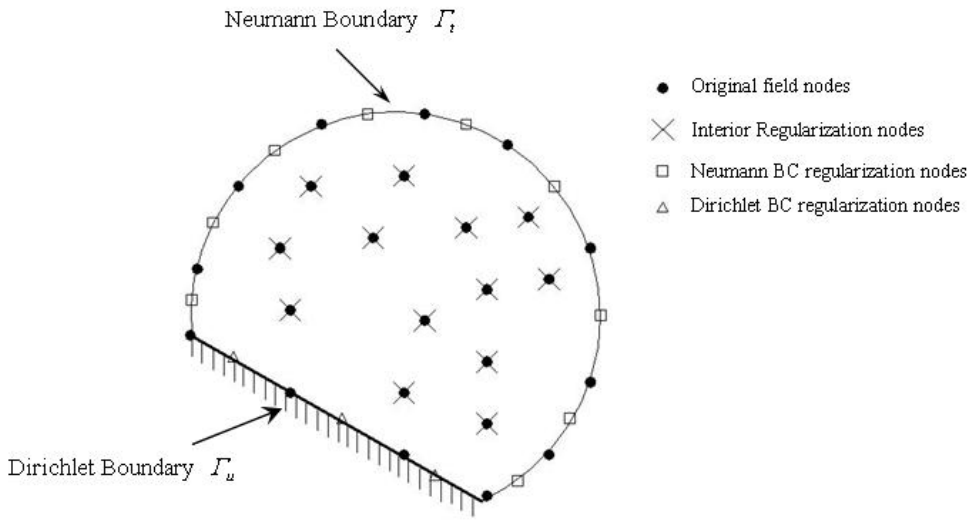

Figure 7.1 Regularization points scattered in the problem domain and on the boundaries

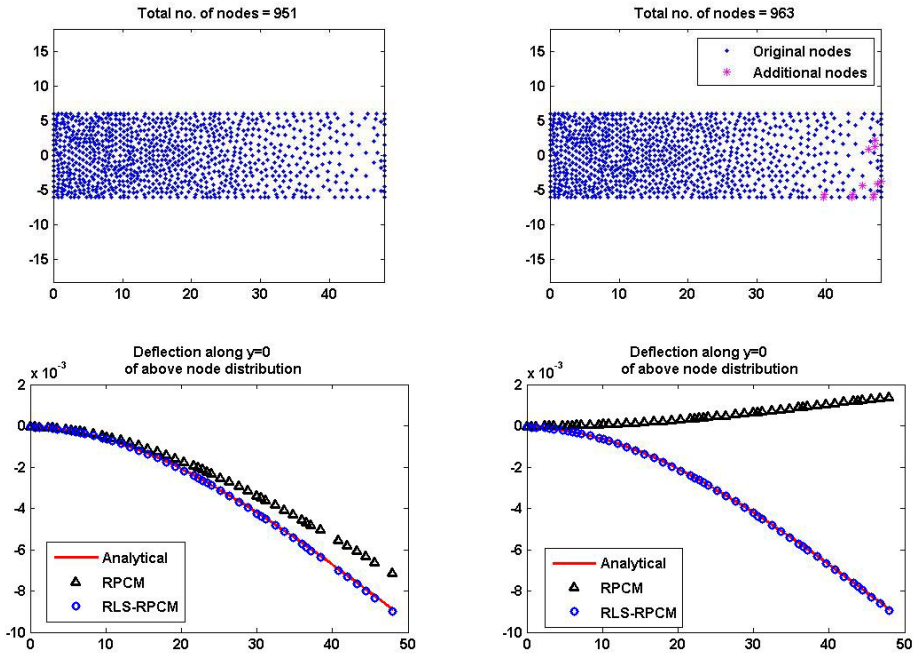

Figure 7.2 Deflection of the cantilever beam along $y = 0$ with two similar sets of nodal distribution.

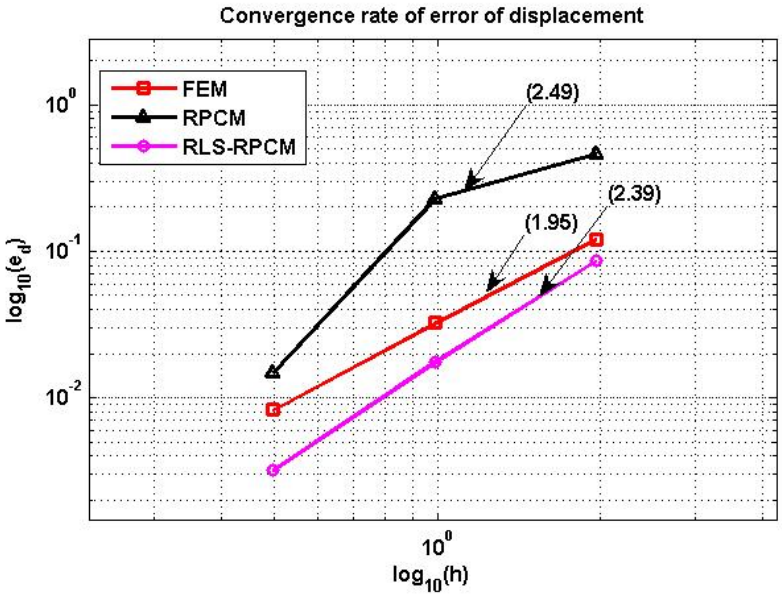

Figure 7.3 Comparison of convergence rate among the FEM, RPCM and RLS-RPCM.

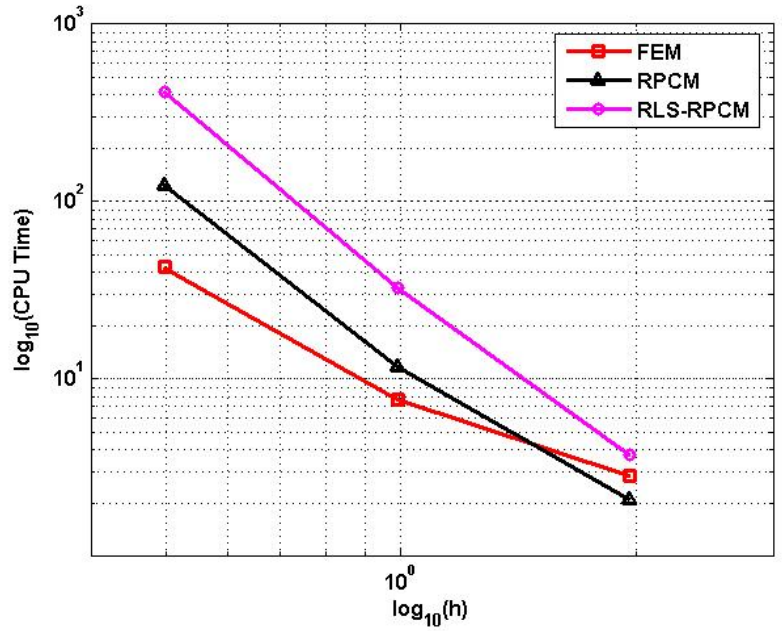

Figure 7.4 Comparison of computational time among the FEM, RPCM and RLS-RPCM.

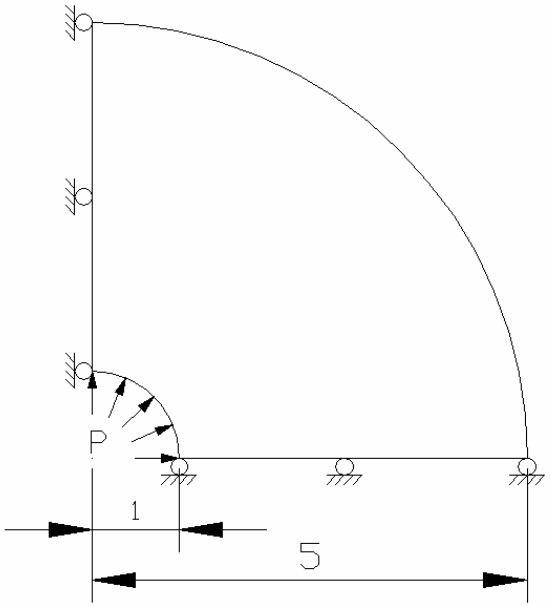

Figure 7.5 A quarter model of hollow cylinder with internal pressure.

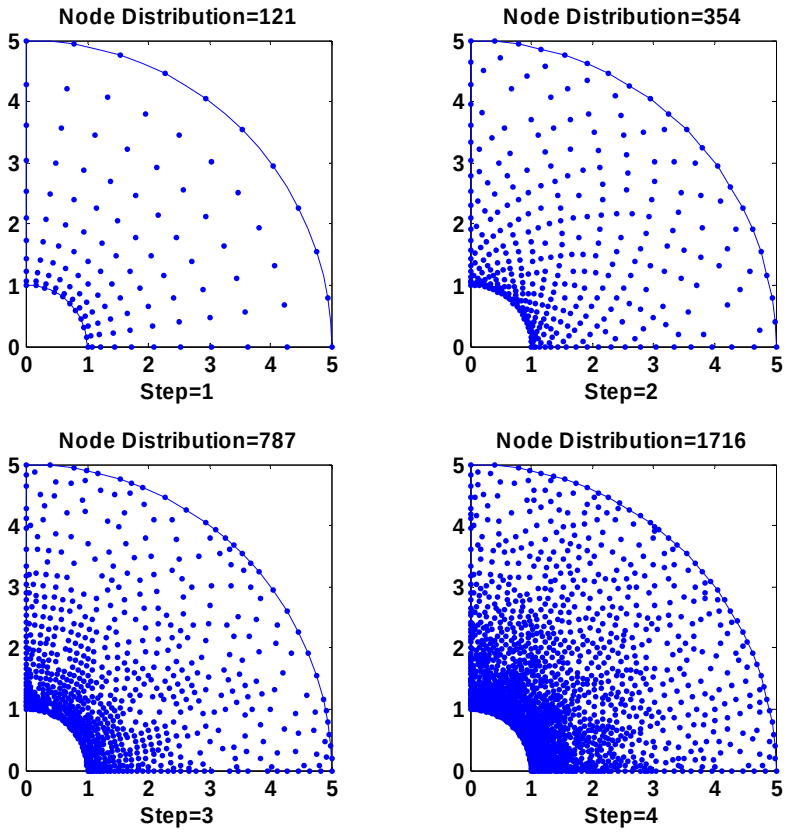

Figure 7.6 Nodal distributions at each adaptive step.

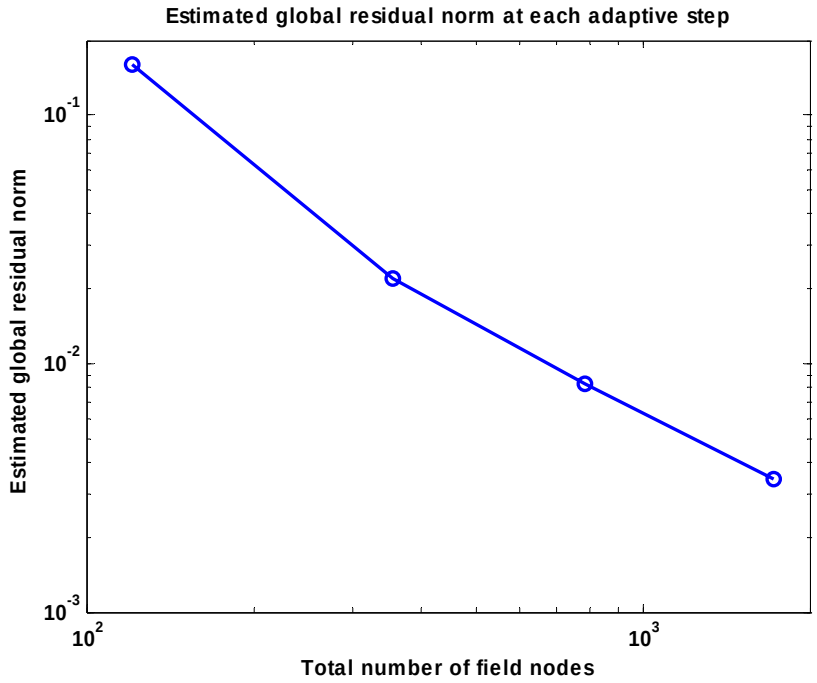

Figure 7.7 The estimated global residual norm at each adaptive step.

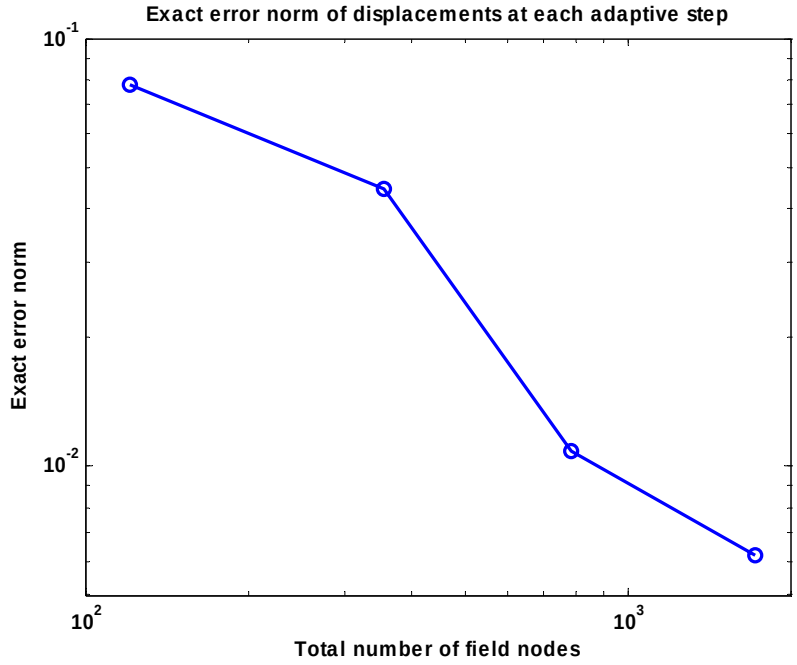

Figure 7.8 Exact error norm of displacements at each adaptive step.

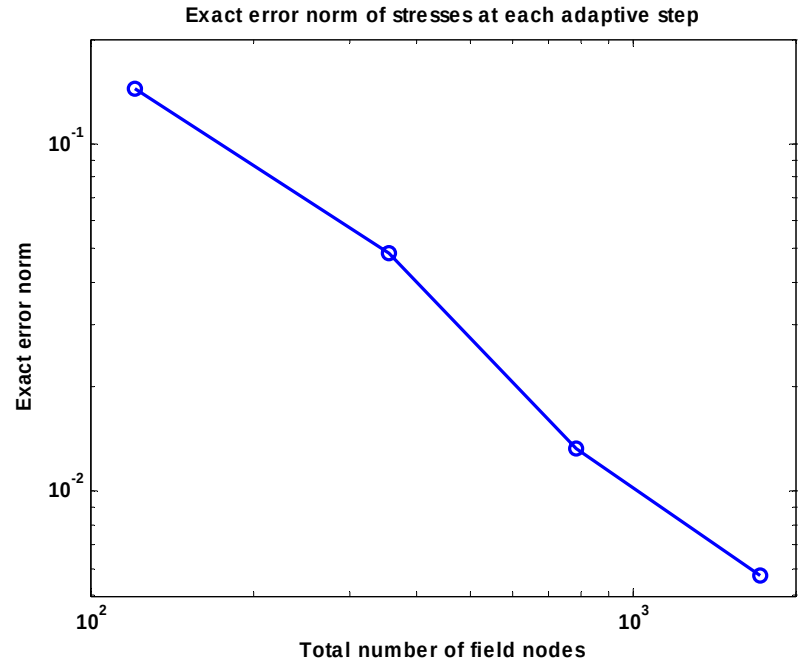

Figure 7.9 Exact error norm of stresses at each adaptive step

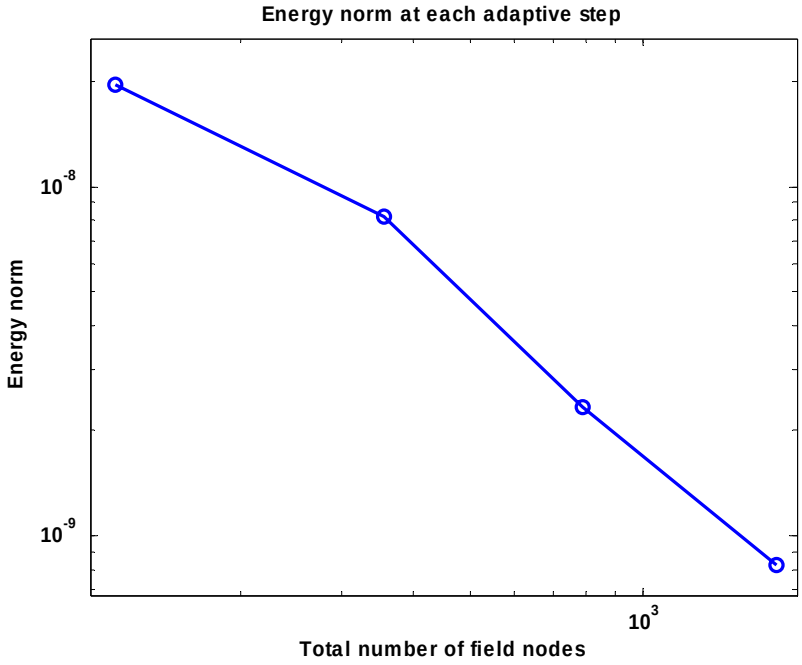

Figure 7.10 Energy norm at each adaptive step.

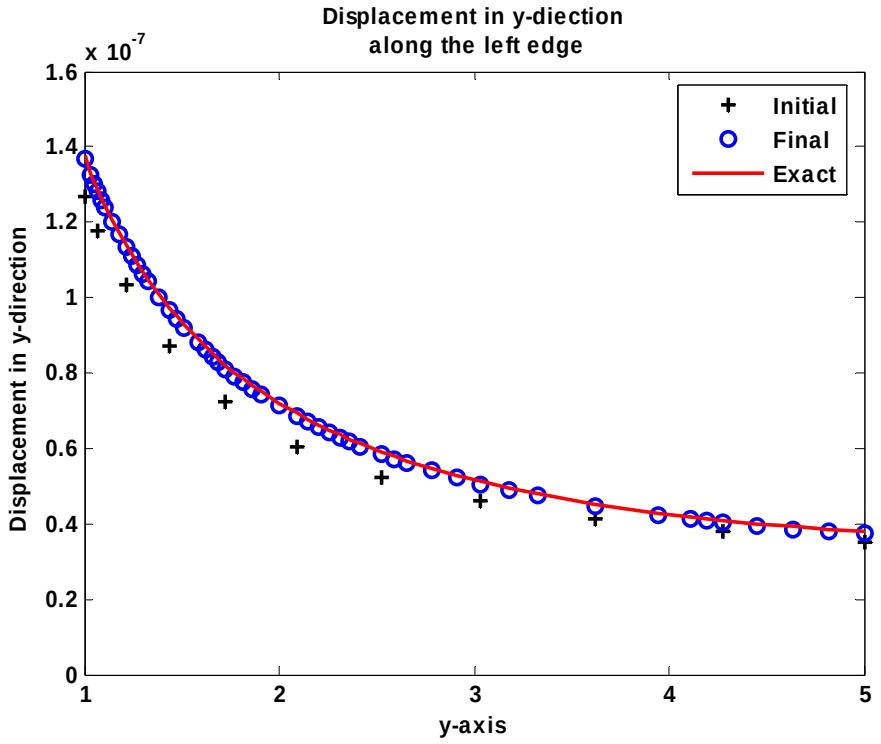

Figure 7.11 Displacements in y-direction along the left edge at initial and final steps.

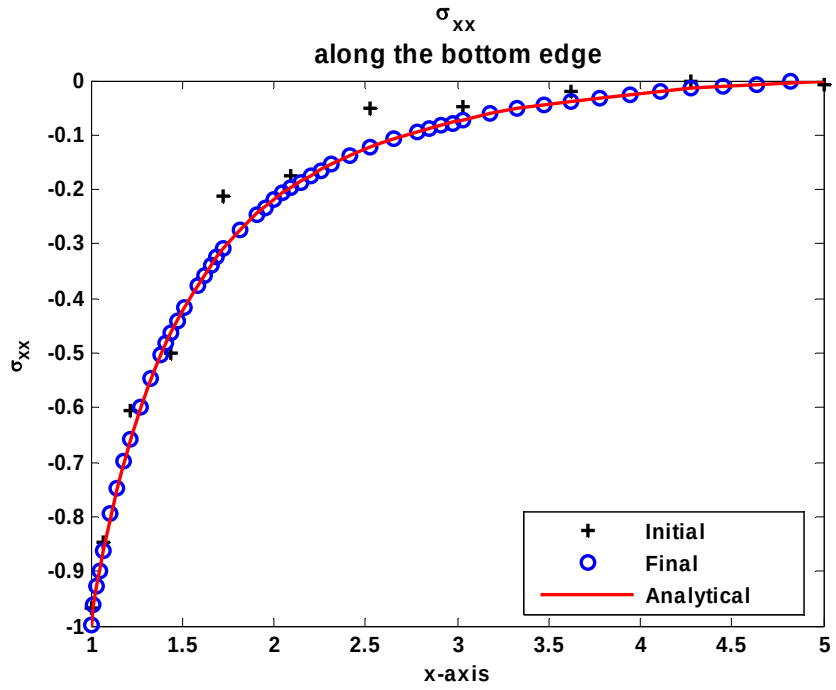

Figure 7.12 The normal stress σ_{xx} along the left edge at initial and final steps.

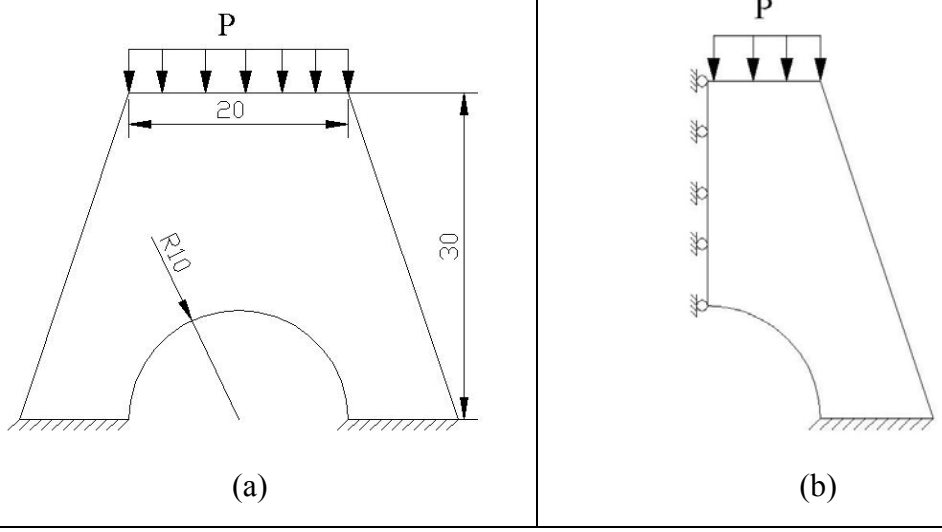

Figure 7.13 (a) A full model and (b) the a model of a bridge subjected to a constant pressure on top.

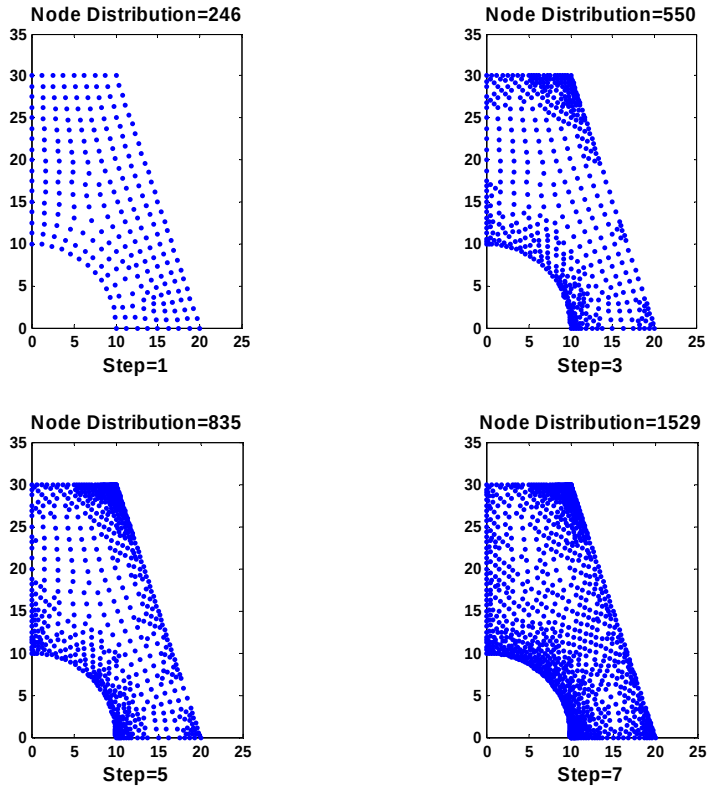

Figure 7.14 Nodal Distribution at 1st, 3rd, 5th and 7th steps in the adaptation for the bridge problem.

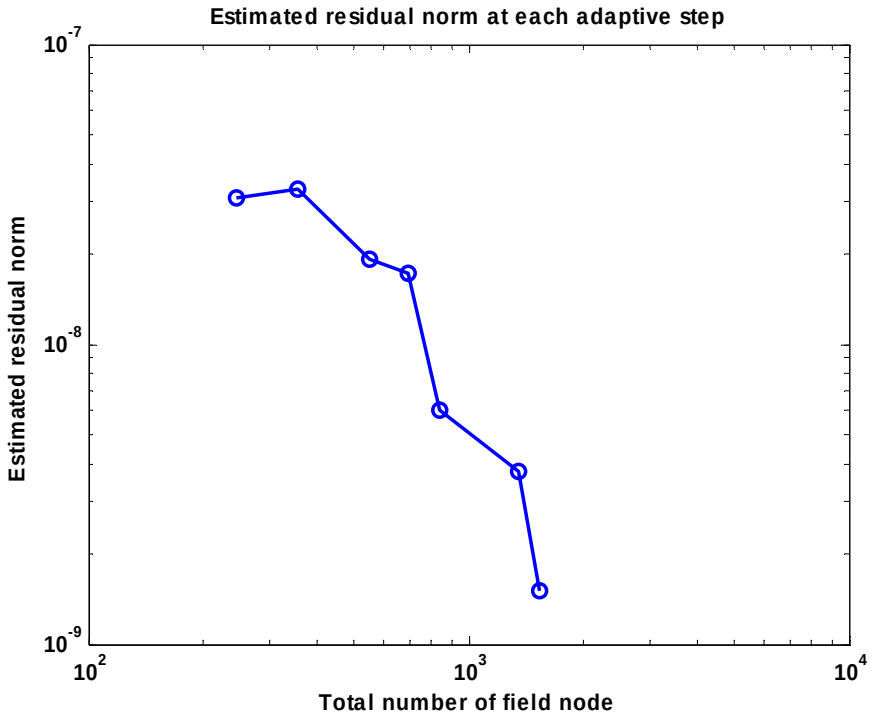

Figure 7.15 Estimated residual norm at each adaptive step for the bridge problem.

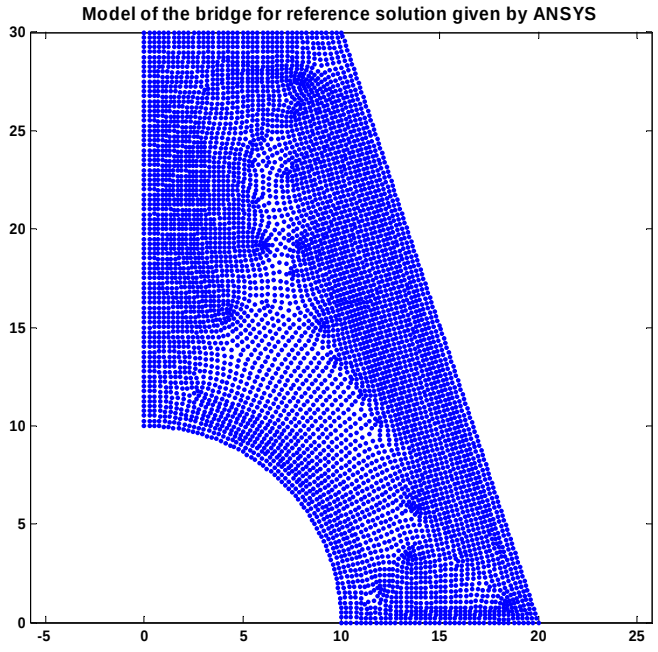

Figure 7.16 Model of the bridge used in ANSYS for reference solution.

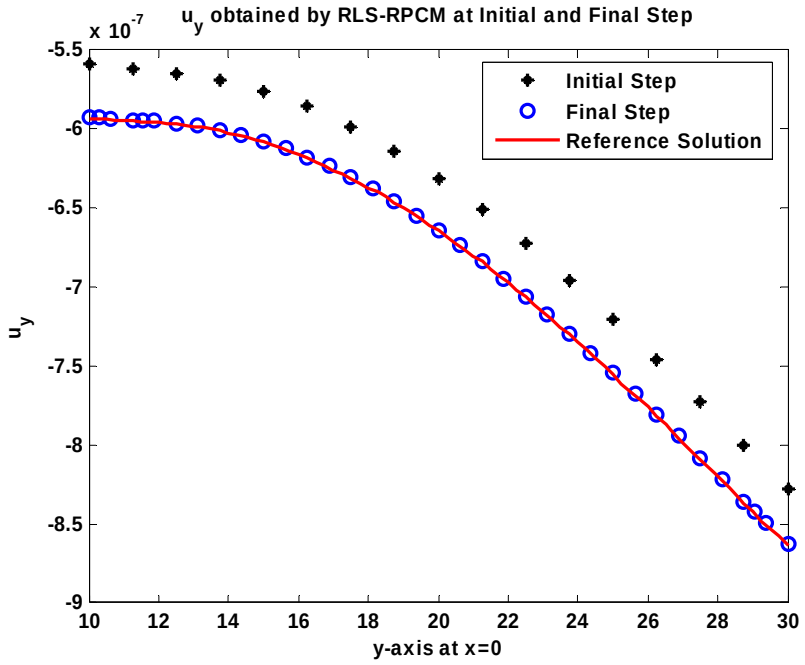

(a)

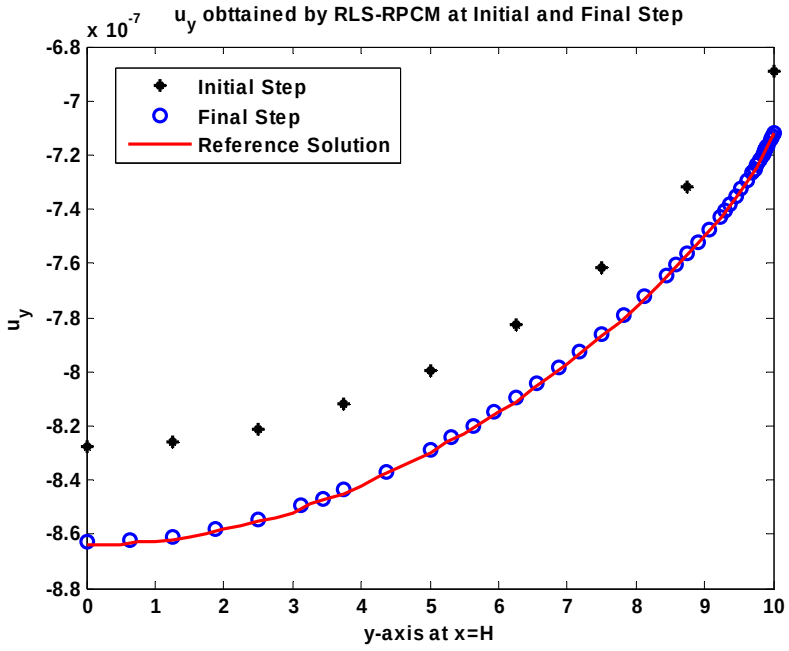

(b)

Figure 7.17 Displacement u_y obtained by RLS-RPCM (a) along the left edge and (b) on top of the bridge at initial and final steps.

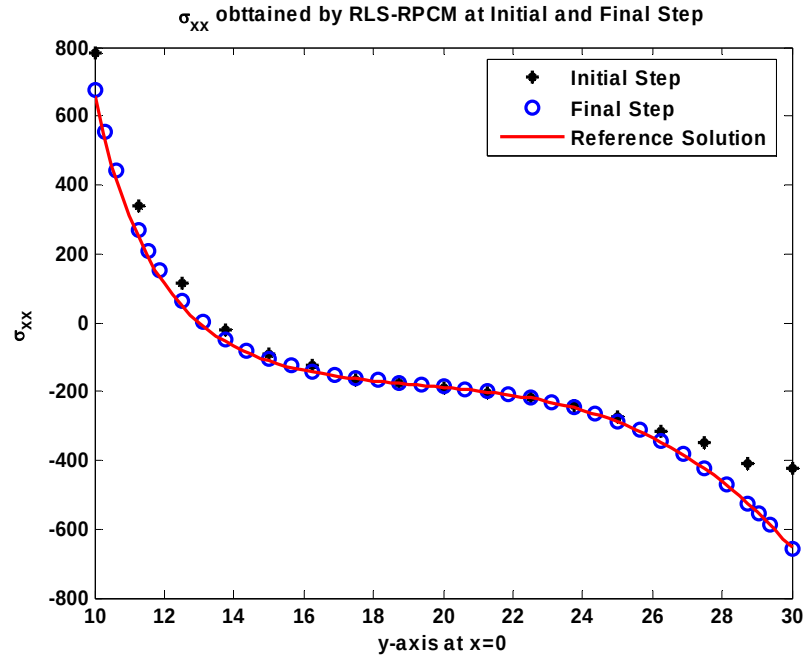

(a)

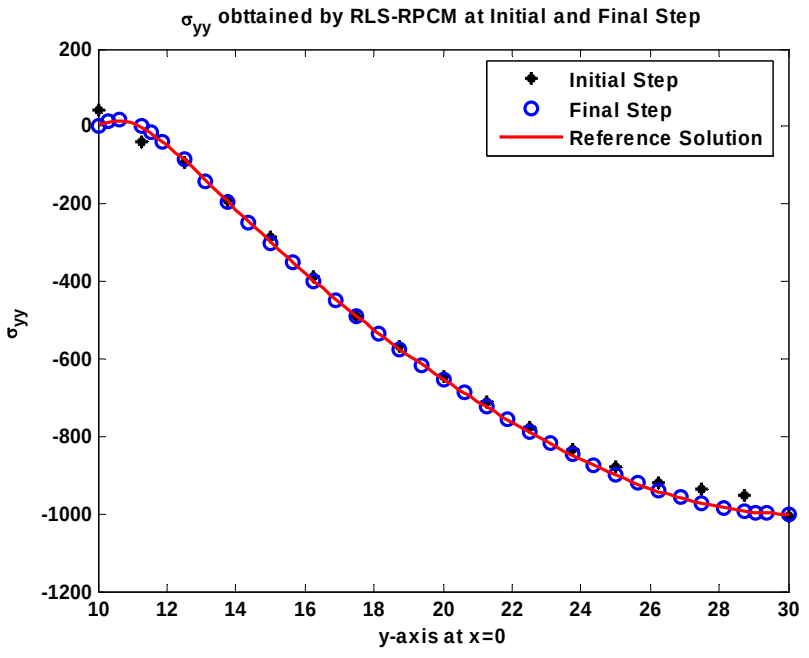

(b)

Figure 7.18 Normal stress (a) σ_{xx} and (b) σ_{yy} obtained by RLS-RPCM along the left edge at initial and final steps

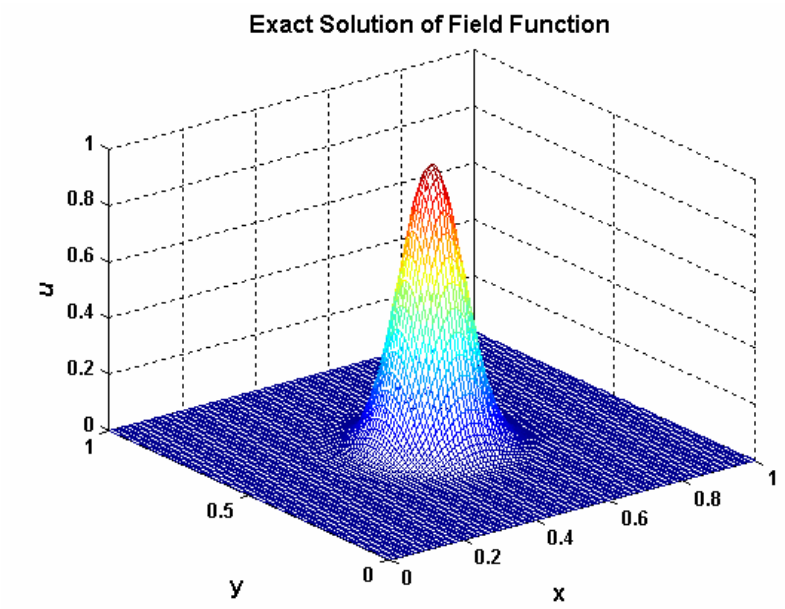

Figure 7.19 Solution of Poisson problem with high gradient.

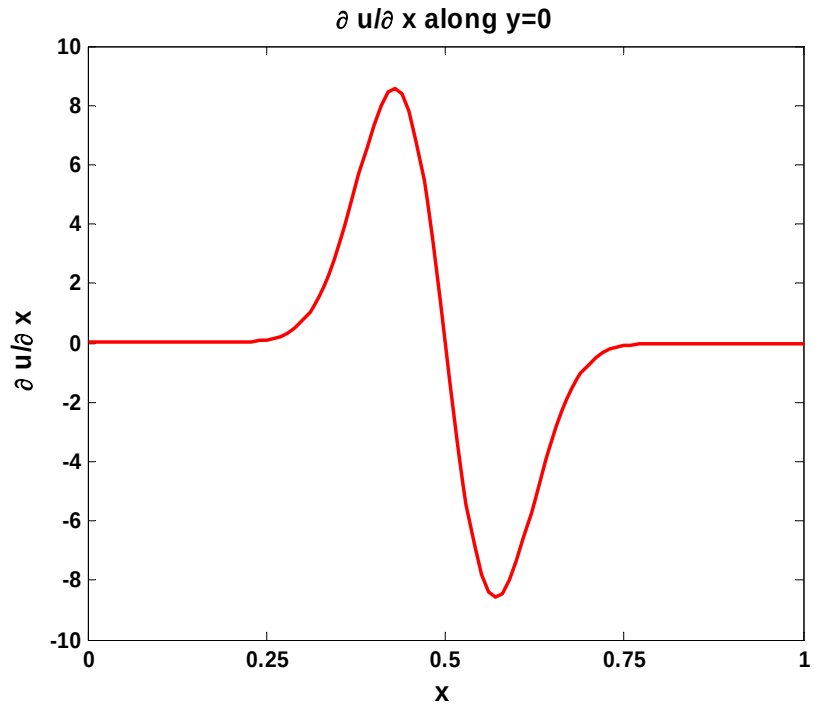

Figure 7.20 The gradient of the solution, $\frac{\partial u}{\partial x}$, along $y = 0$.

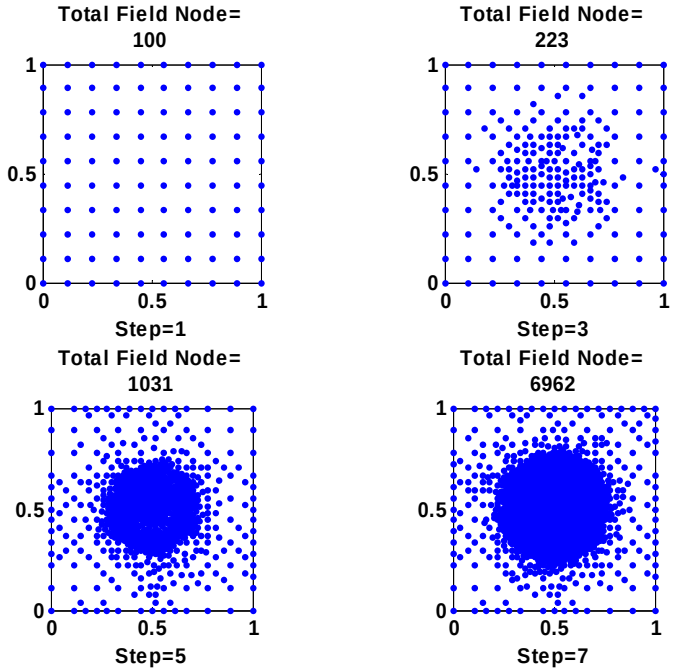

Figure 7.21 Nodal distribution at initial, 3rd, 5th, final steps.

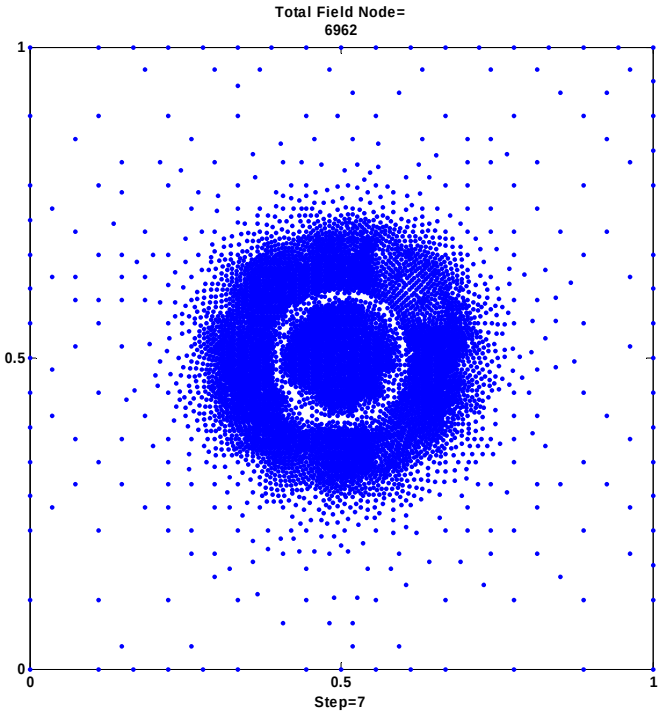

Figure 7.22 Enlarged view of the nodal distribution at final step.

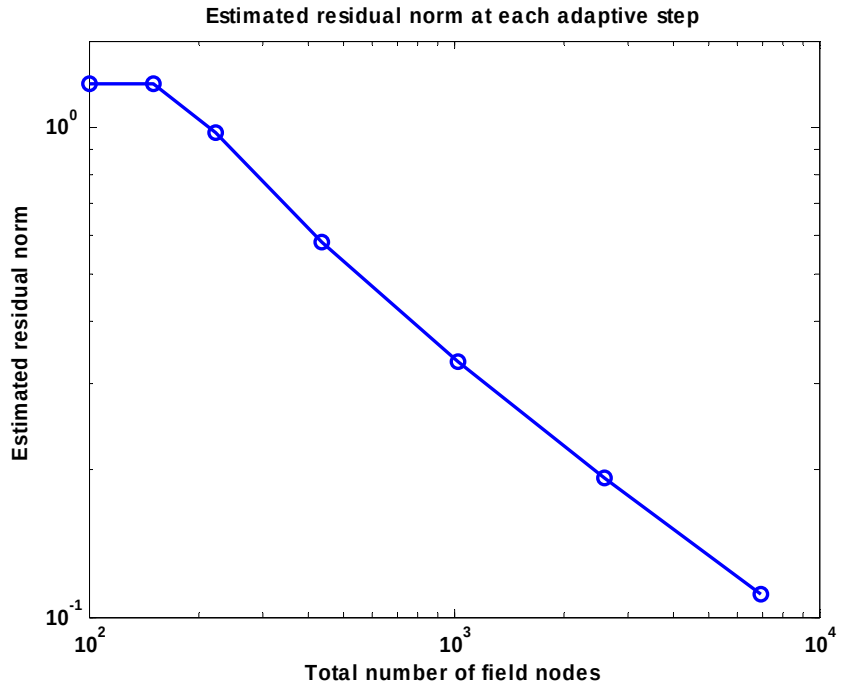

Figure 7.23 Estimated global residual at each adaptive step.

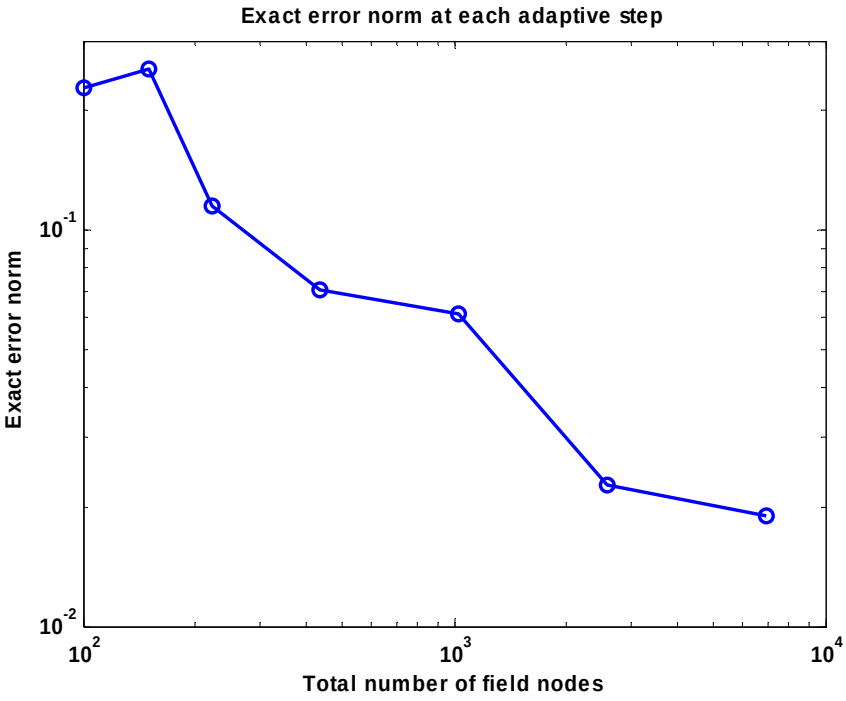

Figure 7.24 Exact error norm of u at each adaptive step.

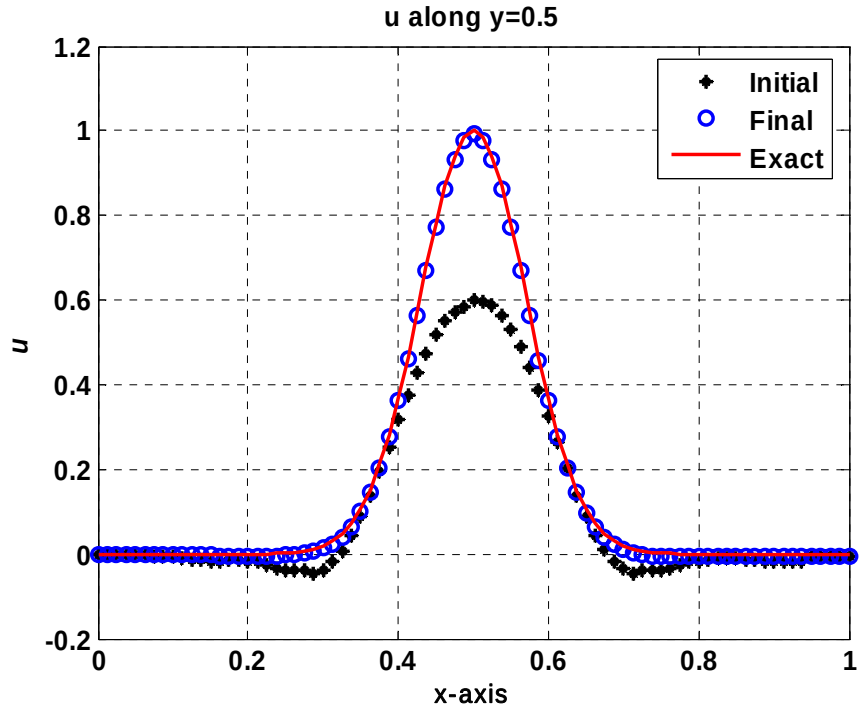

Figure 7.25 The solution of *u* along $y = 0.5$ at initial and final steps.

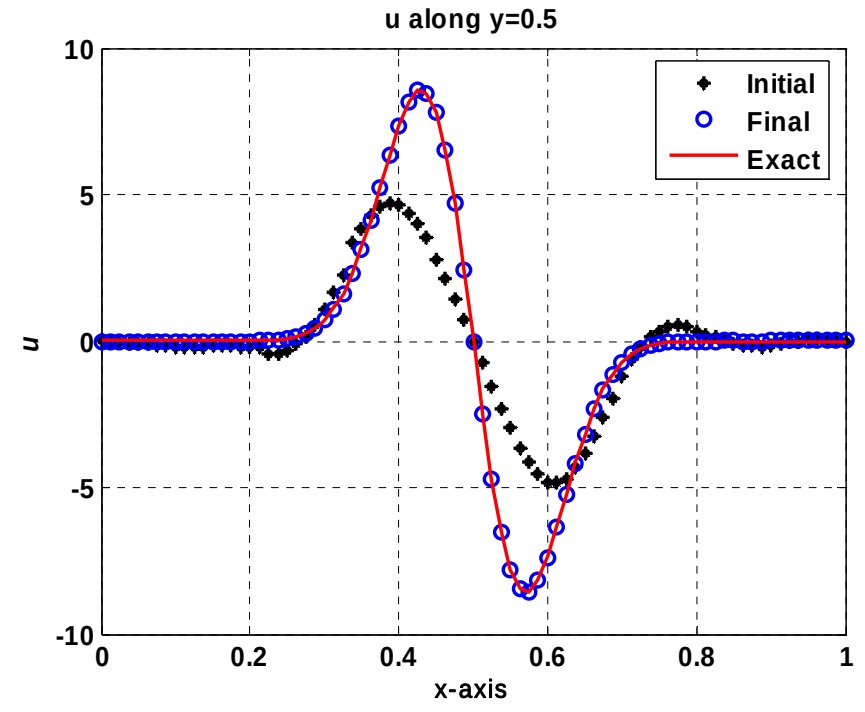

Figure 7.26 The solution of $\frac{\partial u}{\partial x}$, along $y = 0.5$ at initial and final steps.

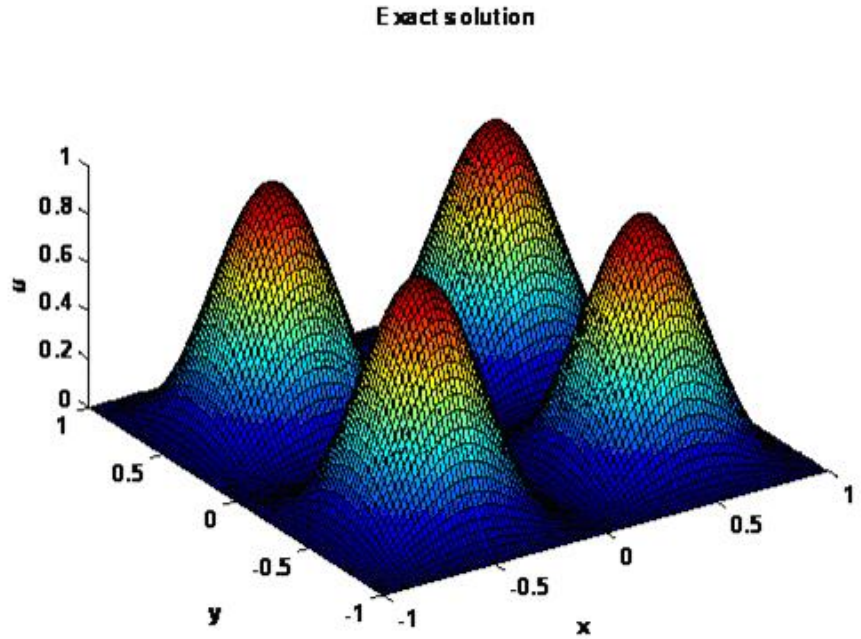

Figure 7.27 The exact solution of Poisson problem with multiple peaks.

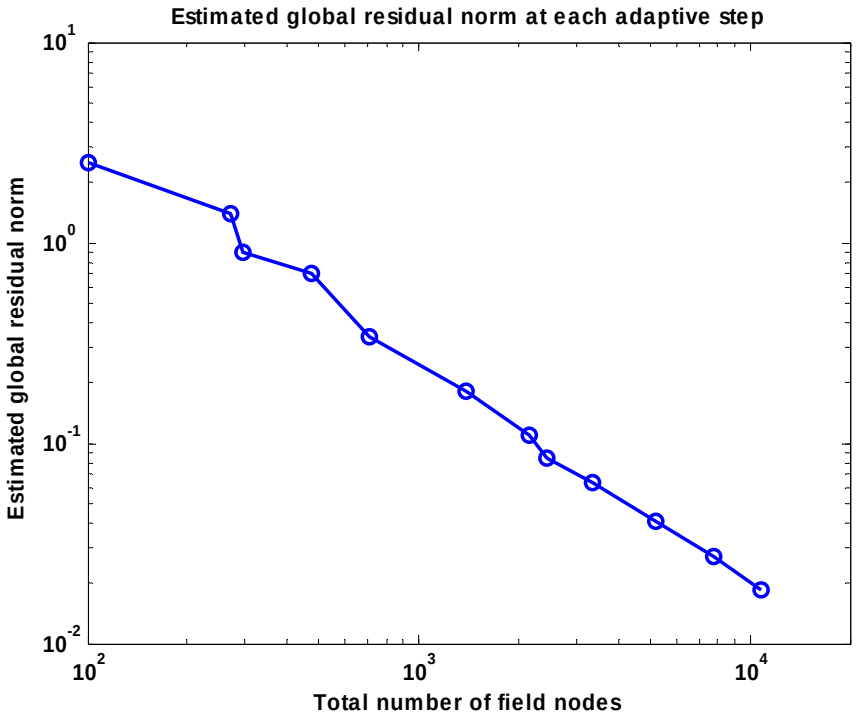

Figure 7.28 The estimated global residual norm at each adaptive step.

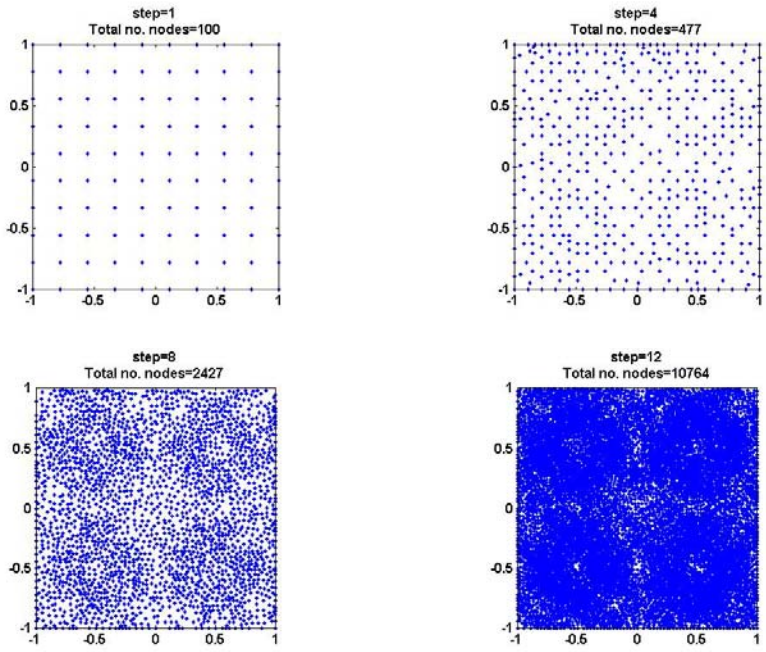

Figure 7.29 The nodal distribution at initial, 4th, 8th and final steps.

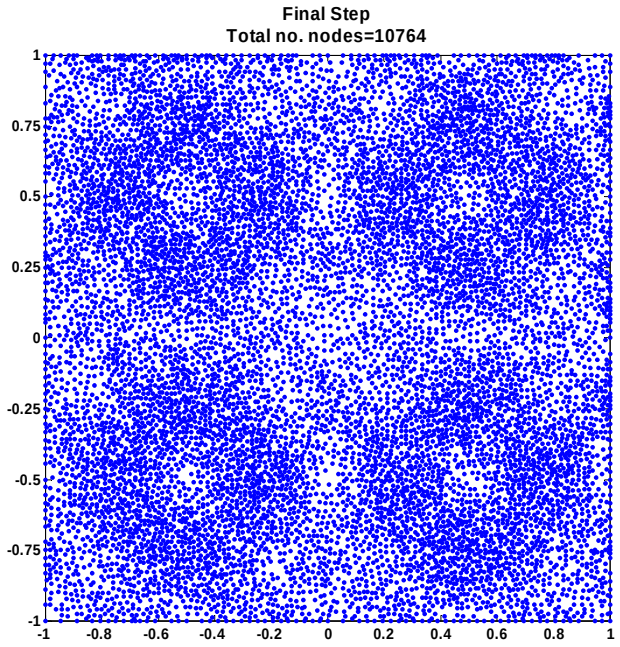

Figure 7.30 Enlarged view of the nodal distribution at final step.

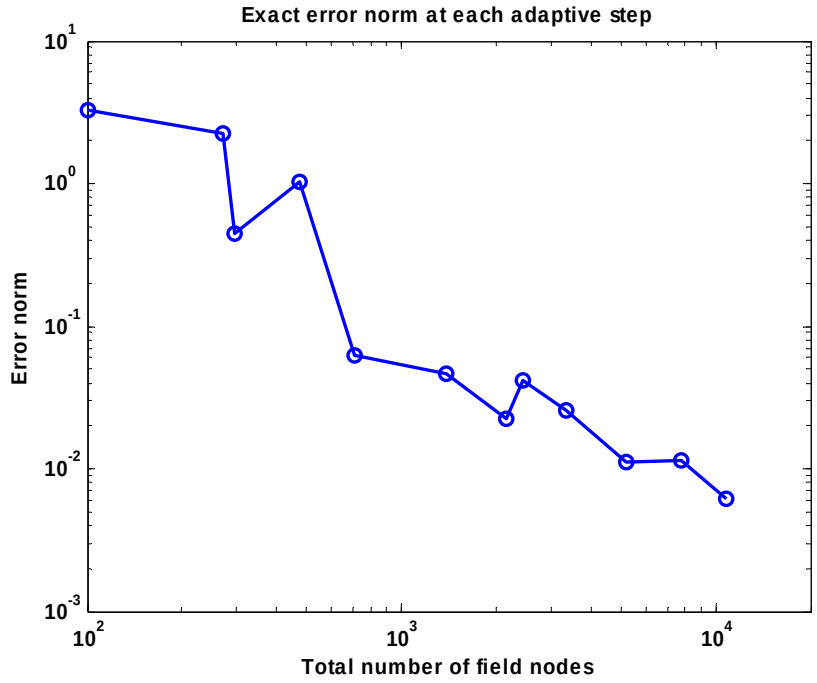

Figure 7.31 The exact error norm at each adaptive step.

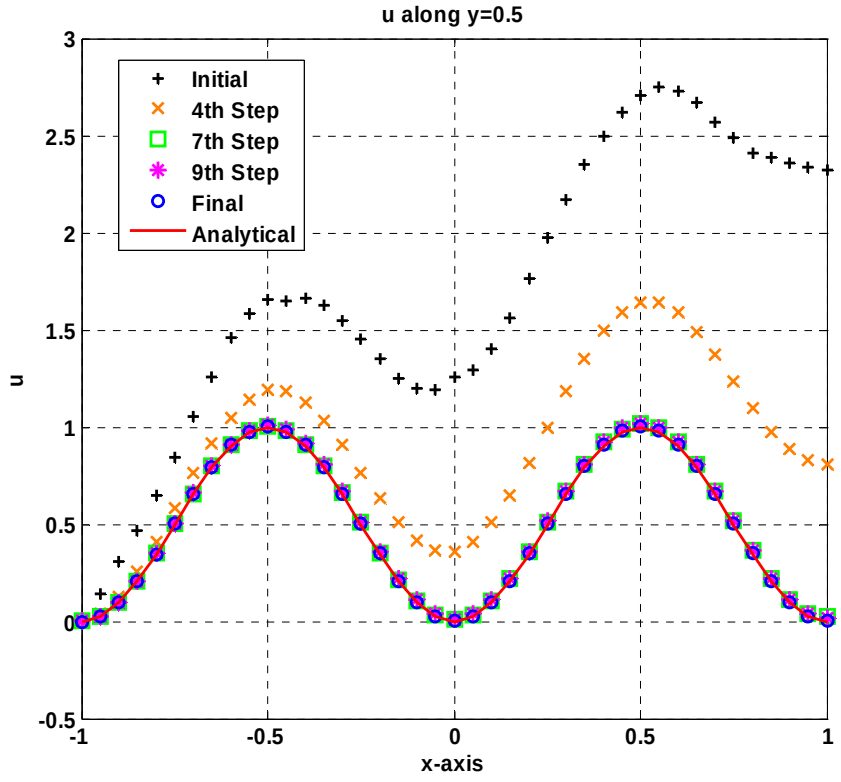

Figure 7.32 The solution of *u* along $y = 0.5$ at initial, 4th, 7th, 9th and final steps.

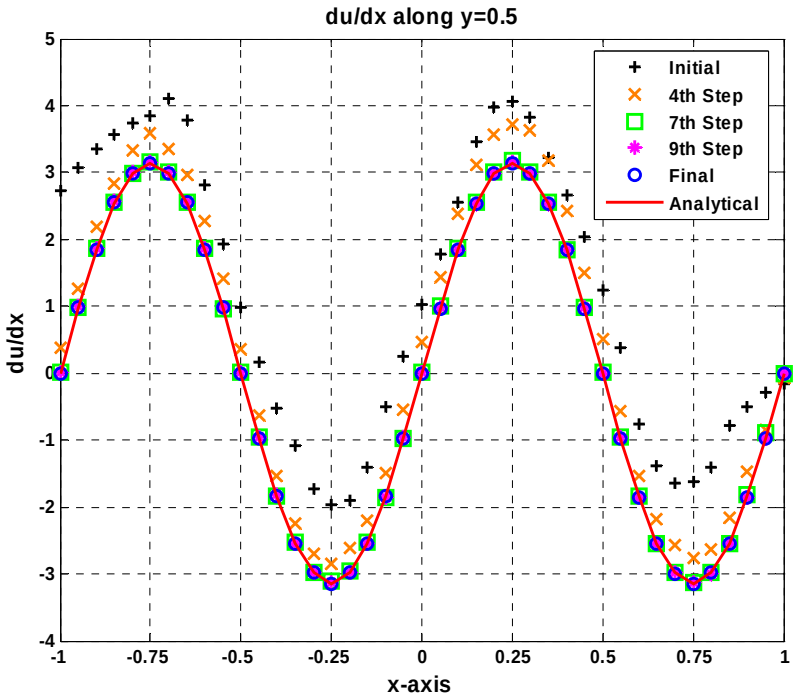

Figure 7.33 The solution of $\frac{\partial u}{\partial x}$ along $y = 0.5$ at initial, 4th, 7th, 9th and final steps.

Chapter 8

A Subdomain Method Based on Local Radial Basis Functions

8.1 Introduction

Subdomain method is a very classical numerical method. Compared to the strong-form method, subdomain method doest not required the governing equations to be satisfied at node. In contrast, subdomain method enforced the satisfaction of the governing equation in an average sense over a subdomain. In the subdomain formulation, each node possesses of its own local domain, called subdomain. The average of the residual is enforced to be zero in the subdomain of the nodes rather than at nodes.

In present subdomain method, the domain integration of the residual is converted into boundary integration by applying Green's Theorem. Boundary integration is one of the best candidates to obtain the average of the residual for local subdomain. As compared to domain integration, boundary integration is performed at lower order of dimension. For instance, one dimensional integration is only required for two dimensional problem domain. Boundary integration procedure is also simple and

straightforward. Furthermore, as most of the subdomain boundaries are interference, the cost of the computation can also be further reduced. Lastly, the Neumann boundary also can be embraced in the formulation naturally and make subdomain method a very stable method. This is a very distinct from conventional weak formulation (weak-form) methods which are formulated in the domain integration form, e.g., Element-free Galerkin method [9], Local Petrov-Galerkin Method [2].

In this chapter, meshfree techniques are integrated into the classical subdomain method to form a new subdomain method. Throughout the experiences gained in the meshfree method, the RPIM approximation that often be used in the meshfree method is suggested to be employed in the present subdomain method. In the present formulation, subdomain procedure can provide a very stable solution; furthermore, the RPIM approximation provides incredible flexibility to construct the shape function using arbitrary scattered nodes.

Delaunay diagram is a set of triangular cells that is formed by a given set of nodes in the problem domain through triangularion. It is very popular in domain discretization [28] due to its applicability to complex domain. In this work, Delaunay diagram provides a background mesh to facilitate the construction of subdomain for each node. As the algorithm of Delaunay triangulation is well established, the implementation is very easy and with low computational cost.

Incorporating with the residual based error estimator and adaptive strategy introduced in Chapter 3, the present method is then further applied in adaptive analysis.

By measuring the residual of the strong-form governing equation, the adaptation can then proceeds based on the determined error estimator. In the simple *h*-refinement process, additional nodes will be inserted in the domain if the local error estimator exceeds the predefined criterion. To have a better nodal distribution after nodes are inserted in the domain, a nodal smoothing procedure is also adopted to reposition the nodes in a better manner. In the smoothing procedure, nodes are relocated to the centre of its first layer of surrounding nodes as demonstrated in **Figure 8.1**. Such procedure can ensure no two nodes are too close to each other. Highly random nodal distribution can therefore be avoided and hence the accuracy of solution is improved.

From the numerous given examples, solutions of the present subdomain method are shown accurate and stable. The residual based error estimator is effectively reflects the error of the local solution. Simple *h*-refinement and nodal smoothing procedure has demonstrated that high accuracy solution can be obtained efficiently in adaptive analysis.

8.2 Formulation of Subdomain Method

Now, consider the following governing equation given in Eq. (4.11) as

$$Lu + f = 0. \tag{4.11}$$

In the strong formulation, Eq. (4.11), is fully satisfied at the field nodes located in the internal domain. As mentioned often in this thesis, such a ‘strong’ enforcement can often lead to unstable behaviour. In the present subdomain method, Eq. (4.11) is

satisfied in an average sense over a local subdomain. In this situation, Eq. (4.11) is not satisfied at nodes. The residual of the governing equation at node *i* is known as

$$R(u_i) = L(u_i) + f_i \neq 0, \quad (i = 1, \cdots, N), \tag{8.1}$$

where *N* is the total number of field nodes in the problem domain.

In the subdomain method, seeking a solution that average of the residual in the local domain is equal to zero leads to the following expression.

$$\int_{\Omega_i} R(u_i) \partial\Omega = 0, \tag{8.2}$$

where Ω_i is the subdomain of node *i*. In terms of stability, subdomain formulation behaves much better than the simple collocation but instability is still observed in the Ref. [46].

In the present subdomain method, Green's Theorem is resorted to convert the domain integral form in Eq. (8.2) into a contour integral form. For an easier description, the deriving of the subdomain method formulation is demonstrated using solid mechanics problem in this context. For a solid mechanic problem, the well-known governing equation is the set of equilibrium equations given in the following expression,

$$div\, \boldsymbol{\sigma} + \mathbf{b} = 0, \tag{8.3}$$

where $\boldsymbol{\sigma}$ is the stress tensor that is obtained using the assumed displacement field **u**, and **b** is the vector of body force. The average of the residual (force) in the subdomain

can then be written as

$$\int_{\Omega_i} (div\,\boldsymbol{\sigma} + \mathbf{b}) \partial\Omega = 0\,, \tag{8.4}$$

where Ω_i is the subdomain of i^{th} node. By applying the Green's Theorem to the first term of Eq. (8.4), the local integration of the residual can be expressed in the following form.

$$\oint_{\Gamma_i} \boldsymbol{\sigma} \cdot \mathbf{n} \partial\Gamma + \int_{\Omega_i} \mathbf{b} \partial\Omega = 0\,, \tag{8.5}$$

where $\mathbf{n}$ is the vector of unit outward normal on the boundary. Note from Eq. (8.5) that differential operators on the stress tensor have been removed and hence the order of differential operation to the assumed displacement vector is reduced, which helps decisively the stability of the present subdomain method.

For all the nodes in the internal domain, Eq (8.5) is directly used to generate the algebraic equations. If the node is located on the Neumann boundary, Eq (8.5) can further be derived as

$$\oint_{\Gamma_i} \boldsymbol{\sigma} \cdot \mathbf{n} \partial\Gamma + \int_{\Omega_i} \mathbf{b} \partial\Omega = \oint_{\Gamma_i^{\text{int}}} \boldsymbol{\sigma} \cdot \mathbf{n} \partial\Gamma + \oint_{\Gamma_i^{t}} \boldsymbol{\sigma} \cdot \mathbf{n} \partial\Gamma + \int_{\Omega_i} \mathbf{b} \partial\Omega = 0\,, \tag{8.6}$$

where Γ_i^{int} is the local boundaries that lies inside domain and Γ_i^{t} is the local boundaries that intersect with the global Neumann boundaries. The Neumann boundary conditions can therefore be imposed as

$$\oint_{\Gamma_i^{\text{int}}} \boldsymbol{\sigma} \cdot \mathbf{n} \partial\Gamma + \oint_{\Gamma_i^t} \mathbf{t}\, \partial\Gamma + \int_{\Omega_i} \mathbf{b} \partial\Omega = 0\,, \tag{8.7}$$

where $\mathbf{t}$ denotes the vector of traction that is given along the Neumann boundaries. Note that Eq. (8.5) can be viewed as a special case of Eq.(8.7) when Γ_i^t vanishes and Γ_i^{int} becomes the Γ_i^{i} for Ω_i of the i^{th} interior node. The discretized form of the Eq. (8.7) can be expressed in matrix form as

$$\mathbf{K}_{ij}\mathbf{u}_j = \mathbf{F}_i\,, \tag{8.8}$$

where

$$\mathbf{K}_{ij} = \oint_{\Gamma_i^{\text{int}}} \mathbf{N}\mathbf{D}\mathbf{B}_j d\Gamma\,, \tag{8.9}$$

$$\mathbf{F}_i = -\oint_{\Gamma_i^t} \mathbf{t} d\Gamma - \int_{\Omega} \mathbf{b} d\Omega\,. \tag{8.10}$$

In Eq. (8.9), the matrix **N**, the strain matrix $\mathbf{B}_j$ can be given as

$$\mathbf{N} = \begin{bmatrix} n_x & 0 & n_y \\ 0 & n_y & n_x \end{bmatrix}, \tag{8.11}$$

$$\mathbf{B}_j = \begin{bmatrix} \dfrac{\partial \phi_j}{\partial x} & 0 \\ 0 & \dfrac{\partial \phi_j}{\partial y} \\ \dfrac{\partial \phi_j}{\partial y} & \dfrac{\partial \phi_j}{\partial x} \end{bmatrix}, \tag{8.12}$$

where n_x, n_y are the component of unit outward normal on the subdomain's

boundaries Γ_i^{int} in the *x* and *y* directions, ϕ_j is the shape function of node *j* and **D** denotes the elasticity matrix for solid material.

The imposition of Dirichlet boundary conditions is straightforward. As RPIM shape function possesses delta property, no special treatment is required. Dirichlet boundary conditions can be simply enforced as usual practice in the well-known finite element method.

$$u_i = \bar{u}_i \,. \tag{8.13}$$

The final system equation can then be assembled in the matrix form as

$$\mathbf{KU} = \mathbf{F} \,, \tag{8.14}$$

where **K** denotes the coefficient matrix (often called as stiffness), **F** denotes the force vector and **U** is the vector of unknown nodal displacements. Finally, the unknown nodal displacements can be solved as

$$\mathbf{K}^{-1}\mathbf{F} = \mathbf{U} \,. \tag{8.15}$$

Construction of Subdomain

The subdomain used in the formulation is a local domain for averaging the residual of the discretized governing equations to be zero. To construct the subdomain, one should ensure the "global conservation (or equilibrium) requirement" that is the union of all subdomains must be equal to the global domain. In other words, global domain has to be fully covered by all subdomains without gap or overlapping. In this

work, Delaunay diagram is provided as a background mesh to facilitate the construction of subdomain as shown in **Figure 8.2**. Consider node *i* located in the interior domain as shown in **Figure 8.3** (a), a set of Delaunay cells can be found to enclose node *i*. **Figure 8.3** (b) shows the subdomain of node *i*, Ω_i , is formed by several sections (dash line) that passing the centre point of the surrounding cells (marked as a '+') to the middle point of the adjacent edges of the corresponding cells.

For node located on Neumann boundary Γ_t, it can also be surrounded by several cells as shown in **Figure 8.4** (a). Follows the similar procedure of forming the subdomain for interior node, the subdomain of the node located on Neumann boundary can be formed as shown in **Figure 8.4** (b). In this case, part of the boundaries of the local subdomain intersects with the global Neumann boundaries.

For some meshless subdomain methods, the subdomain is claimed to be constructed in arbitrary shape. In common practice, regular shape likes circle or rectangular local domain is preferred. The size of the regular subdomain usually depends on the nodal space. However, this type of subdomain constructed based on the Euclidean norm is apparently not robust. It usually either fails to cover the entire domain or is in a very large size. This is definitely not favoured while subdomain method is extended to adaptive analysis. In this work, the advantage of using Delaunay diagram is obvious. Delaunay diagram can is utilized to ensure the global conservation requirement. No matter how random the nodes are scattered, the subdomains are always covered the entire domain with small size. This is particular important in the adaptive analysis where nodes are usually distributed very randomly.

Numerical Integration

Numerical integration is one of the key issues in the subdomain method. In this work, Gauss integration is adopted to perform the numerical contour integration. From our experience, one Gauss point is good enough to provide solution with high accuracy. Integration scheme with more Gauss points does not significantly improve the accuracy of solution.

The contour integration for subdomain of node *i* can then be evaluated numerically as

$$\oint_{\Gamma_i} \boldsymbol{\sigma} \cdot \mathbf{n} \partial\Gamma = \sum_{g=1}^{nl} \boldsymbol{\sigma}\left(x_g^i\right) \cdot \mathbf{n}\left(x_g^i\right) \cdot \Delta l_g^i , \tag{16}$$

where *nl* is the number of sections, x_g^i is the mid point of section and Δl_g^i is the length of the corresponding section.

8.3 Numerical Examples

In the below numerical examples, the local nodes used in the RPIM approximation are not selected based on Euclidean norm. A concept of layers is introduced in the nodal selection. Two layers of supporting nodes are selected for approximation at any interest points. The nodal selection based on layers will be illustrated in more details in Chapter 9.

In the numerical examples of adaptive subdomain method based on local RBFs, residual based error estimator introduced in Chapter 3 is adopted here. In addition to the

h-refinement scheme, a mesh smoothing procedure is also adopted to provide a better nodal distribution and hence the accuracy is improved.

In the given numerical examples in this chapter, polynomial with completed second order, $m = 6$, is adopted in the RPIM approximation and shape parameters of MQ-RBF are known as $\alpha_c = 3.0$ and. $q = 1.03$.

8.3.1 Example 1: Standard and Higher order Patch Tests

The first example is standard and higher order patch tests. In the standard patch test, two different patches with 25 nodes regularly and irregularly distributed in the unit square domain are used as shown in **Figure 4.9**. A linear function of displacements is imposed at the boundary nodes. Results given in **Table 8.1** show the proposed subdomain method passes the standard patch test. The present method is then subjected to the higher order patch tests. Two different patches with 35 regularly and irregularly nodal distribution in the 3×6 rectangular domain as shown in **Figure 4.10** are used for higher order patch tests. The patches are subjected to a constant loading applied on the right end edge in the first case. Whereas the patches are subjected to a loading that linearly varied along the right end in the second case. As listed in **Table 8.2**, the present subdomain method passes the high order patch tests to machine accuracy. The details of the patch tests procedure can be found in Ref. [90].

8.3.2 Example 2: Connecting Rod Subjected to Internal Pressure

In Example 2, a problem domain with more complicated geometry and multi

cavities is analyzed. An automobile part, connecting rod, is subjected to a uniform pressure in the half section of the cavity CD as illustrated in **Figure 8.5**. The problem is assumed as a plane strain elastostatics problem. Loading and the material properties are given as: pressure $P = 1\times10^{6}\,Pa$, Young's modulus $E = 1\times10^{10}$ and Poisson's ratio $\upsilon = 0.3$. As no analytical solution is available, FEM solution with 85934 quadrilateral elements solving by ANSYS is provided as a reference solution.

In this example, the elastostatics problem is solved by the present subdomain method using 4 different sets of nodes given in **Figure 8.6**. **Figure 8.7** shows approximated energy of the present subdomain method is approaching to the reference solution while more nodes are used in the modeling. The subdomain method based on local RBFs provides very accurate solution in term of displacements and stresses. The displacements in *x*-direction along the line AB are plotted in **Figure 8.8**, and show good agreement with reference solution. Furthermore, **Figure 8.9** and **Figure 8.10** also show the normal stresses obtained by the present method are also in good agreement with reference solutions. From **Figure 8.8** to **Figure 8.10**, it can be noticed that even with as little as 339 nodes only, accurate solutions in term of both displacements and stresses can be obtained by the present method.

8.3.3 Example 3: A Cantilever Beam Subjected to a Parabolic Shear at End

To examine the numerical performance of the present subdomain method, a benchmark problem is studied in Example 3. A cantilever beam subjected to parabolic

shear stresses at the end, as shown in **Figure 4.11**, is studied. The dimension of cantilever beam is known as length $L = 48.0m$ and height $H = 12.0m$, and the material properties are given as Young's modulus $E = 3 \times 10^7$ and Poisson's ratio $\upsilon = 0.3$. The loading at the end of the beam is known as $P = \int \tau_{xy} dy = 1000N$. Analytical solution of this problem can be found in Ref. [90]. The governing equations of the solid mechanics problem are known as listed in Eq. (4.19) to Eq. (4.21). In this example, Dirichlet boundary conditions are imposed along the left edge and Neumann boundary condition is applied along the rest of the edges.

To study the convergent rate of the solution, the problem is modelled and solved by using four different sets of regular distributed nodes: 4×13, 7×25, 13×49 and 25×97. The error norm of displacements, energy norm and computational cost of the subdomain method are all listed in **Table 8.3**. For comparison purpose, solutions of FEM with triangular element are also provided. From the error norm of displacements and energy norm plotted in **Figure 8.11** and **Figure 8.12**, one can notice that the proposed subdomain method provides much more accurate solution than FEM. In addition, the convergent rate of energy norm of the present method is also higher than FEM. Although the subdomain method based on local RBFs required higher computational time than FEM generally in **Figure 8.13**, the present subdomain method is still more efficient than FEM as shown in the **Figure 8.14**.

8.3.4 Example 4: Adaptive Analysis of Elastostatics Problem

Another benchmark elastostatics problem, an infinite plate subjected to uniaxial

traction in the horizontal direction, is studied in this example. Due to symmetric, only a quarter of the problem is modelled, and the geometry of the plate is known as: $a = 0.2$ and $b = 2.0$ as shown in **Figure 5.7**. This problem is considered as plane strain problem and the material properties are given as: Young's modulus $E = 1 \times 10^3$ and Poisson's ratio $\upsilon = 0.3$.

The adaptive analysis is conducted for this problem with refinement coefficient and global residual tolerance as $\kappa_l = 0.05$ and $\kappa_g = 0.05$ respectively. The entire adaptive analysis takes four steps to complete and ended up with 970 nodes from 121 nodes initially as shown in **Figure 8.15**. During the adaptation, problem domain is refined based on our adaptive strategy. **Figure 8.16** shows the estimated global residual norm has been gradually reduced at each adaptive step. As analytical solution is available [90], the solution of the subdomain method at each adaptive step can be easily justified. Both error norms of displacements and energy norm have been adaptively improved as shown in **Figure 8.17** and **Figure 8.18** respectively. The approximated stresses along the left edge show good agreement with the analytical solution. One can also notice clearly in **Figure 8.19** and **Figure 8.20** that the solution of stresses is improved significantly. The solutions of the normal stresses, σ_{xx} and σ_{yy}, of the final steps are much closer to the analytical solution than the initial solutions.

8.3.5 Example 5: Adaptive Analysis of Short Beam Subjected to Uniform Loading on the Top Edge

A short beam subjected to a uniform loading on the top edge is studied and

considered as a plane strain problem in Example 5. The dimension of the short beam is indicated in **Figure 8.21** and the material properties are known as: Young's modulus $E = 1.0$ and Poisson's ratio $\upsilon = 0.3$. Loading applied on the top edge is given as $P = 1.0$. As the exact solution is not available, a reference solution given in the Ref. [1] is adopted. The displacement in y-direction of point A is known as -2.875323 and the energy norm is given as $\|u\| = 1.3794663$.

Since there are two singularity points exist at the two corner of the beam near to the wall, region around singularity points are expected to be refined. In this example, the local refinement coefficient and global residual tolerance are predefined as $\kappa_l = 0.02$ and $\kappa_g = 0.02$ respectively. The adaptive analysis takes 9 steps to complete, and nodal distributions at initial, third, fifth and final steps are plotted in **Figure 8.22**. From the final distribution, the residual based error estimator has demonstrated its robustness of identifying the all singularity points exist in the problem domain. Region around the singularity points has been refined with more nodes.

With the robust error estimator and effective adaptive strategy, the accuracy of the proposed subdomain method based on local RBFs is improved significantly and efficiently. The displacements and energy norm plotted in **Figure 8.23** and **Figure 8.24** evidently shows the solution of the present method is progressively approaching the reference solution. The purpose of adaptive analysis is clearly demonstrated here. Compared to the uniform refinement scheme, the adaptive scheme shows much better convergency.

8.3.6 Example 6: Adaptive Analysis of Bridge Subjected to Uniform Loading on the Top Edge

A bridge with uniform loading on top is studied and analyzed by the proposed adaptive subdomain method in Example 6. The geometry of the bridge is shown in **Figure 7.13** (a) and the loading is given as $P = 1000$. As the problem is symmetric, only the right half of the bridge is modelled and assumed as a plane strain problem. For justification purpose, a FEM solution provided by ANSYS with a model of 30251 quadrilateral meshes is considered as a reference solution.

The refinement coefficient and global residual tolerance are predefined as $\kappa_l = 0.05$ and $\kappa_g = 0.05$ respectively. The adaptive analysis starts with only 32 nodes and terminated at 5^{th} step with 1100 nodes irregularly distributed in the domain as shown in **Figure 8.26**. **Figure 8.25** indicates the estimated global residual norm is gradually reduced after the domain is refined by inserting additional nodes in the domain based on the refinement criterion. Clearly, **Figure 8.27** shows our adaptive strategy has effectively improved the approximated energy toward the reference solution. In addition, the contour plots of the approximated stresses in the entire domain are also shown in **Figure 8.28**. To justify the solutions, the displacements and the normal stresses along the left edge at initial and final steps are also plotted in **Figure 8.29** and **Figure 8.30** against reference solution. It has also evidently shown the adaptive scheme is effective to improve the accuracies of both displacements and stresses. Apparently, the solution at final step of the adaptive analysis is better than the

initial step.

8.3.7 Example 7: Adaptive Analysis of Crack Problem

In this example, a crack panel shown in **Figure 3.16** is analyzed adaptive subdomain method. This problem is considered as a plane strain problem and the material properties are known as Poisson's ratio $\upsilon = 0.3$, Young's modulus $E = 3 \times 10^7$. The dimension of the cracked panel is given in **Figure 3.16**, where $a = 0.5m$. Due to symmetric, only half of the model is analysed, see **Figure 3.16** (b). The cracked panel is subjected to a load along the boundaries which described as in **Eq, 3.20** to Eq. **3.22**,

$$\sigma_{xx} = \frac{K_I}{\sqrt{2\pi r}} \cos\frac{\theta}{2}\left(1 - \sin\frac{\theta}{2}\sin\frac{3\theta}{2}\right), \tag{3.20}$$

$$\sigma_{yy} = \frac{K_I}{\sqrt{2\pi r}} \cos\frac{\theta}{2}\left(1 + \sin\frac{\theta}{2}\sin\frac{3\theta}{2}\right), \tag{3.21}$$

$$\tau_{xy} = \frac{K_I}{\sqrt{2\pi r}} \sin\frac{\theta}{2}\cos\frac{\theta}{2}\cos\frac{3\theta}{2}, \tag{3.22}$$

where K_I is stress intensity of mode I.

In this example, two layers of supporting nodes are used for approximation. The refinement coefficient and global residual norm tolerant are given as $\kappa_l = 0.1, \kappa_g = 0.1$. For comparison purpose, subdomain method and FEM using linear triangle element with uniform refiment scheme are conducted.

The adaptive analysis using subdomain method takes eight steps to complete. The number of nodes increased from 231 to 770 nodes at the last step. From the nodal

distribution given in **Figure 8.31**, one can observe that nodes have been increased intensively at the crack tip where the singularity point is. The global residual norm has been tremendously reduced from 0.0879 to 0.0068 as shown in **Figure 8.32**. The displacement and energy norms plotted in **Figure 8.32** and **Figure 8.33** have shown adaptive subdomain has achieved great success. The displacements norm is reduced from 15.78% to 0.98% and the energy norm has dropped from 1.138×10^{-9} to 1.000×10^{-11}. Computed energy at each adaptive step given in Figure 8.34 also shows better convergency than uniform refinement scheme, the solution of adaptive subdomain method with 770 nodes is much better than 10000 nodes.

8.4 Remarks

In this chapter, a popular meshfree shape function, RPIM shape function, is integrated into the formulation of classical subdomain method. Subdomain method based on local RBFs has shown great accuracy and stable solution in the given numerical examples. Compared to FEM using triangular element, present subdomain method, that uses Delaunay diagram as a background mesh, provides much better solution in term of both displacements and stresses. Incorporated with the robust residual based error estimator and effective adaptive strategy, the present adaptive subdomain method has demonstrated remarkable numerical performance in adaptive analysis. The proposed adaptive strategy is shown simple, but yet robust and efficient. Numerous examples in elastostatics have shows high accuracy solution can be achieved efficiently by the proposed adaptive subdomain method based on local RBFs.

Linear patch test	Error norm
Regular nodal distribution	1.8035×10^{-16}
Irregular nodal distribution	4.4798×10^{-16}

Table 8.1 Error norms of the subdomain method for linear patch test.

Higher order patch test	Error norm	
	Case 1	Case 2
Regular nodal distribution	2.6738×10^{-15}	1.4136×10^{-14}
Irregular nodal distribution	5.2851×10^{-15}	9.8631×10^{-16}

Table 8.2 Error norms of the subdomain method for higher order patch test.

Total number of nodes	Displacements error		Energy norm	
	FEM3N	Present	FEM3N	Present
52	26.2910%	2.9424%	1.3216	0.3429
175	8.3546%	0.1313%	0.7691	0.1271
637	2.2404%	0.0401%	0.4013	0.05989
2425	0.5709%	0.0202%	0.2029	0.03190

Table 8.3 Error norm of displacements, energy norm and computational time of the subdomain method and FEM.

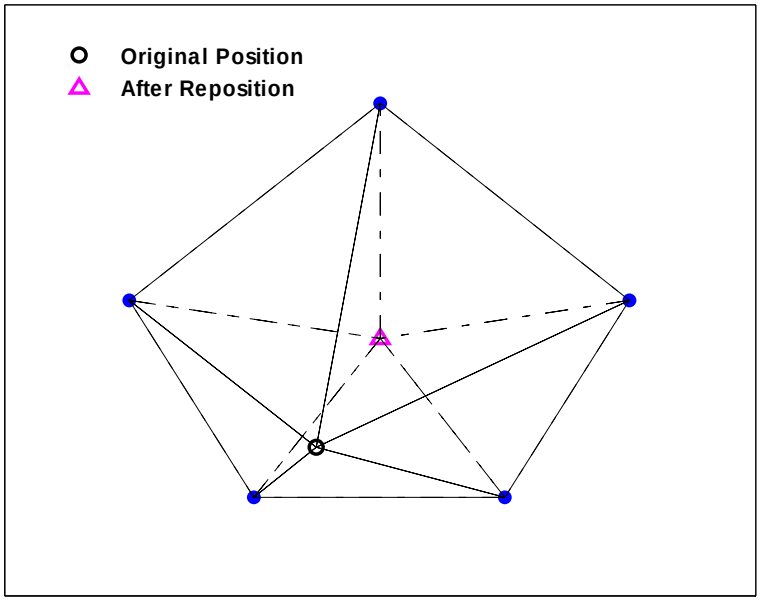

Figure 8.1 Reposition of an interior node to the centre of its first layer of supporting nodes.

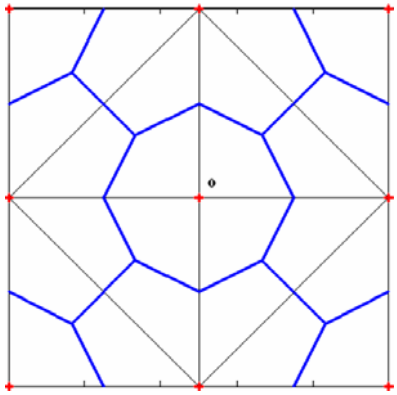

Figure 8.2 Subdomains constructed by the background mesh formed using Delaunay Diagram.

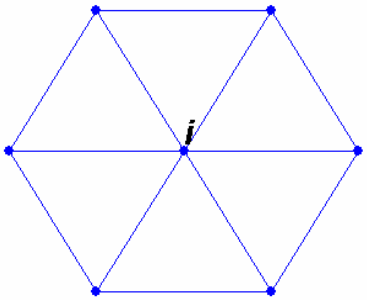

(a)

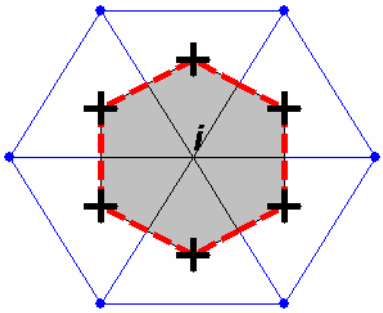

(b)

Figure 8.3 (a) Node *i* in the interior domain and (b) its subdomain.

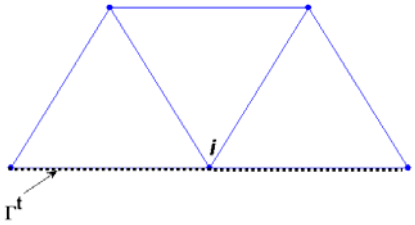

(a)

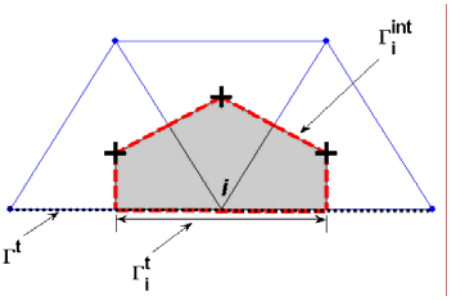

(b)

Figure 8.4 (a) Node *i* on the Neumann boundary and (b) its subdomain.

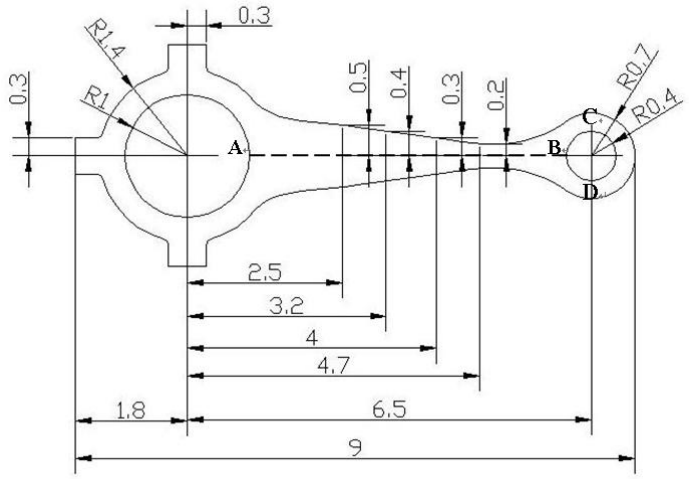

Figure 8.5 The model and dimension of the connecting rod.

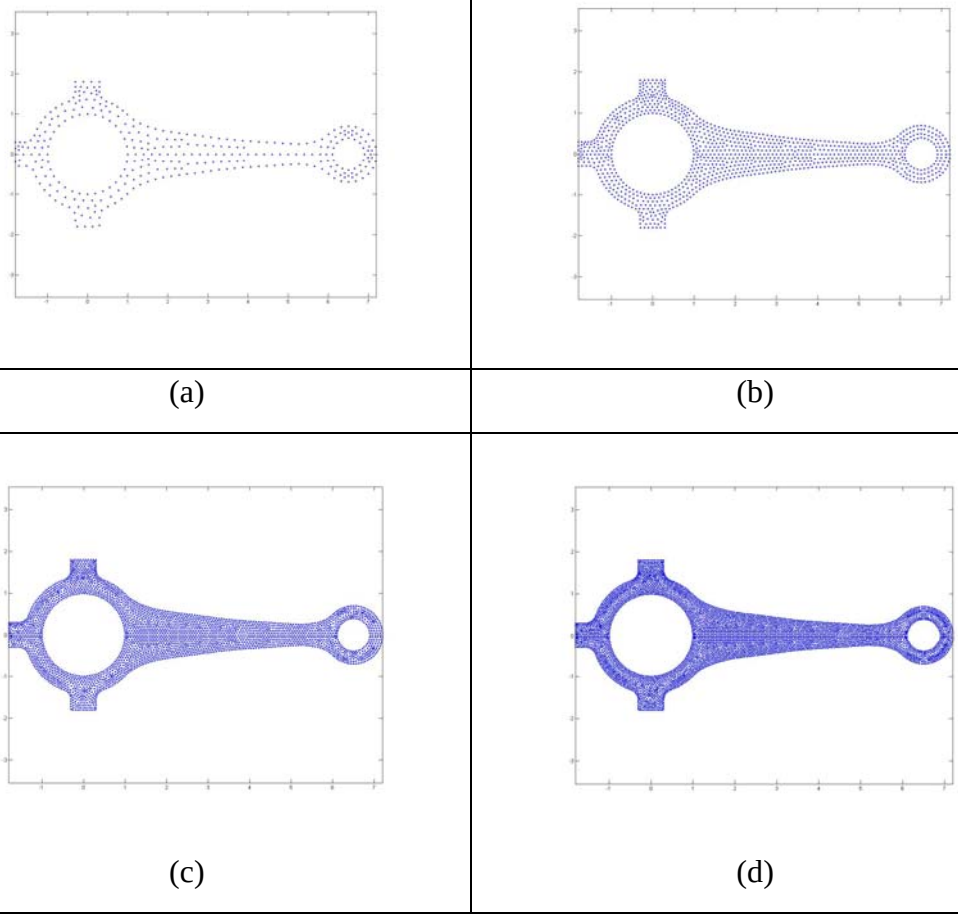

Figure 8.6 The models of connecting rod with (a) 339, (b) 1092, (c) 2979 and (d) 4541 nodes.

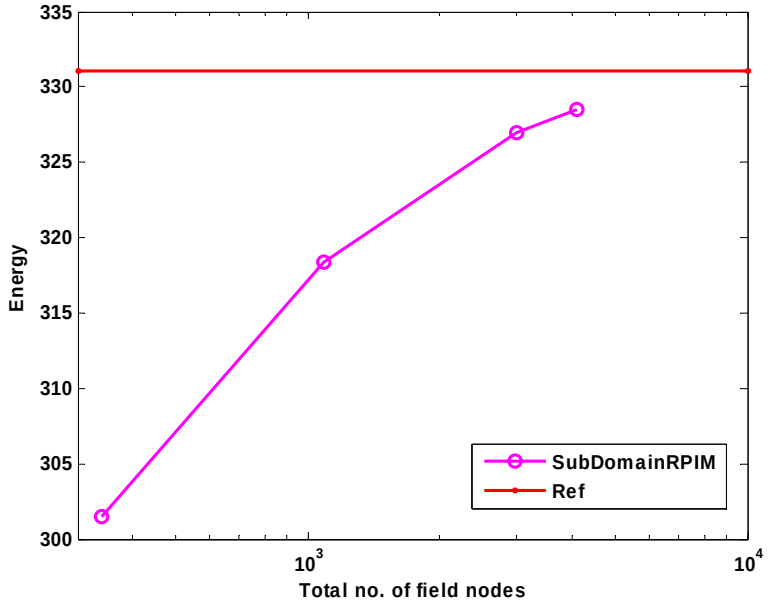

Figure 8.7 The approximated energy obtained by the subdomain method with different field nodes.

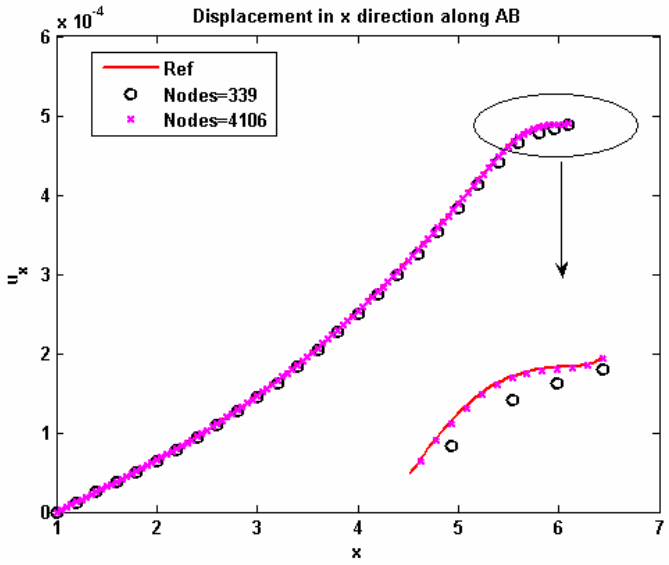

Figure 8.8 The displacements in x-direction obtained by subdomain method along AB with 339 and 4106 nodes in domain.

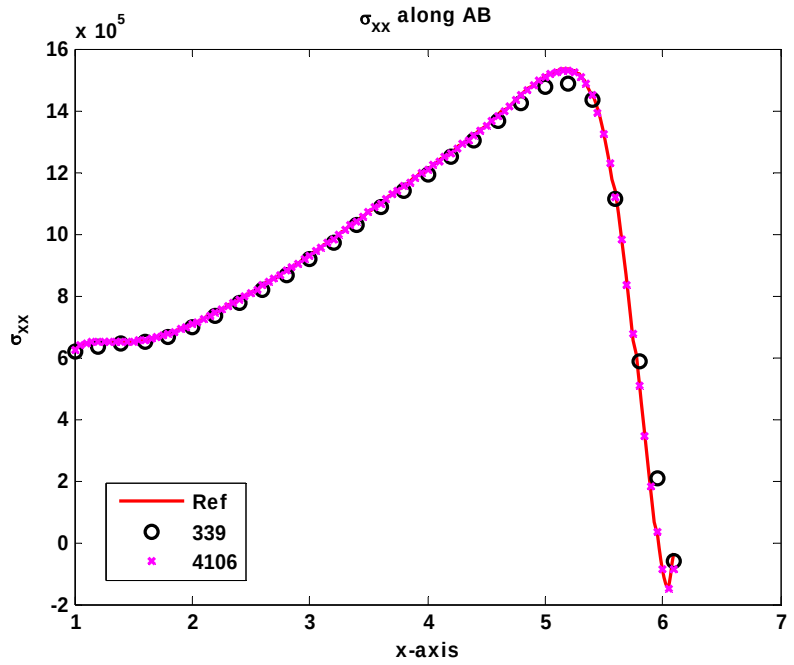

Figure 8.9 The normal stress σ_{xx} obtained by subdomain method along AB with 339 nodes and 4106 nodes in domain.

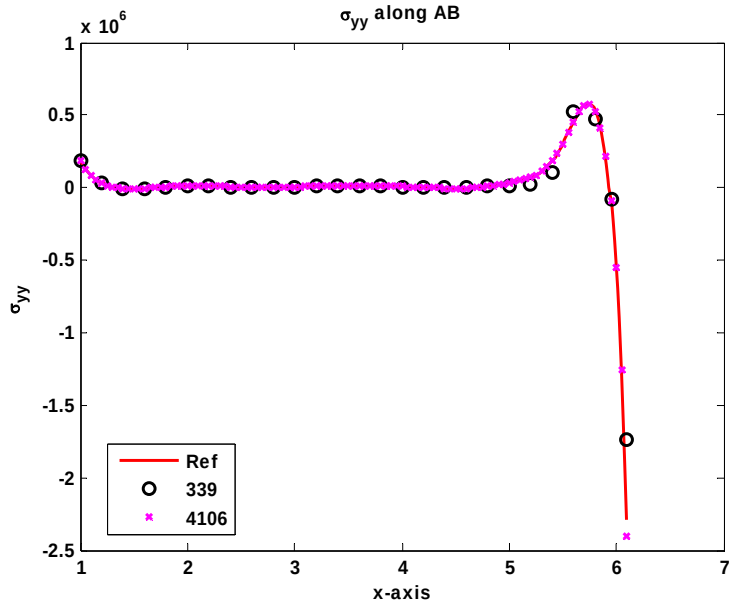

Figure 8.10 The normal stress σ_{yy} obtained by subdomain method along AB with 339 nodes and 4106 nodes in domain.

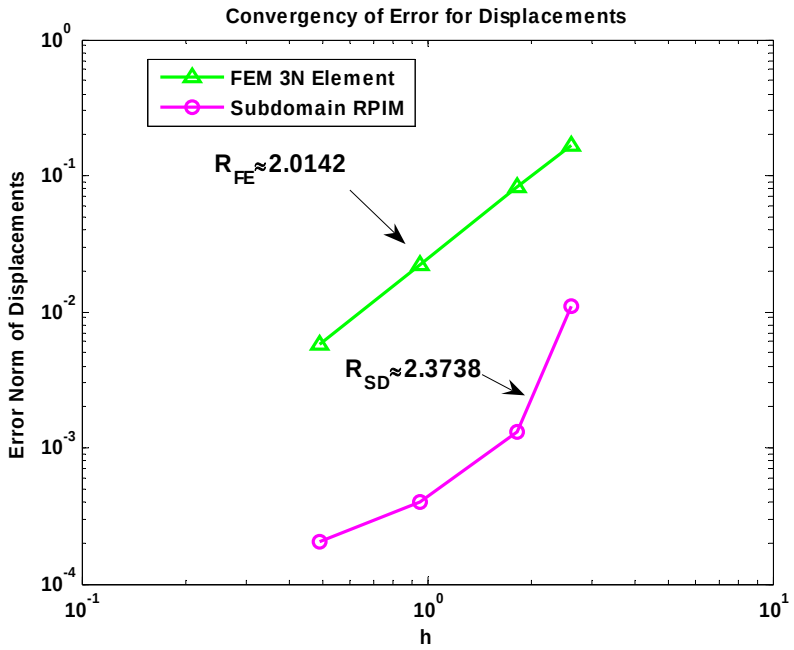

Figure 8.11 The convergent rate in term of the error norm of displacements for the FEM (3-nodes element) and subdomain method.

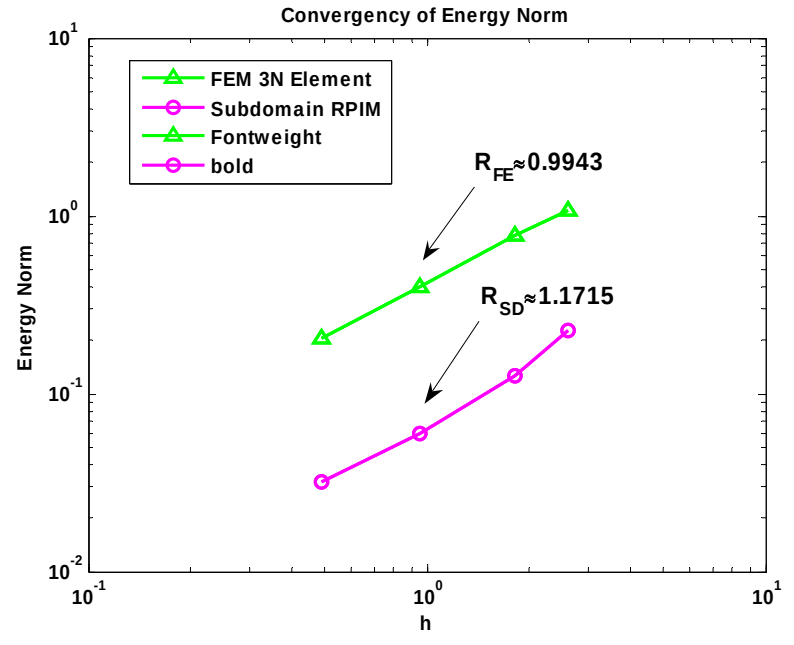

Figure 8.12 The convergent rate in term of the energy norm for the FEM (3-nodes element) and subdomain method.

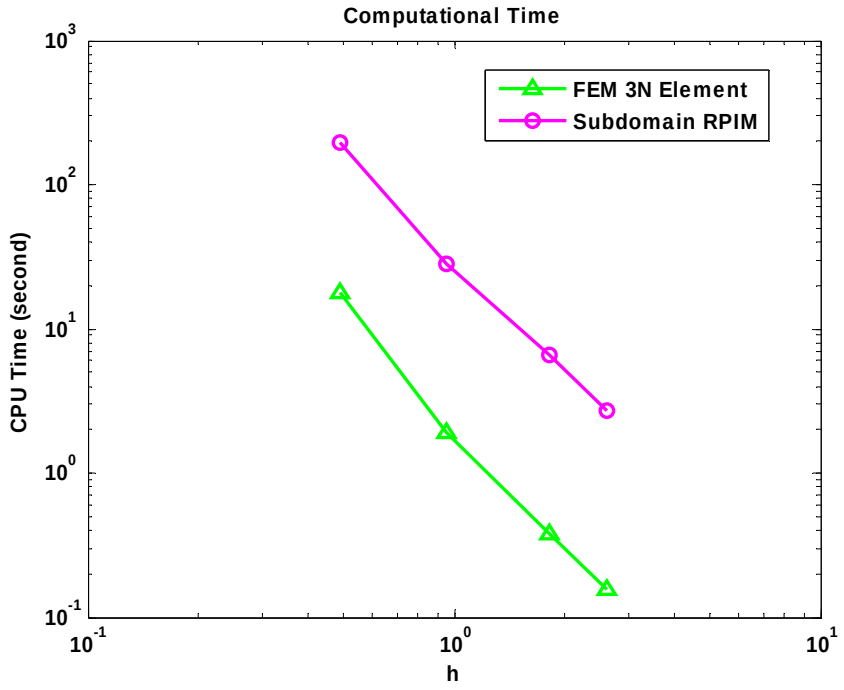

Figure 8.13 The comparison of the computational cost for the FEM (3-node element) and present method.

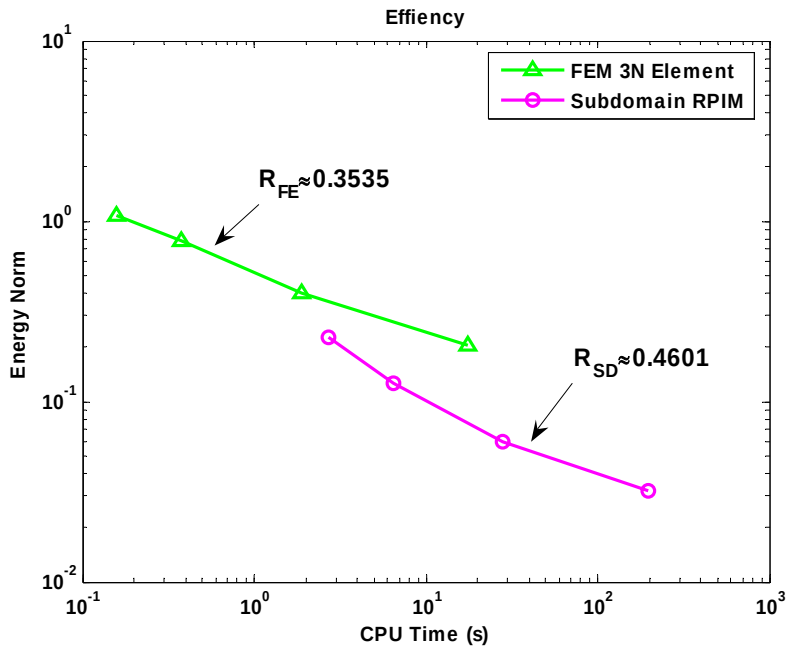

Figure 8.14 Efficiency in term of energy norm of the present method.

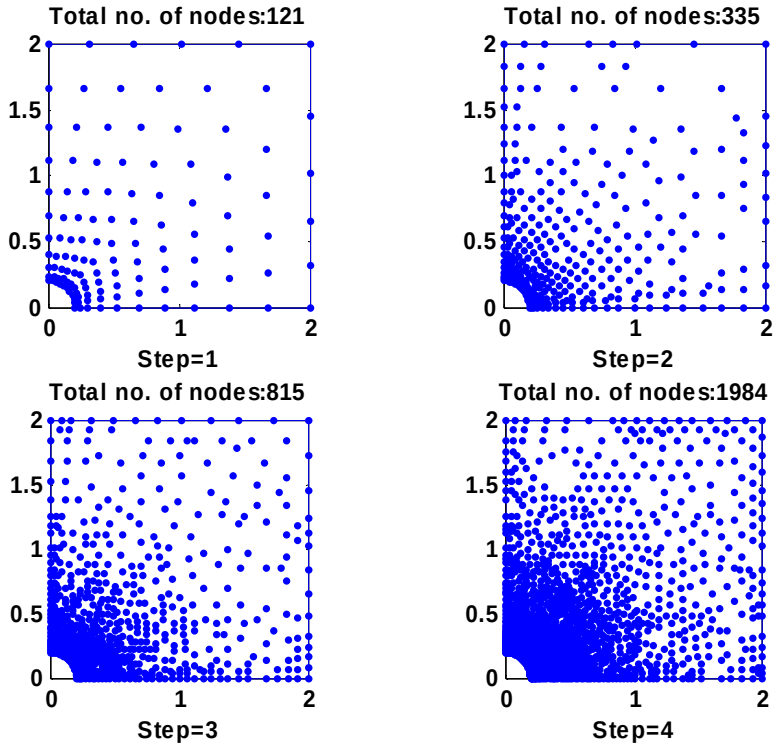

Figure 8.15 The nodal distribution at each adaptive step.

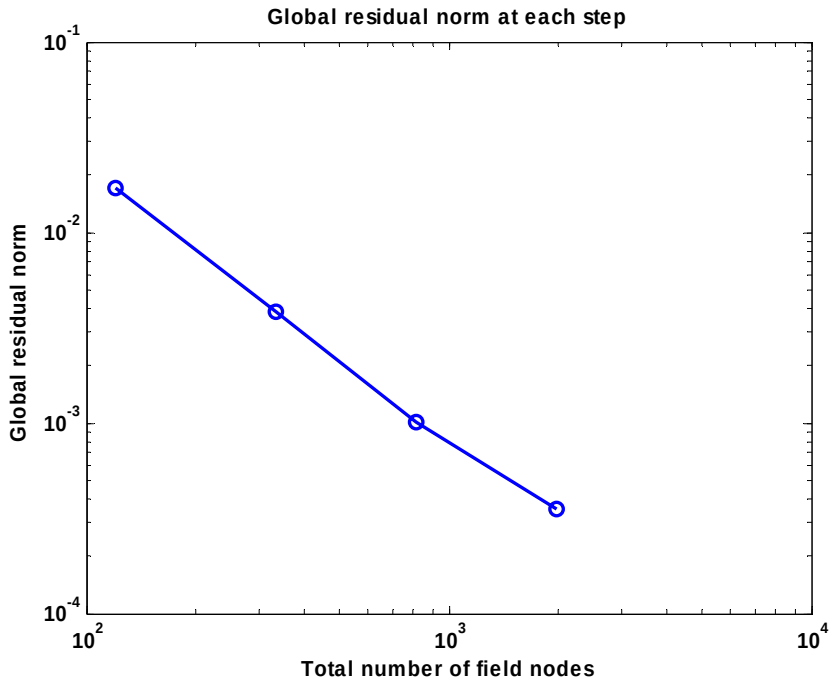

Figure 8.16 Approximated global residual norm at each adaptive step.

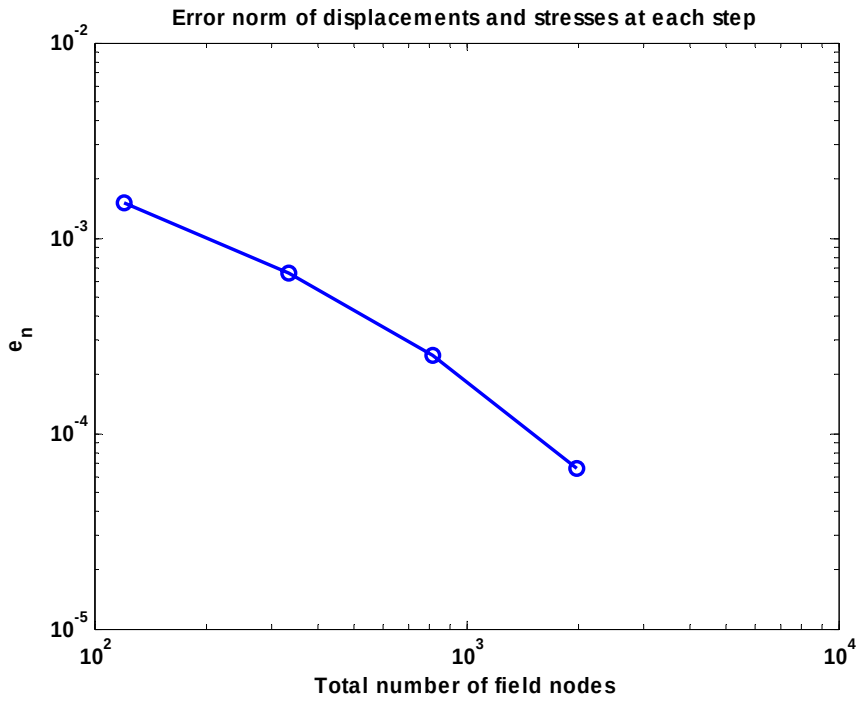

Figure 8.17 Error norm of displacements at each adaptive step.

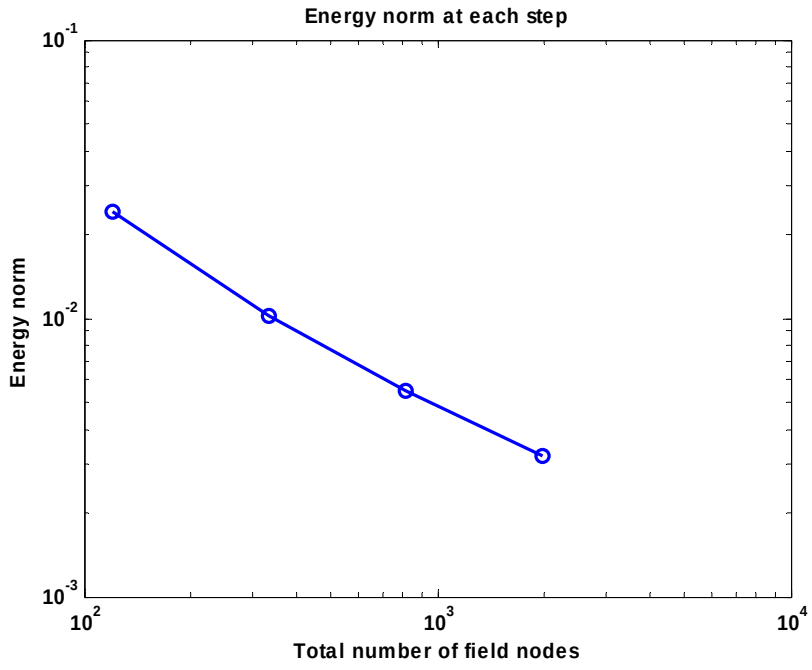

Figure 8.18 Energy norm at each adaptive step.

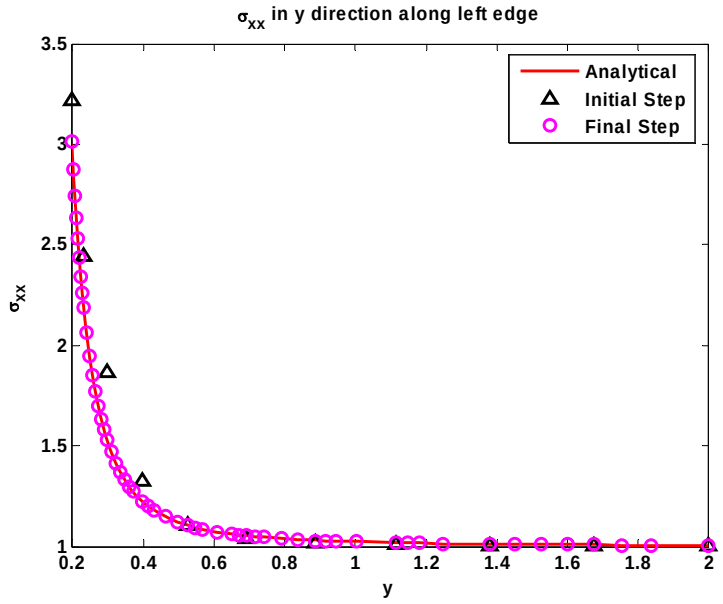

Figure 8.19 The normal stress σ_{xx} obtained by the subdomain method along left edge at initial and final adaptive steps.

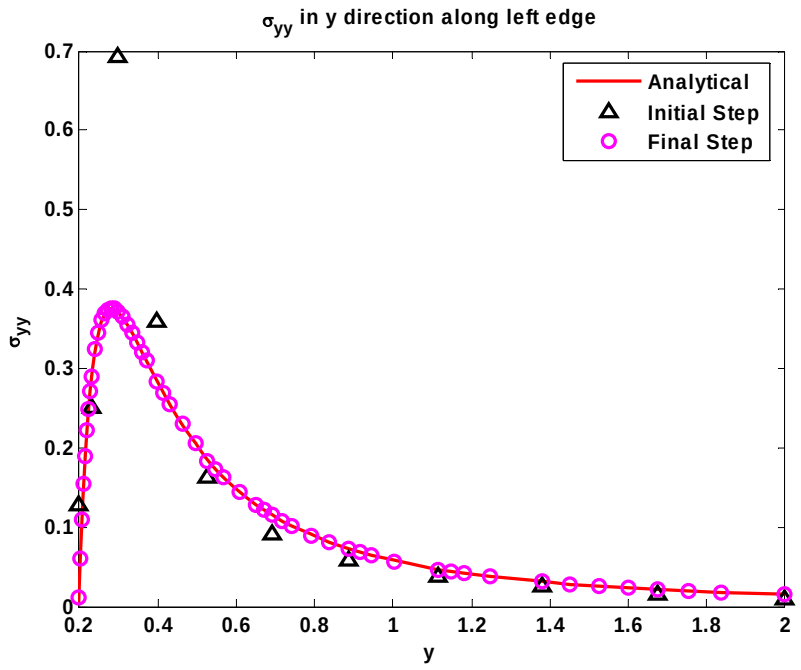

Figure 8.20 The normal stress σ_{yy} obtained by the subdomain method along left edge at initial and final adaptive steps.

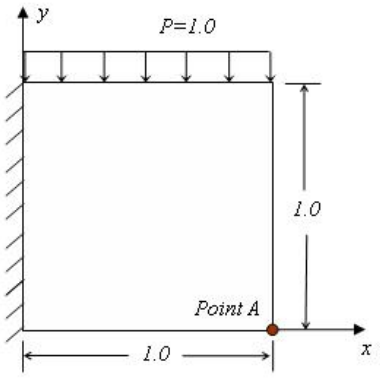

Figure 8.21 Model of a short beam subjected to a uniform loading on top edge.

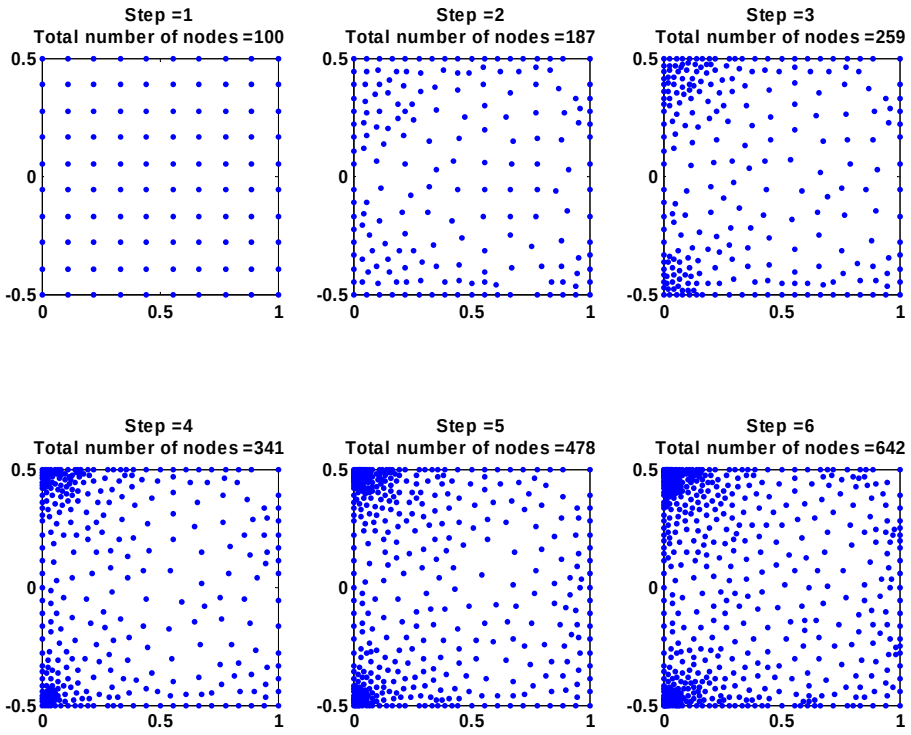

Figure 8.22 Nodal distribution for the model of short beam at each adaptive step.

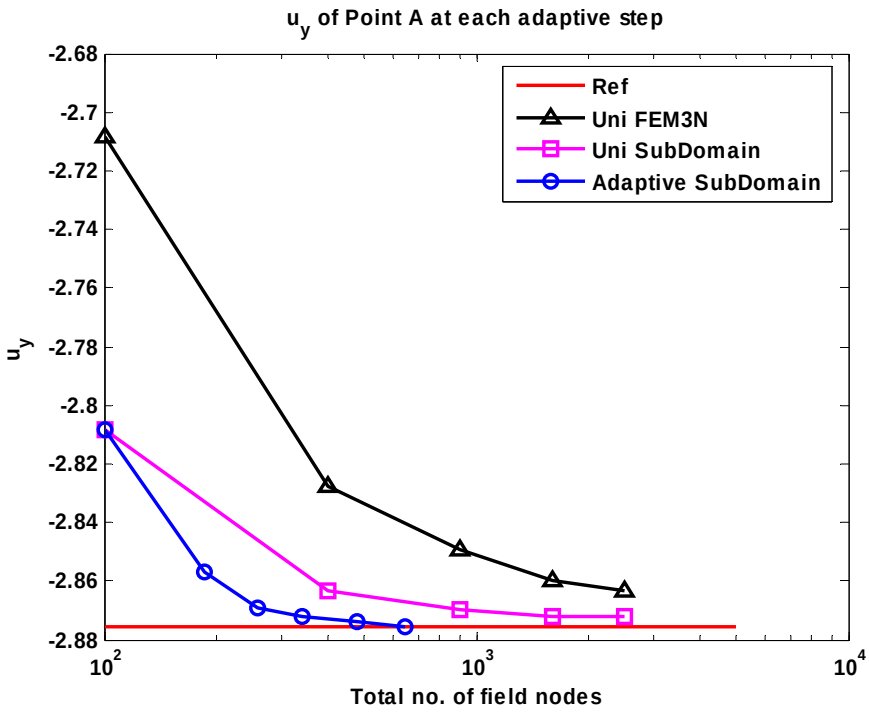

Figure 8.23 The displacement of Point A at each adaptive step.

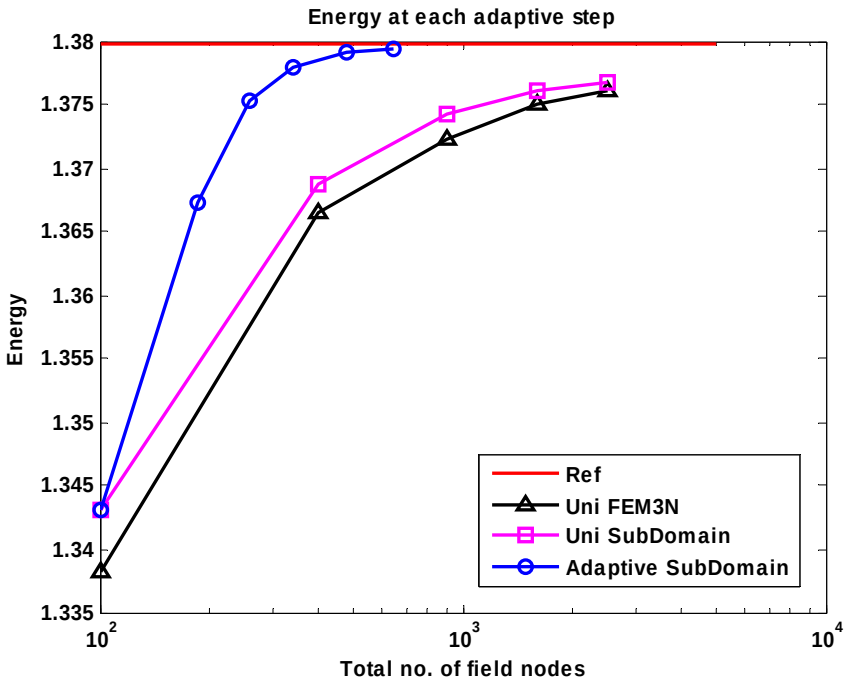

Figure 8.24 The approximated energy obtained by subdomain method at each adaptive step.

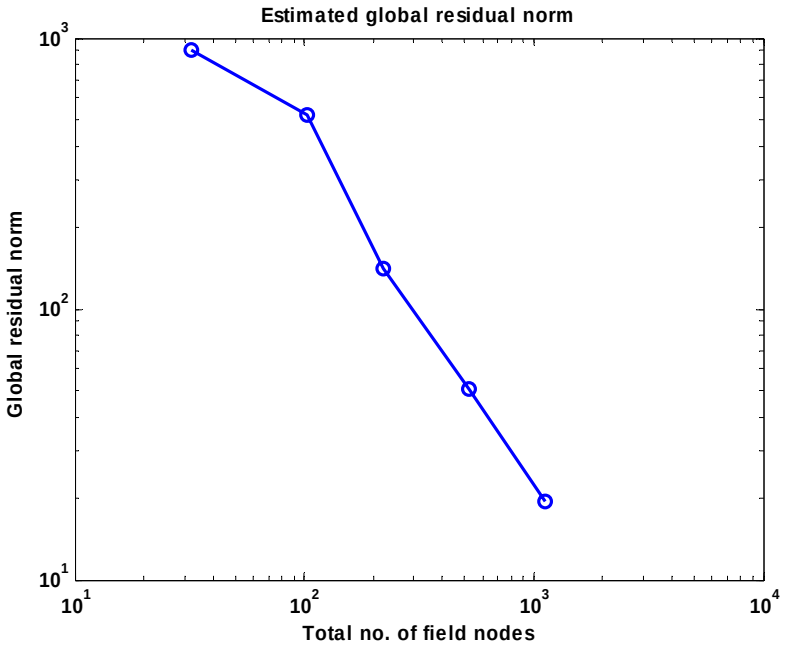

Figure 8.25 The estimated global residual norm at each adaptive step.

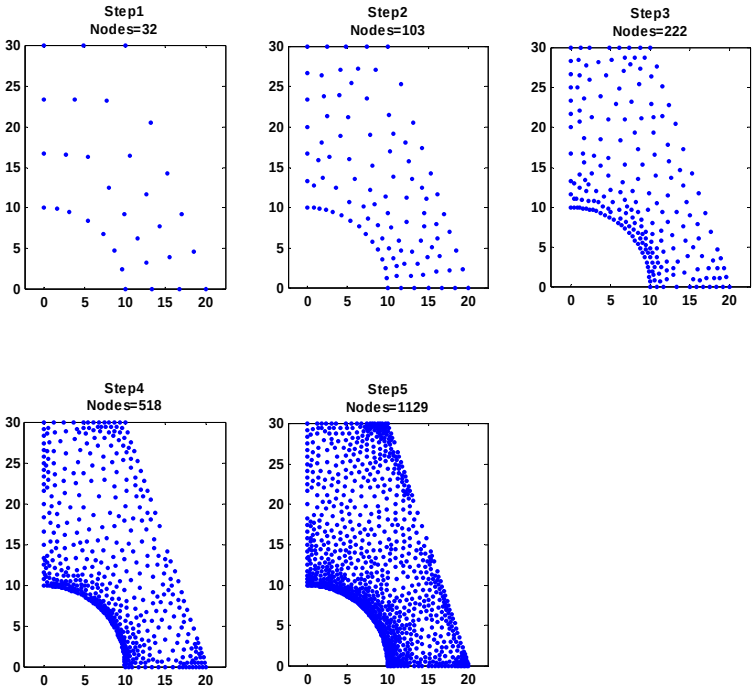

Figure 8.26 The nodal distribution at each adaptive step.

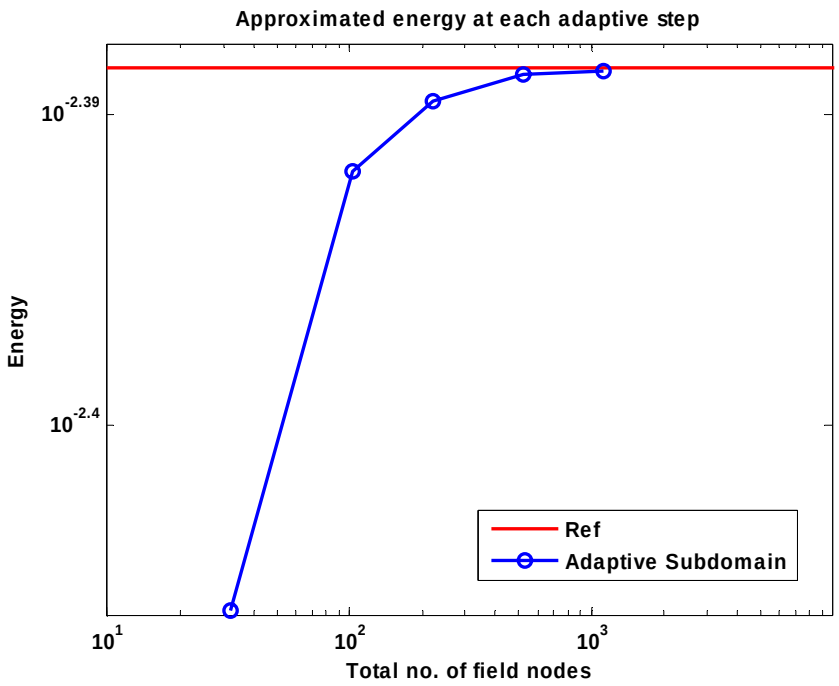

Figure 8.27 The approximated energy at each adaptive step.

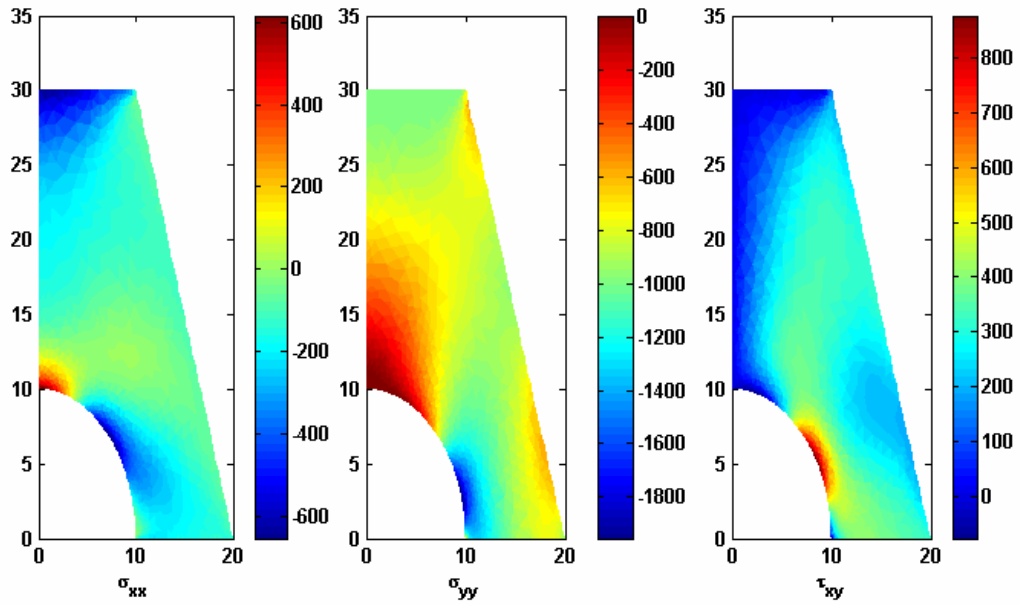

Figure 8.28 Contour plot of the approximated stresses obtained by present method at final adaptive step.

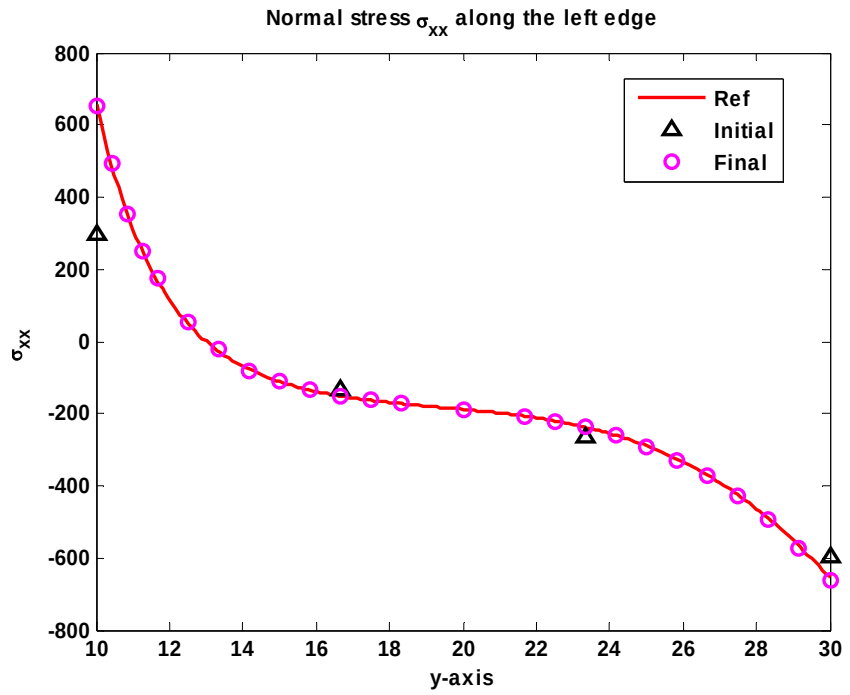

(a)

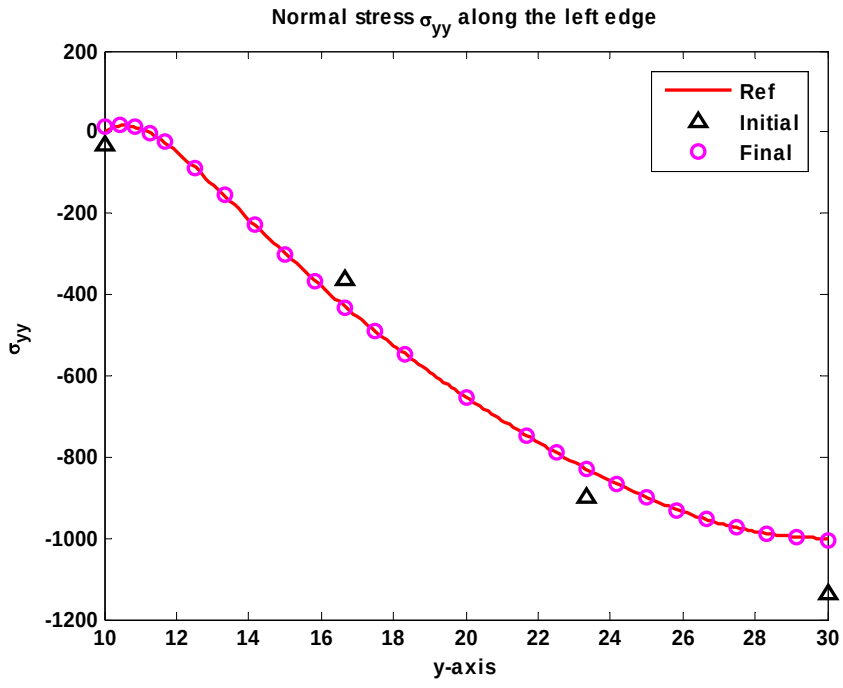

(b)

Figure 8.29 Normal stresses (a) σ_{xx} (b) σ_{yy} along the left edge at initial and final steps.

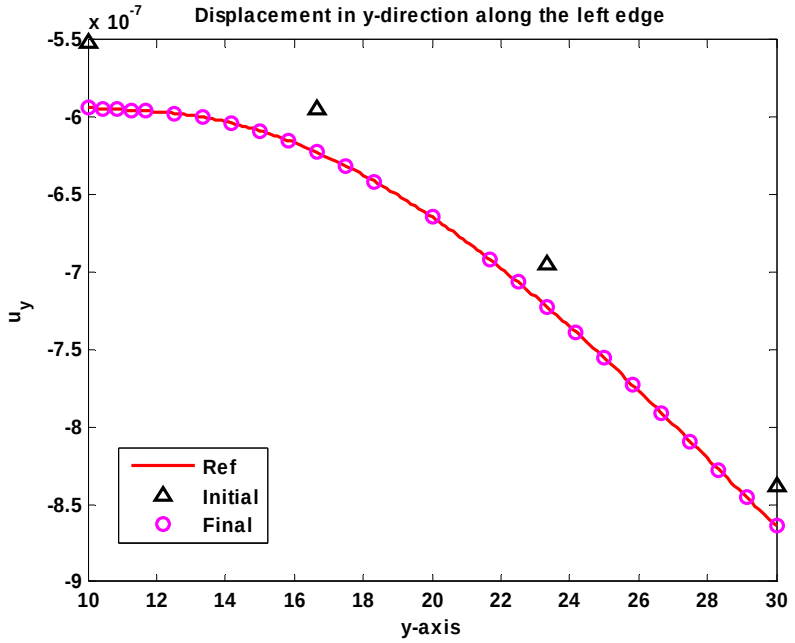

Figure 8.30 Displacements along the left edge at initial and final steps.

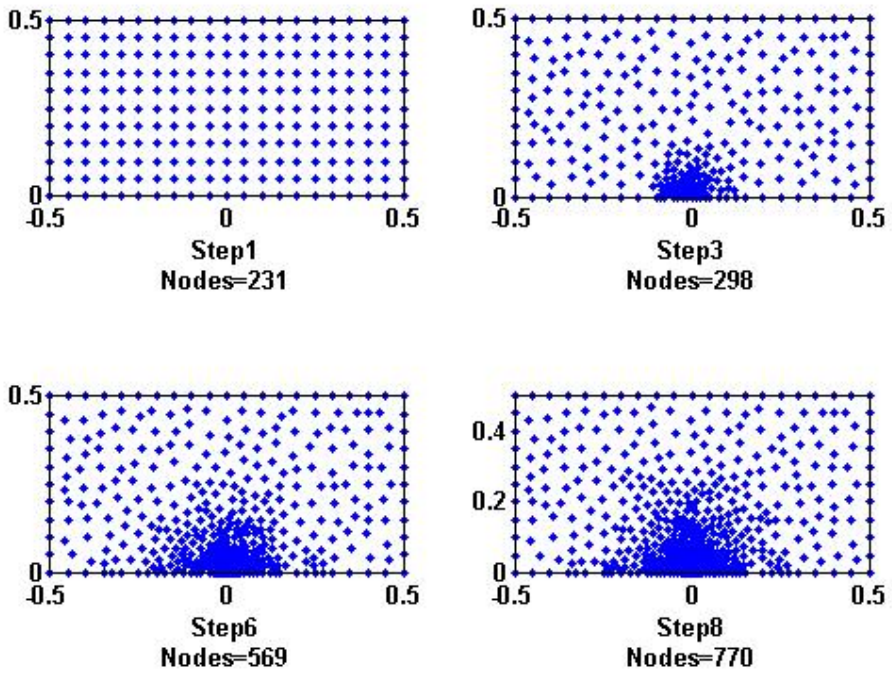

Figure 8.31 Nodal distributions at 1st, 3rd, 6th and final step.

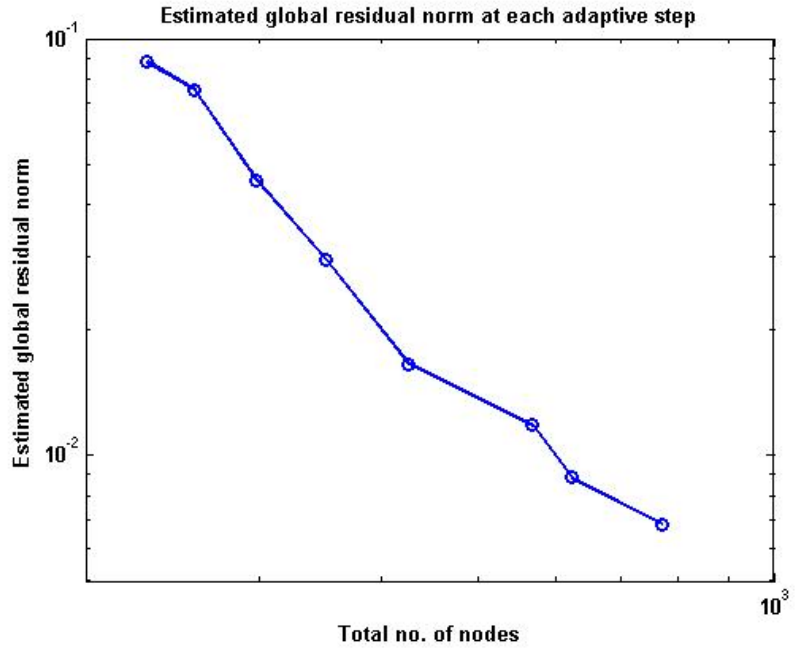

Figure 8.32 Global residual norm at each adaptivel steps.

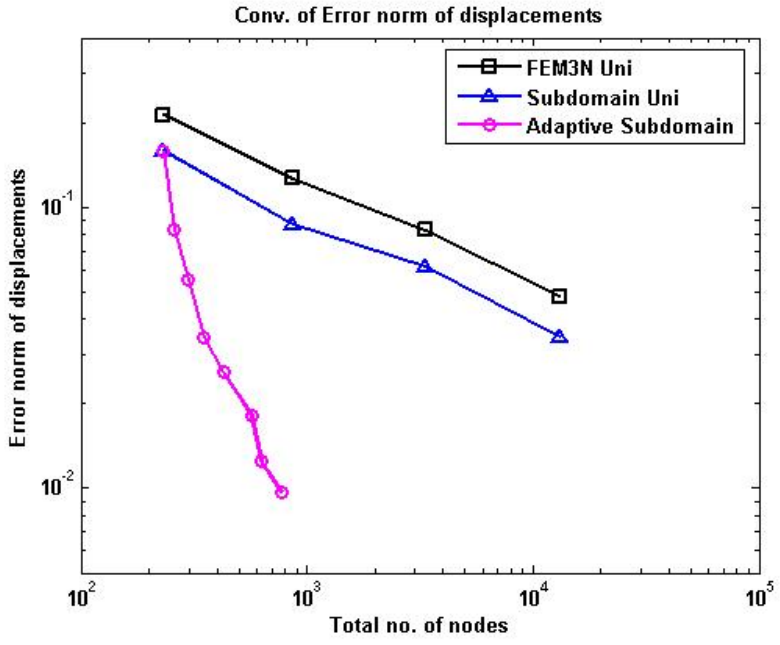

Figure 8.33 Displacements norm at each adaptivel step.

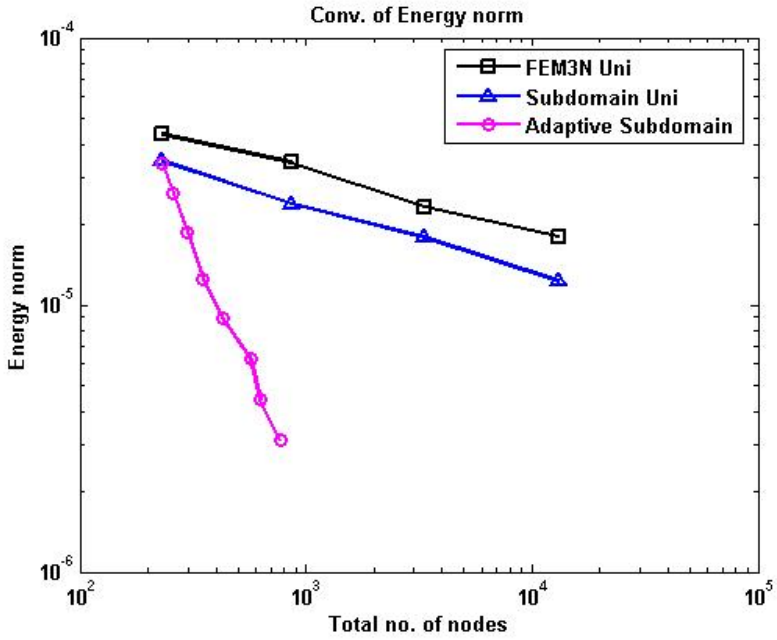

Figure 8.34 Energy norm at each adaptive step.

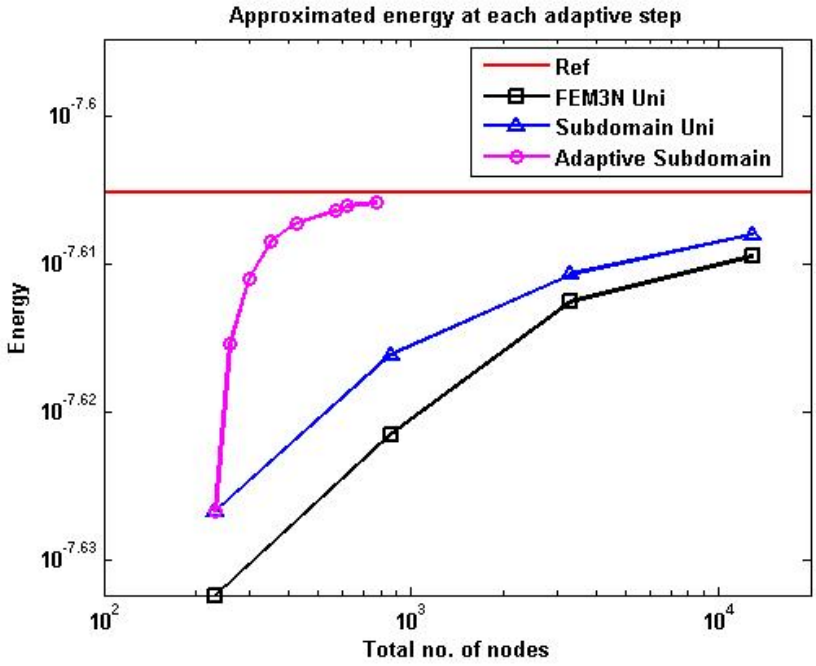

Figure 8.35 Energy at each adaptive step.

Chapter 9

Effects of the Number of Local Nodes for Meshfree Methods Based on Local Radial Basis Functions

9.1 Introduction

All the proposed meshfree methods proposed in this thesis are using RPIM approximation to construct their shape functions. Radial basis functions (RBFs) augmented with polynomial function is used in the RPIM approximation to approximate the local field function. As mentioned in the Chapter 2, RBFs are well-known in the mathematic community for its excellent numerical performance in approximation. Its have also been widely used for scattered data fitting and interpolation [19,31]. RBFs have been shown not only very good for interpolation purpose but also for the partial derivative approximation. Such feature is very attractive to meshfree methods for constructing their shape functions using arbitrary distributed nodes. Kansa is one of the pioneers who extend the application of RBFs in meshfree methods. In the early 90s, Kansa et al first introduced RBFs in the meshfree collocation method for solving partial differential equations (PDEs) [65,66]. Since then many

meshfree methods based on RBFs are proposed [23,32,33,93].

However, in the conventional meshfree method based on RBFs, field function and its partial derivatives are approximated using global nodes. It means that to approximate a field function or its partial derivatives at any interest point, all the nodes in the domain have to be used. The global RBFs will result in the following two critical drawbacks. First, the moment and coefficient matrices are full matrix. It is definitely undesired as computational time for solving the PDEs is huge. Compared to the existing dominant numerical methods such as, finite difference method (FDM), finite element method (FEM), which coefficient matrix are banded, the collocation meshfree methods based on global RBFs are not computational efficient.

Second, the condition of the coefficient matrix of the collocation meshfree method based on global RBFs is often ill. In the later work by Kansa, he had revealed the ill-conditioning problem encountered by global RBFs [66]. Remedies and suggestions such as matrix precondition, truncated interpolation scheme, multizone methods etc [66] had been proposed to prevent the ill-conditioning problem. Nevertheless, these remedies are rather expensive and not very effective. Global RBFs are still not practical for solving real life problems at this stage.

Recently, Liu et al have revised the conventional RBFs interpolation scheme and proposed a novel RBFs interpolation scheme using local nodes. Instead of using all the nodes in the problem domain for function approximation at any interest point, only *local nodes* (neighbouring nodes) of the interest point are selected to approximate the

field function and its partial derivatives. The idea of local RBFs has been devoted to many research works in meshfree methods and good results have been obtained [25-27,41-44,49-52,61-63,67-69].

As local RBFs is a promising scheme and many related research works have been published, the effects of the number of local nodes has to be studied. However, to my best knowledge, only the shape parameters of the local RBFs are thoroughly studied in literature [40,46,92]. A comprehensive study on the effects of the number of local nodes is still very demanding. In this chapter, the effects of the number of local nodes for meshfree methods based on RBFs are investigated. The study has been extended to both strong and weak formulation meshfree methods. A comparison between global and local RBFs is shown in paper through enormous examples in various meshfree methods.

9.2 Nodal Selection

Before the effects of the number of local nodes are studied, one should first understand how to select local nodes appropriately and what is the minimum number of nodes is required. From a computational cost point of view, as little as possible the number of nodes should be used, but provided the moment matrix **G** in Eq. (2.45) is not singular. Furthermore, as long as the field function in local domain is smooth and well modelled by local nodes, the number of local nodes can be varied from point to point in the global domain. It should be depending on the nodal distribution and the number of monomials used in the radial point interpolation scheme. In this work, two rules of

thumb for nodal selection are given:

(1) The number of local number must be greater than the number of monomials in Eq.(2.35), $n >> m$, such that the moment matrix **G** is invertible.

(2) The collocation point should not be located on the local boundary, except global boundary. **Figure 9.1** (a) shows the appropriate local nodes for radial point interpolation at a collocation point and **Figure 9.2** (b) illustrates the inappropriate selected local nodes. The coefficient matrix has high chances of suffering from rank deficiency if the selected local nodes bias on one side of the collocation point as shown in **Figure 9.2** (b).

Conventionally, the local nodes are chosen based on the Euclidean distance from the point of interest. Only nodes located in the neighbourhood of the interest point are favourable and should be selected. Those nodes further away from the interest point are intrinsically having no effect on the local approximation and hence be eliminated. In common practice, the number of nodes is two to three times of the number of monomials used in the radial point interpolation, $n \approx 2 \sim 3m$.

However, nodal selection based on the Euclidean distance is only feasible for problem which is modelled by regularly distributed nodes. Nodal selection based on the Euclidean distance is still not robust enough if the nodes are very randomly scattered in the domain. There are high chances that moment matrix **G** in Eq.(2.35) could be

singular, even the number of local nodes is greatly increased, say $n >> 3m$, rule (2) is still can not be guaranteed. Such problem always arises in the adaptive analysis.

To avoid the awkward scenario happens, the number of local nodes should not be fixed and nodal selection should not solely depends on the Euclidean distance. Thus, nodal selection based on the concept of layer is proposed. In this work, every node can be seemed as being surrounded by numbers of layers of supporting nodes. If the order of the PDEs is *k*, then the same number of layers of nodes is used in nodal selection. This concept of layers has been very successfully implemented in my works [70,71] and it has been shown very robust, efficient and feasible, even for randomly scattered nodes.

9.3 Concept of Layer

As all problems studied in this work are second orders PDEs, double layers of nodes are used. The immediate layer of supporting nodes can be formed by Delaunay diagram as shown in **Figure 9.2** (a). Let $x_1, x_2, \cdots, x_n$ be a set of *n* distinct nodes in the problem domain denoted by $\{x_k\}$ and T_i is the cell of Delaunay which contains three nodes in the problem domain to form that particular cell. Say node *P* in **Figure 9.2** (a), any Delaunay cell which consists of node *P*, all the nodes of that particular cell will become a member of the set of immediate layer of supporting nodes for node *P*.

$$T_i \subset \mathbf{s}_P \quad if \ \mathbf{x}_p \in T_i, \tag{9.1}$$

where $\mathbf{s}_P$ is the set of the immediate layer of supporting nodes for node *P*. The second

layers of supporting nodes are those nodes in their corresponding immediate layers of the first layer's nodes as shown in **Figure 9.2** (b). With such scheme, one can ensure that no 'extrapolation' happens during the construction of shape functions except the boundary nodes. No matter how randomly the nodes scattered in the problem domain, the moment matrix **G** is always invertible. Therefore, this is a very robust nodal selection scheme for adaptive analysis. In the examples given in this paper, scheme with double layer of nodes has been shown cost effective in computation with good accuracy. Similar idea of layer is also found in Ref. [87].

9.4 Numerical Examples

In this work, a large number of numerical examples are presented to study and facilitate the understanding of the effects of number of local nodes for meshfree methods based on local RBFs. These meshfree methods include both strong and weak formulation methods. These examples are given to demonstrate the advantages of RBFs using local nodes. Comparison between global RBFs and local RBFs is made in this work. For simplification purpose, only multi-quadratic (MQ) RBF is studied. The shape parameters, $q = 1.03$ and $\alpha_c = 3.0$, are adopted from recommended values reported by Liu et al [40,46,92]. In the radial point interpolation, completed second order polynomial function, $m = 6$, is augmented with MQ-RBF.

9.3.1 Examples 1: Curve Fitting

The first example is presented to reveal the some important observations of the

local radial point interpolation. A square domain is modelled by a set of 121 regularly distributed nodes. Consider the following smooth field function as

$$u = \sin \pi x \sin \pi y \,, \tag{9.2}$$

in the domain of $\Omega : [0,1] \times [0,1]$, the derivatives of the field function can be derived as

$$\frac{\partial u}{\partial x} = \pi \cos \pi x \sin \pi y \,, \tag{9.3}$$

$$\frac{\partial^2 u}{\partial x^2} = -\pi^2 \sin \pi x \sin \pi y \,, \tag{9.4}$$

$$\frac{\partial^2 u}{\partial x \partial y} = \pi^2 \cos \pi x \cos \pi y \,, \tag{9.5}$$

as plotted in **Figure 9.3**.

The derivatives of the given field function, $\frac{\partial u}{\partial x}, \frac{\partial^2 u}{\partial x^2}, \frac{\partial^2 u}{\partial x \partial y}$, are approximated by radial point interpolation with different number of local nodes used. Their error norms are shown in **Figure 9.4**, and their corresponding computational times are also given in **Figure 9.5**. From **Figure 9.4** and **Figure 9.5**, one can notice the local RBF is not only more accurate than global nodes but also tremendously reduces the computational time. In this example, the absolute error of the approximated derivates of the given field function, $\frac{\partial u}{\partial x}, \frac{\partial^2 u}{\partial x^2}, \frac{\partial^2 u}{\partial x \partial y}$ are also plotted in **Figure 9.6** to **Figure 9.8**. One can observe that the errors along the boundary points are relatively larger than the interior points. This is because the interpolation points on the boundary are no longer at the centre of

the local supporting domain and hence large error is found along the boundary. This observation is very much in line with the finding presented in the Refs. [40,46,62,92].

9.3.2 Examples 2: LC-RPIM (Weak-form Method) for Elastostatics Problem

This example is the study on the effects of the number of local nodes for meshfree weak-form method based on RBFs. In the paper by Li et al [36], a meshfree weak-form method called LC-RPIM is proposed. In the formulation procedure of the LC-RPIM, local RBFs are used for function approximation.

A benchmark solid mechanics problem, cantilever beam subjected to a parabolic shear stress at the end, is used to demonstrate the effects of the number of local nodes. The model of the cantilever beam is shown in the **Figure 4.11**, where $L = 48m$ and $D = 12m$. The material properties are given as Young's modulus $E = 3 \times 10^7$ and Poisson's ratio $\upsilon = 0.3$ and the loading is given as $P = \int \tau_{xy} dy = -1000N$.

The governing equations and the boundary conditions of solid mechanics problems are known [89] as listed in Eq. (4.19) to Eq. (4.21). In this example, Dirichlet boundary conditions are applied along the left edge and the loading is applied along the right edge.

A model made up of 341 regularly scattered nodes is used in the LC-RPIM to study the effects of the number of local nodes. The error norms of displacements and energy norms plotted in **Figure 9.9** and **Figure 9.10** show solutions of the LC-RPIM based on local RBFs are as good as global RBFs. The increase of the local nodes does

not help to improve the accuracy of displacements, though the energy norm seems only slightly better while global nodes are used. The condition number of the stiffness matrix of LC-RPIM with local nodes is slightly lower that the global nodes as shown **Figure 9.11**. Nevertheless, the extremely high computational cost of LC-RPIM based on global RBFs prevents it from solving practical problem. One can notice from **Figure 9.12** that the computational time required by LC-RPIM is increasing exponentially with increase of the local nodes. Solving problem using LC-RPIM based on global RBFs becomes not practical as local nodes scheme is able to provide reasonable good results with only little computational time required.

9.3.3 Examples 3: RPCM (Strong-form Method) for Torsion Problem

In this example, the study on the effects of the number of local nodes is conducted for a meshfree strong-form method. Radial point collocation method (RPCM) [61-63] is a meshfree strong-form collocation method that using local nodes. In the RPCM, field function is approximated based on local RBFs. A linear elastostatics problem is studied in this example. A bar with triangular cross section as shown in **Figure 9.13** (a) is subjected to a torsion moment. The material properties of the bar are known as: Young's modules $E = 1 \times 10^7$ and Poisson's ratio $\upsilon = 0.3$.

The governing equation of torsion problem is well-known as [90]

$$\frac{\partial^2 \varphi}{\partial x^2} + \frac{\partial^2 \varphi}{\partial y^2} = -2G\theta, \tag{9.6}$$

where φ is the stress function, *G* is the shear modulus of the bar and θ is the twisted angle. The relationship between the stresses and stress function is known as

$$\tau_{yz} = \frac{\partial \varphi}{\partial x};\ \tau_{yz} = \frac{\partial \varphi}{\partial x}, \tag{9.7}$$

The boundary conditions of this torsion problem is known as

$$\frac{\partial \varphi}{\partial y}\frac{\partial y}{\partial s} + \frac{\partial \varphi}{\partial x}\frac{\partial x}{\partial s} = \frac{\partial \varphi}{\partial s} = 0, \tag{9.8}$$

and it shows the stress function φ must be a constant along the boundaries of the cross section. φ is arbitrary chosen as zero, and twisting angle is given as $\theta = 1$. The analytical solution of this problem is given as [90]

$$\varphi = -G\theta\left[\frac{1}{2}\left(x^2 + y^2\right) - \frac{1}{2a}\left(x^3 - 3xy^2\right) - \frac{2}{27}a^2\right]. \tag{9.9}$$

In this example, the torsion problem is first modelled by 120 regularly distributed nodes as shown in **Figure 9.13** (b). The error norms of the stress function obtained by the RPCM using different number of local nodes are plotted in **Figure 9.14**. Apparently, the RPCM using global nodes for function approximation is not a practical idea. In **Figure 9.14**, it has shown the accuracy of solution that using global RBFs is relatively low. In addition, **Figure 9.15** also shows the computational cost is tremendously higher than the RPCM using local nodes. Furthermore, it can be seen in **Figure 9.16** that the condition number of the coefficient matrix is increasing greatly while the number of local nodes increases. The condition number of the coefficient matrix of RPCM using

global nodes is the highest as shown in **Figure 9.16**.

To study the convergent rate, the numerical solutions for 5 sets of nodes, 66, 120, 231, 325, 496 are computed. For comparison purpose, the convergent rate of the RPCM with 25 local nodes, global nodes and double layer of nodes are plotted in **Figure 9.17**. The convergent rate of the error norm of RPCM using global nodes is the lowest among the three schemes and the accuracy is not as good as the RPCM using local nodes. The accuracy of the RPCM using double layer of nodes is the best among the three schemes and the convergent rate is also the highest.

The computational time required by each schemes for these five sets of nodes are plotted in **Figure 9.18** for comparison. Among these three schemes, the computational time of the RPCM using global nodes is the highest and increasing with much higher rate while the number of field nodes is increased. RPCM using two layers of nodes requires the least computational time.

In this example, it can be noticed in **Figure 9.19** that the condition number of the coefficient matrix of RPCM using global nodes is the largest and grows faster than RPCM using local nodes while total number of field nodes is increasing.

In short, the efficiency plot shown in **Figure 9.20** has strongly supported the argument that the local RBFs are the more practical, efficient and accurate compared to the global RBFs. The advantages of the function approximation using local RBFs are well demonstrated in this example. And the proposed scheme with double layers of nodes is the best among all schemes.

9.3.4 Examples 4: RLS-RPCM (Strong-form) for Elastostatics Problem

In this example, a solids mechanics problem that solved by the regularized least-square radial point collocation method (RLS-RPCM) [67] using local nodes is investigated. The RLS-RPCM is a strong-form meshfree method, which regularization procedure is adopted to stabilize the solution of RPCM while dealing with Neumann boundary conditions. A benchmark solid mechanics problem, an infinite plate subjected to a horizontal uniaxial traction, $P=1$, is studied. The geometry of the plate is shown in **Figure 5.7**, where $a=0.2$, $b=2.0$. The material properties of the plate are given as Young's modulus $E=1\times10^{3}$ and Poisson's ratio $\upsilon=0.3$.

The governing equations and boundary conditions of solid mechanics problem are as listed in Eq. (4.11) to Eq. (4.13). In this example, due to symmetric, only the right top quarter of plate is modelled. Symmetric conditions are applied along the left and bottom edges of the model as shown in **Figure 5.7**.

The effects of the number of local nodes for meshfree strong-form method are clearly revealed from the results as shown from **Figure 9.21** to **Figure 9.25**. From the error norms of displacements and stresses plotted in **Figure 9.21** and **Figure 9.22**, accuracy of RLS-RPCM solution based on global RBFs is extremely low. The poor accuracy could due to the ill-conditioned coefficient matrix as shown in **Figure 9.21**. The condition number of the coefficient matrix of the global scheme is as high as 5.6179e+015. Another cause of poor accuracy may due to the interpolation for the

concave domain. As RBFs are not appropriate for concave domain, special technique is needed to overcome this difficulty. In practice, as geometry of problem can be rather complex, the global scheme of radial point interpolation is not as robust as local scheme. From a computational cost point of view, the CPU time required by the global scheme is too expensive as shown in **Figure 9.29**. This example clearly shows the global scheme is an impractical and expensive approach, reliable and accurate solution can not be guaranteed also.

9.3.5 Examples 5: Adaptive RPCM for Dirichlet Problem

To further demonstrate the efficiency of RPCM base on different number of local RBFs, an example of adaptive analysis is presented. In this example, a Poisson problem with high gradient solution is studied. The below Poisson equation is considered,

$$\nabla^2 u = \tan^{-1}\left(1000x^2y^2 - 1\right), \quad \Omega : [0,1]\times[0,1]. \tag{9.10}$$

The Dirichlet boundary conditions are imposed along the boundary,

$$u = \tan^{-1}\left(-1\right), \quad \Gamma : x = 0 \; or \; y = 0; \tag{9.11}$$

$$u = \tan^{-1}\left(1000y^2 - 1\right), \Gamma : x = 1; \tag{9.12}$$

$$u = \tan^{-1}\left(1000x^2 - 1\right), \quad \Gamma : y = 1 \tag{9.13}$$

The analytical solution of this Poisson problem is known as

$$u = \tan^{-1}\left(1000x^2y^2 - 1\right), \tag{9.14}$$

Solution of field function and it derivatives are plotted in **Figure 9.26**.

In this example, the adaptive analyses are carried out by three different schemes which are:

(1) local RBFs with 25 nodes,

(2) local RBFs with double layers of nodes,

(3) global RBFs.

All scheme are initiated with 20×20 regularly distributed nodes in the domain $\Omega:[0,1]\times[0,1]$ as shown in **Figure 9.27** (a). In this example, the local refinement coefficient and global residual tolerant are preset as $\kappa_L = 0.05$ and $\kappa_G = 0.05$ respectively. The details of the adaptive strategy can be found in Chapter 3. For comparison, the final nodal distribution of each scheme is shown in **Figure 9.27** (b)-(d). It can be seen that the final nodal distributions of the local scheme are better than the global scheme. In the local scheme, most of the nodes have been inserted at the critical region where the gradient of field function is high, however, not global scheme. The reason of ineffective refinement of the global scheme could due to the unstable numerical solution that affects the performance of the residual error estimator, and hence leads the refinement of the additional nodes to inappropriate position.

All local schemes take 4 steps to complete the computation and done in a few minutes. The adaptive RPCM with 25 local nodes take 224 seconds and the adaptive

RPCM with two layers of nodes take only 177 seconds to complete entire analysis. For the RPCM using global nodes, solution is unstable due to the ill-conditioned coefficient matrix. The adaptive analysis takes more than 4 steps to complete; however, the solution is terminated up to the 4^{th} step for convenience. The computational cost of the RPCM using global nodes is extremely expensive. The initial step already requires 2836 seconds to complete and the computational time accumulated up to the 4^{th} step is 47.5611 hours. Therefore, from the efficiency plot in **Figure 9.29**, one can find that efficiency of the global scheme is tremendously poor. The efficiency of the adaptive RPCM using 25 local nodes and two layers of nodes are comparable to each other. Both schemes required much lesser time than global scheme and able to provide excellent accuracy.

Furthermore, the high condition number of the coefficient matrix of global scheme is also clear shown in **Figure 9.30**. While the total number of field nodes is increased more than 1000 nodes, the condition number for global scheme is very ill, whereas the coefficient matrices of the local scheme are still in the good condition. Hence, the solution of RPCM using global nodes becomes very unstable as the coefficient matrix is almost singular. It again shows the global RBFs not only inefficient but also leads the discretized system to ill condition. This example evidently shows the purpose and the advantages of the local RBFs against the global RBFs for solving practical problem.

9.5 Remarks

In the first examples, RBFs are adopted for the curve fitting purpose. Apparently,

the radial point interpolation using global RBFs is shown computational expensive. In contrast, the radial point interpolation using local nodes can be very much cheaper but yet without compromising the accuracy of solutions. As long as the 'local' field function is smooth enough, good approximation can be achieved. Large interpolation error is observed along the boundaries, and this finding also in line with the observation in other literature [40,46,62] as shown in the second example. As the quality of the local radial point interpolation can be ensured, the reason for meshfree method based local RBFs is clear.

In this work, various types of meshfree methods are used for investigation. A thorough study on the effects of the number of local nodes for different meshfree methods based on RBFs, which includes the meshfree weak-form method: LC-RPIM, and meshfree strong-form methods: RFDM, RPCM and RLS-RPCM. Through the collective results and the experiences gained in the numerical experiments through many of my previous works, the effect of the number of local nodes can be concluded and summarized into the following aspects.

(a) Computational Cost

No doubt, global RBFs scheme is very costly compared to local RBFs scheme. It is clearly demonstrated in all examples that the more the number local nodes, the higher the computational cost. Although the procedure of nodal selection is eliminated (as all field nodes are used) in the global RBFs, the computation of the inverse for the full moment matrix **G** in Eq. (2.46) still incurs huge computational cost. Secondly, global

RBFs result in a full coefficient matrix that cost the solving of the simultaneous algebraic equations to maximum.

A rough comparison of the cost of solving simultaneous equations with sparse matrix versus full matrix is provides as follows. Simultaneous equations with sparse matrix approximately requires $4Np^2$ operations to be solved by Gauss Elimination with partial pivoting, where N is the total number of degree of freedom (d.o.f) and p is the bandwidth of the matrix. Whereas, solving simultaneous equations with the full matrix requires $4N^3$ operations approximately. The ratio of the operations required for global and local RBFs in solving simultaneous equations is roughly $(N/n)^2$, where n is the number of local nodes. This rough estimation is not yet taking the operations required for forming shape functions into the account. For instance, in Example 3, the computational time for RPCM based local RBFs using 25 nodes is 0.3906s and 4.3590s for RPCM based on global nodes. The approximated computational cost of the global scheme is about $N/n = 66/25 = 2.64$ times of the local scheme. The actual ratio of the computational times between local and global scheme is $4.3590/0.9063 = 4.8096 > 2.64$. The actual computational time of the local scheme is much smaller than the approximated one.

(b) Condition of the coefficient matrix and moment matrix

Condition of the coefficient matrix is another important aspect to study. From observation, it is found that the stiffness matrix of the weak-form meshfree method is not sensitive to the number of local nodes. Whether local or global nodes are used, the

stiffness matrix remains in good condition as shown in the Example 2. It is because of the procedure of the weak formulation always produces a symmetric and positive definite matrix (SPD) stiffness matrix. On the contrary, the coefficient matrix of the strong-form meshfree method, a non-symmetric matrix usually, is very sensitive to the number of local nodes. According to the intensive study, the global RBFs always leads to an ill-conditioned coefficient matrix. Similar conclusion can be found in Kansa's works [66]. Compared to global RBFs, one can notice that the local RBFs are always providing a coefficient matrix with better condition as demonstrated in Example 3-5. This is a very strong evidence to show local RBFs is more favourable for meshfree strong-form methods.

The condition of the moment matrix is also another great concern which is influenced very much by the local nodes. While global RBFs is used in the domain with randomly distributed nodes for approximation, most likely some nodes are very close to each other and it will cause their corresponding rows the moment matrix not so linearly independent to each other. Consequently, the condition number of the moment matrix is generally very large and it leads to a very poor approximation for the derivatives. In contrast, the local RBFs only construct shape functions using local nodes, moment matrix is only formed for the local domain. Thus, the nodal distribution in the local domain is not as severely random as compared to the global domain. Additionally, the nodes in the local domain are much lesser than the global domain, and hence the condition of the moment matrix and the approximation of the derivatives of local RBFs are much better global RBFs.

(c) Accuracy

No significant evidence shows global RBFs hold any prominent advantages against local RBFs. In the curve fitting problem illustrated in Example 1, one can find that the approximation of derivatives based local RBFs can be as accurate as global RBFs. In the example of meshfree weak-form method, solution of local RBFs scheme performs as good as the global RBFs with a cheaper computational cost. For strong-form meshfree methods and its adaptive analysis, local RBFs scheme has demonstrated excellence performance with incredible accuracy. Meshfree strong-form methods based on global RBFs is not a robust, efficient and reliable method.

(d) Other aspects

There are some other aspects to be considered such as geometry of the domain. As interpolation scheme based on the RBFs is not appropriate for concave domain, special technique is required to tackle this critical problem. Therefore, while dealing with concave global domain such as Example 3, good approximation can not be achieved. However, the local support domain for local RBFs can be seen as a convex domain to certain extent. Hence, it is more appropriate to use local RBFs generally.

Not to mention, the storage required for the full matrix resulted in global RBFs is also another challenges. The computational cost and the problem of storage will get more expensive and severe when the scale of the problem becomes larger.

From the above findings, concrete evidences are provided and show the performance of local RBFs scheme is more superior to global RBFs scheme. Hence, it

is more recommended to use local RBFs to construct the shape function or approximate the field function.

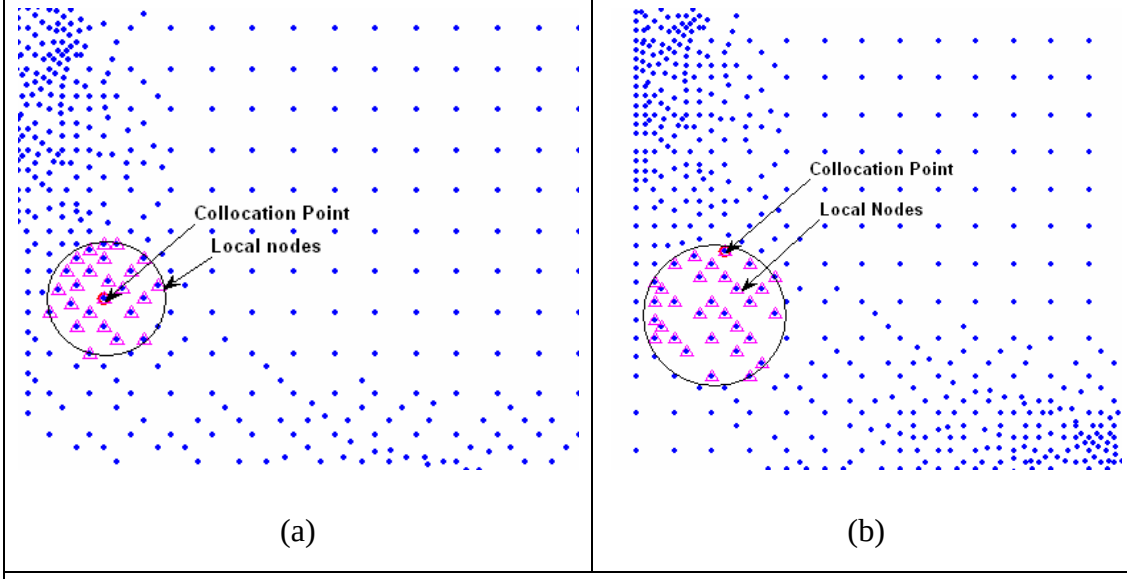

Figure 9.1 (a) Appropriate and (b) inappropriate selection of local nodes for local RBFs.

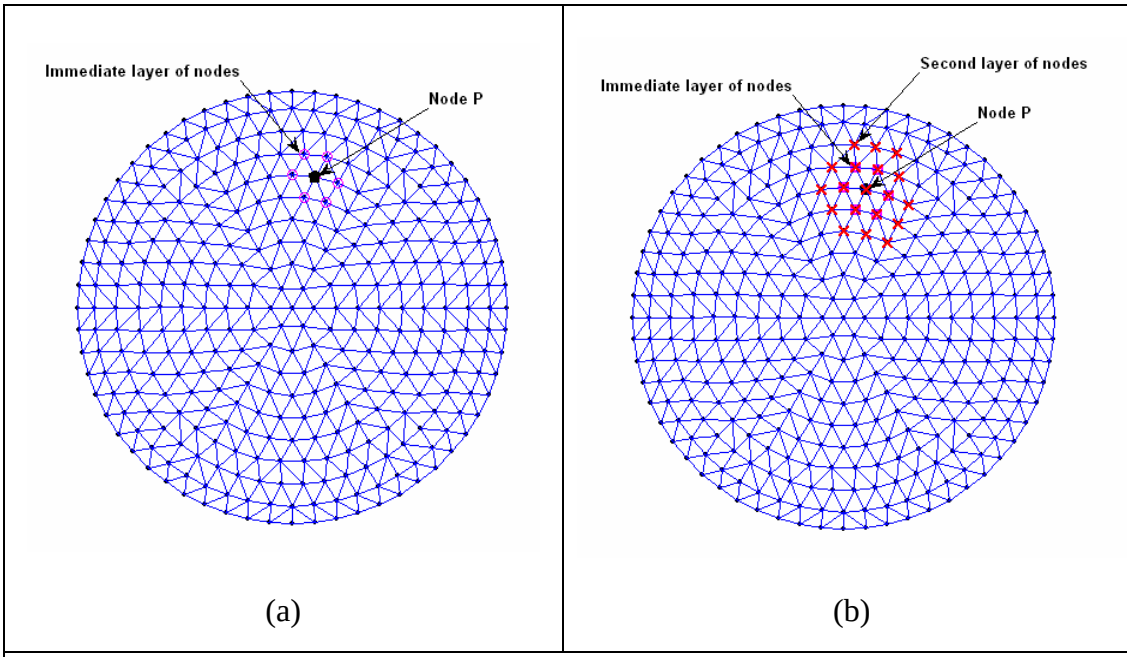

Figure 9.2 (a) Immediate layer and (b) the second layer of supporting nodes.

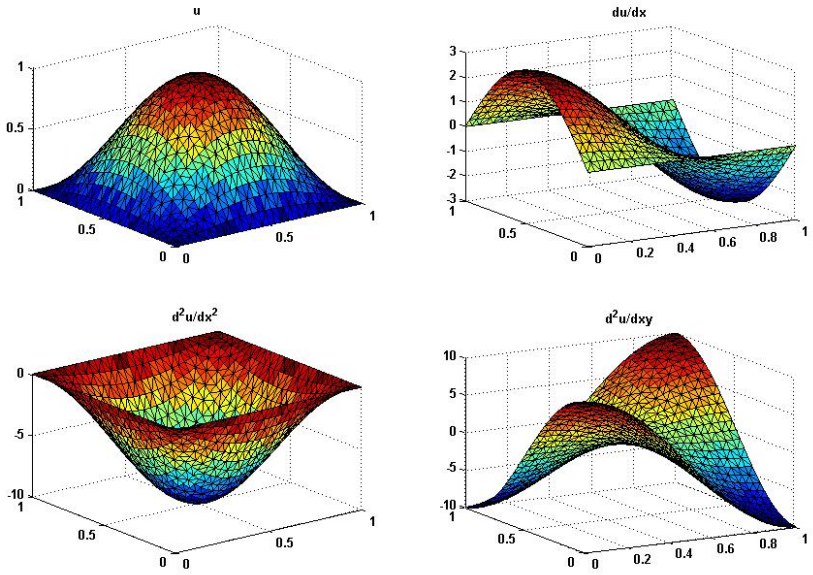

Figure 9.3 The given field function *u*, and the analytical solutions of $\frac{\partial u}{\partial x}$, $\frac{\partial^2 u}{\partial x^2}$ and $\frac{\partial^2 u}{\partial x \partial y}$.

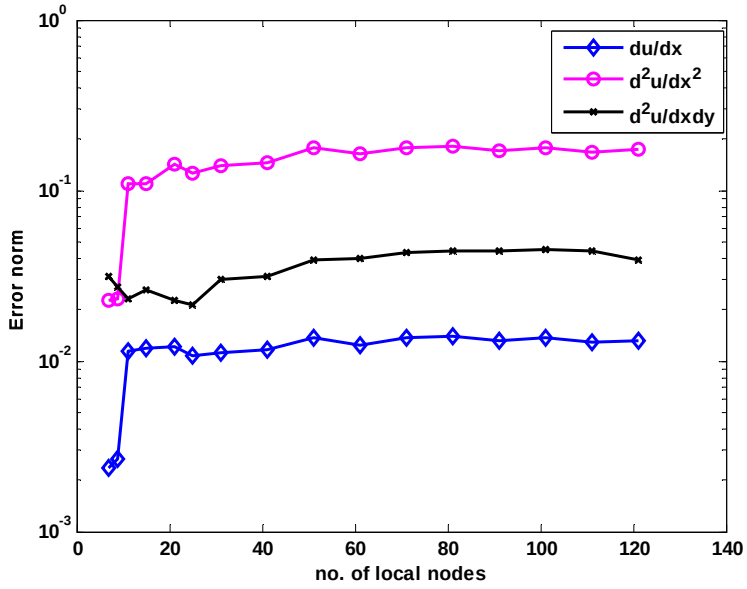

Figure 9.4 The error norms of the approximated $\frac{\partial u}{\partial x}$, $\frac{\partial^2 u}{\partial x^2}$ and $\frac{\partial^2 u}{\partial x \partial y}$ with different number of local nodes.

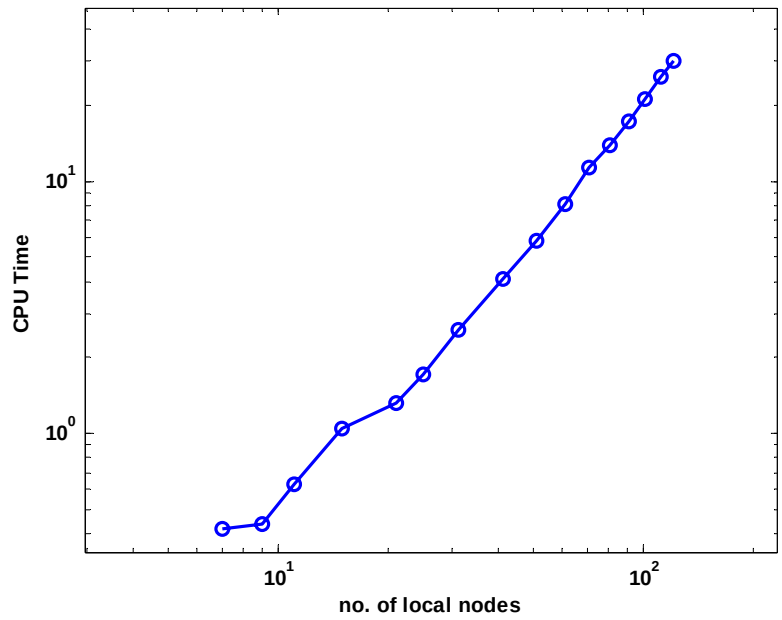

Figure 9.5 Computational time of the interpolation scheme using different local nodes.

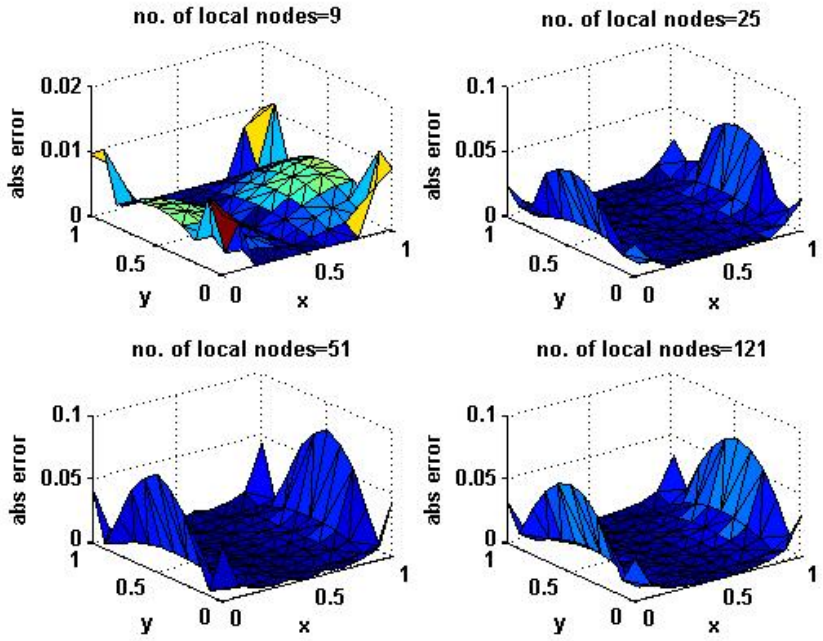

Figure 9.6 The absolute error distribution of $\frac{\partial u}{\partial x}$ approximation.

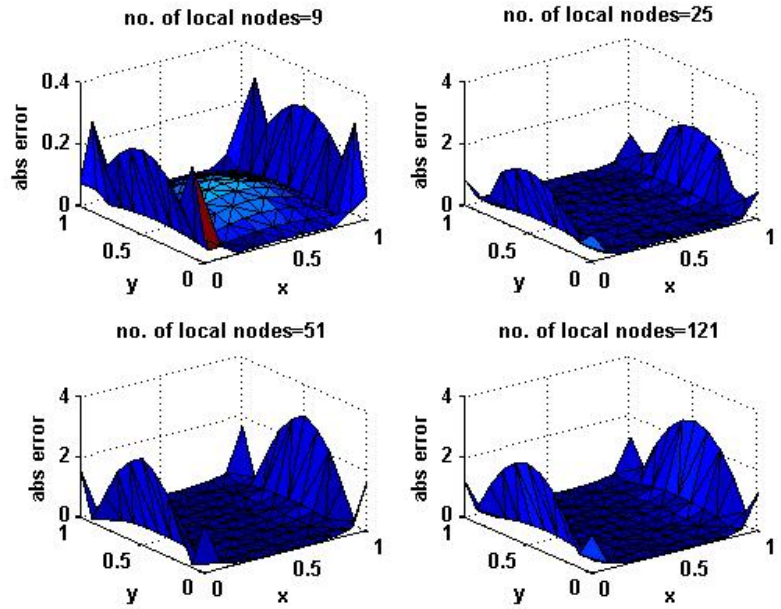

Figure 9.7 The absolute error distribution of $\frac{\partial^2 u}{\partial x^2}$ approximation.

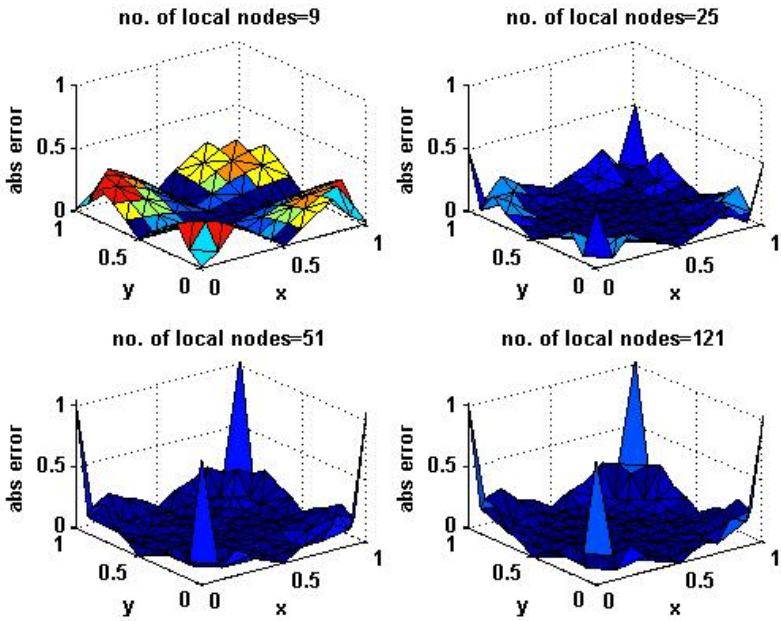

Figure 9.8 The absolute error distribution of $\frac{\partial^2 u}{\partial x \partial y}$ approximation.

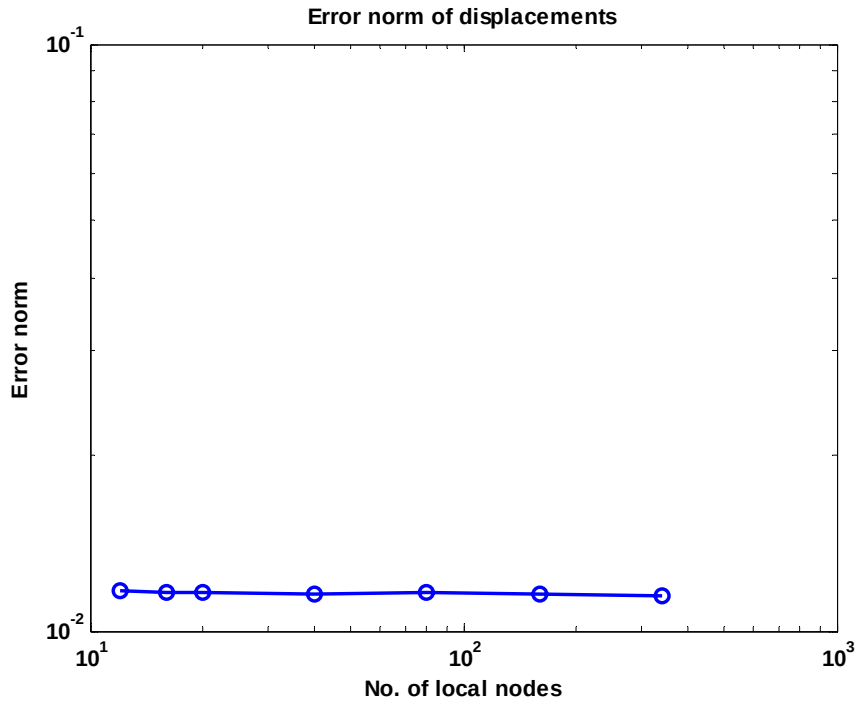

Figure 9.9 Error norms of displacements of the LC-RPIM using different number of local nodes.

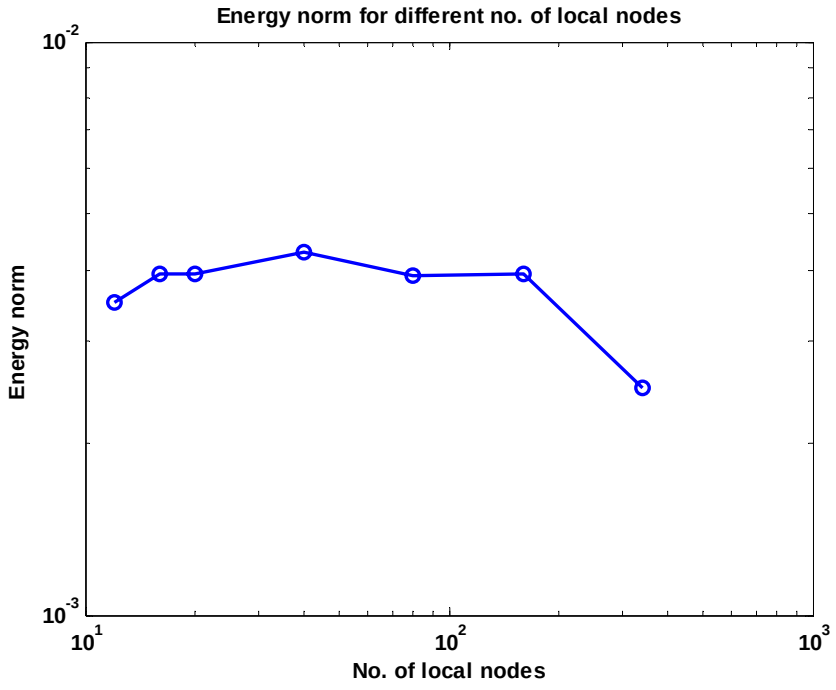

Figure 9.10 Energy norms of the LC-RPIM using different number of local nodes.

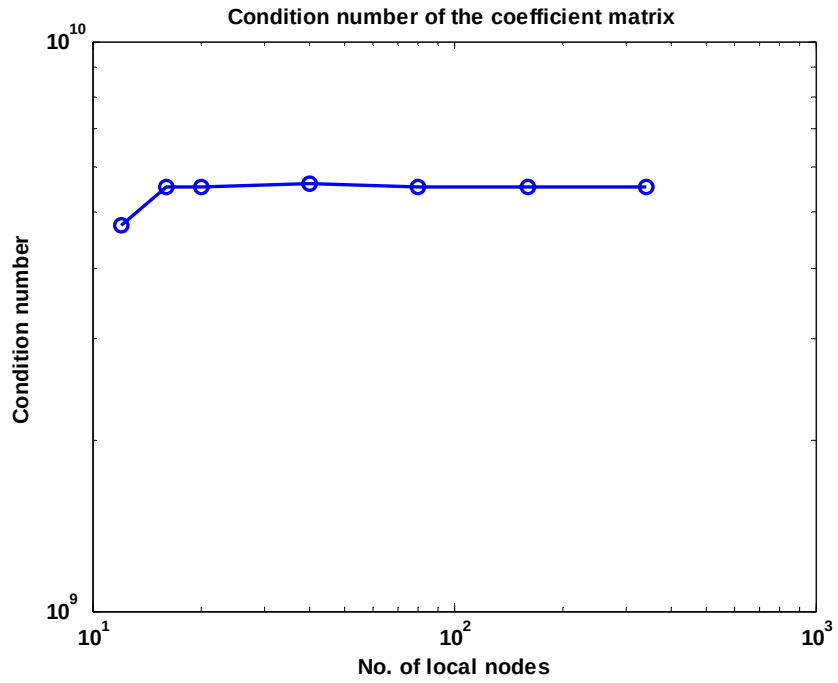

Figure 9.11 Condition number of the stiffness matrix of the LC-RPIM using different number of local nodes.

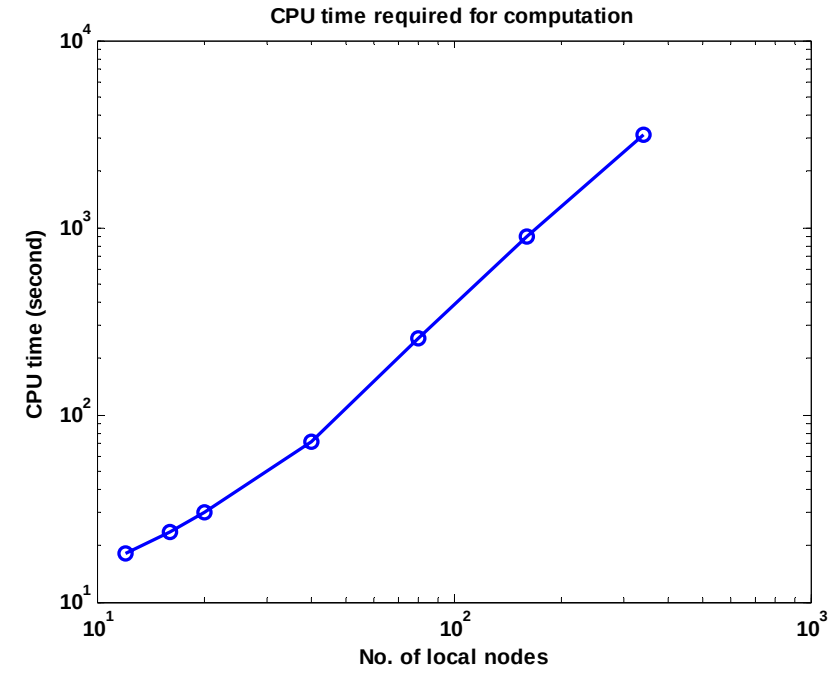

Figure 9.12 Distribution of a set of 100 randomly scattered nodes in a square domain.

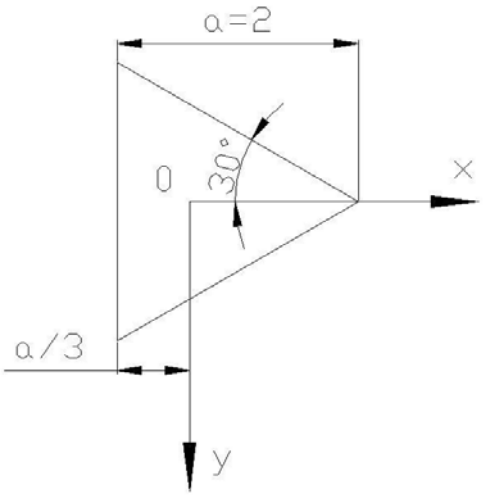

(a)

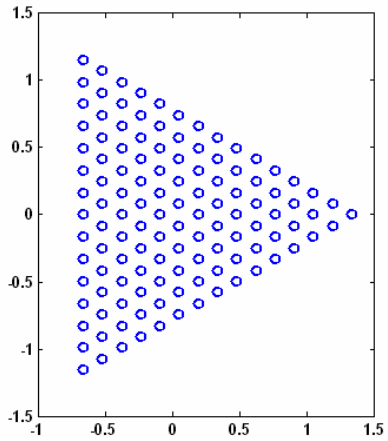

(b)

Figure 9.13 (a) Dimension of a triangular cross section bar, (b) a model of the bar with 120 field nodes.

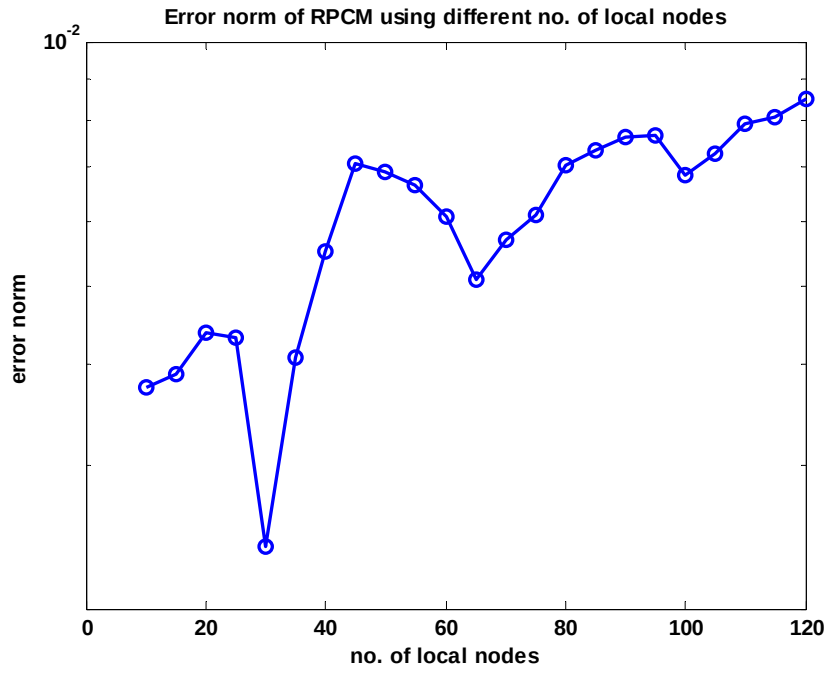

Figure 9.14 Error norm of the RPCM solution with different number of local nodes.

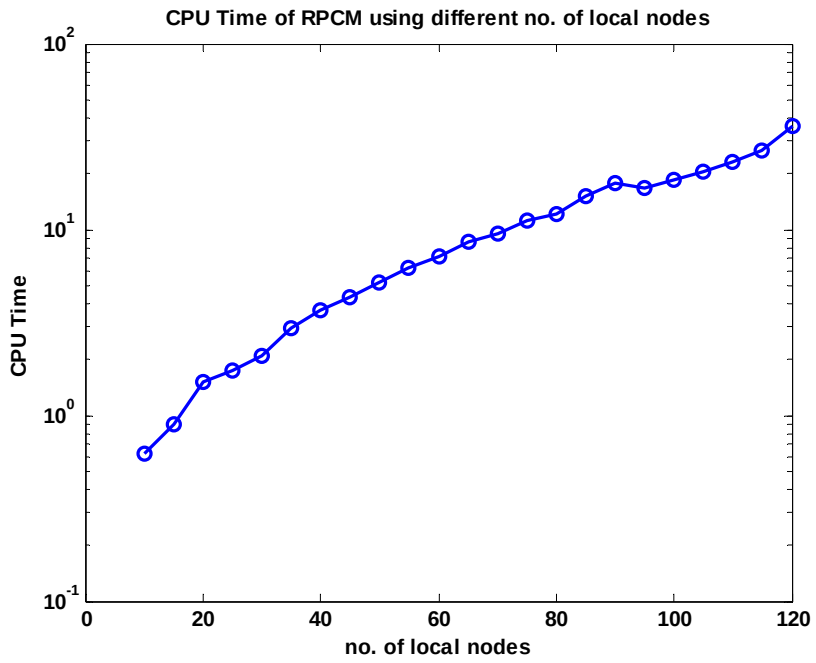

Figure 9.15 Computational time of the RPCM with different number of local nodes.

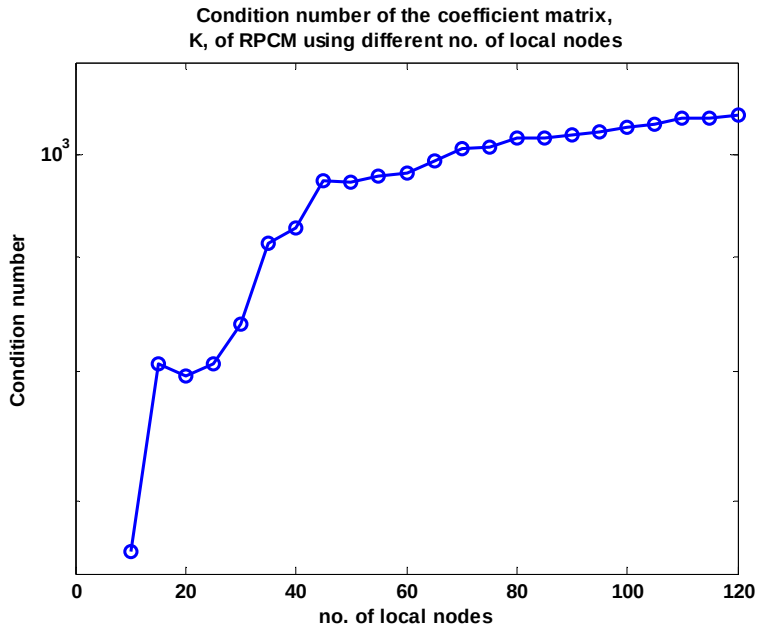

Figure 9.16 Condition number of the coefficient matrix of the RPCM with different number of local nodes.

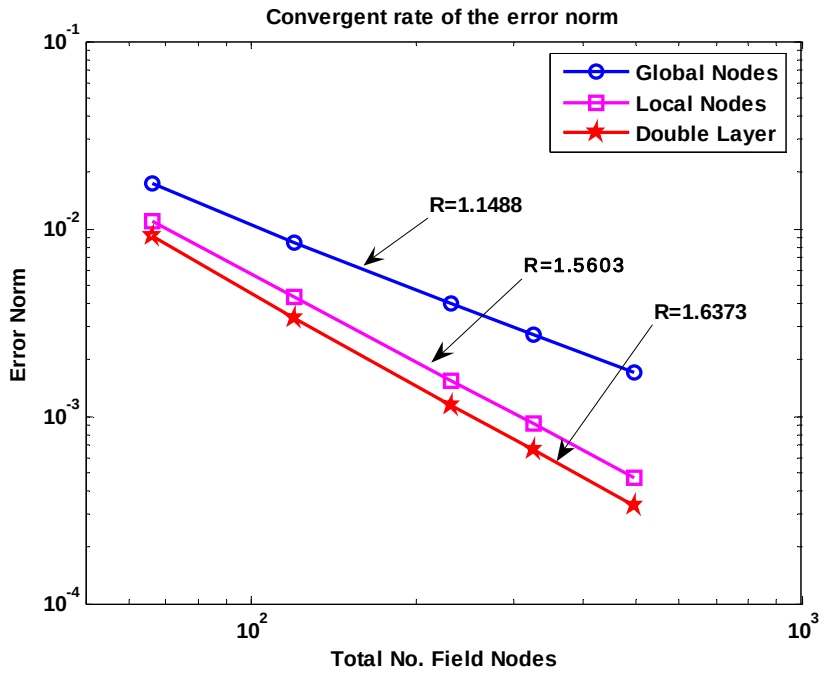

Figure 9.17 Comparison of the convergent rate in term of the error norm among the different schemes.

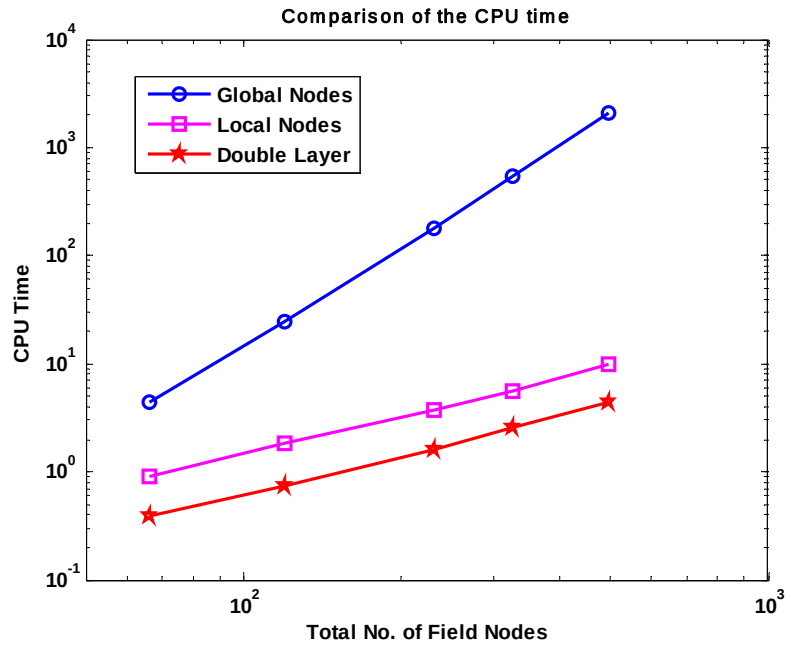

Figure 9.18 Comparison of the computational time among different schemes.

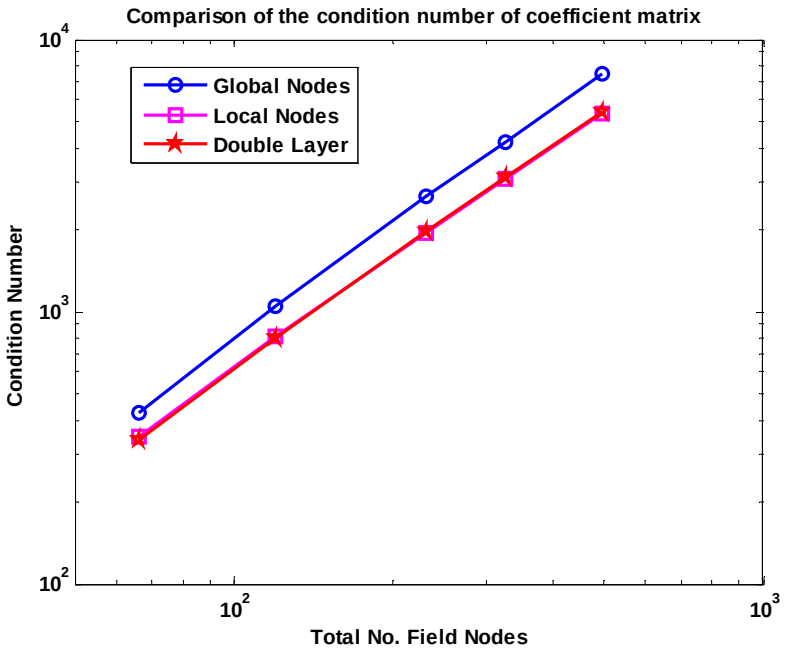

Figure 9.19 Comparison of the condition number of the coefficient matrices among different schemes.

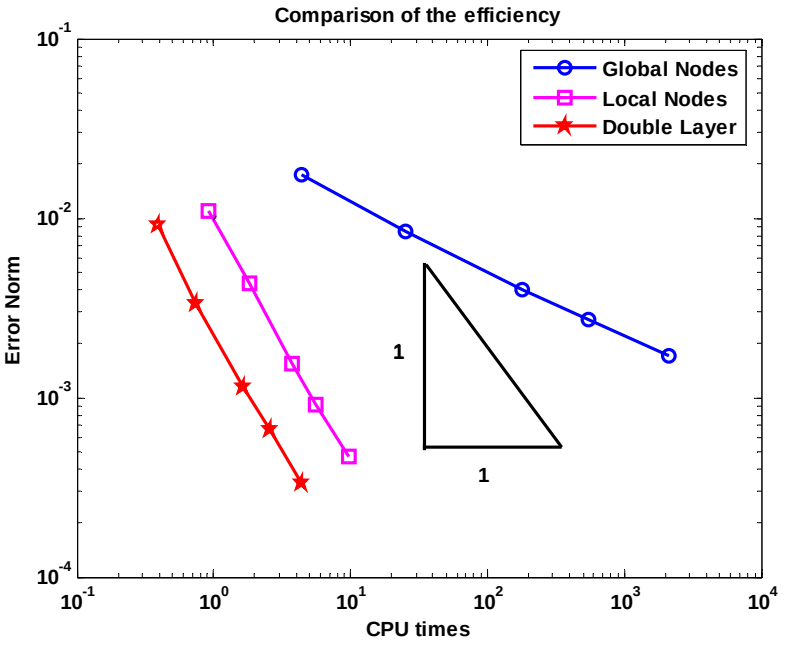

Figure 9.20 Comparison of the efficiency among different schemes.

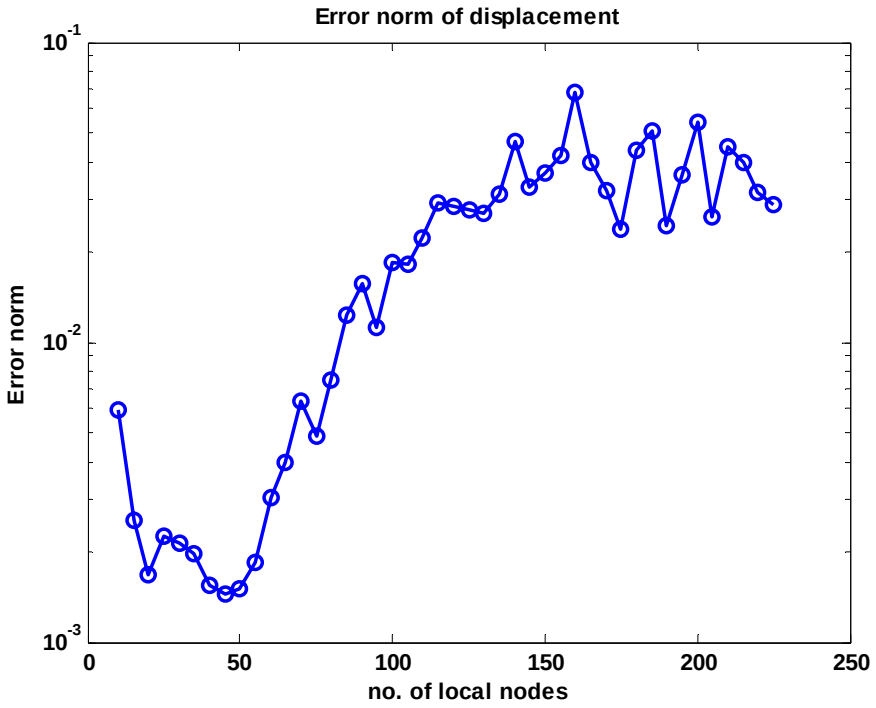

Figure 9.21 Error norm of the displacements obtained by RLS-RPCM.

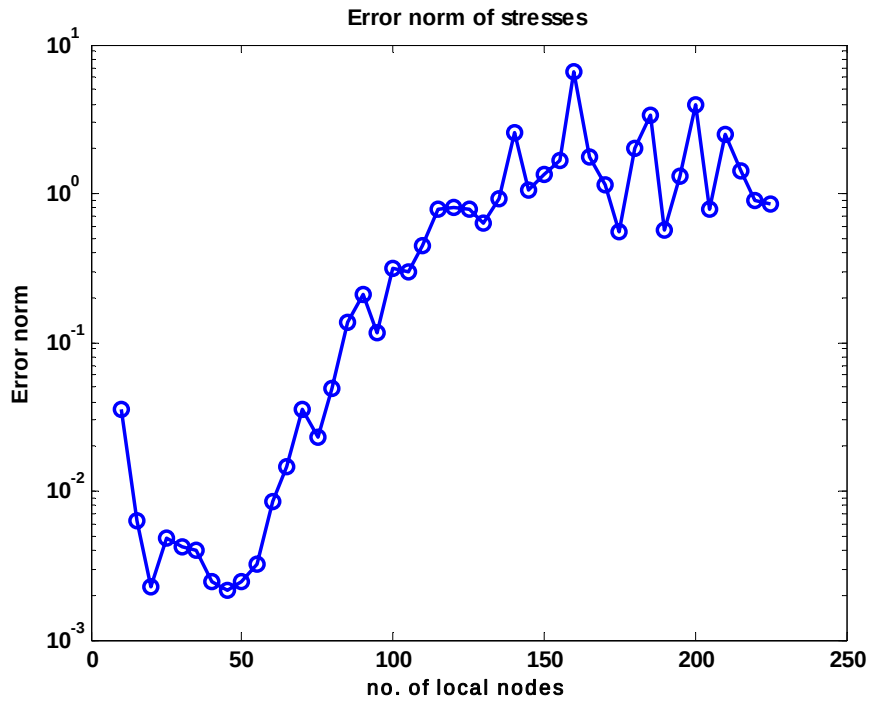

Figure 9.22 Error norm of the stresses obtained by RLS-RPCM.

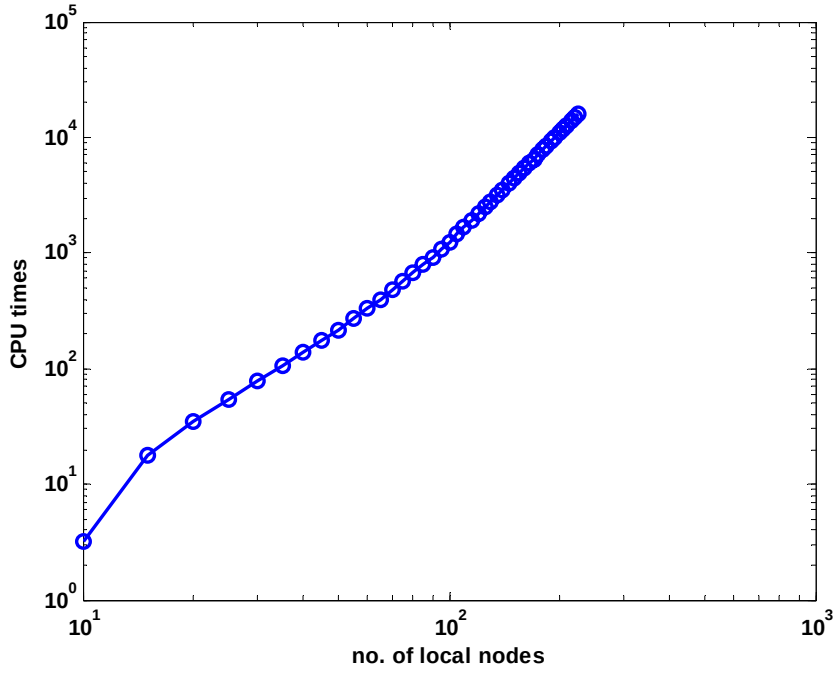

Figure 9.23 Computational time required for the RLS-RPCM with different number of local nodes.

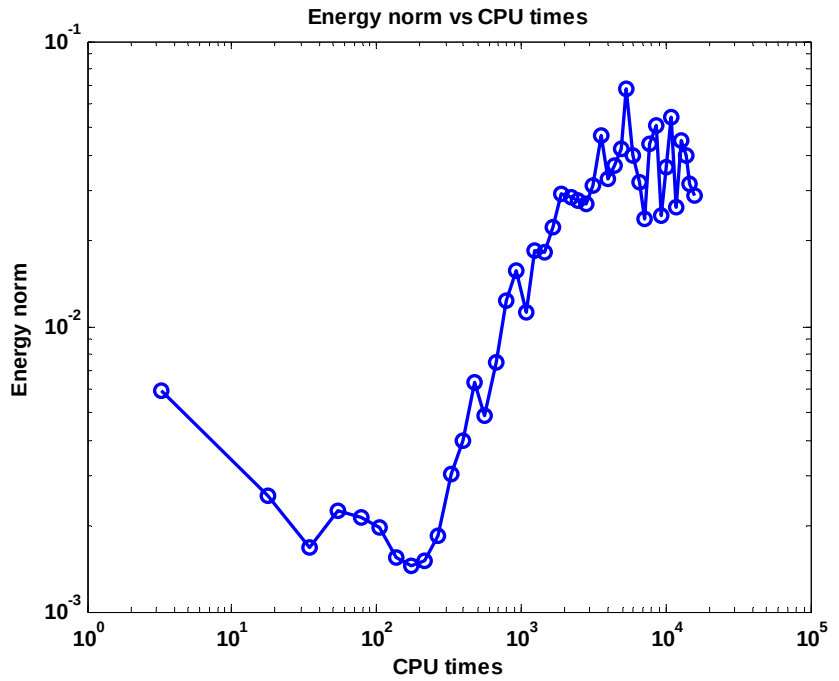

Figure 9.24 Efficiency of the RLS-RPCM with different local nodes in term of energy norm.

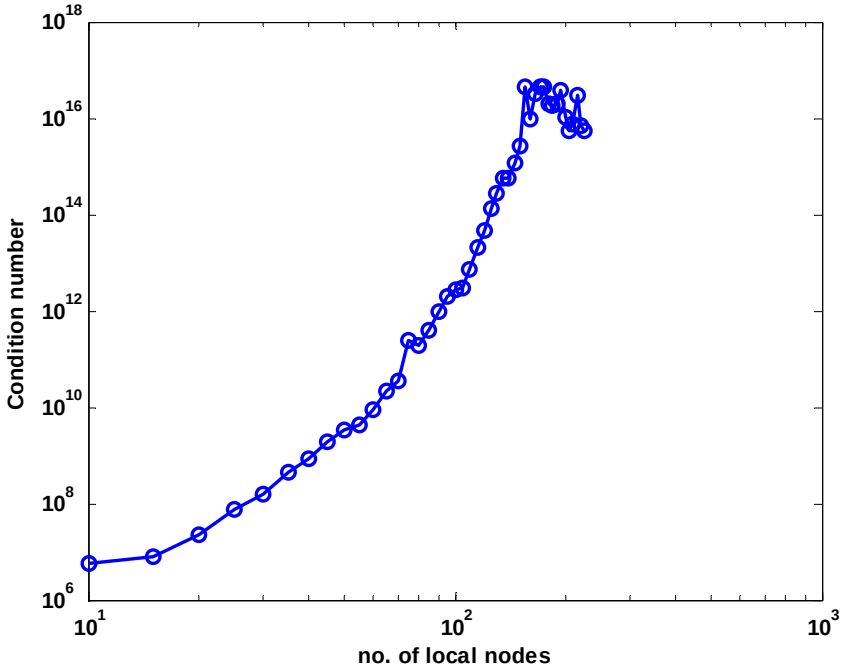

Figure 9.25 Condition number of the coefficient matrix of RLS-RPCM using different number of local nodes.

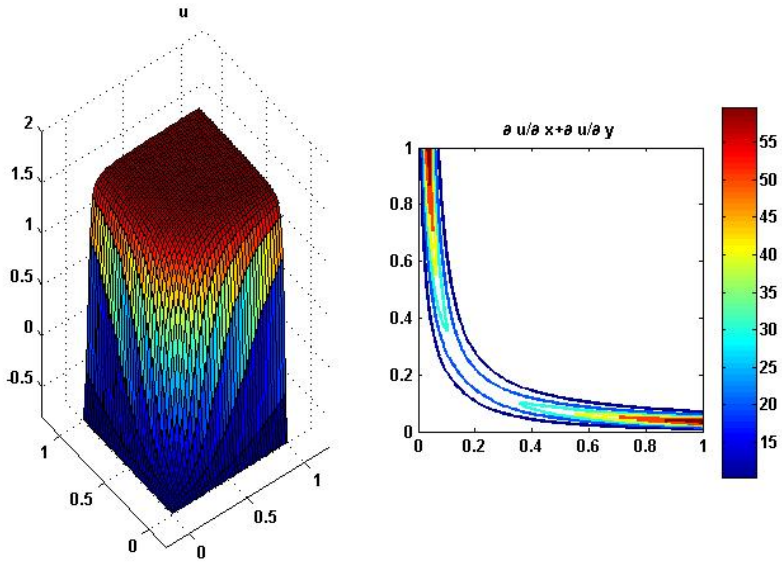

Figure 9.26 The plot of the field function *u* and its derivatives.

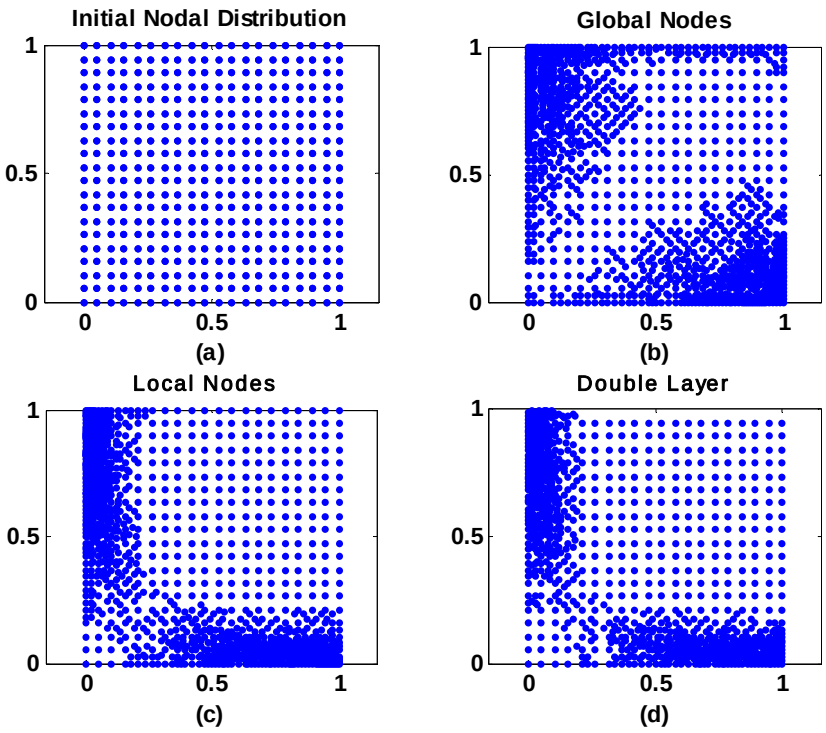

Figure 9.27 (a) The initial distribution, and the final nodal distribution for the adaptive RPCM using (b) global nodes, (c) 25 local nodes and (d) double layers of the local nodes.

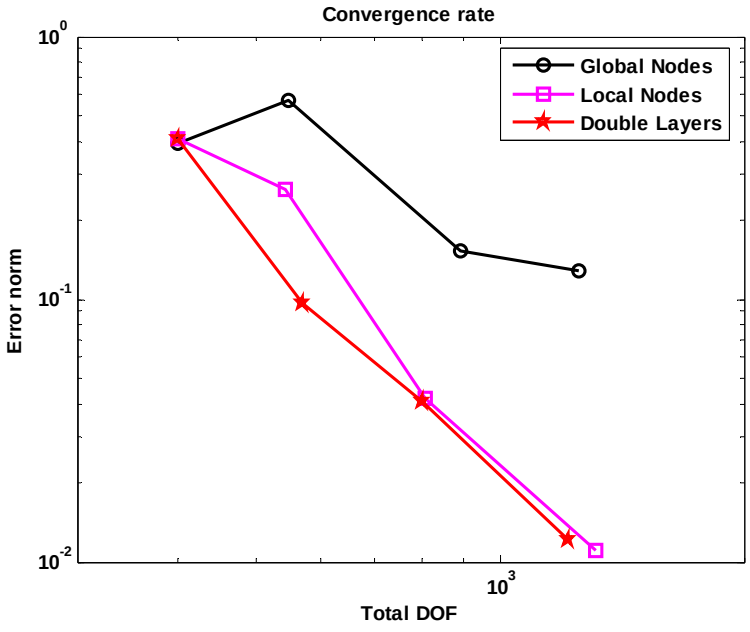

Figure 9.28 The comparison of the error norms of the field function at each adaptive step.

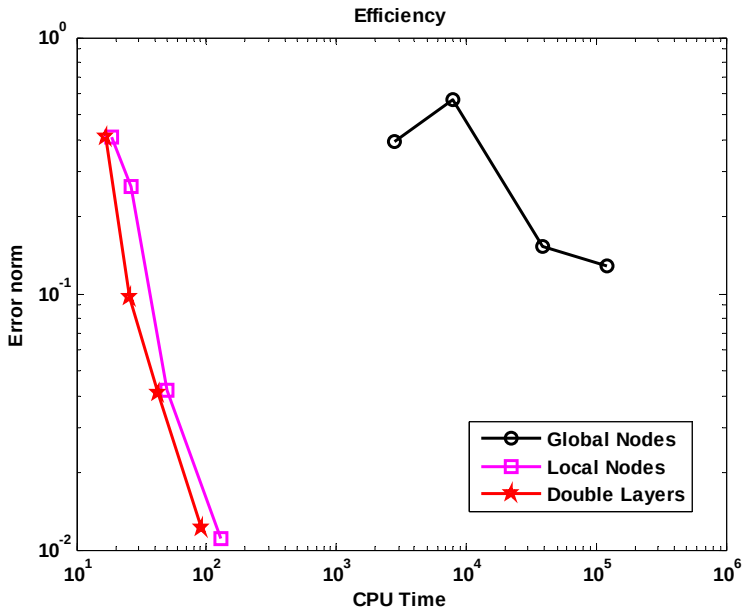

Figure 9.29 The comparison of the computational efficiency among different schemes.

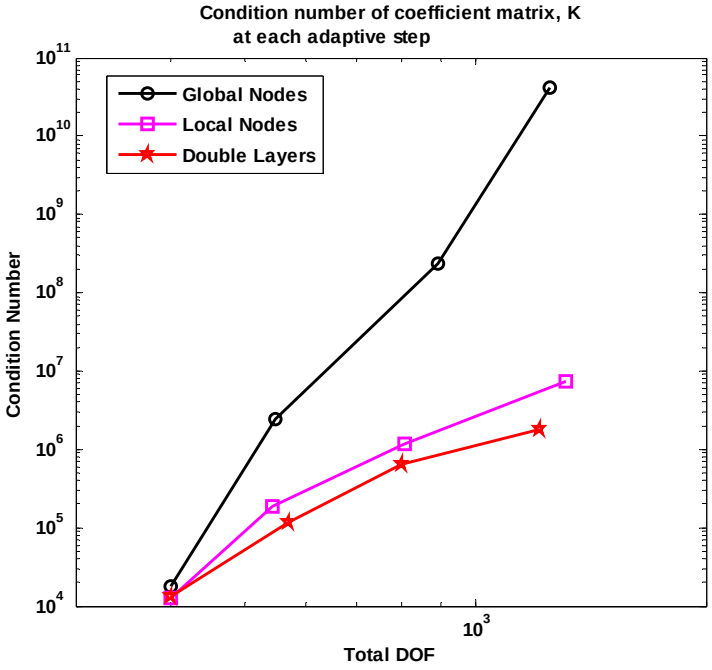

Figure 9.30 The comparison of the condition number of the coefficient matrice among different schemes at each adaptive step.

Chapter 10

Conclusion and Future Work

10.1 Conclusion Remarks

This study has focused on the development of meshfree strong-form methods. The developed strong-form methods have also been successfully extended to adaptive analysis. Through this study, the following conclusions are drawn:

(1) Three stabilization procedures are proposed to restore the stability of RPCM solution before it can be applied in adaptive analysis. The first suggested stabilization procedure is known as stabilization least-squares procedure [51]. In the stabilization least-squares procedure, an additional governing equation is imposed on the Dirichlet boundaries with a stabilization factor α to achieve certain degree of equilibrium on the Dirichlet boundaries. Good accuracy and stable solution is obtained through the proposed stabilization procedure. The stabilized least-squares radial point collocation method (LS-RPCM) has been successfully extended to adaptive analysis. However, the optimal value for the stabilization factor α still remains open. In this work, a very

small number is recommended and $\alpha = 0.05$ is used in this work. The advantages of strong-form meshfree method have been evidently shown in the large number of numerical examples.

(2) As Neumann boundary condition is blamed for the cause of instability, a least-square procedure with special treatment for boundaries is proposed to stabilize the solution of RPCM [68]. In the second stabilization procedure, more collocation points (not nodes) are introduced on the boundaries to reduce the 'strong' requirement of satisfying the governing equation and boundary conditions, and hence a relaxation effect is provided. The well-known least-square technique is applied to solve for the over-determined algebraic equations. Although the boundary conditions and the governing equation are not fully satisfied on nodes, the solution of the LS-RPCM is stable and in good accuracy. As stability is restored, the LS-RPCM is also extended to adaptive analysis. Examples illustrated in this work have clearly shown that good result can be obtained in the adaptive LS-RPCM.

(3) Regularization technique that commonly be used for solving ill-posed inversed problem is used to stabilize the solution of RPCM in this work [67]. The regularization procedure that adopts Tikhonov regularization technique is introduced in the regularization least-squares RPCM (RLS-RPCM). As special regularization equations and regularization points are suggested, no regularization factor has to be determined in the

RLS-RPCM. After stable and accurate solution is obtained through the proposed regularization procedure, RLS-RPCM has also successfully applied in adaptive analysis. A vast number of examples have shown adaptive RLS-RPCM is efficient and good numerical performance is demonstrated.

(4) In addition to the strong-form meshfree methods, a classical subdomain method integrated with RPIM shape functions is proposed [71]. By applying the meshfree techniques in classical subdomain method, the present method has demonstrated good stability and accuracy. Numerous numerical examples have shown the subdomain method can be easily extended to adaptive analysis and good results can be obtained. Subdomain method has also been shown robust, stable and accurate as compared to stabilized RPCM. One of the main reasons may due to the formulation procedure that integrated Neumann boundary condition naturally. The residual in the subdomain is also kept to minimum. For strong form method, the problem domain is only represented by nodes and residual is kept to minimum at nodes only. Nevertheless, strong form method has also possesses several attractive features such as feature of free from domain discretization and integration.

(5) Before all the meshfree strong-form method can be extended to adaptive analysis, a robust and effective error estimator that is customized for the strong-form method has to be developed. This is one of the most

challenging works in this thesis as most of the well established error estimator is only applicable for weak-form and based on mesh. The residual based error estimator proposed in this work is an excellent error estimator [69]. It has been shown effective and robust in the numerous numerical examples of various meshfree strong-form methods. In addition, this versatile error estimator has been successfully implemented in the adaptive FEM and adaptive subdomain method as well. As compared to the conventional error estimators used in the adaptive FEM, the present error estimator has also exhibited great advantages in terms of computational cost and efficiency.

(6) RPIM approximation is used in all the strong-form methods and the proposed subdomain method to construct their shape functions. In RPIM approximation based on the local RBFs, RBFs has significantly influences to the solutions. Hence, a thorough study of the local RBFs is very important. Although the shape parameters of the local RBFs have been comprehensively studied in literature, the effects of the number of local nodes for meshfree methods are not intensively investigated. In this work, an insightful and comprehensive study on the effects of the number of local nodes for meshfree methods based on local RBFs is provided [70]. The local RBFs not only reduce the computational cost drastically, but also provide a more stable coefficient matrix, especially in the strong-form meshfree methods. Instead of suggesting how many local

nodes to be used, a concept of ‘layer’ is introduced to facilitate the nodal selection in the function approximation.

10.2 Recommendation for future work

Based on the presented work in this thesis, the following recommendations are given for future work:

(1) All the examples given in this thesis are one or two dimensional problems. It is possible to extend the presented strong-form meshfree methods to solve for three dimensional problems. The proposed stabilization techniques are still applicable; however, some modifications are required. As the formulation of strong-form method is simple and straightforward, low computational cost is expected in the three dimensional cases.

(2) It is also possible to extend my adaptive works to non-linear and dynamic problems. However, a more complicated adaptive strategy has to be devised. In the dynamics problems, as the field function is varying at different time, coarsening procedure is required to remove the unnecessary nodes in the problem domain.

(3) Since knowledge of meshfree techniques has been gained through the experience in the past, it is possible to apply those techniques to the classical method, e.g., FEM, subdomain method. Besides the RPIM approximation, it is also possible to use PPIM approximation in the subdomain formulation with some special treatments on the boundaries.

(4) Although several stabilization techniques are suggested in the presented work, I believe that these proposed stabilization procedures are not the only possible approaches to provide a stable strong-form solution. As development of strong-form meshfree methods is still at the developing stage, more stabilization procedures or novel formulations may be proposed in the future. A stable strong-form solution is still very much desired and in great demand.

References

1 Ainsworth M and Oden JT (1993) A unified approach to a posteriori error estimation using element residual methods, Numer. Math, 65: 23-50.

2 Atluri SN, Cho JY, Kim HG (1999) Analysis of thin beams using the meshless local Petrov-Galerkin (MLPG) method, with generalized moving least-squares interpolation, Computational Mechanics, 24: 334-347.

3 Argyris JH, Kelsey S (1954) Energy theorem and structural analysis, Aircraft Engineering, 26/27.

4 Babuska I, Duran R and Rodriguez (1992), Analysis of the efficiency of an a posteriori error estimator for linear triangular finite element, SIAM Journal on Numerical Analysis, Vol. 29, No. 4: 947-964.

5 Babuska I, Melenk JM (1997) The partition of unity method, International Journal for Numerical Methods in Engineering, 40(4): 727-758.

6 Babuska I and Rheinboldt WC (1978) A posteriori error estimates for the finite element method, Int. J. Numer. Methods Engrg. 12: 1597-1615.

7 Behrens J, Iske A and Kaser M (2002)Adaptive meshfree method of backward characteristic for non linear transport equations, Meshfree Methods for Partial Differential Equations, M. Gribel and M.A Schweitzer (eds.), Springer-Verlag, Heidelberg, 21-26.

8 Belytschko T, Krongauz Y, Organ D, Fleming M, Krysl P (1996) Meshless methods: an overview and recent developments, Computer methods in applied mechanics and engineering, 139: 3-47.

9 Belytschko T, Lu YY, Gu L (1994) Element-free Galerkin methods, Int. J. Numer. Methods Eng., 37: 229–256.

10 Blacker T and Belytschko T (1994) Superconvergent patch recovery with equilibrium and conjoint interpolant enhancements, Int. J. Numer. Methods Engrg. 37:517-536.

11 Buhmann MD (2000) Radial Basis function, Acta Numrica, 9:1-38.

12 Cheng M, Liu GR (2002) A novel finite point method for flow simulation, International Journal for Numerical Methods in Fluids 39(12): 1161-1178.

13 Carstensen C and Verfürth R (1999) Edge residuals dominate a posteriori error estimates for low order finite element methods, SIAM J. Numer. Anal. 36: 1571–1587.

14 Chung HJ, Belystchko T (1998) Error estimate in the EFG method, Comput. Mech., 21: 91-100.

15 Clough RW (1960) The finite element method in plane stress analysis, Proceedings, Second ASCE Conference on Electronic Computation, Pittsburgh, PA, pp. 345-378.

16 Cook DR, Young WC (1998) Advanced Mechanics and Materials, Prentice Hall.

17 Courant R, Friedrichs KO, Lewy H (1928) Über die partiellen differenzengleichungen de mathematischen Physik. *Mathematische Annalen*, 100:32-74.

18 Duarte CA, Oden JT (1996) An hp adaptive method using clouds, Comput. Methods Appl. Mech. Eng., 139: 237-262.

19 Franke R (1982) Scattered data interpolation: tests of some methods, Math. Comp. 48:181-200.

20 Forsythe GE, Wasow WR (1960) Finite-difference methods for partial differential equations, Wiley, New York.

21 Gingold RA, Monaghan JJ (1977) Smooth particle hydrodynamics: theory and application to non-spherical stars, Monthly Notices of the Royal Astronomical Society, 181(2):375-389.

22 Girault V (1974) Theory of a finite difference method on irregular networks, SIAM Journal on Numerical Analysis, 11(2): 260-282.

23 Golberg MA, Chen CS (1996) Improved multiquadric approximation for partial differential equations, Engrg. Anal. Bound. Elem. 18: 9-17.

24 Gordon WJ, Wixom JA (1978), Shepard's method of 'Metric Interpolation' to bivariate and

multivariate data. Mathematics of Computation, 32: 253-264.

25 Gu YT, Liu GR (2002) A boundary point interpolation method for stress analysis of solids, Computational Mechanics, 28: 47-54.

26 Gu YT, Liu GR (2003) A boundary radial point interpolation method (BRPIM) for 2-D structural analyses, Structural Engineering and Mechanics, 15(5): 535-550.

27 Gu YT, Liu GR (2005) A meshfree weak-strong (MWS) form method for time dependent problems, 35(2): 134-145.

28 Guibas L, Knuth D and Sharir M (1992) Randomized incremental construction of Delaunay and Voronoi diagram, Algorithmica, 7: 381-413.

29 Gutzmer T and Iske (1997) A detection of discontinuities in scattered data approximation, Numerical Algorithms, 16: 155-170.

30 Hansen PC (1992) Analysis of discrete ill-posed problems by mean of the L-curve, SIAM Rev., 34: 561-580.

31 Hardy RL (1990) Theory and applications of multiquadrics-Biharmonic method (20 years of discovery 1968-1988). Comput. Math. Appl. 19 (8/9):163-208.

32 Hon YC, Mao XZ (1997) A multiquadric interpolation method for solving initial value problems, Sci. Comput. 12(1): 51-55.

33 Hon YC, Schaback R (2001) On unsymmetric collocation by radial basis functions, Appl. Math. Comp. 119: 177-186.

34 Lancaster P, Salkauskas K (1981) Surfaces generated by moving least-squares methods, Math. Comput., 37: 141-158.

35 Lee CK, Liu X, Fan SC (2003) Local multiquadric approximation for solving boundary value problems, Comput. Mech., 30:396-409.

36 Li Y, Liu GR, Dai KY, Luan MT, Zhong ZH, Li GY, Han X (2007) Contact analysis for solids based on linearly conforming radial point interpolation method (LC-RPIM), Computational Mechanics, 39(4): 537-554.

37 Liszka T, Orkisz J (1977) Finite difference methods pf arbitrary irregular meshes in non-linear problems of applied mechanics. In Proc. 4th Int. Conf. on Structural Mech. In Reactor Tech., San Francisco, USA.

38 Liszka T, Orkisz J (1979) The finite difference method at arbitrary irregular grids and its application in applied mechanics, Comp. Struct., 11:83-95.

39 Liszka TJ, Duarte CAM, Tworzydlo WW (1996) Hp-Meshless cloud method, Comput. Methods Appl. Mech. Engrg., 139:263-288.

40 Liu GR (2002) Meshfree methods: moving beyond the finite element method. CRC press, Boca Baton, USA.

41 Liu GR, Gu YT (2001), A point interpolation method for two-dimensional solids. International Journal of Solids and Structures, 50: 937-951.

42 Liu GR, Gu YT (2001) A local radial point interpolation method (LRPIM) for free vibration analyses of 2-D solids. J. Sound Vib. 246: 29-46.

43 Liu GR, Gu YT (2002) A truly meshless method based on the strong-weak-form, Advances in Meshfree and X-FEM Methods, Proceeding of the 1st Asian Workshop in Meshfree Methods, Singapore, 259-261.

44 Liu GR, Gu YT (2003) A meshfree method: Meshfree weak-strong (MWS) form method, for 2-D solids, Computational Mechanics 33(1): 2-14.

45 Liu GR, Gu YT (2003) A matrix triangularization algorithm for point interpolation method, Computer Methods in Applied Mechanics and Engineering, 192(19): 2269-2295.

46 Liu GR, Gu YT (2005) An Introduction to Meshfree Methods and Their Programming. Springer Dordrecht, The Netherlands.

47 Liu GR, Han X, Computational inverse Techniques in Nondestructive Evaluation, CRC Press, 2003.

48 Liu GR, Kee BBT (2005) An adaptive meshfree least-square method (***keynote***), Computational & Experimental Mechanics 2005, UKM, Bangi, Malaysia, p1-9, 2005 May.

49 Liu GR, Kee BBT (2005) An adaptive meshfree method based on regularized least-squares formulation, 13th International conference on computational & experimental engineering and sciences (ICCES), Chennai, India.

50 Liu GR, Kee BBT (2006) A regularized strong-form meshfree method for adaptive analysis (keynote), III European Conference on Computational Mechanics (ECCM) Solids, Structures and Coupled Problems in Engineering, Lisbon, Portugal.

51 Liu GR, Kee BBT, Lu C (2006) A stabilized least-squares radial point collocation method (LS-RPCM) for adaptive analysis, Comput. Methods Appl. Mech. Engrg. 195:4843-4861.

52 Liu GR, Kee BBT, Zhong ZH, Li GY, Han X (2006) Adaptive meshfree methods using local nodes and radial basis functions (semi-plenary lecture), Computational Methods in Engineering and Science EPMESC, Sanya, Hainan, China.

53 Liu GR, Li Y, Luan MT, Dai KY, Xue W (2006) A linearly conforming radial point interpolation method for solid mechanics problems, International Journal of Computational Methods (in press).

54 Liu GR, Liu MB (2003) Smoothed particle hydrodynamics-A meshfree particle method, World Scientific, Singapore.

55 Liu GR, Wu YL, Ding H (2004) Meshfree weak-strong (MWS) method and its application to incompressible flow problems, International Journal for Numerical Methods in Fluids, 46(10): 1025-1047.

56 Liu GR, Zhang GY, Gu YT Wang YY (2005) A meshfree radial point interpolation method (RPIM) for three-dimensional solids. Comput. Mech. 36: 421-430.

57 Liu GR, Zhang J, Li H, Lam KY, Kee BBT (2006) Radial point interpolation based finite different method for mechanics problems, Int. J. Numer. Mech. Engrg. 68: 728-754.

58 Liu WK, Jun S, Zhang YF (1995) Reproducing kernel particle methods, International Journal for Numerical Methods in Engineering, 20: 1081-1106.

59 Liu WK, Jun S, Sihling DT, Chen Y, Hao W (1997) Multiresolution reproducing kernel

particle method for computational fluid dynamics, International Journal for Numerical Methods in Fluids, 24(12): 1391-1415.

60 Liu WK, Jun S (1998) Multiple scale reproducing kernel particle method for large deformation problems, International Journal for Numerical Methods in Engineering, 141: 1339-1362.

61 Liu X, Liu GR, Tai K, Lam KY (2002) Radial basis point interpolation collocation method for 2-d solid problem, Proceedings of The 2nd International Conference on Structural Stability and Dynamics Singapore, December 16–18, pp. 35–40.

62 Liu X, Liu GR, Tai K, Lam KY (2005) Radial point interpolation collocation method (RPICM) for partial differential equations, International Journal Computers and Mathematics with Applications, 50:1425-1442.

63 Liu X, Liu GR, Tai K, Lam KY (2005) Radial point interpolation collocation method (RPICM) for the solution of nonlinear Poisson problems, Comput. Mech. 36:298:306.

64 Lucy L (1977) A numerical approach to testing the fission hypothesis, Astron. J., 82: 1013-1024.

65 Kansa EJ (1990) Multiquadrics: a scattered data approximation scheme with applications to computational fluid-dynamics I&II. Comput. Math. Appl. 19(8/9): 127-161.

66 Kansa EJ and Hon YC (2000) Circumventing the ill-conditioning problem with multiquadric radial basis functions: application to elliptic partial differential equations. Comput. Math. Appl., 39:123-137.

67 Kee BBT, Liu GR, Lu C (2007) A regularized least-squares radial point collocation method (RLS-RPCM) for adaptive analysis, Computational Mechanics, 40:837-853.

68 Kee BBT, Liu GR, Lu C (2006) A least-square radial point collocation method in linear elasticity, Eng. An. Bound. Elements (Accepted).

69 Kee BBT, Liu GR, Lu C (2007) A residual based error estimator using radial; basis functions, Finite Elements in Analysis and Design (Accepted).

70 Kee BBT, Liu GR, Song CX, Zhang J, Zhang GY (2007) A study on the effects of the number of local nodes for meshfree methods based on radial basis functions, Computer modeling in Engineering & Science (Summitted)

71 Kee BBT, Liu GR, Lu C (2007) An Adaptive Subdomain Method Based Local Radial Basis Functions (In Writing Process)

72 Mclain DH (1974), Drawing contours from arbitrary data points. Comput. J., 17: 318-324.

73 Melenk JM, Babuska I (1996) The partition of unity finite element method: basic theory and applications, Computer Methods in Applied Mechanics and Engineering, 139: 289-314.

74 Monaghan JJ (1982) Why particle methods work, SIAM Journal on Scientific and Statistical Computing, 3(4): 422-433.

75 Monaghan JJ (1988) An introduction to SPH, Computer Physics Communications, 48(1):89-96.

76 Monaghan JJ (1992) Smoothed particle hydrodynamics, Annu. Rev. Astron. Astrophys., 30: 543-574.

77 Monaghan JJ, Lattanzio JC (1991) A simulation of the collapse and fragmentation of cooling molecular clouds, Astrophysical Journal, 375(1): 177-189.

78 Mukherjee YX, Mukherjee S (1997) Boundary node method for potential problems, International Journal for Numerical Methods in Engineering, 40: 797-815.

79 Nayroles B, Touzot G, Villon P (1992) Generalizing the finite element method: diffuse approximation and diffuse elements, Computational Mechanics, 10: 307-318.

80 Onate E, Idelsohn S, Zienkiewicz OC, Taylor RL (1996) A finite point method in computational mechanics. Application to convective transport and fluid flow, International Journal for Numerical Methods in Engineering, 39(22): 3839-3866.

81 Onate E, Perazzo F, Miquel J (2001) A finite point method for elasticity problems, Computers & Structures, 79(22-25): 2151-2163.

82 Perrone N, Kao R (1975) A general finite difference method for arbitrary meshes,

Computers and Structures, 5(1): 45-57.

83 Powell MJD (1992) The theory of radial basis function approximation in 1990. Advances in Numerical Analysis, W. Light, ed., Oxford: Oxford Science Publications, pp. 105-210.

84 Rank E and Zienkiewicz OC (1987) Simple error estimator in the finite element method, Communications in Applied Numerical Methods, 3: 243-249.

85 Richtmyer RD, Morton KW (1967) Difference methods for initial-value problems, Interscience, New York.

86 Schaback R (1994) Approximation of polynomials by radial basis functions. Wavelets, image and surface fitting. (Eds. Laurent P.J., Mehaute Le and Schumaker L.L., Wellesley Mass.), 445-453.

87 Schonauer W (1998) Generation of Difference and Error Formulae of Arbitrary Consistency Order on an Unstructured Grid, ZAMM, 78(3): 1061-1062.

88 Snell V, Vesey DG, Mullord P (1981) The application of a general finite difference method to some boundary value problems, Computers and Structures 13(4): 547-552.

89 Tikhonov AN, Stepanov AV, Yagola AG (1990) Numerical methods for the solution of ill-posed problems. Kluwer Academics Publisher, Dordrecht.

90 Timoshenko SP, Goodier JN (1970) Theory of Elasticity, McGraw-Hill. New York.

91 Wang JG, Liu GR (2002) A point interpolation meshfree method based on radial basis function, Int. J. Numer. Meth. Engng. 54: 1623-1648.

92 Wang JG, Liu GR (2002) On the optimal shape parameters of radial basis function, Comput. Methods Appl. Mech. Eng. 191:21-26

93 Wendland H (1995) Piecewise polynomial positive definite and compactly supported radial basis functions of minimal degree. Adv. Comput. Math. 4:389-396.

94 Wiberg NE and Abdulwahab F (1993) Patch recovery based on the superconvergent derivatives and equilibrium, Int. J. Numer. Methods Engrg. 36:2703-2724.

95 Wiberg NE and Abdulwahab F (1994) Enhanced superconvergent patch recovery incorporating equilibrium and boundary conditions, Int. J. Numer. Methods Engrg. 37:3147-3440.

96 Wu ZM, Schaback R (1993) Local error estimates for radial basis function interpolation of scattered data, IMA Jouranl of Numerical Analysis 13:13-27.

97 Zhang GY, Liu GR, Kee BBT, Wang YY (2006) An adaptive analysis procedure using the linearly conforming point interpolation method (LC-PIM), International Journal of Solids and Structures (submitted).

98 Zhang X, Liu XH, Song KZ, Lu MW (2001) Least-squares collocation meshless method, International Journal for Numerical Methods in Engineering, 51: 1089-1100.

99 Zhang X, Song KZ, Lu MW, Liu X (2000) Meshless methods based on collocation with radial basis functions, Computational Mechanics, 26(4) 333-343.

100 Zienkiewicz OC, Taylor RL (1992) The Finite Element Method. McGraw-Hill: New York. Vol. 1, 1989, Vol. 2, 1992.

101 Zienkiewicz OC and Zhu JZ (1987) A simple error estimator and adaptive procedure for practical engineering analysis, Int. J. Numer. Methods Engrg., 24: 337-357.

102 Zienkiewicz OC and Zhu JZ (1992) The superconvergent patch recovery and a posteriori error estimates. Part 1: The recovery technique, Int. J. Numer. Methods Engrg., 33: 1331-1364.

103 Zienkiewicz OC and Zhu JZ (1992) The superconvergent patch recovery and a posteriori error estimates. Part 2: Error estimates and adaptivity, Int. J. Numer. Methods Engrg., 33: 1365-1382.

104 Zienkiewicz OC and Zhu JZ (1992) The superconvergent patch recovery (SPR) and adaptive finite element refinement, Comput. Methods Appl. Mech. Engrg. 101: 207-224.

Publications Arising From Thesis

Conference Papers:

[C1] Liu GR, **Kee BBT** (2005) An adaptive meshfree least-square method (***keynote***), Computational & Experimental Mechanics 2005, UKM, Bangi, Malaysia, p1-9, 2005 May.

[C2] Liu GR, **Kee BBT** (2005) An adaptive meshfree strong-form method based on regularized least-squares procedure, International Conference on Computational & Experimental Engineering and Sciences 2005, Chennai, India, p207-212, 2005 Dec.

[C3] Liu GR, **Kee BBT** (2006) A regularized strong-form meshfree method for adaptive analysis (***keynote***), III European Conference on Computational Mechanics (ECCM) Solids, Structures and Coupled Problems in Engineering, Lisbon, Portugal, 2006 July.

[C4] Liu GR, **Kee BBT**, Zhong ZH, Li GY, Han X (2006) Adaptive meshfree methods using local nodes and radial basis functions (***semi-plenary lecture***), Computational Methods in Engineering and Science EPMESC, Sanya, Hainan, China, Aug 2006.

Journal Papers:

[J1] Liu GR, **Kee BBT**, Lu C (2006) A stabilized least-squares radial point collocation method (LS-RPCM) for adaptive analysis, Comput. Methods Appl. Mech. Engrg., 195: 4843-4861

[J2] **Kee BBT**, Liu GR, Lu C (2007) A regularized least-square radial point collocation method (RLS-RPCM) for adaptive analysis, Comp. Mech., (Available Online).

[J3] **Kee BBT**, Liu GR, Lu C (2007) A Least-square Radial Point Collocation Method for

Adaptive Analysis in Linear Elasticity, Engineering Analysis with Boundary Elements, (Accepted)

[J4] **Kee BBT**, Liu GR, Lu C (2007) A Residual Based Error Estimator Using Radial Basis Functions, Finite Elements in Analysis and Design, (Submitted)

[J5] **Kee BBT**, Liu GR, Song CX, Zhang J, Zhang GY (2007) A Study on the Effect of the Number of Local Nodes for Meshfree Methods Based on Radial Basis Functions, Computer modeling in Engineering & Science (Summitted)

[J6] **Bernard B. T. Kee**, G. R. Liu, C. Lu (2007) An Adaptive Subdomain Method Based Local Radial Basis Functions, (In writing process)